

# Construction of a Low Background Facility for the COBRA Experiment and its Performance

Dissertation  
zur Erlangung des akademischen Grades  
eines Doktors der Naturwissenschaften  
des Fachbereichs Physik  
der Universität Dortmund



vorgelegt von  
**DIPL. PHYS. DANIEL MÜNSTERMANN**

Lehrstuhl für Experimentelle Physik IV  
Fachbereich Physik  
Universität Dortmund



Dortmund, den 12. September 2007

*In memory of my father, who passed his passion for science on to me.*

# Construction of a Low Background Facility for the COBRA Experiment and its Performance

Dissertation  
zur Erlangung des akademischen Grades  
eines Doktors der Naturwissenschaften  
des Fachbereichs Physik  
der Universität Dortmund

vorgelegt von  
DIPL. PHYS. DANIEL MÜNSTERMANN

Dekan:	Prof. Dr. M. Tolan
Referent:	Priv. Doz. Dr. K. Zuber
Korreferent:	Prof. Dr. C. Gößling
Beisitzer:	Dr. J. Becker

Tag der mündlichen Prüfung: 12. Oktober 2007

Teilergebnisse dieser Arbeit waren Gegenstand verschiedener Veröffentlichungen und Tagungsbeiträge. Eine Liste befindet sich am Ende der Arbeit ab Seite 153.

## Abstract

The COBRA experiment is investigating neutrinoless double-beta decays of Cd, Zn and Te isotopes with an array of CdZnTe semiconductor detectors. The current development stage consists of 64 CPG-type detectors of  $1\text{ cm}^3$  size each that will be arranged in form of a 3-dimensional  $4 \times 4 \times 4$ -array. At the time of writing, the first 16-detector layer was installed and has been collecting data since January 2007. The remaining three layers are currently being assembled.

Within the course of this work, key experimental components for the COBRA setup have been developed, among them several versions of custom-built preamplifiers, shapers and large parts of COBRA's VME-based ADC. Furthermore, the detector suspension and contacting were completely re-designed and the shielding concept was significantly enhanced.

Based on roughly 4.2 kg-d of data collected with the first operational 16-detector layer, a coincidence-based analysis has been performed focusing on neutrinoless double-beta decays of  $^{116}\text{Cd}$ ,  $^{128}\text{Te}$  and  $^{130}\text{Te}$  into excited states. For one of the decays, previously published limits on the half-life could be improved. Moreover, the power of the coincidence analysis method was demonstrated for decays involving gamma emission.



# Contents

<b>1</b>	<b>A Brief Status of Neutrino Physics</b>	<b>9</b>
<b>2</b>	<b>An Introduction to COBRA</b>	<b>17</b>
2.1	The Concept of COBRA . . . . .	17
2.1.1	History . . . . .	21
2.1.2	Components of COBRA . . . . .	24
2.2	Scope of this Work . . . . .	24
<b>3</b>	<b>Detectors and Contacting</b>	<b>25</b>
3.1	General Remarks . . . . .	25
3.2	CdZnTe Detectors . . . . .	25
3.2.1	Material Properties . . . . .	25
3.2.2	Electron-only Readout Devices . . . . .	27
3.2.3	Detector Selection for COBRA . . . . .	30
3.2.4	Detector Characterisation . . . . .	35
3.2.5	Zinc Content . . . . .	40
3.3	Detector Mountings . . . . .	41
3.4	Contacting . . . . .	44
3.5	Wiring . . . . .	46
<b>4</b>	<b>Shielding</b>	<b>53</b>
4.1	General Remarks . . . . .	53
4.2	The COBRA low-level setup . . . . .	54
4.2.1	Cosmic Rays and Muons: Vetoing and going Underground . . . . .	54
4.2.2	Shielding against Neutrons . . . . .	55
4.2.3	Faraday Cage and Nitrogen Flushing . . . . .	57
4.2.4	Environmental Radioactivity: Lead Shielding . . . . .	59
4.2.5	The Copper Core and NEST . . . . .	62
4.2.6	Performance of the Setup . . . . .	65
4.3	Outlook . . . . .	66
<b>5</b>	<b>Electronics</b>	<b>67</b>
5.1	Pre-Amplifiers . . . . .	67
5.1.1	Charge Sensitive Amplifiers . . . . .	67
5.1.2	General Design Remarks . . . . .	68
5.1.3	1st Generation: The 'Pertinax' Preamplifier . . . . .	69

5.1.4	2nd Generation: The Four-Channel Preamplifier . . . . .	70
5.1.5	3rd Generation: The 16-Channel Preamplifier . . . . .	71
5.1.6	Outlook . . . . .	71
5.2	Shapers . . . . .	72
5.2.1	Pulse Forming . . . . .	72
5.2.2	Main Amplifiers and shapers in COBRA . . . . .	73
5.2.3	The first shaper . . . . .	73
5.2.4	The inverting shaper . . . . .	74
5.2.5	The NIM-shaper for the 64 detector array . . . . .	75
5.2.6	Outlook . . . . .	76
5.3	ADCs . . . . .	78
5.3.1	General Remarks . . . . .	78
5.3.2	Early ADCs . . . . .	78
5.3.3	The VME-ADC . . . . .	79
5.3.4	Outlook . . . . .	85
5.4	Additional Electronics . . . . .	85
5.4.1	The 64-channel High-Voltage Supply . . . . .	85
5.4.2	The grid-bias supply . . . . .	85
5.4.3	The central control computer . . . . .	85
5.4.4	Outlook . . . . .	86
<b>6</b>	<b>Data Collection</b>	<b>87</b>
6.1	Improvement Stages . . . . .	87
6.2	Data Collection . . . . .	87
<b>7</b>	<b>Analysis</b>	<b>91</b>
7.1	Analysis Methods . . . . .	91
7.2	Decays Selected for Analysis . . . . .	93
7.3	Monte Carlo . . . . .	95
7.4	Experimental Data . . . . .	96
7.5	Results . . . . .	99
7.6	Evaluation of Method and Results . . . . .	99
<b>8</b>	<b>Summary and Outlook</b>	<b>103</b>
<b>A</b>	<b>Results of Detector Characterisations</b>	<b>105</b>
<b>B</b>	<b>Lead Brick Arrangement</b>	<b>109</b>
<b>C</b>	<b>NEST-Drawings</b>	<b>115</b>
<b>D</b>	<b>Circuit Diagrams and Silk Screens</b>	<b>131</b>
<b>E</b>	<b>DAQ-commands</b>	<b>133</b>
	<b>List of Tables</b>	<b>140</b>
	<b>List of Figures</b>	<b>142</b>

<i>CONTENTS</i>	7
<b>References</b>	<b>145</b>
<b>Publications</b>	<b>153</b>
<b>Acknowledgements</b>	<b>155</b>





# Chapter 1

## A Brief Status of Neutrino Physics

Amazingly, neutrinos play an important part in all our lives: Without them, the nuclear fusion that drives the sun would not be possible. Besides, they are participating in all  $\beta$ -decays. Since their proposal by Pauli in 1930 [Pau30] in order to explain the continuous electron energy spectrum observed in  $\beta$ -decay, it has been discovered that there are plentiful neutrinos in every single  $\text{cm}^3$  of space in and around us – however, the fact that they only take part in the weak and gravitational interactions causes them not to be seen without the help of extremely large detectors: due to their tiny interaction cross sections one has to observe huge numbers of nuclei – hundreds of kilograms or even tons of target matter – to see few of them interact. This is illustrated by the fact that it took until 1953 before neutrinos could be experimentally detected for the first time with a scintillation detector containing 283 litres of target liquid [Cow53].

For a long time, the question for the neutrino's rest mass was rather academic;  $\beta$ -decay experiments were not able to see any shift in the endpoint of the energy spectra with respect to the decay's released energy caused by a finite neutrino rest mass. Besides, the standard model of elementary particle physics which was developed in the 1970s was working extremely well with the assumption of a zero rest mass. Due to the huge number of neutrinos in the universe, however, the rest mass is nevertheless of some importance: in cosmology, it still plays an important role as a dark matter constituent even though it has lost its status as major dark matter candidate because structure formation surveys now require mostly cold dark matter<sup>1</sup> while neutrinos are virtually always moving with relativistic speeds and are therefore attributed to hot dark matter.

The recent years have seen neutrino physics change from a – statistically – rather 'coarse' branch of particle physics into one that is doing precision measurements: First, neutrino oscillations were discovered by Super-Kamiokande<sup>2</sup> [Hos06]: the experiment saw less upward going muons generated by neutrinos from the other side of the earth than expected with respect to downward going muons that were generated by neutrinos coming from the atmosphere above the experiment. Neutrino oscillations designate the fact that a neutrino which is e.g. produced in the atmosphere as  $\nu_\mu$  will with a certain probability act as  $\nu_e$  or  $\nu_\tau$  after it has travelled a certain distance. This is possible if the mass eigenstates – which propagate through space – are not identical with the weak or flavour eigenstates which govern the interaction in which

---

<sup>1</sup>Cold dark matter (CDM) is referred to as only very weakly interacting non-relativistic matter. Neutrinos are due to their small masses always ultra-relativistic. Candidates for CDM are so-called weakly interacting massive particles which can be motivated e.g. by supersymmetric theories (SUSY).

<sup>2</sup>official website: [http://www-sk.icrr.u-tokyo.ac.jp/sk/index\\_e.html](http://www-sk.icrr.u-tokyo.ac.jp/sk/index_e.html)

the neutrino is generated. A simplified description of the connection of the eigenstates can be written as

$$\begin{pmatrix} \nu_\mu \\ \nu_\tau \end{pmatrix} = U \cdot \begin{pmatrix} \nu_2 \\ \nu_3 \end{pmatrix}, \quad \text{with } U = \begin{pmatrix} \cos \theta & \sin \theta \\ -\sin \theta & \cos \theta \end{pmatrix}. \quad (1.0.1)$$

which links the flavour eigenstates, in our example  $\nu_\mu$  and  $\nu_\tau$ , to the mass eigenstates  $\nu_2$  and  $\nu_3$  by means of a rotation matrix which maps the two spaces onto each other by rotation about an angle  $\theta$ . This angle can be viewed as a leptonic analog to the Cabibbo-angle. After the generation as pure flavour eigenstate, the mass eigenstate (which is a linear combination of the three flavour eigenstates) begins to propagate through space. Therefore, the flavour of the neutrino – which can only be detected if it interacts weakly – might change during flight. An exhaustive derivation using the correct quantum mechanics can be found in [Zub04]. Therein, the transition probability to find a  $\nu_\tau$  of energy  $E$  at a distance  $L$  from where the neutrino was generated as a  $\nu_\mu$  is derived to be

$$P(\nu_\mu \Rightarrow \nu_\tau) = \sin^2(2\theta) \sin^2 \left( \frac{1.27 \Delta m^2 [eV^2] L [km]}{E [GeV]} \right). \quad (1.0.2)$$

Obviously, the probability is only non-vanishing if the rotation angle is different from zero and if  $\Delta m^2 = m_3^2 - m_2^2$  is non-zero. The observation of atmospheric neutrino oscillations by Super-Kamiokande hence proved the existence of neutrino rest masses even though nothing can be said about the absolute neutrino masses.

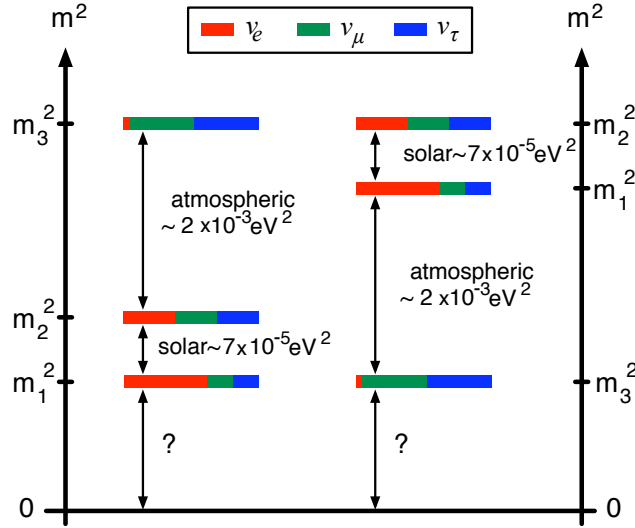
A bit later, SNO<sup>3</sup> explained the solar neutrino deficit – the fact, that the  $\nu_e$ -flux from the sun was around a factor two lower than expected from solar models – by finding that the ‘missing’ portion of  $\nu_e$ s had just oscillated into other flavours [Aha07, Aha05]. Currently, other accelerator-based oscillation experiments like K2K [Ahn06] and MINOS [Mic06] are struggling to measure the oscillation parameters more and more precisely, among them the mass differences between the neutrino generations. A large drawback of all oscillation experiments is that they cannot measure the absolute mass of any neutrino.

A standard but very sophisticated kinematic approach to this question is realised by the KATRIN<sup>4</sup> collaboration [KAT01]: By means of a giant electrostatic spectrometer the endpoint energy of the <sup>3</sup>H-decay will be investigated. It is commonly agreed that the successor of the Mainz-experiment [Wei99] will be the last and final step in kinematic experiments with tritium as it is hardly conceivable to build an even larger and more complex setup – KATRIN is a quite large collaboration compared to the Mainz-experiment’s, but its design goal is merely to improve Mainz’ limit ( $m_{\nu_e} \leq 2.3 \text{ eV}/c^2$  [Kra05]) by one order of magnitude and search for  $m_{\nu_e}$  down to 0.2 eV. Knowing that the oscillation experiments find mass differences of  $\Delta m_{\text{solar}}^2 \sim 10^{-4} \text{ eV}^2$  and  $\Delta m_{\text{atmospheric}}^2 \sim 10^{-3} \text{ eV}^2$ , it is not impossible but appears improbable that the electron neutrino’s mass can be found by KATRIN: for all other particle families, the mass of the lightest generation is much lower than the difference to the second generation. While, e.g., the mass of the electron is 0.511 MeV, the muon’s mass is 105.658 MeV so the mass difference is 105.147 MeV which is on the order of the muon’s mass. Naively, one could expect similar relations to hold for the neutrinos which would mean that the mass differences are on the order of the absolute masses of the heavier particle while the lighter particle dwells at a  $\Delta m$  lower mass accordingly.

<sup>3</sup>official website: <http://www.sno.phy.queensu.ca>

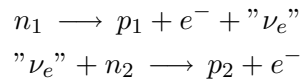
<sup>4</sup>official website: <http://www-ik.fzk.de/~katrin/index.html>

Sophisticated theoretical models can easily create almost degenerate neutrino masses at a comparatively large mass offset as well as a normal or even an inverted hierarchy where the mass eigenstate which is dominantly  $\nu_e$  is not the lightest one [Zub04]; Fig. 1.1 depicts the two favoured models. In any case it is possible that the rest mass of the electron neutrino  $\nu_e$  might be very small; preparing for an experimental search down to 50 meV seems to be indicated [Fer02, Fer03] which will be very challenging with a kinematic approach.



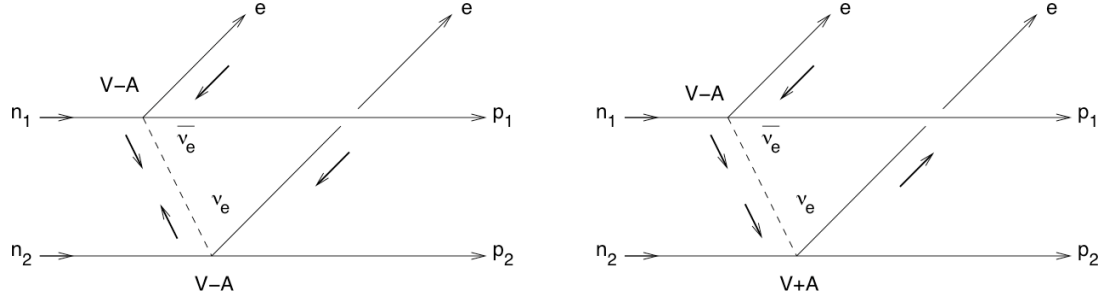
**Figure 1.1:** Normal and inverted neutrino mass hierarchies. The colours indicate the contributions of the different weak eigenstates to the mass eigenstates. In both models, the position on an absolute mass scale is unknown.

One possible solution to this dilemma is neutrinoless double-beta decay ( $0\nu\beta\beta$  decay): This special form of beta-decay can be depicted as a sequence of consecutive  $\beta^-$ -decay and inverse  $\beta^-$ -decay called "Racah sequence" [Rac37, Boe87, Zub04]



that could occur if there is in principle no difference between  $\nu_e$  and  $\bar{\nu}_e$  which is indicated by the notation "  $\nu_e$  ". In this case, the neutrino would be a so-called Majorana particle (its own anti-particle, only "  $\nu_{eL}$  " and "  $\nu_{eR}$  " exist) as opposed to all other elementary particles being Dirac particles (where e.g.  $e_L^+$ ,  $e_R^+$ ,  $e_L^-$  and  $e_R^-$  exist while only  $e_L^-$  and  $e_R^+$  take part in the weak interaction). As the neutrino carries no electric charge and does not interact via the strong force this would be conceivable.

In addition, if it carried a small rest mass – as indicated by the oscillation experiments – the neutrino's helicity would not be a conserved quantum number any more. Hence, there would be a small admixture of  $\bar{\nu}_{e(R)}$  to each  $\nu_{e(L)}$  and vice versa. A  $\bar{\nu}_e$  could leave the first vertex after a 'standard'  $\beta^-$ -decay and enter the second vertex as a  $\nu_e$  to make neutrinoless double beta decay possible while violating total lepton number conservation by two units. However, also other mechanisms enabling  $0\nu\beta\beta$  decay would be possible, e.g. a right-handed admixture to the



**Figure 1.2:** Schematics of  $0\nu\beta\beta$  decays via helicity flip (left) and right handed current (V+A) at the second vertex (right). The helicities are represented by the arrows. Taken from [Kie05]

weak force which is discussed in left-right-symmetric models could be dominant[Hir94]. Here, the right handed current (V+A) at the second vertex enables the reaction which is illustrated in Fig. 1.2.

Neutrinoless double beta decays can appear in four channels analogous to normal  $\beta$ -decay which occurs as  $\beta^-$ ,  $\beta^+$  and electron capture EC:

$$\begin{aligned}
 (Z,A) &\rightarrow (Z+2,A) + 2\beta^- && [0\nu\beta^-\beta^-] \\
 m_{\text{atom}}(Z,A) &= (m_{\text{atom}}(Z+2,A) - 2 \cdot m_e) + 2 \cdot m_e + E \\
 (Z,A) &\rightarrow (Z-2,A) + 2\beta^+ && [0\nu\beta^+\beta^+] \\
 m_{\text{atom}}(Z,A) &= (m_{\text{atom}}(Z-2,A) + 2 \cdot m_e) + 2 \cdot m_e + E \\
 e^- + (Z,A) &\rightarrow (Z-2,A) + \beta^+ && [0\nu\beta^+\text{EC}] \\
 m_{\text{atom}}(Z,A) &= (m_{\text{atom}}(Z-2,A) + 1 \cdot m_e) + m_e + E \\
 2e^- + (Z,A) &\rightarrow (Z-2,A) && [0\nu\text{ECEC}] \\
 m_{\text{atom}}(Z,A) &= (m_{\text{atom}}(Z-2,A)) + E
 \end{aligned}$$

The physics signature of the decays is unique for  $\beta$ -decays: As no neutrinos leave the nucleus, the exiting electrons or positrons carry away the complete decay energy yielding a line in the sum energy spectrum. The decay energy is simply given by the mass difference between mother and daughter nucleus. It is most often called 'Q-value':

$$Q = m(Z, A) - m(Z + 2, A) - 2m_e \quad \text{for } \beta^-\beta^-\text{-decays} \quad (1.0.3)$$

For kinematic reasons, the phase space of the decays involving positrons is reduced by 1022 keV per  $e^+$  so the corresponding half-life (which depends on the phase space) is larger.

Interestingly, it might be possible to disentangle the underlying physical mechanisms by comparing the decay rates of  $\beta^-\beta^-$  and  $\beta^+\text{EC}$  decays. While the former are dominated by the 'standard' mass-driven  $0\nu\beta\beta$  mechanism, the latter would be dominated by right-handed currents. Also decays into excited states might give some insight as the mass-driven mechanism only allows ground state to ground state transitions where angular momentum  $J$  and parity  $\pi$  stay at  $J^\pi = 0^+$ . Other mechanisms might allow decays into excited states with  $J^\pi = 2^+$ .

For the mass-driven mechanism, the half-life is given by [Zub04] as

$$(T_{\frac{1}{2}}^{0\nu})^{-1} = G^{0\nu}(Q, Z) |M_{GT}^{0\nu} - M_F^{0\nu}|^2 \left( \frac{\langle m_{\nu_e} \rangle}{m_e} \right)^2 \quad (1.0.4)$$

with  $G^{0\nu}(Q, Z)$  being the phase space integral and  $M_x^{0\nu}$  being the Gamow-Teller and Fermi nuclear matrix elements, respectively. The latter have to be numerically calculated for each nucleus, which is strongly model-dependent and inaccurate – estimations vary by a factor of 2–3 [Suh98, Cau07]. The phase space is analytically accessible and scales with

$$G^{0\nu}(Q, Z) \sim Q^5 \quad (1.0.5)$$

resulting in shorter half-lives of isotopes with larger Q-values. The effective Majorana neutrino mass  $\langle m_{\nu_e} \rangle$  is defined as

$$\langle m_{\nu_e} \rangle = \left| \sum_i U_{ei}^2 \eta_i m_i \right| \quad (1.0.6)$$

with  $\eta_i = \pm 1$  being the relative CP-phases,  $U_{ei}$  being the PMNS matrix elements and  $m_i$  being the corresponding mass eigenvalues.

The Pontecorvo-Maki-Nakagawa-Sakata (PMNS) matrix [Mak62] which describes the mixing of the neutrino eigenstates is the analog of the Cabibbo-Kobayashi-Maskawa (CKM) matrix. As demonstrated with the two-flavour example above, here the three neutrino flavour eigenstates  $\nu_e$ ,  $\nu_\mu$  and  $\nu_\tau$  are connected to the mass eigenstates  $\nu_1$ ,  $\nu_2$  and  $\nu_3$  according to the following generalised equation:

$$\begin{pmatrix} \nu_e \\ \nu_\mu \\ \nu_\tau \end{pmatrix} = \begin{pmatrix} U_{e1} & U_{e2} & U_{e3} \\ U_{\mu1} & U_{\mu2} & U_{\mu3} \\ U_{\tau1} & U_{\tau2} & U_{\tau3} \end{pmatrix} \begin{pmatrix} \nu_1 \\ \nu_2 \\ \nu_3 \end{pmatrix}. \quad (1.0.7)$$

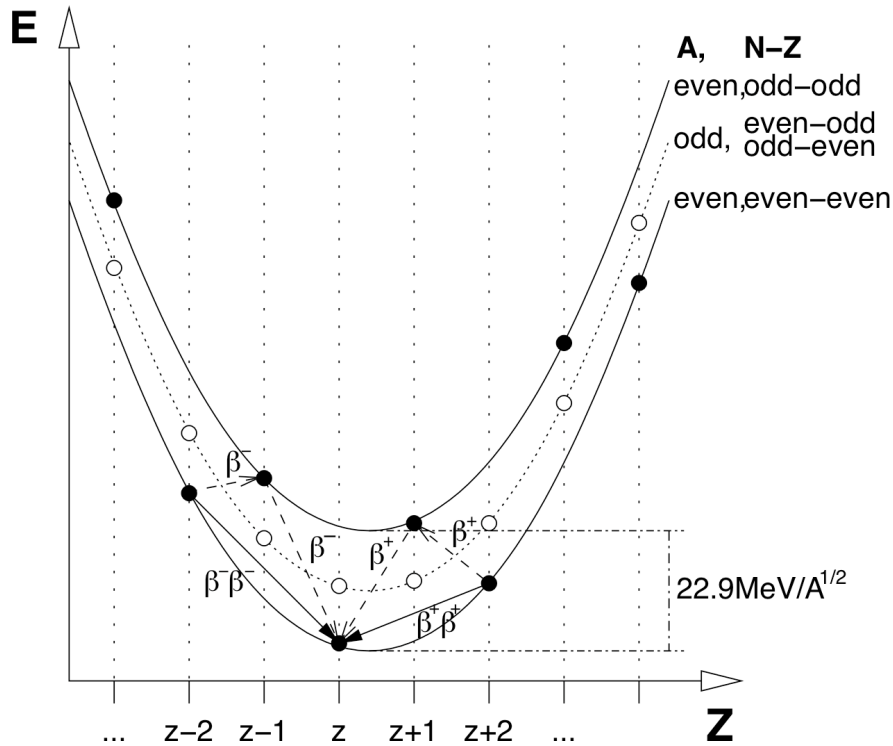
While it can be expected that  $\langle m_{\nu_e} \rangle$  will be dominated by the electron neutrino's mass, it is yet unclear how large the contributions from the other matrix elements will be and how the CP-phases will modify their contributions. Nevertheless, currently  $\langle m_{\nu_e} \rangle$  is assumed to be a good estimator for  $m_{\nu_e}$ .

It should be kept in mind, though, that neutrinos do not have to be Majorana particles – but the proof or falsification of neutrinoless double beta decay is one of only two ways to find out: the discovery that neutrinos possess a static magnetic moment would prove that they are Dirac-particles. However, this seems to be experimentally even more challenging than searches for  $0\nu\beta\beta$  decay and was pursued by the MUNU experiment [Dar05] which reached a lower limit on  $\mu_\nu$  about 9 orders of magnitude above the theoretical expectation for Dirac neutrinos.

Double beta decay was first proposed in its neutrino-accompanied form by Goeppert-Mayer in 1935 [GM35] as a second-order beta decay:

$$\begin{aligned} (Z, A) &\rightarrow (Z+2, A) + 2\beta^- + 2\bar{\nu}_e & [2\nu\beta^-\beta^-] \\ (Z, A) &\rightarrow (Z-2, A) + 2\beta^+ + 2\nu_e & [2\nu\beta^+\beta^+] \\ e^- + (Z, A) &\rightarrow (Z-2, A) + \beta^+ + 2\nu_e & [2\nu\beta^+EC] \\ 2e^- + (Z, A) &\rightarrow (Z-2, A) + 2\nu_e & [2\nu EC EC] \end{aligned}$$

Beta decays are processes mediated by the weak force and therefore in general rather slow (if compared to strong decays, for example). Second order processes will thus have extremely



**Figure 1.3:** Mass parabola for isobaric nuclei. While nuclei with an even number of nucleons have to "jump" between upper (odd-odd) and lower (even-even) parabola, odd nuclei simply decay towards the valley of least energy  $E$ . There are isotopes on both sides of the energetic minimum on the even-even parabola that energetically cannot decay towards their nearest neighbour on the odd-odd parabola but must undergo double beta decay to their neighbour on the even-even parabola. Taken from [Kie05]

long half-lives. Therefore, they are normally only visible if first-order decays are energetically forbidden as it is often the case with even-even nuclei (see Fig. 1.3). The neutrinoless mode was suggested by Furry in 1939 [Fur39] since when there have been many experiments trying to find evidences for double beta decay in either form. Geochemical experiments searching for an excess of daughter nuclei in old ore deposits were carried out as early as 1949 but it took until 1967 before convincing evidence was found [Kir67] in Se and Te ores. This approach, however, cannot distinguish between  $0\nu\beta\beta$  decay and  $2\nu\beta\beta$  decay.

The excellent energy resolution of semiconductor detectors combined with large source masses due to the rather high density of solid-state detectors – compared to gaseous detectors like cloud chambers or TPCs<sup>5</sup> – led to first experiments using germanium spectrometers. Thanks to the isotope  $^{76}\text{Ge}$  which has a natural abundance of 7.8%, the counting efficiency could be optimized by using the 'source=detector' ansatz where the whole source volume – the germanium – is used as detector. Essentially one then measures the detector's decay where almost all decay electrons deposit their energy inside the active volume. First attempts with this approach were done already in 1967 [Fio67] and today the best available bounds on the

<sup>5</sup>Time-Projection Chambers, gaseous ionisation detectors used in particle physics.

neutrino's mass stem from the Heidelberg-Moscow experiment that has obtained [KK01b]

$$\begin{aligned} T_{\frac{1}{2}}^{0\nu} &> 1.9 \times 10^{25} \text{ years} \quad \text{at 90\% C.L.} \\ \langle m_{\nu_e} \rangle &< 0.35 \text{ eV} \end{aligned}$$

Later, individuals from the collaboration published a Bayesian analysis of the collected data claiming to see evidence for  $0\nu\beta\beta$  decay [KK01a] which provoked a controversial discussion (see e.g. [Aal02] and [Zde02]). This first paper was in 2004 backed up by thorough re-analysis [KK04] that improved the plausibility by a great deal. It now appears possible that Heidelberg-Moscow's data might indeed show a first hint for neutrinoless double beta decay. Current claims from [KK04] are:

$$\begin{aligned} T_{\frac{1}{2}}^{0\nu} &= (0.69 - 4.18) \times 10^{25} \text{ years} \quad \text{at 90\% C.L.} \\ \langle m_{\nu_e} \rangle &= 0.24 - 0.58 \text{ eV} \end{aligned}$$

Experiments like GERDA<sup>6</sup> and Majorana<sup>7</sup> are currently trying to essentially repeat the experiment after mainly improving the background levels to either confirm or refute the above claim within the next years.

---

<sup>6</sup>official website: <http://www.mpi-hd.mpg.de/ge76/home.html>

<sup>7</sup>official website: <http://majorana.pnl.gov/>





## Chapter 2

# An Introduction to COBRA

### 2.1 The Concept of COBRA

The success of efforts that use the 'source = detector' ansatz like the Heidelberg-Moscow experiment [KK01b] gave rise to thoughts of how to utilise the advantages of semiconductors,

- very high radio-purity
- excellent energy resolution
- no need for usually radioactively contaminated photomultiplier tubes,

while studying the best-suited isotopes that can undergo  $\beta\beta$ -decay instead of only  $^{76}\text{Ge}$  which has a rather low Q-value (2038 keV) and natural abundance  $a$  (7.8%). While the latter disadvantage can be compensated by isotope enrichment which is expensive and becomes more difficult the lower the natural abundance is, the Q-value causes the expected  $0\nu\beta^-\beta^-$ -line to lie within the Compton continuum of decays from the ubiquitous  $^{232}\text{Th}$  and  $^{238}\text{U}$  chains. The fact that this background consists of  $\gamma$ -radiation from the main natural decay chains makes it very difficult to suppress it: high-energetic  $\gamma$ s are very penetrating and hard to shield. Besides, traces of uranium and thorium can be found in almost all materials used for the construction of detector setup and contacting. Indeed, this kind of background is the reason that all germanium-based experiments have not yet reached limits beyond  $T_{1/2}^{0\nu} \sim 10^{25}$  years.

It would therefore be advantageous to use decays that have a Q-value of above 2614 keV which is the highest-energetic naturally occurring  $\gamma$ -line with noteworthy branching ratio. It originates from the decay of  $^{208}\text{Tl}$  within the  $^{232}\text{Th}$  chain. At the same time, isotopes with higher Q-values also have larger decay rates: the decay rate  $\lambda$  scales with  $\lambda \sim Q^5$  due to phase space reasons [Zub04] so experiments with a fixed source mass can expect significantly more decays when using high-Q isotopes. Typically, a so-called 'figure of merit'  $n$  is given when discussing the suitability of isotopes for  $\beta\beta$ -decay searches. It is defined in [Sta90] as

$$n = T_{\frac{1}{2}}^{0\nu} \langle m_{\nu_e} \rangle^2, \quad (2.1.1)$$

being the product of the calculated half-life for the neutrinoless double beta decay of the isotope under study when  $\langle m_{\nu_e} \rangle$  is the (assumed) effective Majorana neutrino mass. Within this rather simple framework, different  $n$  can be interpreted as

1. given a fixed number of source nuclei, experiments with isotopes having a better figure of merit can reach the same limit on  $\langle m_{\nu_e} \rangle$  by excluding a half-life which is reduced by a factor  $n$  or
2. having reached the same half-life  $T_{1/2}^{0\nu}$  as a competing experiment, the possible limit on  $\langle m_{\nu_e} \rangle$  is a factor of  $\sqrt{n}$  better.

Compiled figures of merit can be found in [Sta90].

Avignone et al. give a different definition aimed more at experimental considerations in [Avi05a] and [Avi05b]. According to the authors, one of the most important features for promising double-beta decay experiments is the combination of good experimental energy resolution with a good figure of merit – independent of the exact definition of the figure of merit. They criticise that background events will always be present which attributes great importance to the experimental energy resolution: the experimental sensitivity to detect a decay with a line signature within an energy spectrum scales according to

$$T_{1/2} \sim a\epsilon \sqrt{\frac{M \cdot t}{\Delta E \cdot B}} \quad (2.1.2)$$

where the parameters natural isotopical abundance  $a$  and detection efficiency  $\epsilon$  enter linearly while source mass  $M$ , measurement live time  $t$ , energy resolution  $\Delta E$  and background level  $B$  show only a square-root dependence. The standard figure of merit, however, does not take into account any information about the background or energy resolution.

Browsing through listings of known  $\beta\beta$ -decaying isotopes (e.g. [Boe87]), one first stumbles over  $^{48}\text{Ca}$  with an unsurpassed Q-value of 4271 keV. Sadly, the low abundance of only 0.187% and rather poor nuclear matrix elements ruin its figure of merit. Besides, it seems almost impossible to invent a semiconductor containing large quantities of calcium which is intended for the reasons given above.

Other good candidates seem to be  $^{150}\text{Nd}$  and  $^{100}\text{Mo}$  with Q-values still above 3000 keV, good matrix elements and fair abundances. Again, however, building semiconductors with these elements appears to be difficult if not impossible. Besides,  $^{150}\text{Nd}$  is a rare earth element and hence rather expensive.

Below a Q-value of 3000 keV,  $^{116}\text{Cd}$  ( $Q = 2809$  keV,  $a = 7.5\%$ ) and  $^{130}\text{Te}$  ( $Q = 2529$  keV,  $a = 34.5\%$ ) show up. For more than 20 years, so-called 'room-temperature semiconductors' have been examined, among them CdTe and  $\text{Cd}_{0.9}\text{Zn}_{0.1}\text{Te}$ . The ultimate goal was to combine the ease-of-use of silicon detectors with higher atomic numbers to improve the photopeak-efficiency for gamma detection primarily for medical applications. To benefit from industrial development, CdTe and CdZnTe seem to be the best suited semiconductors for a 'source=detector'  $\beta\beta$ -decay experiment after  $^{76}\text{Ge}$ . A first attempt with a CdTe detector was published by Mitchell and Fisher in 1988 [Mit88], however, no further development has been reported since then. The feasibility of operating modern CdZnTe-detectors was first examined with a test setup at the University of Dortmund [Mue01] before the COBRA-proposal containing first spectra was published [Zub01].

When looking into CdZnTe, one finds the following properties:

- contained isotopes

Of all naturally occurring nuclei that exhibit  $\beta\beta$ -decay, CdZnTe contains an amazing 9, CdTe 7 isotopes as described in table 2.1. The most interesting among them are

- $^{116}\text{Cd}$   
 $^{116}\text{Cd}$  is a classical  $\beta^-\beta^-$ -isotope like  $^{76}\text{Ge}$ . It has a fair natural abundance of 7.47%, a good phase space due to its high Q-value of 2809 keV and, according to [Cau07], outstanding nuclear matrix elements. Its decay energy is beyond the most energetic naturally occurring gamma line ( $^{208}\text{Tl}$  from the  $^{232}\text{Th}$ -decay chain at 2614 keV), therefore it will see significantly less ( $\gamma$ -)background than isotopes with Q-values below. The remaining background will stem from alpha and beta contaminations within the crystal (which is known to be very pure) or on its surface, cosmic rays and neutron interactions:  $^{113}\text{Cd}$  which has a natural abundance of 12.2% has a capture cross-section for thermal neutrons of around 20 kbarn in a  $^{113}\text{Cd}(n,\gamma)^{114}\text{Cd}$  reaction yielding gammas of up to 9 MeV.
- $^{130}\text{Te}$   
 $^{130}\text{Te}$  also decays via  $\beta^-\beta^-$ -decay. It possesses a superb natural abundance of 33.8%, great nuclear matrix elements [Cau07] and still a good phase space. Its Q-value of 2529 keV is luckily between  $^{208}\text{Tl}$ 's photopeak at 2614 keV and the compton continuum, therefore more background than with  $^{116}\text{Cd}$  is expected, but much less than at energies within the continuum.
- $^{106}\text{Cd}$   
 $^{106}\text{Cd}$  is a  $\beta^+\beta^+$ -decaying isotope. It has a rather poor abundance of only 1.25%, but its Q-value of 2771 keV allows all possible  $\beta^+\beta^+$ -decays:  $\beta^+\beta^+$ ,  $\beta^+/\text{EC}$  and  $\text{EC}/\text{EC}$ . Once  $\beta\beta$ -decay has been confirmed with  $\beta^-\beta^-$ -isotopes that have shorter half-lives than  $\beta^+\beta^+$ -emitters, it will soon be necessary to use  $\beta^+\beta^+$ -isotopes to investigate the underlying mechanisms of  $\beta\beta$ -decay:  $\beta^+\beta^+$ -decays (in particular  $\beta^+/\text{EC}$ -decays) are more sensitive to contributions of right-handed weak currents [Hir94]. Examining neutrinoless double beta decay therefore means measuring several  $\beta^-\beta^-$ - and  $\beta^+\beta^+$ -isotopes, CdZnTe detectors enriched in  $^{106}\text{Cd}$  being probably best-suited for the task.

- radioactive contamination

As with germanium or silicon detectors, CdZnTe can be expected to be quite clean due to the crystal growth process. The ability to operate the detectors at room temperature

Isotope	decay mode	Q-value[keV]	nat. abundance [%]
$^{64}\text{Zn}$	$\beta^+/\text{EC}, \text{EC}/\text{EC}$	1096	48.6
$^{70}\text{Zn}$	$\beta^-\beta^-$	1001	0.6
$^{106}\text{Cd}$	$\beta^+\beta^+, \beta^+/\text{EC}, \text{EC}/\text{EC}$	2771	1.25
$^{108}\text{Cd}$	$\text{EC}/\text{EC}$	231	0.89
$^{114}\text{Cd}$	$\beta^-\beta^-$	534	28.72
$^{116}\text{Cd}$	$\beta^-\beta^-$	2809	7.47
$^{120}\text{Te}$	$\beta^+/\text{EC}, \text{EC}/\text{EC}$	1722	0.096
$^{128}\text{Te}$	$\beta^-\beta^-$	868	31.69
$^{130}\text{Te}$	$\beta^-\beta^-$	2529	33.80

**Table 2.1:** Decay modes, Q-values and natural abundances of isotopes contained in CdZnTe [Kie03].

means that one is not hindered by the necessity for a cryostat or cold finger and can select materials for the detector mounting freely avoiding contamination of the construction materials.

- energy resolution

After several years of research, techniques have been demonstrated that reach a resolution of below 1% FWHM<sup>1</sup> at 662 keV. Standard detectors can be expected to show 3–5% which is worse than Ge or Si, but easily better than scintillators or still more experimental semiconductors like CdSe. It can be expected that CdZnTe detectors will in the long term reach similar resolutions as experiments using germanium spectrometers or cryogenic bolometers [Arn04].

- tracking/pulse-shape analysis, background reduction

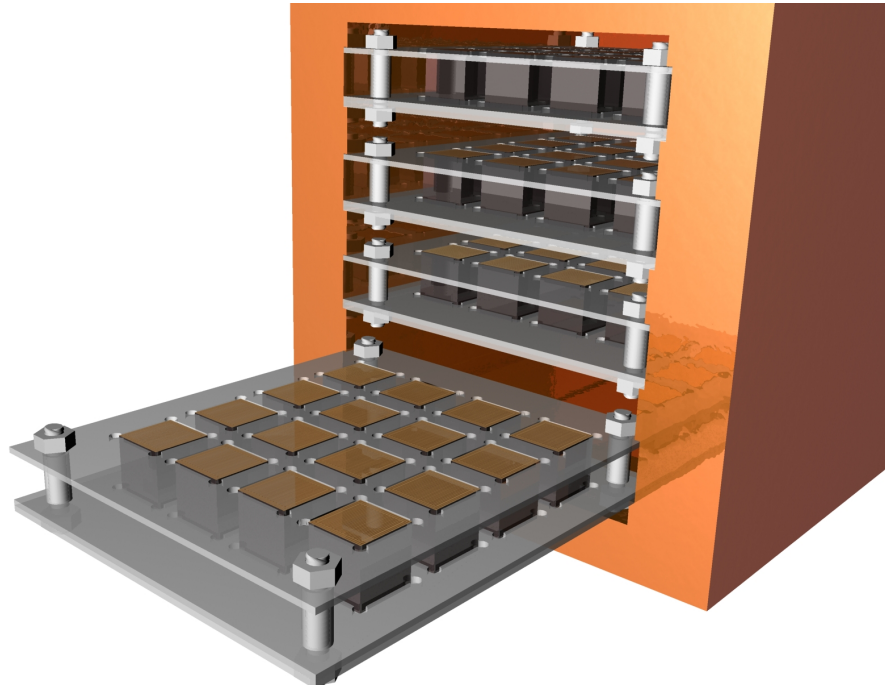
While pixel detectors are not common in germanium, the medical industry's need for large gamma cameras with sub-mm resolution has driven research for CdZnTe pixel detectors. Using these one can determine the exact position of any interaction with sub-mm precision allowing for improvement of the detector's resolution (see chapter 3.2), for fiducial cuts and for background reduction: most background events will look different from double beta events. According to simulations done at the COBRA group at the University of Birmingham [Blo07b], it is quite easy to refuse a large fraction of all high-energy gamma events – they are very likely to produce multiple-site interactions – and nearly all alpha events which are almost always very compact events limited to one pixel. When the pixel size is chosen carefully (e.g.  $(200 \times 200) \mu\text{m}^2$ ), one can even distinguish single  $\beta$ -particles from double beta decays with up to 70% efficiency. In total, a background reduction of up to three orders of magnitude seems to be feasible.

CdZnTe is – compared to Ge and Si – a rather young semiconductor material and its crystal growth technology has thus still to be substantially improved to reach the same level. Besides, binary and ternary crystals are always more difficult to grow due to stress within the crystal because of different atomic radii: defects partially relax the crystal structure rather than to cause more tension. This results in the fact that while for Si and Ge huge single crystals with unsurpassed homogeneity are readily available, CdZnTe ingots often suffer from grain boundaries, twinning, Te inclusions and large defect densities. In order to produce good detectors, it is necessary that the active volume is rather homogeneous which only holds up to now for rather small volumes within an ingot. Therefore, small cubes or planar detectors of few  $\text{cm}^2$  area and 1–10 mm thickness are normally cut out of the ingot.

While normal germanium spectrometers can weigh some kg per crystal, CdZnTe detectors are due to the above reasons limited to  $O(10\text{g})$ . To probe  $\langle m_{\nu_e} \rangle$  down into the meV region, however, several hundred kg of source mass are necessary. It is therefore envisaged to create a 3-dimensional array of small detector cubes (see figure 2.1), starting with a  $4 \times 4 \times 4$  detector prototype that should be subsequently enlarged to several hundred detectors. In its final upgrade stage, up to 64000 detectors are foreseen [Wil05b].

---

<sup>1</sup>In  $\gamma$ -spectroscopy, the energy resolution  $\Delta E$  of a detector is usually given as full-width-at-half-maximum FWHM ( $1\Delta E = 2.35\sigma$  for the Gaussian approximation). The value can be given in keV or per-cent for a reference energy. In most cases, the 662 keV line from <sup>137</sup>Cs is chosen.



**Figure 2.1:** Rendered drawing of COBRA's first stage with 64 detectors[Dob05].

While the 64-detector prototype will use CPG-type<sup>2</sup> detectors, COBRA groups in Birmingham and Liverpool are investigating how pixel detectors behave under low-rate conditions. At the same time, a joint proposal from the University of Dortmund and the Materialforschungszentrum Freiburg was approved by the Deutsche Forschungsgemeinschaft: Together, they will survey different possibilities to create CdZnTe detectors which are optimised for low-level experiments. Apart from investigating methods to grow crystals from isotopically enriched material, the production of cost-efficient high-purity large-volume detectors with acceptable energy resolution will be the focus of the collaboration.

### 2.1.1 History

The work on investigating the suitability of CdTe and CdZnTe detectors for rare decay searches began in 2000 [Mue01]. At first, commercial CdTe detectors from Eurorad and commercial CdZnTe detectors from eV Products were acquired and their properties compared. The CdTe detectors showed instabilities due to severe polarization effects. Furthermore, their simple planar electrode geometry yielded a rather poor energy resolution exhibiting asymmetric photopeaks while the CdZnTe detectors used the so-called co-planar grid (CPG) technology (see chapter 3.2.2) to compensate for charge carrier losses and thereby exhibited superior energy resolution. Besides, they demonstrated stable behaviour.

After building up a sufficient shielding consisting of a plastic scintillator-based cosmic ray veto, a combined Faraday-cage/air-tight box for nitrogen flushing against radon and a 20cm-thick outer lead shielding around a  $(20 \times 20 \times 20)\text{cm}^3$  inner copper core it was possible even

<sup>2</sup>Co-Planar Grid, see chapter 3.2.2)

Isotope	Level [keV]	Mode	$T_{1/2}$ [yrs]	existing limit on $T_{1/2}$ [yrs]
$^{70}\text{Zn}$	(0 <sup>+</sup> ) g.s.	$\beta^-\beta^-$	$1.3 \times 10^{16}$	$4.8 \times 10^{14}$ [Fre52]
$^{114}\text{Cd}$	(0 <sup>+</sup> ) g.s.	$\beta^-\beta^-$	$6.4 \times 10^{18}$	$2.0 \times 10^{20}$ (90% CL)[Geo95]
$^{116}\text{Cd}$	(0 <sup>+</sup> ) g.s.	$\beta^-\beta^-$	$8.0 \times 10^{18}$	$7.0 \times 10^{22}$ (90% CL)[Dan00]
$^{128}\text{Te}$	(0 <sup>+</sup> ) g.s.	$\beta^-\beta^-$	$8.8 \times 10^{18}$	$8.6 \times 10^{22}$ (90% CL)[Ale00]
$^{130}\text{Te}$	(0 <sup>+</sup> ) g.s.	$\beta^-\beta^-$	$3.3 \times 10^{19}$	$2.1 \times 10^{23}$ (90% CL)[Arn03]
$^{64}\text{Zn}$	(0 <sup>+</sup> ) g.s.	$2\nu\text{EC EC}$	$6.0 \times 10^{16}$	$8.0 \times 10^{15}$ [Ber53]
	(0 <sup>+</sup> ) g.s.	$0\nu\beta^+\text{EC}$	$2.8 \times 10^{16}$	$2.3 \times 10^{18}$ (68% CL)[Nor85]
$^{106}\text{Cd}$	(2 <sub>1</sub> <sup>+</sup> ) 512	$2\nu\text{EC EC}$	$8.3 \times 10^{17}$	$3.5 \times 10^{18}$ (90% CL)[Bar96] (0+2 $\nu$ )
	(0 <sup>+</sup> ) g.s.	$0\nu\beta^+\beta^+$	$1.5 \times 10^{17}$	$2.2 \times 10^{19}$ (90% CL)[Dan96]
	(0 <sup>+</sup> ) g.s.	$0\nu\beta^+\text{EC}$	$3.8 \times 10^{17}$	$3.7 \times 10^{20}$ (90% CL)[Bel99]
$^{106,108}\text{Cd}$	(0 <sup>+</sup> ) g.s.	$2\nu\text{EC EC}$	$1.0 \times 10^{18}$	$1.5 \times 10^{17}$ (68% CL)[Nor84] (g.s.+512)
$^{120}\text{Te}$	(0 <sup>+</sup> ) g.s.	$0\nu\beta^+\text{EC}$	$2.2 \times 10^{16}$	$4.2 \times 10^{12}$ [Fre52]
	(0 <sup>+</sup> ) g.s.	$2\nu\text{EC EC}$	$9.4 \times 10^{15}$	—
	(2 <sub>1</sub> <sup>+</sup> ) 1171	$2\nu\text{EC EC}$	$8.4 \times 10^{15}$	—

**Table 2.2:** Lower limits (90% C.L.) for  $\beta^-\beta^-$ ,  $0\nu\beta^+\beta^+$ ,  $0\nu\beta^+\text{EC}$  and  $2\nu\text{EC EC}$ -decay to ground state (g.s) and some excited states obtained with the first COBRA test setup (a 0.5 cm<sup>3</sup> CPG-type CdZnTe detector operated in Dortmund) compared with limits existing at the time of the study. Modified after [Kie03].

at surface level in Dortmund to acquire data that lead to the publication of some world-leading half-life limits[Kie03]. The low noise edge of the preamplifier electronics that were housed close to the detector allowed the refutation of a positive detection of the second forbidden electron-capture of  $^{123}\text{Te}$  yielding a half-life limit of  $T_{1/2} > 5.3 \times 10^{16}$  years while Watt and Glover[Wat62] had published  $T_{1/2} = (1.24 \pm 0.10) \times 10^{13}$  years. Some results from this setup are shown in the table 2.2.

The early setup had several drawbacks, the most important being

- the shallow depth (about 5m.w.e.<sup>3</sup>) leading to large cosmic ray background despite the veto
- background from the preamplifier electronics which is in the same housing as the detector
- unsatisfactory scalability
- no event-by-event readout

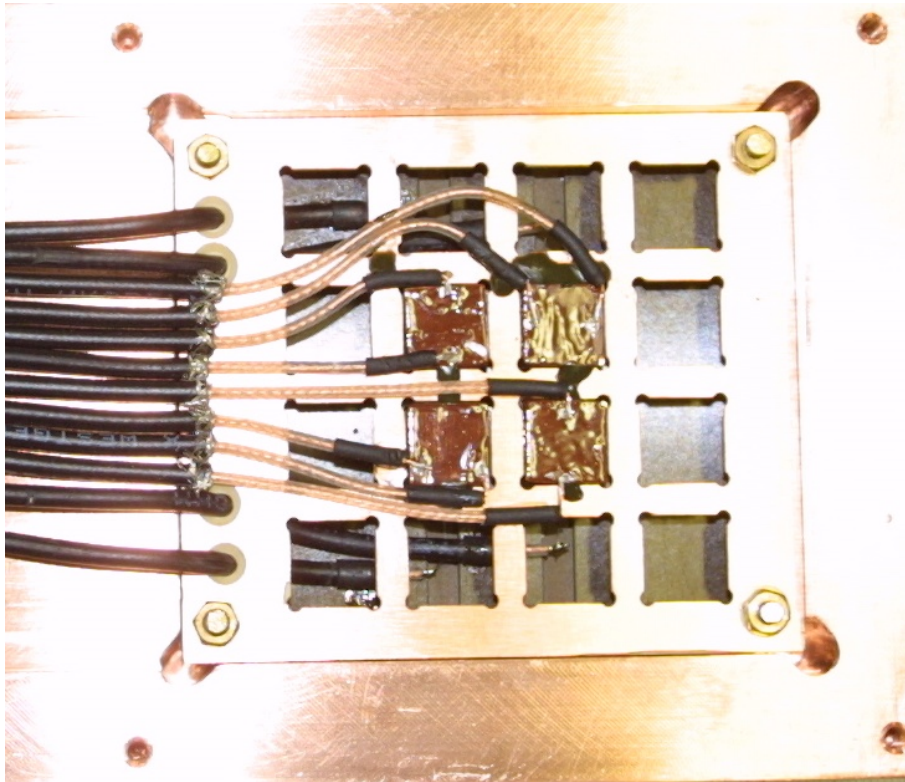
Therefore in 2002, a first 2×2-array with remote preamplifier electronics and CAMAC<sup>4</sup>-based ADCs<sup>5</sup> instead of an MCA<sup>6</sup>-card was built using 1 cm<sup>3</sup>-sized CdZnTe CPG-type detectors. A photograph of it inside the innermost copper shielding brick is depicted in Fig. 2.2.

<sup>3</sup>Meters of Water Equivalent is the common unit of overburden. It is simply calculated by multiplying the overburden's density with the experiment's weighted depth.

<sup>4</sup>CAMAC is an acronym for Computer Automated Measurement And Control and was a standard bus for data acquisition and control used in nuclear and particle physics.

<sup>5</sup>Analogue-to-Digital Converters

<sup>6</sup>Multi-Channel Analyser, an ADC with buffer memory which histograms by itself.



**Figure 2.2:** Picture of the  $2 \times 2$ -array consisting of  $1 \text{ cm}^3$ -sized CdZnTe CPG-type detectors inside their Pertinax (FR2) holder structure. Wiring is done via RG-174 coaxial cables. The structure is located inside the innermost copper shielding brick.

The CAMAC electronics, the software architecture and results from this setup are described in [Kie05]. It differed from the  $4 \times 4 \times 4$ -setup described in this work in the following aspects:

- detector contacting: contact between detector and cable was made with the industry standard for CdZnTe contacting – Epo-Tek’s H20E silver-filled conductive epoxy. It has two drawbacks: joints cannot be reworked (once cured it cannot be non-destructively removed) and silver might contain radioactive contamination mainly in form of  $^{110m}\text{Ag}$  due to cosmogenic neutron activation. For details, see chapter 3.4.
- cabling: the  $2 \times 2$ -array used RG-174 ‘Lemo-type’ coaxial cables. For a bigger array, they have too large a footprint; besides, they bring more mass than necessary and unknown contaminations close to the detectors.
- shapers: instead of shapers, Ortec 572 main amplifiers were used. For larger numbers of detectors, they would have been too space-consuming and too costly.
- CAMAC-ADCs: LeCroy 3511 and 3512 ADCs were used. They were capable of event-by-event readout, but had several disadvantages. See [Kie05] for details.

Data taken with this setup was used to publish [Goe05] and in part for [Blo07a].

### 2.1.2 Components of COBRA

COBRA's setup today consists of the following parts that will be described in the following chapters:

- shielding
  - plastic scintillator-based cosmic muon veto
  - paraffin and borated polyethylene-based neutron shield
  - gas-tight Faraday cage
  - lead-castle
  - copper-core
  - calibration system
- detector-to-ADC-chain
  - detectors
  - copper-filled nitrocellulose-based conductive contacting glue
  - Kapton (i.e. polyimide)-based detector-preamplifier cabling
  - modular custom-designed charge-sensitive preamplifier
  - RG-178-based preamplifier-ADC cabling
  - shaper
  - VME<sup>7</sup>-based custom-built ADC
- additional electronics
  - high voltage supply
  - grid-bias supply
  - central control computer including slow-control

## 2.2 Scope of this Work

In this thesis, the technical solutions found for the experiment's components mentioned above shall be described in some detail. Evaluation of their performance is given where appropriate. The improvement of the background levels due to enhancement of shielding, contacting and ADCs is shown. Finally, on the basis of the most recent data set the current performance of the setup is demonstrated and a new promising analysis method based on coincidences is used to search for neutrinoless double-beta decays into excited states.

---

<sup>7</sup>VersaModule Eurocard bus, ANSI/IEEE 1014-1987, a computer bus standard.



## Chapter 3

# Detectors and Contacting

### 3.1 General Remarks

A semiconductor detector for ionising radiation consists of a semiconductor crystal whose electrodes are connected to a charge-sensitive preamplifier. For a general introduction into semiconductor radiation detectors and radiation interaction with matter see textbooks by Knoll[Kno00], Leo[Leo92] or Gilmore/Hemingway[Gil95]. Spieler [Spi06] covers detector systems including special forms of CdZnTe detectors as well as subsequent electronics.

Except for its early phase[Mue01], COBRA has used CdZnTe detectors manufactured by eV PRODUCTS<sup>1</sup>. This is due to the fact that CdTe detectors have up to now not been available in large volumes capable of delivering adequate energy resolutions. In principle, they may well be used within COBRA's concept and will also be investigated in the cooperation between the Materialforschungszentrum Freiburg and the University of Dortmund.

This chapter will deal with details of the CdZnTe detectors used for COBRA, with their mountings, contacting and wiring. Contacting of CdZnTe detectors is still no simple task due to the fact that standard methods of contacting like ultrasonic bonding cannot be used for CdZnTe as they damage the crystal structure. In comparison to standard semiconductor detectors made from silicon or germanium, CdZnTe detectors show a wide spread in performance parameters like energy resolution and efficiency. Besides, they can show degradation or at least variation of their parameters over time hence sufficient characterisation measurements were necessary upon delivery and after contacting.

### 3.2 CdZnTe Detectors

#### 3.2.1 Material Properties

CdZnTe is a ternary so-called II-VI semiconductor – one constituent is from the periodic table's group IIB (old IUPAP nomenclature) while the other is from group VI<sup>2</sup>. Its 'base-semiconductor' CdTe which has similar properties (see table 3.1) is modified by replacing usually 7-13% of all cadmium atoms with zinc. Due to its different atomic radius, it reduces

---

<sup>1</sup>[www.evproducts.com](http://www.evproducts.com)

<sup>2</sup>Examples for IV semiconductors are silicon and germanium, the best-known III-V semiconductor is gallium-arsenide

Property	CdZnTe	CdTe	Ge	Si
Atomic numbers $Z$	48, 30, 52	48, 52	32	14
Density $\rho_m$ [ $g/cm^3$ ]	5.78	5.85	5.33	2.33
Band Gap $E_g$ [eV]	1.572	1.5	0.67	1.12
$e^-h^+$ creation energy $E_{\text{pair}}$ [eV]	4.64	4.43	2.95	3.62
Resistivity $\rho$ [ $\Omega\text{cm}$ ]	$3 \times 10^{10}$	$10^9$	50	$< 10^4$
Electron mobility $\mu_e$ [ $\frac{cm^2}{Vs}$ ]	1000	1100	3900	1400
Hole mobility $\mu_h$ [ $\frac{cm^2}{Vs}$ ]	50-80	100	1900	480
Electron lifetime $\tau_e$ [s]	$3 \times 10^{-6}$	$3 \times 10^{-6}$	$> 10^{-3}$	$> 10^{-3}$
Hole lifetime $\tau_h$ [s]	$10^{-6}$	$2 \times 10^{-6}$	$10^{-3}$	$2 \times 10^{-3}$
$(\mu\tau)_e$ [ $cm^2/s$ ]	$(3 - 5) \times 10^{-3}$	$3.3 \times 10^{-3}$	$> 1$	$> 1$
$(\mu\tau)_h$ [ $cm^2/s$ ]	$5 \times 10^{-5}$	$2 \times 10^{-4}$	$> 1$	$\approx 1$

**Table 3.1:** Some crystal properties of CdZnTe, CdTe, Si and Ge measured at room temperature [eV-07].

the stress within the crystal structure leading mainly to better yields in crystal growth apart from more beneficial mechanical properties like less brittleness. II-VI semiconductors are normally well characterised by assuming a mainly ionic bonding character while III-V semiconductors exhibit more covalent behaviour.

Main differences of CdZnTe compared to germanium and (in part) silicon are a larger band-gap, higher resistivity and worse charge carrier mobilities and lifetimes. The larger bandgap causes a larger electron-hole-pair creation energy which enables room-temperature operation while limiting the theoretically possible energy resolution. This is given by [Tak01] as

$$\text{FWHM}_{\text{theoretical}} = 2.35\sqrt{FE_{\text{pair}}E_{\gamma}}, \quad (3.2.1)$$

with FWHM being the resolution as full-width half-maximum of the photopeak measured in units of energy of  $E_{\gamma}$  (the incident radiation's energy) and  $E_{\text{pair}}$ .  $F$  denotes the so-called Fano-factor [Fan47] which is a material constant related to the fluctuations of the electron-hole-pair ( $e^-h^+$ ) creation in the detector; its calculation is possible but depending on a good knowledge about the system under study [Alk67]. For CdZnTe,  $F$  was measured to be between 0.1 and 0.15; for silicon and germanium literature values are also around 0.1. Assuming  $F = 0.1$  for all materials, the best achievable resolution for a typical calibration source, e.g.  $^{137}\text{Cs}$  at 662 keV, will be as good as 0.44 keV or 0.066% for Germanium and drop to 0.55 keV or 0.084% for CdZnTe. In practice, however, this disadvantage is not relevant as the best published resolutions of CdZnTe devices cluster around 1% at 662 keV which is due to issues of the detector material itself (e.g. charge carrier trapping, mobilities, crystal non-uniformity).

The high resistivity allows for room-temperature operation as ohmic resistors with homogeneous electric field distributions while silicon- and germanium-based detectors have to be operated as diodes and/or cooled. Up to now all grown crystals exhibit rather limited lifetime-mobility products  $\mu\tau$  for the charge carriers – especially the holes. This can be partially attributed to crystal defects and inhomogeneities due to the not yet perfected crystal growth techniques which can be understood as consequence the comparatively early phase of research

in CdZnTe detectors<sup>3</sup>. In addition, the ionic character of the compound makes it more difficult to grow crystals with only few impurities like vacancies and interstitial atoms which act as trapping centers. Common are Te-precipitates, twin boundaries and Cd vacancies[Sze98] which are mainly caused by the large discrepancy in melting temperatures and vapour pressures among the constituents leading to a de-mixing during the melting process. Large advances in crystal growth have been made by using extremely pure ingredients (up to 7N materials<sup>4</sup> have been used [Fau06]) and a well-defined temperature profile during crystal growth [Sze04, Fau06].

### 3.2.2 Electron-only Readout Devices

The range of holes in CdZnTe still is much too short for standard planar readout methods like in high-purity Ge detectors where electrons and holes can travel for several cm: In CdZnTe, only electrons can travel for several mm and even here one should compensate for the losses on their path. This means that according to the Ramo-theorem[Ram39], the total collected charge is strongly inhomogeneous: If an event occurs close to the cathode, the electrons contribute most of the induced charge as they travel most of the distance through the crystal and are therefore responsible for most of the induction. If, however, the interaction is located close to the anode, the electrons will all reach the electrode, but will induce only very little charge as they have only a very short distance to do so. In Ge- and Si-detectors, the hole-movement will now induce most of the signal. In CdZnTe, however, the holes will not get very far and therefore the total induced charge will be only a fraction of the deposited charge (for illustration see Fig. 3.1). This behaviour leads to a wide spread in charge collection for interactions of the same energy (e.g. photopeak-events) and hence to spectra with photopeaks heavily tailing towards lower energies. Planar detectors with sufficient energy resolution have up to now only been realised for very thin detectors around 1 mm thickness which are mainly used for X-ray spectroscopy as their photopeak efficiency is too low above 100 keV.

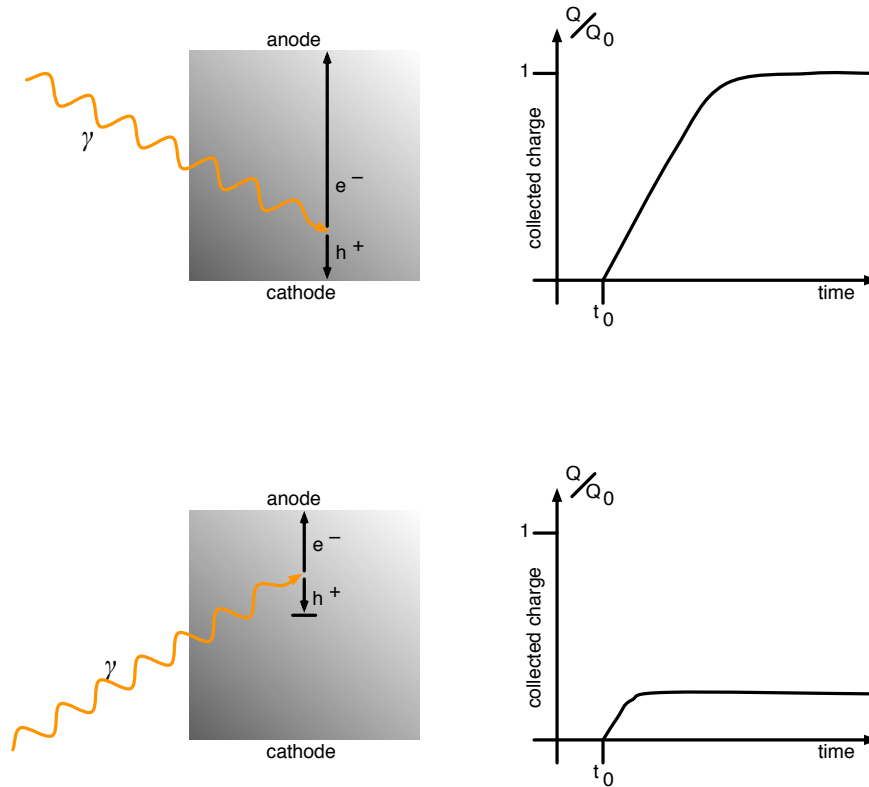
A method to get rid of this dependence of the interaction depth is to create electron-only readout devices – here, only the much less severe electron trapping has to be dealt with (if necessary). Up to now there are two common approaches for CdZnTe-detectors:

#### Pixel Detectors

Pixel detectors use the so-called 'small-pixel effect' (SPE) [Bar95] to be sensitive only for electrons. In simple words, the hole signal is distributed over the large area cathode and hence is only very weak while the electron movement is 'focused' on the small pixel electrode only when the electrons come close to it. The electron signal is thereby 'amplified' compared to the contribution of the holes and the dependence of the signal's amplitude on the interaction depth – which is *mainly* due to the larger contribution of the (almost non-existing) hole movement and *not* due to the  $e^-$ -trapping – is greatly reduced. Mathematically, the effect can be understood via the weighting potential method [Ram39].

<sup>3</sup>For comparison: it took more than 20 years until high-purity silicon replaced germanium in specialised types of diodes and rectifiers. Germanium detectors had to be lithium-drifted for over 20 years until high-purity germanium detectors (HPGe) were introduced only in the early 1980s.

<sup>4</sup>xN describes the chemical purity by stating how many digits of the percentage are '9's. 7N Cd states for example that less than  $10^{-5}\%$  of all atoms are *not* Cd.

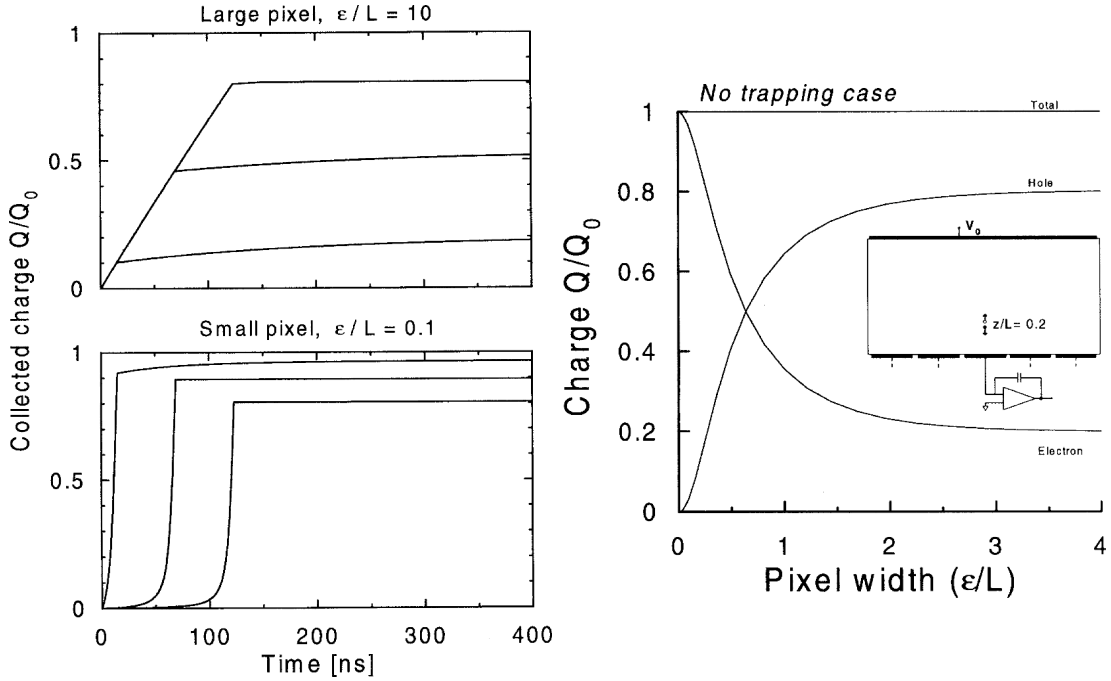


**Figure 3.1:** Sketch illustrating the dependence of the pulse height on the interaction depth in the case of hole trapping: if the interaction takes place near the cathode, the drift distance for the holes might be small enough to be collected; only a small fraction of the electrons gets trapped which results in (almost) full charge collection. If, however, the interaction takes place near the anode, the holes will not get very far before they get trapped. Within the charge collection time of around a  $\mu\text{s}$ , they will not get de-trapped so they can (almost) not contribute to the charge collection. Even though all electrons reach the anode, the total collected charge – and therefore, in a planar detector, also the preamplifier’s pulse amplitude – is only a fraction of the deposited charge.

In principle, the contribution of a charge to the signal is calculated as

$$\Delta q = Q \Delta V_W \quad (3.2.2)$$

where  $\Delta q$  is the incremental charge induced at the chosen electrode,  $Q$  is the charge travelling and  $\Delta V_W$  is the change in the weighting potential  $V_W$  over the path of the charge [Luk94]. If it would be possible to keep the weighting potential to be 0 everywhere in the detector, but 1 at the anode, all electrons would contribute fully to the signal, independent of the interaction point, while the holes – which are trapped anyway – do not contribute at all. The calculation of the weighting potentials for pixel detectors with different pixel sizes exhibits that a pixel detector with very small pixel edge lengths  $\epsilon$  (compared to the detector’s thickness  $L$ ) comes very close to this ideal detector (see Fig. 3.2). Further improvement can be reached by identifying the interaction depth of each event and correcting for the electron trapping which is proportional

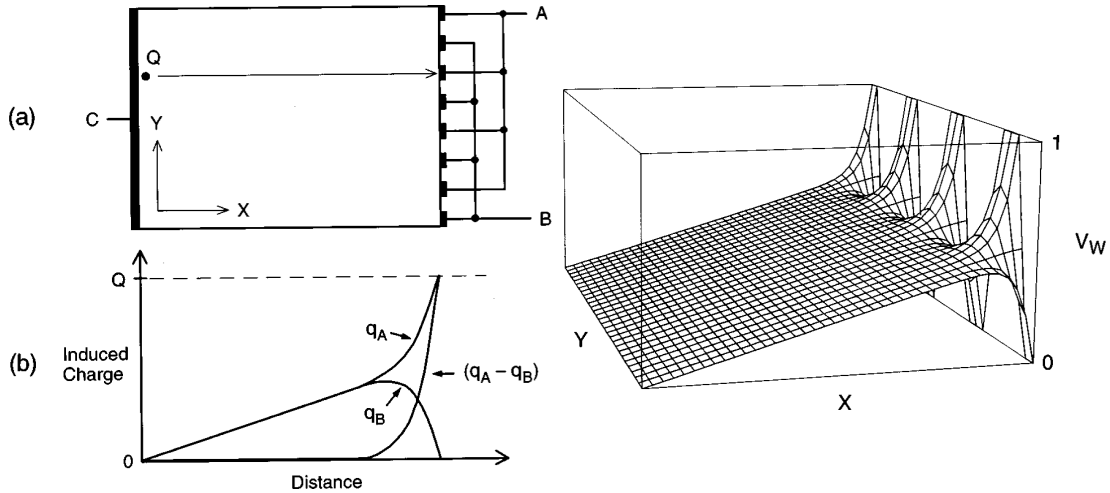


**Figure 3.2:** Left: collected charge vs. time for different pixel sizes  $\epsilon$  in relation to the detector's thickness  $L$ . The interaction depths are at  $z = 0.2L$ ,  $0.5L$  and  $0.8L$ , respectively. For the large pixel it can be seen that – if the interaction takes place near the anode pixel – only a fraction of the expected charge is collected due to the severe hole trapping in CdZnTe. For small pixels, however, the collected charge is only weakly depending on the interaction point. Right: total collected charge vs. pixel width for interactions at depth  $z = 0.2L$ . While for large pixels, only the expected fraction of about 20% is collected due to the lacking contribution of the holes, for small pixels the electrons dominate the charge collection which reaches unity at very small values of  $\epsilon/L$ . Taken from [Bar95].

to the travelled distance. Resolutions as good as 0.76% at 662 keV have been reached [Zha05] as displayed in Fig. 3.6.

### Frisch-Grid or Co-Planar Grid (CPG) Detectors

Another idea is to mimic the effect of a Frisch-grid in ionisation chambers which shields the anode wires from the movement of charge carriers inside the detector until they pass through the grid. In CdZnTe devices, a Frisch-grid-like electrode arrangement is introduced that does not shield the anode, but senses the drift of the charge carriers. In its most simple form, this arrangement consists of two sets of narrow strips which are connected interdigitally to gain two independent sets of grid electrodes. If the weighting potential is now calculated for both sets (see Fig. 3.3), it unfolds that for most of the volume of the detector, the values are equal due to the symmetry of the arrangement. At the electrodes, however,  $V_W$  reaches 1 for the observed electrode while it is 0 for the other one. If the two signals are now subtracted from each other, the result is a constant induced charge independent from the interaction point (except for a region very close to the anodes).



**Figure 3.3:** *Upper left corner:* cross section of the anode arrangement with the drift path of a charge  $Q$ . *Lower left corner:* induced charge at electrode a ( $q_a$ ) and b ( $q_b$ ) and the difference signal ( $q_a - q_b$ ) as a function of the distance travelled by the charge  $Q$ . *Right:* weighting potential for one of the grid electrodes. For the other electrode, the distribution is symmetric; therefore, a subtraction of the induced signals yields 0 for most of the detector until the charge carriers get near the collecting anode. Taken from [Luk94]

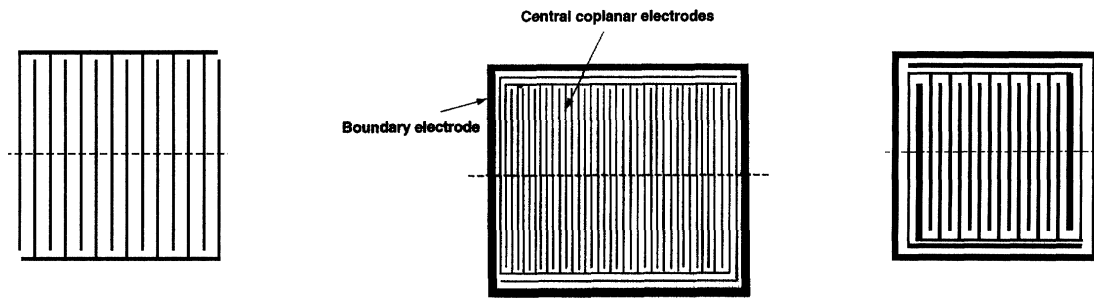
Luke [Luk94] first proposed this modified Frisch-grid called 'co-planar grid'. To avoid ambiguities due to the symmetry of the arrangement, he proposed to apply a voltage difference between the anodes: While the bias voltage normally is negative in CdZnTe and the electron-collecting anode (CA) is at ground potential, he suggested to place a moderate negative potential to the con-collecting anode (NCA). Thereby, the charge carriers will be collected on the CA. To correct for the (moderate, but perceivable) electron loss by electron trapping, the so-called 'relative gain compensation technique' was introduced [Luk95] where the NCA-signal is attenuated to between 50 and 70 % of the original amplitude prior to subtraction. Later, He et al. [He96] extended Luke's principle by additionally sensing the interaction depth which allowed further improvements of the energy resolution. There are different design generations for co-planar grid electrodes (see Fig. 3.4) which differ mainly in the form of the weighting potential at the edges: to get a uniform response over the whole detector, the weighting potential must be (almost) equal for both electrodes which was not the case for the generation 1 design. For details, see [He98].

### 3.2.3 Detector Selection for COBRA

The experimental sensitivity to detect a decay with a line signature within an energy spectrum scales according to

$$T_{1/2} \sim a\epsilon \sqrt{\frac{M \cdot t}{\Delta E \cdot B}} \quad (3.2.3)$$

where the parameters natural isotopic abundance  $a$  and detection efficiency  $\epsilon$  enter linearly while source mass  $M$ , measurement live time  $t$ , energy resolution  $\Delta E$  and background level  $B$  show only a square-root dependence. The natural abundance can only be adjusted at large



**Figure 3.4:** From left to right: generation 1, 2 and 3 co-planar anode grid designs. It is visible that the designers tried to overcome unbalanced asymmetries of the weighting potential towards the edges by introducing additional edge tongues of the boundary electrodes as well as a guard ring and modifications of some tongues' thickness. For details see [He98].

cost, but enters linearly. Within the scope of this work, isotopical enrichment was not yet pursued. The efficiency is mainly depending on the geometry of the detectors. Here, a compact three-dimensional arrangement will increase  $\epsilon$ . From model calculations with typical numbers it is known that COBRA has to use several hundred kg of CdZnTe in its final upgrading stage to reach the necessary number of source nuclei in order to detect the extremely small decay rate expected for  $0\nu\beta^-\beta^-$ -decay [Wil05b]. Therefore, a suitable way of limiting the number of readout channels while instrumenting large source masses had to be found. A sensible measurement time frame is several years. The achievable energy resolution is depending on the readout method and also a question of affordability: the higher the resolution requirement, the worse the production yield. In the end, the background level is depending on proper material selection and shielding.

The aim of all detector evaluation is to find a reasonable compromise between the points mentioned above:

- source mass per channel

Each electronics circuit, e.g. each preamplifier channel, represents possibly contaminated material, cost, power dissipation and a possible source for failure. Therefore, it would be



**Figure 3.5:** Left: Typical CPG detector by eV Products with red polymer-based passivation coating. Right: Naked detector used for TCT measurements [Oeh04]; the generation 3 CPG-electrodes can be clearly recognised.

advantageous to maximise the source mass per channel. Due to trapping, thick CdZnTe detectors (more than 3–5 mm) are only possible with electron-only sensing devices (see section 3.2.2 above). Of these, only CPG-type detectors and pixel detectors are commercially available and technically mature. In 2002, when the first development for a  $2 \times 2$ -detector array started,  $1 \text{ cm}^3$ -sized detectors had the best pricing per gram and a good enough yield in the production process. At the time of writing,  $(1.5 \times 1.5 \times 1) \text{ cm}^3$  sized detectors can be considered readily available so in future developments, these might be used.

One of the projects in cooperation with the Materialforschungszentrum Freiburg is to use whole ingot slices of about 1 cm thickness with only few grain boundaries, deposit CPG-type electrodes covering the complete surface and use only crystal/electrode areas with good enough efficiency and energy resolution. This would drastically reduce the cost for preparation while maximising the packing density. This project would also be possible with pixel detectors – while a single pixel contains of course only a tiny mass, all pixels of a detector or a front-end ASIC<sup>5</sup> can be considered one detector in terms of source mass per channel.

Nevertheless, the source mass per channel will be on the order of  $O(10\text{g})$  which requires  $O(10^4)$  channels to reach  $O(100\text{kg})$  of detector mass.

- low background

Background reduction is a key question of low level spectroscopy: If the background could be eliminated, equation 3.2.3 would be changed into

$$T_{1/2} \sim a \cdot \epsilon \cdot M \cdot t \quad (3.2.4)$$

where the energy resolution would only be important to distinguish between  $0\nu\beta\beta$  and  $2\nu\beta\beta$  decays: only if this is also possible near the endpoint of the  $2\nu\beta\beta$ -spectrum, the measurement is background-free. Then, however, the accessible half-life would scale linearly with time and source mass. But even with a finite background level, it is crucial to keep it as low as possible which is mainly done by careful material selection.

Semiconductor detector materials are generally said to be rather clean concerning radioactive impurities due to being crystals which do not tolerate high levels of impurities at all. Normally, the ingredients for the crystal growth are required to have a chemical purity of better than 5N, and purity is also very important for all containers used during the melting process. Measurements in the low-level counting facility at LNGS verified this assumption as shown in table 3.2. Both raw materials and CdZnTe crystals did not show any activity above the detection limits.

CdZnTe detectors generally require a surface passivation as their detector properties would slowly degrade due to chemical reactions with water vapour. The market leader for CdZnTe detectors, eV Products, typically uses a reddish resin colloquially called "red paint" which exhibits excellent passivation properties and provides stable operation for several years. The red colour, however, indicates the presence of pigments which are often contaminated with radioactivity. Unfortunately, this assumption was confirmed by

---

<sup>5</sup>Application-Specific Integrated Circuit, a custom-designed chip.



decays	Cd	Zn	Te	CdZnTe	paint	clear paint
$^{232}\text{Th};^{228}\text{Ra}$	< 4	< 8	< 7	< 12	(1100 ± 100)	< 180
$^{232}\text{Th};^{228}\text{Th}$	< 4	< 8	< 7	< 9	(730 ± 70)	< 190
$^{238}\text{U};^{226}\text{Ra}$	< 4	< 8	< 7	< 10	(2100 ± 100)	< 140
$^{238}\text{U};^{234}\text{Th}$	< 200	< 150	< 240	< 250	(1100 ± 300)	< 1500
$^{238}\text{U};^{234m}\text{Pa}$	< 70	< 150	< 140	< 220	(1600 ± 100)	< 4300
$^{235}\text{U}$	< 4	< 5	< 5	< 7	(170 ± 30)	< 15
$^{40}\text{K}$	< 24	< 55	< 51	< 91	(6900 ± 800)	< 1000
$^{60}\text{Co}$	< 2	< 3	< 4	< 5	(< 20)	< 72
$^{137}\text{Cs}$	< 1	< 2	< 2	< 4	(< 15)	< 56

**Table 3.2:** Radioactive contaminations of detector and passivation materials as measured at LNGS[Lau04] in mBq/kg. While neither the raw materials Cd, Zn and Te, nor the passivation-free CdZnTe show any sign of contamination above the detection limit, the red passivation paint clearly contains rather large amounts of radioactivity. Due to the limited sample size which was available for measurement, the exclusion limits for the clear passivation paint are not extremely low, but it is obvious that the replacement of the red passivation coating should yield a much lower radioactive background.

measurements at LNGS exhibiting activities on the Bq/kg level. After sharing our findings with eV Products, the manufacturer initiated a R&D effort to find a non-pigmented replacement with similar passivation properties. The first result of this program was designated "clear paint" and showed much less activity; in fact, no decays from the (small) sample could be found yielding upper limits that are about a factor five below the values for the red paint.

Both, detector bulk and surface coating play a prominent role in low level experiments: while the most energetic naturally occurring  $\gamma$ -line is at 2.614 MeV,  $\alpha$ - and  $\beta$ -decays can reach much higher energies of up to above 8 MeV which enables them to fake any double-beta decay. Due to their short range,  $\alpha$ -particles are only dangerous if emitted inside or on the surface of a detector. Therefore, the radiopurity of crystal bulk and its surfaces and coatings is of utmost importance.  $\beta$ -particles would also be able to travel a few cm through air so here, also contaminations of cables, holder structures and near-detector electronics are important.

The first holder structures were made of 'Pertinax' or FR2-PCB-material which was subsequently found to be quite contaminated (see Tab. 3.3). It was hence replaced by a Delrin or POM<sup>6</sup> holder found to be much cleaner. Nevertheless, simulations showed that the contribution of the holder structure was low compared to the contribution of the red paint [Blo07a].

Electronic components, however, are generally said to be very dirty, especially SMD<sup>7</sup> devices[Heu95]. It is currently unknown whether this is also true for ASICs. Due to the very strict background limitations for COBRA [Wil05b], it is therefore necessary

<sup>6</sup>PolyOxyMethylene

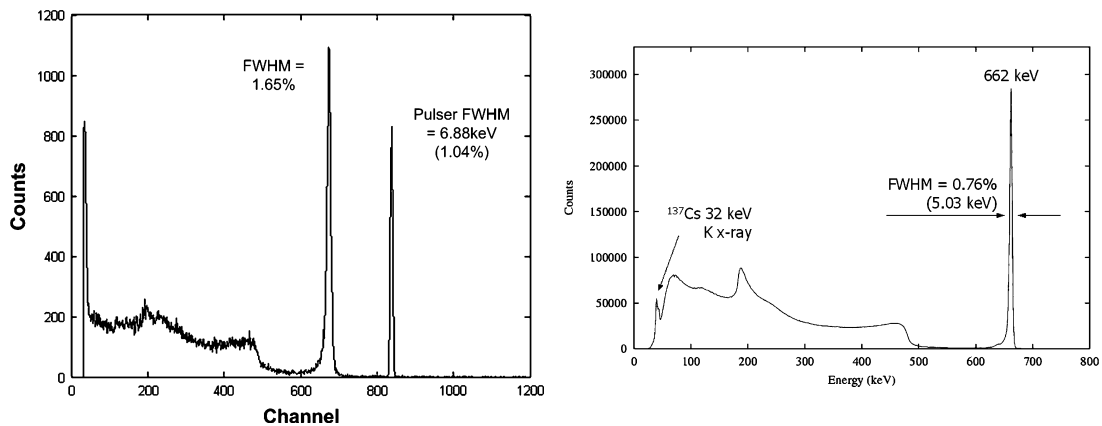
<sup>7</sup>Surface-Mounted Devices, electronic components with very small footprints.

to shield the detectors from the electronics'  $\beta$  and  $\gamma$  radiation which could reach the detector if the first preamplifier stage would be mounted in the direct vicinity of the crystal. The necessary distance and shielding can be accomplished for CPG-type detectors by using low-mass cables connecting the detectors and the first preamplifier stage. For pixel-detectors, however, this approach seems to be impossible: normally the pads on an ASIC are directly bump-bonded to the detector's pads. The low-background suitability of pixel-detectors is therefore still an open question.

- energy resolution and background rejection capability

With current CPG-type detectors, energy resolutions of below 2% at 662 keV are possible [He05, Stu05] also with large-volume detectors (see Fig. 3.6). This is much better than achievable with scintillators. As mentioned in chapter 2.1, good energy resolution is a key feature for competitive double beta decay experiments as it allows to search for a line within a rather flat background instead of mainly counting any excess above the background inside of a search window. Due to the fact that any given signal becomes the background for any other search with the same source, it is also important to be able to identify the physical background of  $2\nu\beta\beta$ -decays. In particular, for the detection of  $\beta^-\beta^-$ -decays to the ground state, good energy resolution is required to distinguish the endpoint of the continuous  $2\nu\beta\beta$ -spectrum with half-lives on the order of  $10^{19}$  years from the  $0\nu\beta\beta$ -line at the Q-value of the decay with theoretically predicted half-lives of up to  $10^{27}$  years.

With pixel detectors, one can reach even better resolutions of up to 0.76% or 5.03 keV at 662 keV [Zha05] for single-pixel events. This incredible resolution which in itself improves the signal-to-background ratio by a great deal is accompanied by the possibility to distinguish single-site events from multiple-site events.



**Figure 3.6:** Exemplary CdZnTe spectra of  $^{137}\text{Cs}$  as published by detector developers. Left: Spectrum taken with a  $1.5 \times 1.5 \times 0.95 \text{ cm}^3$  CPG-type detector showing a FWHM of 1.65% [Stu05]. Right: Spectrum taken with a 3-D position sensitive pixel detector exhibiting a resolution of 0.76% [Zha05], detector size was  $1.5 \times 1.5 \times 1 \text{ cm}^3$  with  $1.27 \times 1.27 \text{ mm}^2$  pixel size.

Thereby, it is feasible [Blo07b] to suppress

- alpha particles by up to 99.1%, depending on their energy. Criteria are here the extremely short range together with a high energy density of the deposition.
  - single  $\beta$ -decays with respect to  $\beta\beta$ -decays of the same energy by 70%. This is done by comparing the number of pixels fired by a single vs. two electrons originating from the same vertex.
  - high energy gamma interactions ( $^{208}\text{Tl}$  at 2614 keV) by 50%. They very often consist of one or more compton-processes followed by a photoeffect for full energy deposition within one crystal. The suppression mechanism here is that the deposition sites of compton and photoeffect are often not adjacent. Suppression of distributed deposition over several crystals is of course also possible as well as applying the  $\beta$ -suppression successively (single site interactions produce photoelectrons that behave like  $\beta$ -particles) which can suppress 70% of the remainder yielding a total suppression of 85%.
- cost and availability

If only a single detector is needed for spectroscopy, the cost for superior energy resolution is normally of less concern if it is necessary to get better results. As COBRA has to operate several hundred kg of CdZnTe, it is important to find a good ratio between cost, resolution/efficiency and availability. Crystal growth normally yields a much larger number of lower-grade detectors than optimum detectors which means that both pricing and availability in large numbers are much better. COBRA's current concept recognises this by foreseeing a high-grade core surrounded by a shell made from lower-grade detectors. In the  $4 \times 4 \times 4$ -detector array, the innermost  $2 \times 2 \times 2$  detectors are higher-priced (2000 US-\$/\$piece) detectors with resolutions around 3% FWHM at 662 keV while the outer 56 detectors are lower-grade (3–8% FWHM at 662 keV) detectors at 500 US-\$/\$piece.

Due to the doubts about the suitability of pixel-detectors for low-background applications mentioned above and owing to the fact that readout for pixel detectors has much longer development cycles, it was decided that the Dortmund and Sussex groups will operate a low-(background-)level test setup at the Gran Sasso underground laboratory LNGS<sup>8</sup> with CPG-type detectors. COBRA groups from Birmingham and Liverpool will at the same time explore pixel detectors. A typical CPG detector with reddish passivation coating as well as an unpassivated one that has been used for<sup>9</sup> studies [Oeh04] can be seen in Fig. 3.5.

### 3.2.4 Detector Characterisation

In 2005, a total of 72 detectors was acquired from eV Products, among them 12 high-grade detectors. The manufacturer supplied measurements of their masses before and after passivation, values for the energy resolution at 662 keV and  $^{137}\text{Cs}$ -spectra for all of them. In order to

<sup>8</sup>Laboratori Nazionali del Gran Sasso in I-67010 Assergi (AQ), Italy, a branch of the Istituto Nazionale di Fisica Nucleare (INFN).

<sup>9</sup>Transient Current Technique, a method to study detector properties by examining the time-resolved charge carrier induction signal after depositing a well-known charge at a defined position, e.g. by means of a laser or with  $\alpha$ -particles. See, for example, [Kra04].

know the behaviour of all crystals before contacting them and to verify the supplier's data, all crystals were characterised by conducting the following measurements:

- leakage current vs. bias voltage measurements (I-V curves) between cathode and anodes as well as between the anode grids (I-V-ag curves)
- capacitance vs. bias voltage measurements (C-V curves)
- leakage current at fixed bias voltage over time measurements (I-T curves)
- absolute efficiency calibrations with  $^{137}\text{Cs}$  at a fixed source-detector distance
- energy calibrations with  $^{57}\text{Co}$ ,  $^{137}\text{Cs}$  and natural Th

A photograph of the test setup is depicted in Fig. 3.7. Temporary contacting has been done by using Süss MicroTec PH100 needle probes for the anode grids and by placing the detector with its solid cathode electrode onto a gold-plated PCB<sup>10</sup>. To improve the reliability of the cathode's contact, a small piece of conductive rubber was placed between PCB and detector. The probe needles and the PCB were connected to a Keithley 487 picoamperemeter/voltage-source, a LCR-meter<sup>11</sup> or to a COBRA preamplifier, respectively, for the individual measurements.

Exemplary plots of I-V-, I-V-ag, I-T- and C-V-measurements are depicted in Fig. 3.9 to 3.12. As expected, most detectors exhibited a fairly ohmic leakage current behaviour as well as a stable and small capacitance (around 1 pF) which is independent of the applied bias voltage. The small decrease in leakage current over time displayed in Fig. 3.11 is typical for all examined CdZnTe detectors. Fig. 3.8 depicts all recorded I-V- and I-V-ag curves. Most leakage current and capacitance measurements did not generate unexpected results. While a direct correlation between bulk leakage current and energy resolution was not seen, all good detectors exhibited a low I-V-ag value and therefore belonged to the lower group of curves. This is in line with publications which report that the energy resolution of CdZnTe detectors does not largely depend or is limited by bulk leakage currents, but rather by crystal inhomogeneities [Bol07] or surface passivation [Pre01].

The energy resolution measurements were evaluated offline by an automated peak finding and fitting routine based on ROOT<sup>12</sup> implemented by J. Dawson. Exemplary  $^{137}\text{Cs}$  and Thorium spectra including the fitted peaks are depicted in Fig. 3.13. By this automated procedure, energy resolution data was gathered for all detectors. A compilation of their energy resolution at 662 keV and 2614 keV together with the 662 keV resolution reported by eV Products can be found in appendix A.

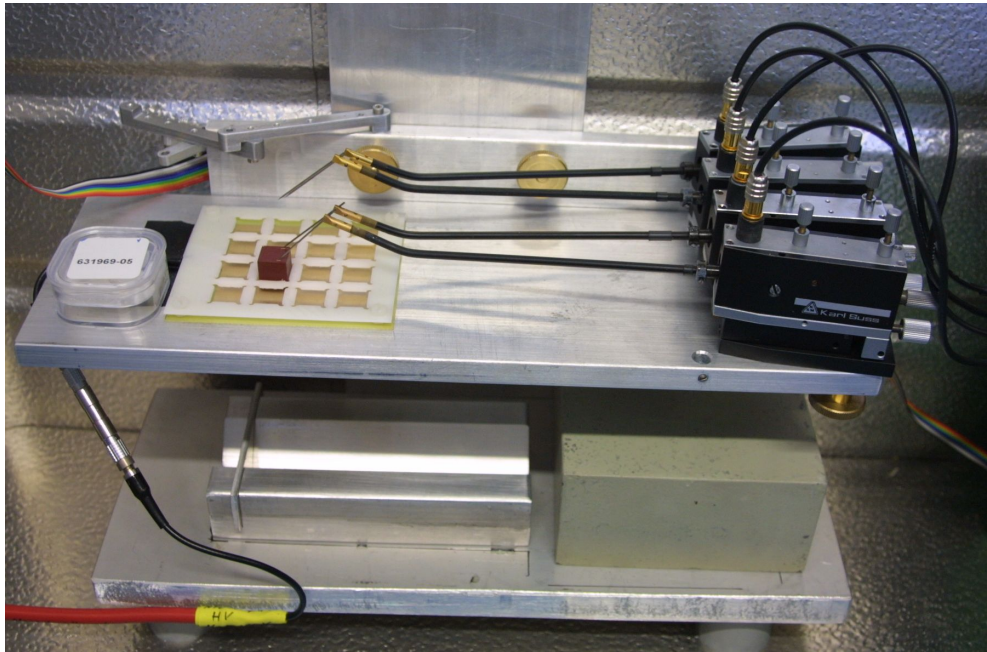
The outcome of the energy resolution measurements was unexpected: As can be seen in Fig. 3.14, the measured resolutions differed quite much from the ones reported by the manufacturer. Values inferior to eV's specifications could be explained by bad or unreliable cathode contacting. Besides, our setup was never able to yield resolutions better than about 20 keV probably due to cable lengths causing too much noise. On the other hand, we were surprised by the fact that many crystals showed significantly better results than declared by eV Products. It is still unclear whether short- or long-term changes in detector behaviour can account for the change.

---

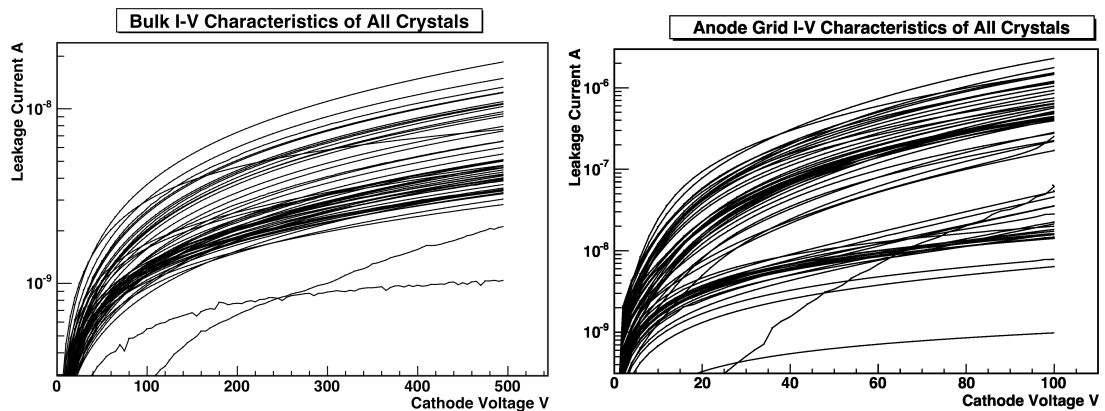
<sup>10</sup>Printed Circuit Board

<sup>11</sup>A measurement device for resistivity R, capacitance C and inductance L.

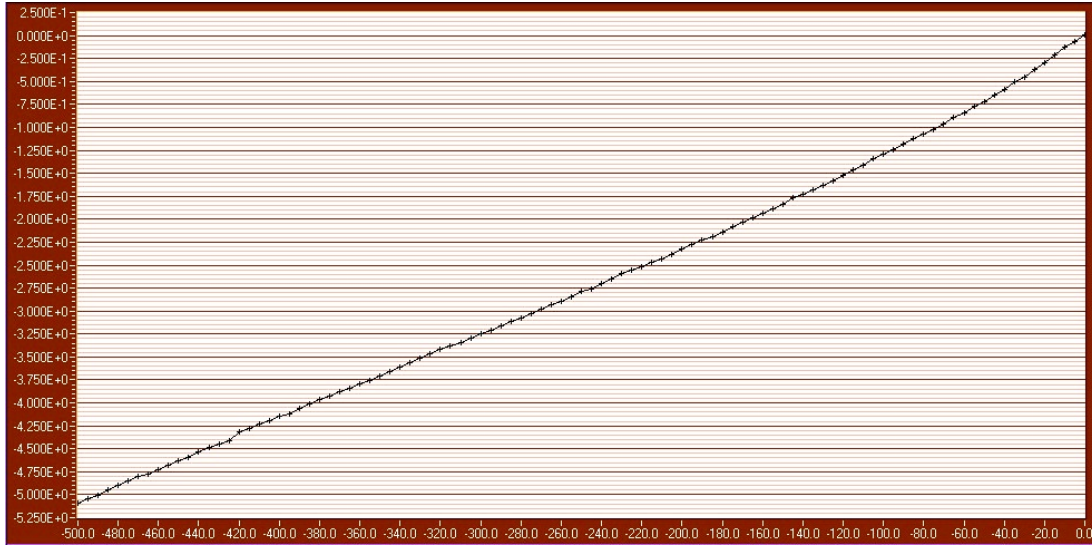
<sup>12</sup>An object-orientated data analysis framework. Visit [root.cern.ch](http://root.cern.ch) for details.



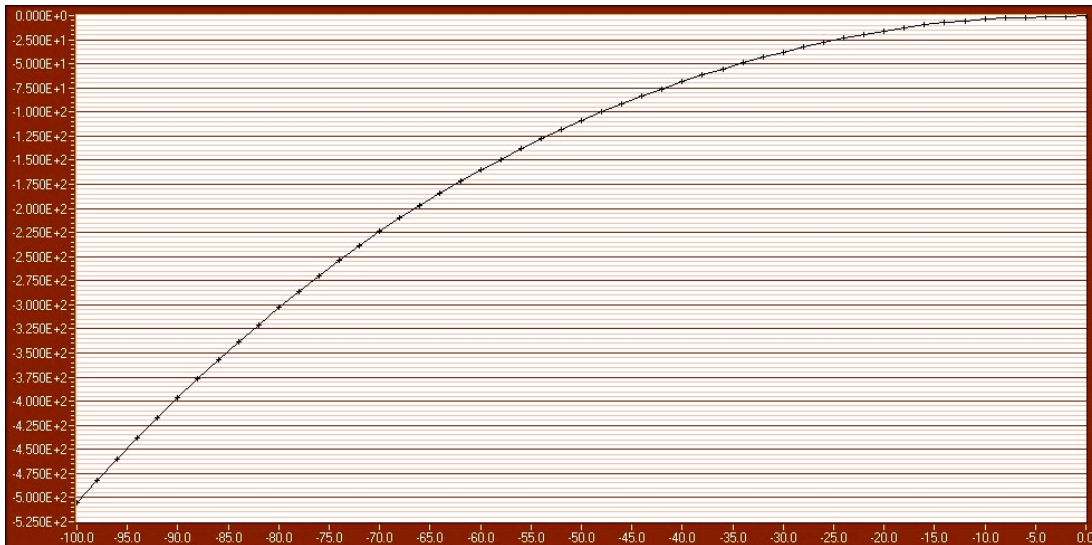
**Figure 3.7:** Photograph of the characterisation setup. A standard-passivated detector can be seen within a Delrin guidance plate on the gold-plated PCB for the cathode contacting. Four Süss MicroTec PH100 probes for the anode contacting of two detectors are displayed; underneath the detector, the aluminium holder with its V-shaped notch for the  $^{137}\text{Cs}$ -source can be seen which was used to maintain a fixed and reproducible distance between source and detector(s).



**Figure 3.8:** Left: all recorded I-V-curves plotted onto one canvas. No obvious arrangement in groups can be seen; the two deviating low-current measurements are assumed to be faulty. Right: all recorded I-V-ag curves plotted onto one canvas; again two deviating curves can be seen. They are assumed to be flawed, too, but not to be correlated to the deviating I-V-measurements. Here, the measurements can be coarsely categorized into a low- and high-current group, respectively, representing the different quality grades that were obtained. Apparently, the different detector qualities are only reflected within the anode-grid-resistivity while the bulk leakage current is no indicator for the detector properties within CdZnTe. Compiled by J. Dawson [Daw06].



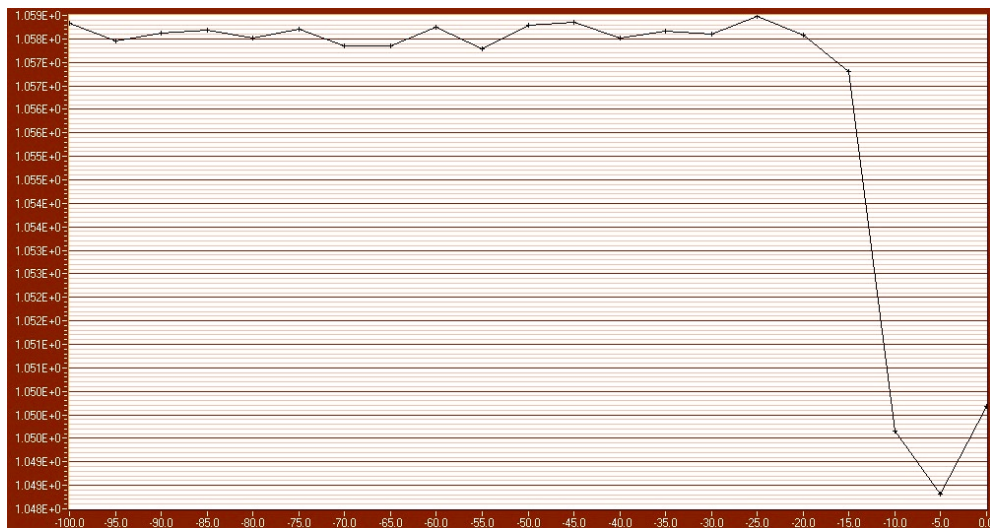
**Figure 3.9:** Plot of the leakage current between cathode and anodes (I-V-curve) (range:  $-5$  nA to  $0$  nA) vs. voltage (range:  $-500$  V to  $0$  V). The measurement was conducted starting at  $0$  V, however, due to the negative voltage/current the graph is running towards the lower left quadrant of the coordinate system. The plot acts as exemplary I-V-measurement and was done with a 'reference'-detector (631972\_07). It demonstrates the dominating ohmic behaviour of the detector.



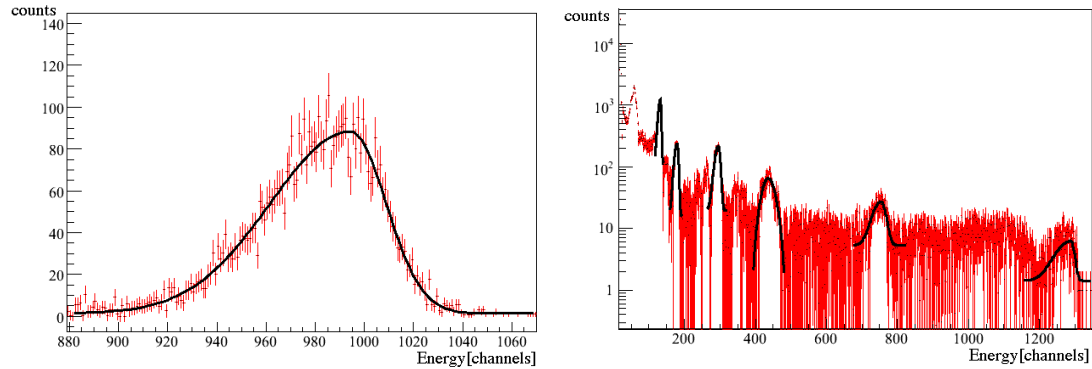
**Figure 3.10:** Plot of the leakage current between the two anode grids (I-V-ag curve) (range:  $-500$  nA to  $0$  nA) vs. voltage (range:  $-100$  V to  $0$  V). The measurement was conducted starting at  $0$  V, however, due to the negative voltage/current the graph is running towards the lower left quadrant of the coordinate system. The plot acts as exemplary I-V-ag-measurement and was done with a 'reference'-detector (631972\_07). Contrary to the expectation of again ohmic behaviour, a partial quadratic dependence is clearly visible. This was observed on all detectors.



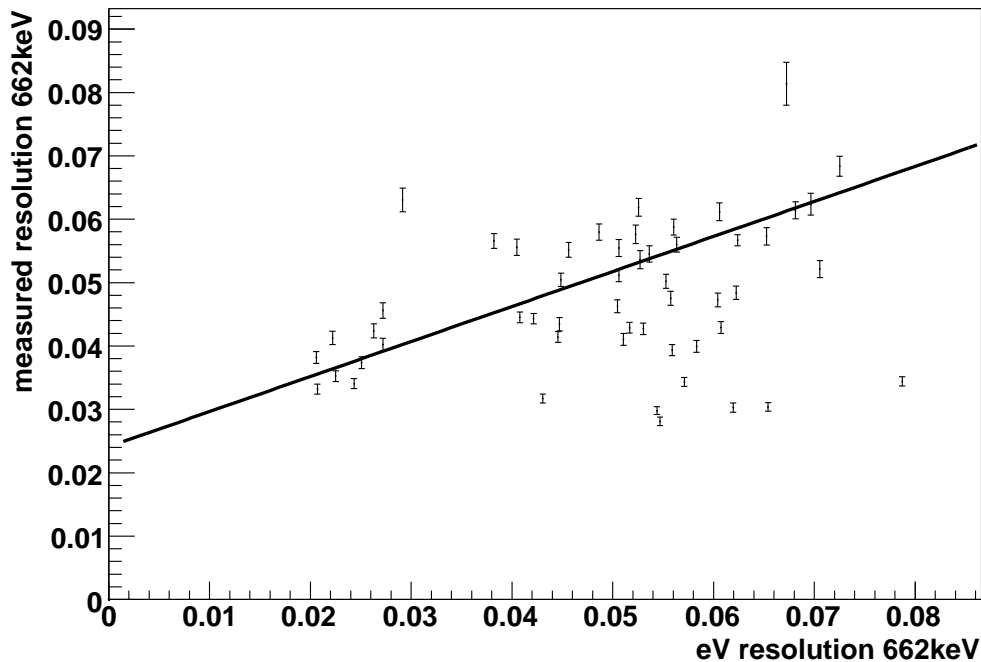
**Figure 3.11:** Plot of the leakage current between cathode and anodes (range:  $-5.28$  nA to  $-5.04$  nA) at 500V bias voltage vs. time (range: 0 to 1900 seconds). The moderate and apparently asymptotic decrease of the leakage current from its initial value at  $-5.27$  nA to  $-5.06$  nA after about 30 minutes is characteristic for CdZnTe detectors. The plot is displayed as exemplary measurement and was done with a 'reference'-detector (631972\_07).



**Figure 3.12:** Plot of the detector's capacitance measured between cathode and anodes (range: 1.048 pF to 1.059 pF) at 1 MHz vs. voltage (range:  $-100$  V to 0 V). Beyond  $-20$  V, the capacitance stays constant indicating full depletion. Up to this voltage, the Schottky behaviour of the metal-semiconductor interface of the electrodes is visible acting partly like a diode. The large offset can be attributed to the dominating ohmic character of the detector. Its large thickness yields a very small capacitance compared to other semiconductor devices. The plot is displayed as exemplary measurement and was done with a 'reference'-detector (631972\_07).



**Figure 3.13:** Left: fit of the 662 keV gamma line of  $^{137}\text{Cs}$ . Note the asymmetric peak shape due to non-optimised CPG-gain matching which is taken into account by the fitting routine. Right: fit of all relevant peaks of a natural thorium spectrum.



**Figure 3.14:** Scatter plot of the energy resolution (FWHM) measured with  $^{137}\text{Cs}$  in fractions of 1 (FWHM/662keV) reported by eV Products versus the resolution measured with the Dortmund test setup. The line of best fit displays that apart from the large deviation of the values from the expected correlation there is also an offset indicating that the Dortmund setup seems to generate additional noise limiting the achievable energy resolution to about 2.8%.

### 3.2.5 Zinc Content

A piece of information not delivered by eV Products is the individual zinc content of each detector which typically substitutes between 7 and 13 % of the cadmium. For the cadmium and especially for the zinc half-life results, the absolute number of observed nuclei is quite important. Therefore, the zinc content should be known with about the same precision as the



detectors' active volume is known, at least on the per-cent level.

Non-destructive measurement methods are preferred as they enable a determination of the zinc content before the low-level measurement takes place; hence, all deduced half-life limits can immediately be calculated with better precision. Two non-destructive measurements available at DELTA<sup>13</sup> are X-ray fluorescence and the determination of the lattice constant. The first method uses X-rays to excite the K- and L-shell electrons of Cd, Zn and Te inside the bulk material. A suitable detector then observes the fluorescence. From the intensity ratios, one can deduce the amounts of Cd, Zn and Te under study. The lattice constant method uses the fact that the precise value of the constant depends on the zinc content. According to Vegard's law [Veg21], the lattice constant  $a_{\text{Cd}_x\text{Zn}_{1-x}\text{Te}}$  of the compound can be interpolated linearly between its 'pure' states, in the present case between the values of CdTe and ZnTe:

$$a_{\text{Cd}_x\text{Zn}_{1-x}\text{Te}}(x) = a_{\text{CdTe}} \cdot x + a_{\text{ZnTe}} \cdot (1 - x) = 0.6482 \text{ nm} \cdot x + 0.61034 \text{ nm} \cdot (1 - x) \quad (3.2.5)$$

where  $x$  denotes the fraction of Cd in the compound. To achieve an accuracy for  $x$  of better than 1%, the measurement of  $a$  must be at least as precise. Measurements at synchrotron light sources like DELTA are capable of accuracies of better than 1‰, however, the orientation of the crystals to find the X-ray reflexes necessary for the measurement might be tedious.

First fluorescence measurements were done by C. Sternemann at DELTA in 2006, but a high iron content of the passivation resin and fairly thick (around 150nm) Au-on-Pt electrodes prevented the clean detection of fluorescence X-rays. Besides, it appears that at least Te is in principle difficult to detect with the fluorescence method as also measurements at ISAS<sup>14</sup> of Te nanoparticles failed with a totally different setup. Currently, measurements of the lattice constant are in progress at DELTA.

### 3.3 Detector Mountings

There are many different possibilities to mount semiconductors that take into account the special needs of the detector technology and applications: low-energy X-ray Si-detectors will have a very thin entrance window and a special electrode to avoid a dead layer beneath the surface while this is not important for high-energy Ge-detectors. For them, however, a copper cold-finger and vacuum insulation is necessary. In general, all mountings have to protect the detector from mechanical and thermal stress and to allow for easy contacting.

For COBRA, it was necessary to develop a scalable mounting for a detector array with high packing density and low radioactive contamination – the holder structure represents the largest fraction of unshielded mass close to the detector that is not part of the detector itself or the copper shielding. Normal CdZnTe holders which are commercially used are made from Al<sub>2</sub>O<sub>3</sub> or other ceramics. Unfortunately, these are known to contain large amounts of radioactivity which was also verified by measurements at the low-level counting facility at LNGS [Lau04]. The next natural choice would have been FR4 PCB material which is used extensively in electronics and would have allowed easy manufacturing of copper traces on the surface. Again, this material is heavily contaminated because of the glass fibres which are used for mechanical stability: these contain much natural potassium and hence also <sup>40</sup>K. Heusser [Heu95] quotes activities of up to 20Bq · kg<sup>-1</sup> for fibre-reinforced PCBs.

<sup>13</sup>Dortmund ELecTron Accelerator

<sup>14</sup>Institute for Analytical Sciences, Dortmund

decay	copper	FR2 base plate	FR2 guiding plate	Delrin
$^{232}\text{Th};^{228}\text{Ra}$	< 2.1	(29 ± 7)	(18 ± 3)	< 5
$^{232}\text{Th};^{228}\text{Th}$	< 2.3	(32 ± 7)	(15 ± 3)	< 5
$^{238}\text{U};^{226}\text{Ra}$	< 2.5	(170 ± 10)	(66 ± 4)	< 5
$^{238}\text{U};^{234}\text{Th}$	< 100	(250 ± 110)	< 92	unknown
$^{238}\text{U};^{234m}\text{Pa}$	< 47	< 480	< 180	< 700
$^{235}\text{U}$ -chain	< 1.4	(12 ± 3)	(2 ± 1)	< 3
$^{40}\text{K}$	< 11	(330 ± 40)	(430 ± 30)	< 31
$^{60}\text{Co}$	< 0.6	< 4	< 2	< 2
$^{137}\text{Cs}$	< 0.9	(650 ± 40)	(19 ± 2)	(3 ± 1)

**Table 3.3:** Activities in [mBq/kg] found in different construction materials caused by contaminations as measured in the LNGS low-level measurement facility. While in copper no significant contamination could be found within the measurement time, the FR2 material is unacceptably contaminated. The  $^{137}\text{Cs}$ -activity found in Delrin could be due to surface contaminations.

In COBRA's early phase, so-called Pertinax (FR2) PCB material was used because it was said to be rather clean compared to FR4. Because the background did not decrease significantly after moving the setup from Dortmund to the LNGS, contaminants were assumed to be close to the detectors. Table 3.3 contains an overview of trace radioactivity found in the main construction materials which have been copper and two different kinds of FR2 for base and guiding plate, respectively. The necessary measurements of material samples were conducted by M. Laubenstein with low-background HPGe detectors<sup>15</sup> in LNGS' underground low level laboratory [Lau04]. While copper does not contain any detectable contamination, the FR2 samples exhibit a significant amount of radioactivity.

Upon learning this, a brief survey of suitable construction materials known to contain almost no radioactivity resulted in two proposals: Teflon (polytetrafluoroethylene or PTFE) and Delrin (polyoxymethylene or POM). Because Teflon is impossible to glue and seemed to be too elastic to yield stiff enough holder structures, Delrin was chosen as next holder material and measured at LNGS. The results are listed in table 3.3 and prove the suitability of Delrin. It is believed that the measured activity of  $^{137}\text{Cs}$  is mainly due to surface contaminations, therefore different cleaning procedures have been tested on Delrin. First, the holders are degreased using ultrasonic baths with acetone and 2-propanol. To remove hydrophilic contaminations, subsequent acid etching is used. While etching with concentrated  $\text{HNO}_3$  resulted in an intense exothermal chemical reaction, diluted  $\text{HNO}_3$  as well as  $\text{H}_2\text{SO}_4$  and  $\text{HCl}$  can be used. This is followed by thorough rinsing with distilled water. Because the measured activity is near the detection limit and due to the limited time allocation at the LNGS low-level measurement facility, samples of surface-cleaned Delrin could not yet be measured.

The holder's layout which is depicted in Fig. 3.15 was governed by the following aspects:

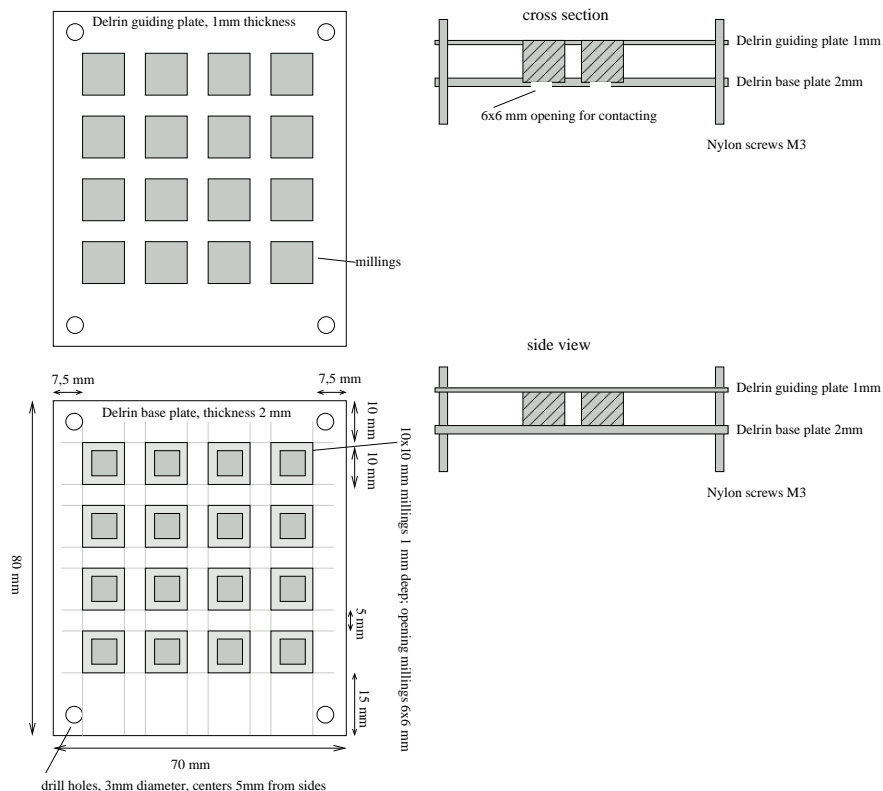
- as little mass as possible
- scalability

<sup>15</sup>High-Purity Germanium radiation detectors

- guidance for anode and cathode cables
- mechanical stability while applying no pressure

To be able to apply a strain relief to the cables running between electrodes and preamplifiers, support close to the top and bottom faces of the detector had to be foreseen. A low-mass solution seemed to be the usage of two plates at the necessary distance held together by threaded rods. Mechanical tests showed that for the base plate 2 mm material thickness was needed for the necessary stability while for the guiding plate 1 mm was enough. To avoid pressure on the detectors which could due to their brittleness lead to macroscopic damaging, the detectors should rest on the base plate while the guiding plate would only stabilise them and prevent them from tilting. To be able to contact/re-contact the detectors in place, a 6 by 6 mm hole was planned for cathode contacting while the anodes were well accessible from above. Additional stability was expected from a 1 mm deep milling around the detectors' positions preventing any movement on the base plate.

Because a  $4 \times 4 \times 4$ -detector array was foreseen, the array size on the holder was already defined. From a mechanical point of view, also significantly larger holder structures could be built. The space in between the detectors was chosen to be 5 mm so discharges between detectors would be avoided and the traces running to the anode contacts could run on the bars instead of over other detectors (see chapter 3.5). Finally, the base plate was extended by 2 mm on each side to act like a drawer when inserted into the innermost shielding, the NEST (see chapter 4.2.5).



**Figure 3.15:** Technical drawings of the Delrin (POM) holder structure for the  $4 \times 4 \times 4$ -detector array.

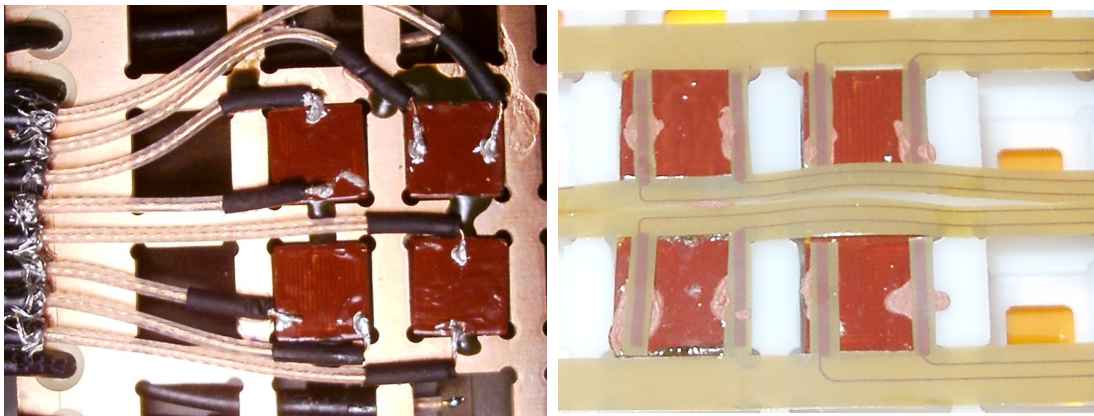
### 3.4 Contacting

Contacting CdZnTe is as already mentioned a difficult task. The standard contacting method for silicon is ultrasonic bonding where the joint between electrode metal and wire is made by means of mechanical energy. Due to the brittleness of CdZnTe, this method often induces crystal damages around the bond-pad leading to significant degradation of the detector properties. NASA scientists have successfully wire-bonded CdZnTe [Sta06], however, special electrodes with large thicknesses of up to  $1\ \mu\text{m}$  absorbed much of the energy. First experiments with a wire-bonder and Al-wire in Dortmund were unsuccessful.

A second widespread method are thermal connections like soldering or bump-bonding. Here, too, CdZnTe takes damage: temperatures above roughly  $80^\circ\text{C}$  damage the detector permanently [Fau06]. The industry solution to this problem is to use conductive glue to connect contact pad and cable, usually with a silver-filled conductive epoxy resin by EpoTek<sup>16</sup>, H20E, which can be cured at  $80^\circ\text{C}$  within three hours. This method for contacting has been used for the  $2 \times 2$ -detector array (see Fig. 3.16), but from COBRA's point of view, it has two disadvantages:

Firstly, epoxy resins cannot be removed in a non-destructive way once they are cured as they are two-component glues. Very probably it will be necessary to test several different setups and it is highly desirable to be able to detach the cables from the detector and re-gluce them afterwards.

Secondly, H20E is silver-filled. Natural silver comprises the stable isotopes  $^{107}\text{Ag}$  and  $^{109}\text{Ag}$  which are converted into radioactive nuclei by neutron activation, e.g. by secondary neutrons from cosmic radiation. The  $(n,\gamma)$ -reaction partially produces the metastable nuclei  $^{108m}\text{Ag}$  and  $^{110m}\text{Ag}$  with half-lives of 418 years and 250 days, respectively. They then decay via  $\beta$ -decays with Q-values of up to 2892 keV. For details, see [Chu99]. Hence, silver should be avoided due to its neutron activation potential within the vicinity of the detectors as it may emit  $\beta$ - and  $\gamma$ -radiation of up to almost 3 MeV.



**Figure 3.16:** Left: contacting done with H20E silver-filled conductive epoxy. Right: one of the first contactings done with the final copper-filled dissolvable Dortmund-mixture.

Glues which can be dissolved are normally one-component glues. From copper powder, only negligible radioactive content is expected. Therefore, several commercially available one-

<sup>16</sup>official website: [www.epotek.com](http://www.epotek.com)

glue/test-joint #	1	2	3	4	5	6	7	8	9	10
U:C:A 2:2:1	1.22	0.05	0.35	0.16	0.36	0.06	0.08	0.11	0.06	0.03
U:C:A 2:2:0.5	0.12	0.04	0.08	0.03	0.06	0.03	0.08	fluct.	0.15	8.71
U:C:A 1.5:2.5:0.5	10.74	0.33	0.4	0.15	0.82	fluct.	OL	0.27	1.22	0.12
U:C:A 3:1:0.5	fluct.	OL	2.07	1.9	1.36	0.33	2.87	fluct.	0.6	fluct.
U:C:A 2:2:0.25	fluct.	1.28	0.99	fluct.	0.48	fluct.	0.37	0.26	1.50	0.07

**Table 3.4:** Exemplary results of resistivity-measurements of copper-on-copper test-joints with different copper-filled conductive glues given as raw multi-meter readings in [ $\Omega$ ]. Mixture composition in parts of U="UHU hart", C=copper powder and A=acetone. fluct.=resistivity value fluctuated, OL=resistivity  $\geq 10 \text{ M}\Omega$ .

component glues have been filled with copper powder in different fill-factors and the joint conductivity as well as their processibility and adhesiveness have been assessed, among them UHU hart, UHU Alleskleber, UHU extra Alleskleber tropffrei, UHU Alleskleber Kraft and for comparison reasons a two-component glue, UHU schnellfest. The survey was not exhaustive but limited to glues that were readily available in hardware stores. Most glues surprisingly failed the processibility test after filling with copper powder, and many showed rather poor conductivity results yielding a large spread of resistivities over the copper-on-copper test joints.

The two best-working glues were UHU schnellfest, the two-component epoxy resin, and UHU hart, a nitrocellulose-based re-solvable single-component glue. UHU hart has been assessed thoroughly with different fill factors and several dozens of test-joints. An exemplary selection of conductivities measured during these tests can be found in table 3.4. The drying time depended strongly on the acetone addition: more acetone caused the glue to dry faster, get more liquid and hence have better wetting abilities. The manufacturer affirmed that diluting the glue with acetone is an acceptable procedure. It was found that a mix of UHU hart, copper powder and acetone of 2:2:1 weight parts worked reliable (less than 3% of all copper-on-copper test-joints failed) while exhibiting good processibility: curing of a joint takes about 30 seconds, the glue wets the contacts quite well and is easily applied by dropping instead of smearing. Disadvantages are a limited pot life of about 30 minutes even if enclosed air-tight (probably due to an unknown reaction of the copper with the glue) making it necessary to freshly prepare the mixture before each gluing process. A picture of the 2x2-detector array glued with this mixture to the self-developed Kapton cable is shown in Fig. 3.16.

For detaching the contact, several organic solvents were assessed. It was found that methanol worked best. Other substances working only slightly worse are acetone and chloroform while less aggressive solvents like 2-propanol worked rather poorly. Because acetone is by far less harmful than methanol, it was chosen to use acetone for re-contacting procedures. Several recontactings done with a dedicated detector (631959\_04) proved that re-contacting using acetone is possible. At the same time, it was shown that acetone also damages the passivation coating leading to openings after several (> 4–5) re-contactings. These cannot be repaired, unfortunately, as eV Products considers the passivation coating one of their most important trade secrets. Due to a short shelf life, this resin can also not be delivered as a ready-to-use mixture.

A drawback of the currently used Dortmund-mixture seems to be that apparently some

contact degradation takes place. If a full layer of 16 detectors is freshly contacted at three electrodes each, several regularly fail hours to days after gluing. Seemingly, the cathode contact is particularly affected, maybe due to the fact that both gravity and a clean gold-only surface work against the adherence while the anode contacts rest on the detector and the glue can make use of the comparatively rough surface of the passivation resin around the anode openings. Most often, a macroscopic failure is not visible. However, already in the  $2 \times 2$ -detector array contacted with H20E different quality levels of the contacts and also some evolution were noted. This is reflected in the fact that for a long time, detector D4 was yielding the best data while at late stages of data taking, D1 became superior. Currently, tests are underway to replace the gluing with needle-style pressure contacts.

### 3.5 Wiring

Commercially available detectors are normally glued to a thin (bonding-)wire or directly to a coaxial cable. In COBRA's first stage, RG-174 coaxial cables with 2.8 mm diameter were used (see Fig. 3.16). Later it was noted that these cables consist of significantly more material than would be necessary and that nothing is known about the radioactivity they carry. It proved to be difficult to find a supplier capable of delivering an unchanging quality with regard to the production process – the cable's properties are standardised so most suppliers acquire their stock from rather small no-name Asian companies. This leads to a certain unpredictability of the radioactive content of such cables.

Apart from radioactivity concerns, already the footprint of 'only' 64 cables was too large to handle – this cabling method is not scalable. It was briefly considered to use RG-178 cables with 2.0 mm diameter and a Teflon insulation (which is believed to be quite free of radioactivity), but using cables will always limit the achievable array size if it is desired to run the cables not over detectors but rather over the Delrin bars between them. Therefore, it was decided to use a technology that can reach very high trace-densities while being capable of replacing cables of some meters length: Kapton<sup>17</sup>-based flexible printed circuit boards. Their base material polyimide is said to be rather clean, besides the base foil is normally only 50  $\mu\text{m}$  thick leading to very little material in the detectors' vicinity. Commonly, traces can be as narrow as 125  $\mu\text{m}$  with 125  $\mu\text{m}$  pitch leading to 4 traces per mm bar width which results in reasonable array sizes. This number can be increased if necessary by roughly one order of magnitude by using multi-layer flexible PCBs.

The PCB design was done with the software-package EAGLE by CadSoft<sup>18</sup> which is available for all major operating systems. Key points were to

- keep the cables as short as possible
- allow the removal of individual detectors from the Delrin holder without affecting the remaining ones
- avoid as far as possible additional connectors between detector and preamplifier
- keep the cables' capacitance as low as possible

---

<sup>17</sup>Kapton is a trade-name for foils made from polyimide.

<sup>18</sup>official website: [www.cadsoft.de](http://www.cadsoft.de)

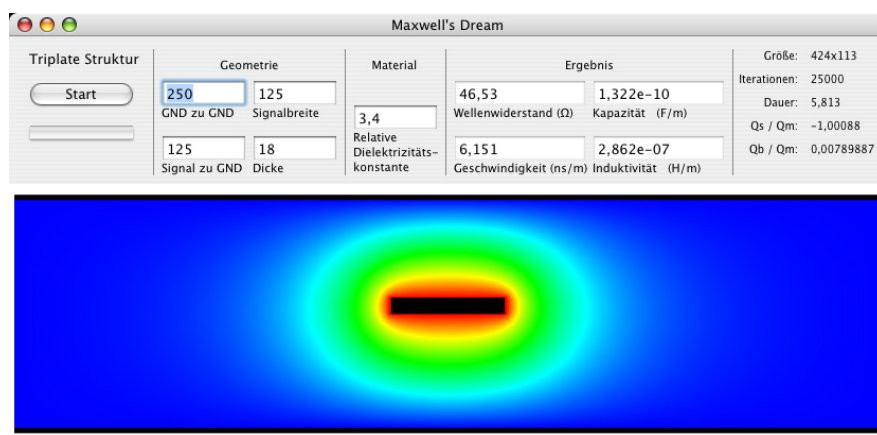
- avoid crosstalk

The cable length is only important for the anode-side cables as here additional capacitance will increase the noise level: CPG-type detectors are very thick compared to their electrode area so their capacitance is very low (in the few pF region) compared to e.g. silicon detectors. Therefore, the cables' capacitance will be the dominant contribution ranging from roughly 100 to 200 pF/m. Assuming cable lengths of 30 to 40 cm, this yields between 30 and 80 pF resulting in noise contributions of about 3 to 5 keV. Comparing this value to currently reached resolutions (see spectra on page 34) shows that the effect is still not dominant at the present status but should be kept in focus.

By forming 'tongues' as contact pads and running the traces on the Delrin bars between the detectors, it is possible to keep the Kapton out of the way of the detectors. By flipping the anode tongues, it is possible to remove single detectors without affecting the neighbours granted that a stress relief has been applied by e.g. gluing the traces to the Delrin bars with cyanoacrylate.

Using a flexible PCB makes it possible to have a transitionless connection between preamplifier and detector while being able to have  $\gamma$ -catching kinks in the cables' path through the lead castle: these are necessary to avoid a 'tunnel' through which gammas may directly propagate to the detectors without having to penetrate at least several cm of lead. Currently, they are formed by a lead brick that was sawn in a V-shaped manner. The brick is taken apart and the parts are arranged on top and underneath the flexible PCB; see Fig. 4.8 for details. For the time being, the connection to the preamplifier is established by two 37-pin Sub-D connectors to maintain flexibility during the development cycle. Later, a direct solder connection to the preamp's PCB is possible resulting in still higher connection conductivity and reliability.

While coaxial cables always have a capacitance of around 100 pF/m, this value can be influenced with flexible PCBs: unshielded PCBs have extremely low (yet not well-defined) capacitances but lack protection against crosstalk and electronic pick-up. Shielded cables are normally manufactured either as 'microstrip' or as 'triplate' designs. While the first consists of a ground-plane on one side of the cable only, the latter encloses the traces with ground-planes



**Figure 3.17:** Screenshot of the simulation program 'Maxwell's Dream' which was used to calculate the cable's capacitance. Depicted is the original concept with 125  $\mu\text{m}$  distance between ground planes and trace yielding a capacitance of about 132 pF/m.

on both sides. Due to the huge width-to-thickness ratio, in both cases the electric field lines are mostly kept between trace and ground-plane damping crosstalk similarly well. Naturally, the microstrip design is inferior concerning the protection against external pick-up while differences in capacitance are not very large. Therefore, the triplate design has been chosen to build shielded cables for COBRA. The program 'Maxwell's Dream' by Elkosoft<sup>19</sup> was used to estimate the capacitances of different layer configurations. A screenshot of the user interface is displayed in Fig. 3.17.

Minimisation of the capacitance can be obtained by narrow traces and large distances between trace and ground plane. While the minimum available width of a trace is governed by the manufacturer's guidelines, the configuration of the cable's cross-section is better accessible – blind layers, spacers or thicker base foils can be used. Enlarging the distance, however, also leads to stiffer cables which consume more space. Considering arguments, the following decision was made:

- narrow traces: using the standard minimum value of 125  $\mu\text{m}$  minimizes the capacitance and leaves room for comparatively large gaps of 1.1 mm between the traces to avoid crosstalk.
- ground-plane distance: the signal layer is attached to the shielding layers with a 75  $\mu\text{m}$  bondply sheet<sup>20</sup> yielding a total distance between trace and ground of about 125  $\mu\text{m}$  while keeping the cable's flexibility satisfactory.

First cables were made in Dortmund with aid of the Elektronik-Werkstatt (see Fig. 3.18). Due to rather poor photoresist, the traces' width was limited to only about 500  $\mu\text{m}$ . The shielding layers were soldered to a 'preamplifier-end' casing which also contained connectors soldered to the cable. At the detectors' side, one shielding layer ended at the beginning of the Delrin holder while the other was insulated with a coverlay and extended to the end of the Delrin holder. It could be flipped back to enable access to the detectors and forward to float in a distance of a few mm and protect the detectors from pick-up. The four detectors of the  $2 \times 2$ -array have been recontacted to these cables in December of 2004 using the Dortmund-mixture copper-filled conductive glue. Due to the fact that all H20E-joints had to be broken mechanically, only two detectors performed well afterwards. Nevertheless, a significant background reduction due to the switch to the Delrin holder and to the cleaner Kapton-cables could be seen. The anode side capacitance of this prototype was measured to be around 62 pF.

After this successful test, a finalised cable layout was put together accommodating a full 32 (anode side) or 16 (cathode side) contact tongues, respectively (see Fig. 3.19). Instead of cutting the tongues out with a scalpel, laser cutting was used which permitted very lightweight, fragile tongue structures. Holes drilled into the Kapton should improve the adherence of the conductive glue by allowing it to 'get a grip' on the tongue. Because only capacitance on the anode side of the detector is said to influence its energy resolution, it was decided to use very long high-voltage cables in order to allow the High-Voltage(HV)-transition box to be kept out of the way. This was done because the four necessary 16-channel preamp boxes (see chapter 5.1.5) were each 5 cm high making it impossible to stack HV boxes in between them. Therefore, the HV cable was intended to run between two preamp boxes, make a 90° turn,

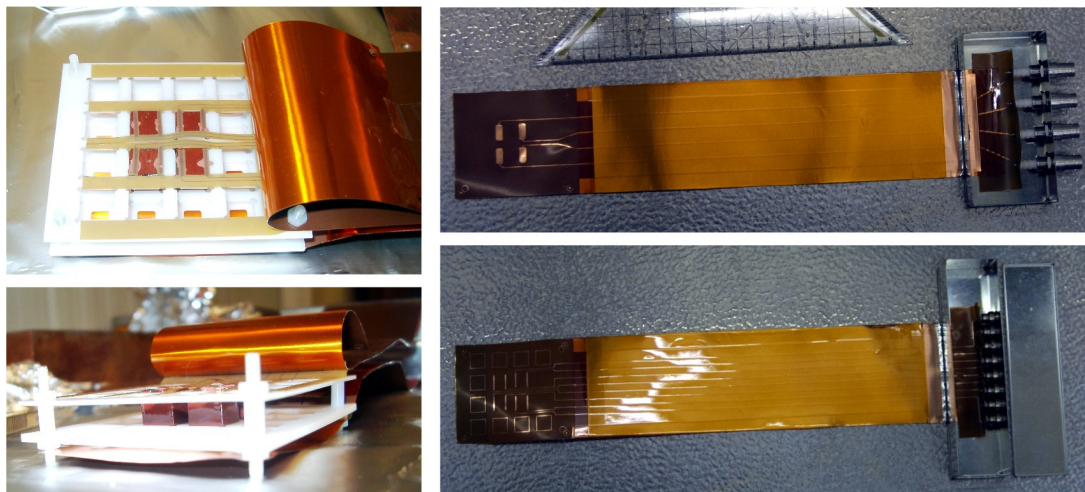
<sup>19</sup>official website: <http://www.elkosoft.de>

<sup>20</sup>Bondply LF0111 is the designation of DuPont for a connection layer consisting of two 25  $\mu\text{m}$  thick glue layers on a 25  $\mu\text{m}$  thick Kapton support.



exit sideways and enter its own transition box in a place without space constraints. To further reduce the cable capacitance on the anode side, two measures were taken:

- **Minimisation of cable length:** The necessary cable length is dictated by the thickness of the lead castle (see chapter 4.2.4). Due to the fact that cables for all four layers run in the same central tunnel through the shielding, however, the two outer layers (topmost and bottommost) require some additional centimeters of cable length compared to the two inner layers to reach the detectors as well as the outer preamplifier boxes. The necessary cable lengths were calculated from the NEST's construction drawings (see appendix C) and evaluated with a mock setup. It was found that while for the inner layers a distance of 260 mm between Delrin-edge and connector-edge is sufficient, 340 mm are necessary for the outer layers. This leads to trace lengths of 300–370 mm on the short cables and 370–440 mm on the long cables. 5–75 mm of these (the distances on the Delrin holder structure) can normally be subtracted when calculating the capacitances because here the shielding is normally kept at a few mm range.
- **Screening:** COBRA's LNGS setup is operated inside a Faraday cage. Therefore, pick-up should be already screened by this measure while internally generated noise was not expected. Due to the fact that the probably not necessary screening layers of the Kapton cable are responsible for almost all of the cables' capacitance, it was decided briefly before placement of orders to at first omit the shielding layers for both anode and cathode cables. Instead, spare sheets of raw material that will allow the addition of shielding layers afterwards were ordered. This decision additionally reduces the cost for the production of the Kapton cables by a significant factor. Instead of the original layer composition used for the prototype cables which is depicted in Fig. 3.20, only signal layer and coverlay were commissioned (see Fig. 6.1 for comparison).

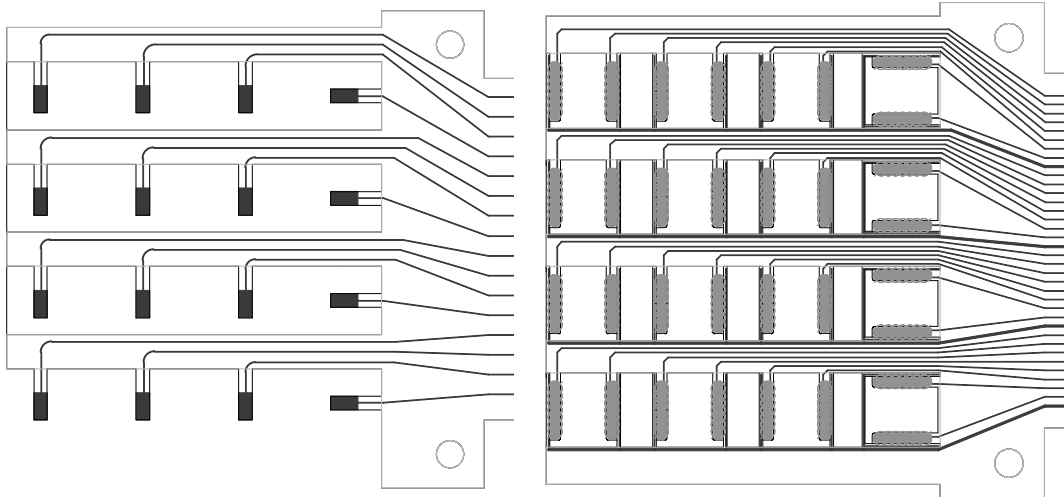


**Figure 3.18:** Kapton cables produced in Dortmund. Left side: the 'tongues' for the anode contacts and the flipped-back ground plane can be seen after re-contacting of the  $2 \times 2$ -detector array. Right side: both cathode side (top) and anode side (bottom) cables and their attachment to the opened transition-box for connection to the preamplifier are visible.

After several months of testing it was found that while the anode cables worked well without shielding, the high-voltage cables apparently 'generated' events of at least two distinguishable forms. Due to the sparseness of their occurrence, it proved difficult to reproduce them in a laboratory environment at the University of Sussex which is located at sea level. It was discovered that traces which were not attached to any crystal were able to induce crosstalk into neighbouring traces. After literature research, J. Wilson attributed this effect to so-called micro- or partial discharges [Hee00, Dan05, Ort02] that inject charge at interfaces of discontinuity between dielectrics in a strong electric field. Due to the lack of a ground layer attached to the high-voltage cable, the electric field is not well-defined and might become very strong at some places (e.g. if a HV-trace is located directly beneath a ground-trace of the anode cable) while being rather weak at others. To counter fake events generated by these microdischarges, the following measures were taken:

- grounding: to properly define the electric field, one HV-cable was equipped with a shielding (see Fig. 6.1) similar to the originally planned grounding layers (see Fig. 3.20) reaching from a high frequency-tight casing on the far side to the principal tongues on the detector side. Because the lamination was done in Dortmund, a simplified procedure was used omitting a coverlay on top of the top ground layer. Instead, the top ground layer was turned around so the copper was insulated by its own carrier foil. Thereby, the distance between top ground layer and trace was only about  $75 \mu\text{m}$  instead of  $125 \mu\text{m}$ , raising the capacitance from about  $132 \text{ pF/m}$  to about  $170 \text{ pF/m}$ . However, no noise side effects are expected from this measure as the HV cable's capacitance is of no importance compared to the signal cable's capacitance.
- crosstalk: by shielding the HV-cable, the generated pulses could not couple to the anode cable any more. Crosstalk was now only possible through the detector. Crosstalk between neighbouring traces of the HV-cable should also be strongly suppressed.
- veto: in order to compare the effectiveness of the shielding and to suppress all suspicious events, a veto was added:  $1000 \text{ pF}$  coupling capacitors were soldered to all HV-traces in the far side casing feeding the HF component of the high voltage into fast amplifiers. Two times eight channels were then mixed by an addition circuit to save ADC channels. After shaping, the two resulting veto signals were fed into an ADC.

Adding the ground layers to the HV-cable proved to be quite successful, as the event rates dropped to a level comparable to earlier measurements with shielded Kapton cables (the  $2 \times 2$ -detector array) (see Fig. 6.2). The 8-to-1-channel veto, however, only showed effect at signals larger than  $4 \text{ MeV}$ . It is assumed that this is due to the probably not sensitive enough implementation of the amplifier circuits and will be improved by a second version of the veto circuit which is currently under development. While using a Kapton cable for the signal side is still undisputed, the HV properties of thin coaxial cables are being investigated at the time of writing which may replace the Kapton HV cable if they prove to be less affected by partial discharges at high voltages.



**Figure 3.19:** Left: Electrode pattern on the high-voltage kapton-cable supplying the detector’s cathode side. Right: Electrode pattern for the anode side.

layer	Cu	Thickn.	film-side	layer composition	material designation	thickness in um
↓	↓	↓	↓	↓	↓	↓
				coverlay	LF0110	50
				mechanically treated		
<b>BS</b>	<b>Cu</b>	18	▼	shielding	<b>Flexmat.</b>	50
				bondply	LF0111	75
<b>2</b>	<b>Cu</b>	18	▼	signal layer	<b>Flexmat.</b>	50
<b>3</b>	blind layer		▲	bondply	LF0111	75
				bondply	LF0111	75
<b>LS</b>	<b>Cu</b>	18	▼	shielding	<b>Flexmat.</b>	50

**Figure 3.20:** Schematic of the layer composition of the anode cable. For the 64-detector array, only the signal layer and coverlay were implemented.



# Chapter 4

## Shielding

### 4.1 General Remarks

Background is a well known and often inescapable problem of all experimental physics. There are many techniques – depending on the measurement and the type of background – to either reduce it or enhance the distinguishability from the signal. While in particle physics, for example, information from different subdetectors is often complementary, in nuclear spectroscopy the energy deposition often is the only source of information.

Neutrinoless double beta decay searches are looking for extremely rare signal events: expected half-lives of  $10^{25}$  years lead to only few decays per year in some hundred kilograms of source mass. At the same time, environmental radioactivity – that is usually not noticed at all – yields around 9 orders of magnitude more events at the Q-value of the decay. Only very limited means exist to differentiate between signal and background event: pulse-shape analysis techniques have been successfully used with Ge detectors to discriminate single-site from multiple-site events that are often found in higher-energy  $\gamma$ -interactions [Maj99]. CdZnTe pixel detectors can also accomplish this and distinguish forms of radioactivity like  $\alpha$ -decays [Blo07b]. The combined efficiency of such efforts, however, usually reaches between 30 and 90 percent which is some eight orders of magnitude short.

For the above reasons it is obvious that protecting the measurement device – the detectors – from environmental radioactivity is vital for the feasibility of any low counting-rate experiment or rare event search. Therefore, all possible sources of decays that represent background have to be found and suppressed by appropriate measures. The following list names the most important 'enemies' of low-rate experiments and possible counter-measures:

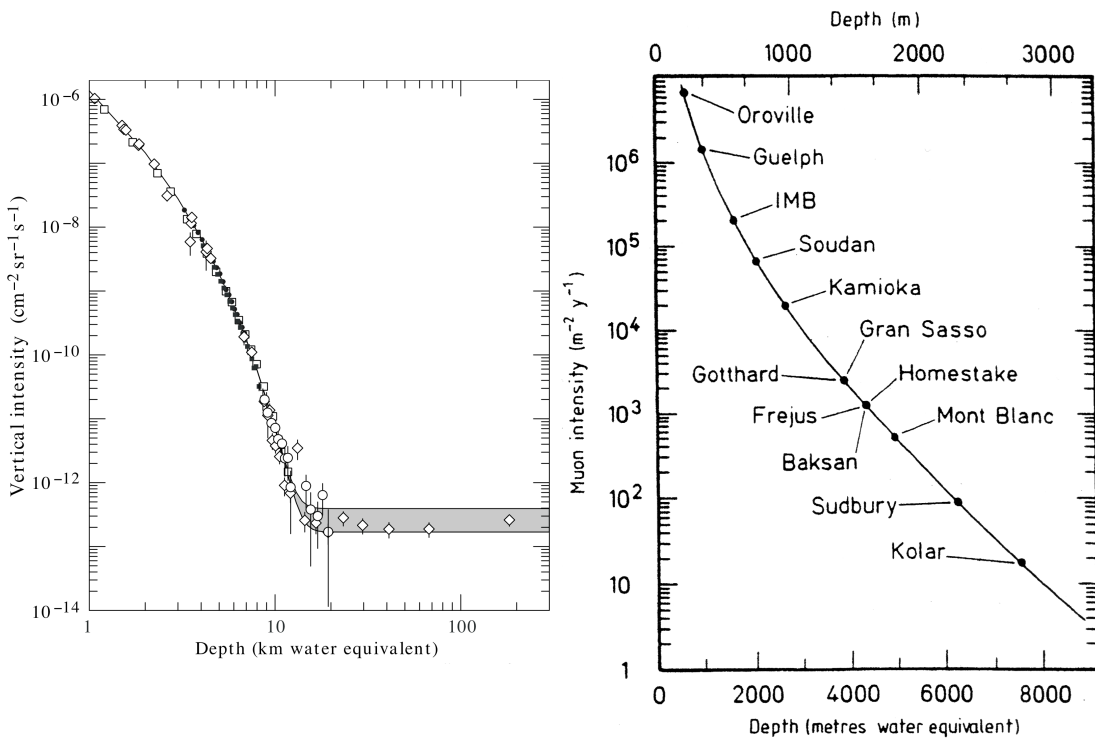
- cosmic radiation: veto counters, shielding (i.e. going underground)
- neutrons: neutron shield consisting of a moderator and an absorber
- (electronic) pick-up: 'blind' veto traces/circuits, Faraday cage
- radon contamination: flushing with ultra-pure nitrogen
- environmental ( $\gamma$ -)radioactivity from U and Th decay chains: lead shielding
- $\alpha$ - and  $\beta$ -decays: these are mainly within the bulk or on the surface of the detector crystals and their holder structure. Hence, cleaning/selecting clean construction materials, usage of a special copper inner shield to screen lead impurities (especially  $^{210}\text{Pb}$ ),

pulse shape analysis to identify  $\alpha$ s, multiple-site  $\gamma$ s and the position of the interaction for possible fiducial cuts.

## 4.2 The COBRA low-level setup

### 4.2.1 Cosmic Rays and Muons: Vetoing and going Underground

The sources of cosmic radiation are manifold and several of them still hypothetical. It is well-known, however, that a primary component consisting of mainly high-energetic protons and  $\alpha$ -particles hits the atmosphere with no preferred origin where it interacts mainly with nitrogen to form showers and muons which are the secondary cosmic radiation. While hadronic and also electromagnetic showers can be shielded rather easily by only some meters of water or soil cover<sup>1</sup>, the muon component is extremely penetrating and represents roughly 1 muon/(cm<sup>2</sup> · minute) at surface level [Eid04]. This rate decreases roughly exponentially with depth reaching a steady state of 10<sup>-11</sup> muons/(cm<sup>2</sup> · minute) or one muon per cm<sup>2</sup> every 20000 years at about 20 km depth. Here, muon generation in matter by cosmic neutrinos via charged current interactions becomes dominant.



**Figure 4.1:** Left: vertical muon intensity vs. depth. Note that the x-axis only begins at 1 km depth. The saturation by neutrino-induced muons at just below 10 km water equivalent is clearly visible. Taken from [Yao06]. Right: muon intensity vs. depth of some of the most important underground laboratories. Taken from [Zub04]

<sup>1</sup>The common unit for 'cover' is m.w.e. meaning Meters of Water Equivalent. Conversion is done simply by multiplying the material column's length with its density.

Nowadays, there are several underground laboratories in many countries, mostly established in (former) mines or inside mountain tunnels. Most of them host only few experiments and their infrastructure is rather poor. After measurements at surface level in Dortmund reached the limit of the available cosmic muon veto made from plastic scintillators [Mue01], it was decided to apply for space in an underground laboratory. Sites close to Dortmund were briefly evaluated<sup>2</sup> but were discarded. The next-best candidates were the Mont Blanc tunnel which would have been quite close to CERN, and the Laboratori Nazionali del Gran Sasso (LNGS) in the Abruzzo mountains between Rome and the Adriatic Sea being home to a large number of low-level experiments already. Mont Blanc turned out to be not too appealing due to a lack of infrastructure. A request for experimental space at LNGS to the scientific committee was successful, subsequently the full setup was moved to Italy in 2003.

The LNGS offers a shielding depth of about 3600 m.w.e. which reduces the muon flux to about  $0.96 \text{ muons}/(\text{m}^2 \cdot \text{hour})$  or one muon per  $\text{cm}^2$  every year which corresponds to only a few hits per year per detector. Due to the granularity of the array, this is currently sufficient for itself. In future upgrades, the plastic scintillator veto that was used in Dortmund (see [Mue01] for details) will be operated again resulting in a reduction of muon events by at least two orders of magnitude. Difficulties are rather generated by muon-induced neutrons. A neutron shield is used to reduce the fast neutron flux (see section 4.2.2).

#### 4.2.2 Shielding against Neutrons

Having shielded cosmic rays and muons by some thousand m.w.e. of rock in an underground laboratory, the next most penetrating background source the setup is left with are neutrons. In these depths, neutrons are mainly generated in the rock of the experimental halls by spontaneous fission of uranium and thorium as well as by  $(\alpha, n)$ -reactions. Moreover, the remaining cosmic muons can generate so-called tertiary neutrons both in rock and the lead  $\gamma$ -shield by negative muon capture, photonuclear reactions, deep inelastic scattering and photofission.

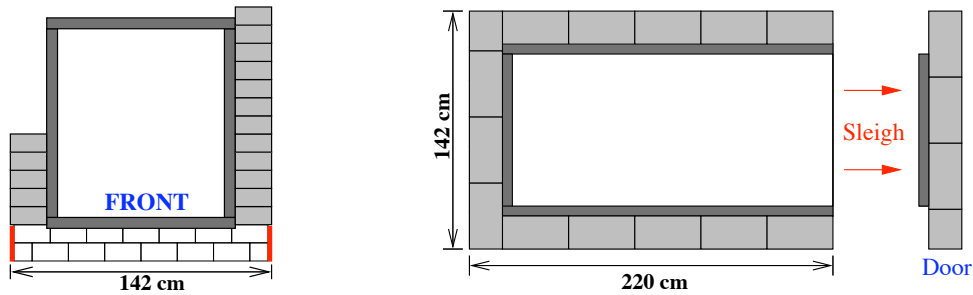
Neutrons are especially dangerous for a CdZnTe-based low-background experiment as  $^{113}\text{Cd}$  is always contained with a natural abundance of 12.2 %. This isotope has a huge capture cross section of above 20 kbarn for thermal neutrons which is the reason for the use of Cd-foils to stop thermal neutrons. Unfortunately, this is a  $(n, \gamma)$ -process releasing many photons up to several MeV. This means that almost every (thermal) neutron which enters one of the detectors has a very large probability to be absorbed and cause the emission of high-energetic  $\gamma$ s which then can fake  $\beta\beta$ -events by Compton scattering within the same or one of the neighbouring crystals.

Shielding neutrons is rather difficult as neutron capture cross sections are generally decreasing towards higher energies. Capturing, however, is the only way to absorb a neutron permanently. Hence it will generally be necessary to first slow neutrons down and then use materials with a high thermal neutron capture cross section such as boron ( $^{10}\text{B}$ ) or cadmium ( $^{113}\text{Cd}$ ).  $\gamma$ s which are produced during capture must be shielded by lead.

The large penetration ability of neutrons is due to their non-participation in the electromagnetic force. Lacking an electric charge, they only interact via their dipole moment or via the strong force. Hence, most of the volume of matter is completely transparent to them, only

---

<sup>2</sup>A coal mine in the Ruhr district would not allow high voltages due to the danger of explosions. The underground site UDO of the Physikalisch-Technische Bundesanstalt PTB in the Asse II salt mine was comparatively shallow and was already announced to be closed in the not too distant future.



**Figure 4.2:** Schematic drawings of the neutron shield [Oeh04]. The borated PE is depicted in dark grey while the paraffin bricks are light grey or white.

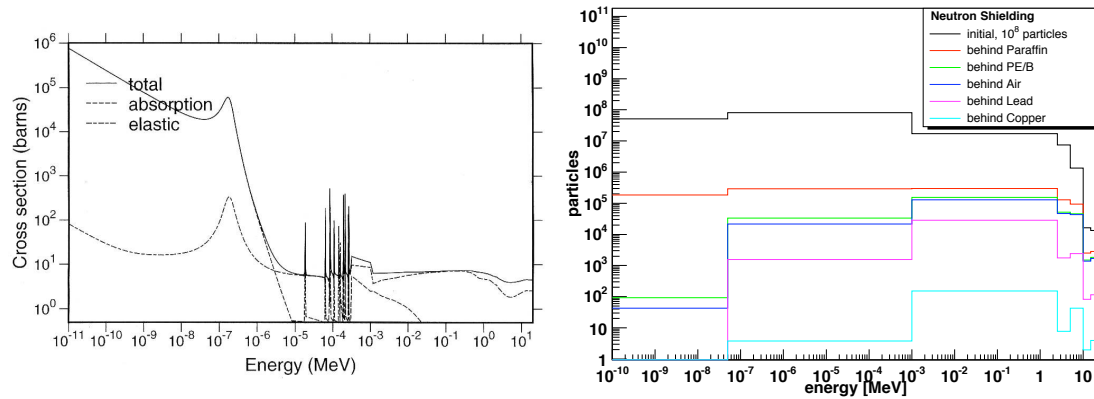
scattering on nuclei in their path whereby most interactions are elastic. For kinematic reasons, neutrons statistically lose most energy in elastic scattering with hydrogen nuclei as they have almost the same mass. To slow neutrons down it is therefore most efficient to use materials with high densities of hydrogen such as water, paraffin or plastics. After they have reached thermal equilibrium at around  $1/40$  eV, a cadmium foil or borates like borax ( $\text{Na}_2\text{B}_4\text{O}_7$ ) are used to capture the neutron. Because  $\gamma$ s from the  $^{113}\text{Cd}(n,\gamma)^{114}\text{Cd}$ -reaction in the shielding would be indistinguishable from those generated inside the detectors, the use of the  $^{10}\text{B}(n,\alpha)^7\text{Li}$ -reaction is favourable.

As described by Sandra Oehl in her diploma thesis [Oeh04], COBRA's neutron shield combines paraffin bricks for moderation of very fast neutrons with 7 cm thick borated polyethylene (PE) plates which surround the Faraday cage. Schematic drawings can be found in Fig. 4.2. According to simulations carried out by her with MCNP, the thermal neutron flux will be suppressed by more than seven orders of magnitude (see Fig. 4.3), even without the paraffin bricks more than five orders or magnitude remain. Additionally, it should be noted that the flux inside the LNGS laboratory (see table 4.1) is already about three orders of magnitude lower than at sea level. Nevertheless, for later stages of COBRA where even very small neutron fluxes might get important, it should be kept in mind that MCNP has not simulated the tertiary neutron production inside the lead shield. Fortunately, neutrons produced in this way by muons are normally quite energetic where the capture cross section on  $^{113}\text{Cd}$  is low (see Fig. 4.3).

Energy Bin [MeV]	Flux in LNGS Hall A [ $10^{-6}\text{cm}^{-2}\text{s}^{-1}$ ]
$< 5 \cdot 10^{-9}$	$1.08 \pm 0.02$
$< 1 \cdot 10^{-3}$	$1.84 \pm 0.20$
$< 2.5$	$0.54 \pm 0.01$
$< 5$	$0.27 \pm 0.14$
$< 10$	$0.05 \pm 0.01$
$< 15$	$(0.6 \pm 0.2) \cdot 10^{-3}$
$< 25$	$(0.5 \pm 3.0) \cdot 10^{-6}$

**Table 4.1:** Neutron flux in hall A of the LNGS underground laboratory [Bel89].





**Figure 4.3:** Left: cross section of  $^{113}\text{Cd}$ . The huge increase towards thermal energies ( $\sim 2.5 \cdot 10^{-8}$  MeV) is clearly visible. Right: MCNP simulation of the performance of the full neutron shield based on input spectra measured at LNGS [Bel89] (see table 4.1). A reduction of the thermal neutron flux of more than seven orders of magnitude is visible.

As already anticipated, the first installation of the neutron shield at COBRA's first underground location between LUNA and LUNA II sites did not show much effect. This is due to the fact that at the time of installation, COBRA's standard CPG detectors were still background limited by the red passivation resin applied to all CPG detectors by the manufacturer (see Tab. 3.2) and by Rn decays (see chapter 4.2.3). Therefore, it was decided to refrain from installing the paraffin bricks again after the move to COBRA's second location in the hallway between LNGS halls A and B. Here, a second borated PE plate was installed underneath as a precaution, but regarding all other sides, the current setup consists only of 7 cm of borated PE. It is expected that less paraffin dust will yield better background reduction than the extra order of magnitude neutron attenuation provided by the paraffin bricks.

### 4.2.3 Faraday Cage and Nitrogen Flushing

Semiconductor ionisation detectors yield only some thousand electrons per interaction. Therefore, the signal – the charge pulse – has to be amplified by quite extreme amounts. This of course means that also pick-up from ground loops or other antenna-like circuits will very much interfere with any normal operation. One possible way to prevent as much pick-up as possible is the construction of a Faraday cage around the detectors.

Another important source of background is from radon which diffuses mainly out of the rocks and concrete and into the vicinity of a detector after its generation as an intermediate primordial decay-chain daughter nucleus: In the  $^{238}\text{U}$  decay chain,  $^{222}\text{Rn}$  is generated which has a half-life of 3.8 days – enough time to diffuse into low-background experiments – before it decays under emission of a 5.49 MeV  $\alpha$ -particle. The half-life of  $^{219}\text{Rn}$  from the  $^{235}\text{U}$  decay chain amounts to only about 4 seconds which is too short to travel very far.  $^{220}\text{Rn}$  from the  $^{232}\text{Th}$  decay chain only sometimes plays a role due to its intermediate half-life of 55.6 seconds, therefore we will focus on  $^{222}\text{Rn}$ .

Due to its chemical nature as a noble gas, it is very hard to prevent it from entering sealed compartments. However, it is not capable of circumventing the diffusion laws. Therefore, low counting rate experiments are often flushed with purified nitrogen to prevent radon from getting close to the detectors. Normal air in buildings and laboratories contains about  $40\text{Bq}/\text{m}^3$

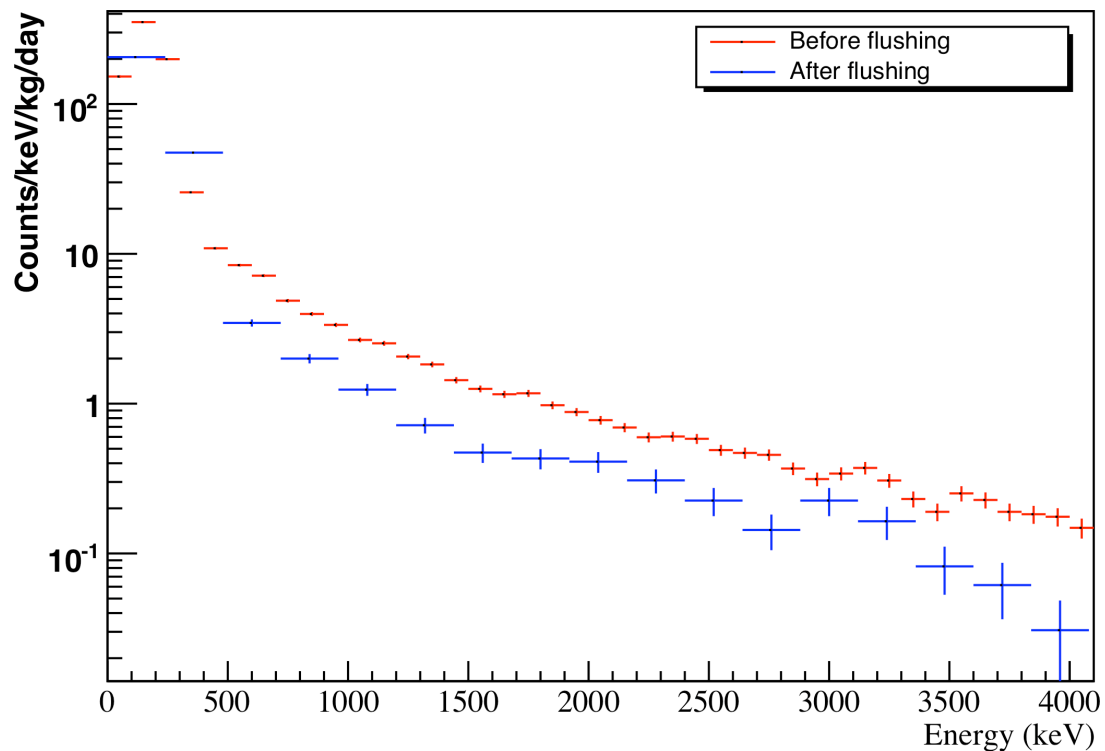
activity mainly from  $^{222}\text{Rn}$  [Heu95]. Its decay first feeds into nuclei with half-lives of some minutes; noticeable decays which might penetrate into a low-background detector are  $^{214}\text{Bi}$  with  $\gamma$ -emission of up to 2.20 MeV and  $\beta$ -emission of up to 3.28 MeV as well as  $^{214}\text{Po}$  which emits 7.69 MeV  $\alpha$ -particles. From this it is conceivable that Rn is a dangerous substance which can carry high-energetic  $\alpha$ ,  $\beta$  and  $\gamma$ -radioactivity into a well-shielded experimental setup by diffusion.

Even if a strong diffusion barrier has been built, one is still confronted with the legacy of  $^{222}\text{Rn}$ ,  $^{210}\text{Pb}$  with a half-life of 22.3 years. Lead is chemically very adhesive and will stick to almost any surface after being produced in air, even more so as it will generally be created with positive ionisation. Therefore, statically charged surfaces like plastic or glass are exceedingly affected. The progenies,  $^{210}\text{Bi}$  and  $^{210}\text{Po}$  emit a 1.16 MeV  $\beta$  and a 5.30 MeV  $\alpha$ , respectively. This illustrates that the dangers of surface contamination – the so-called plate-out effect – by Rn daughter nuclei persist even if after the Rn-diffusion has been cut off. Surface cleaning procedures to remove as much of these as possible include, depending on the material, degreasing with acetone or methanol followed by ethanol or 2-propanol followed by leaching with concentrated hot nitric acid.

Both aims – a Rn diffusion barrier and electromagnetic shielding – can be reached with a Faraday cage made of thin (0.5 or 1 mm) copper sheets located inside the neutron shield and hosting the lead castle. While at COBRA's first underground location a soldered 0.5 mm strong cage was used where the door was connected to the cage via pressure contact over a conductive seal, for its second location between halls A and B 1 mm thick copper sheets were screwed to a brass frame (see Fig. 4.4). Due to the large number of signal wires, no feedthroughs but a cable channels was used. While resistance measurements of the new Faraday cage yielded satisfying results, it is possible at the time of writing to induce disturbances with a wireless transmitting set showing that the shielding effect is not ideal yet. This behaviour is subject to ongoing optimisation efforts.



**Figure 4.4:** Photograph of COBRA's second Faraday cage. The screws used to fix the 1 mm thick copper onto the brass frame are visible. The small hole in the lower right corner of the side door is the cable channel.



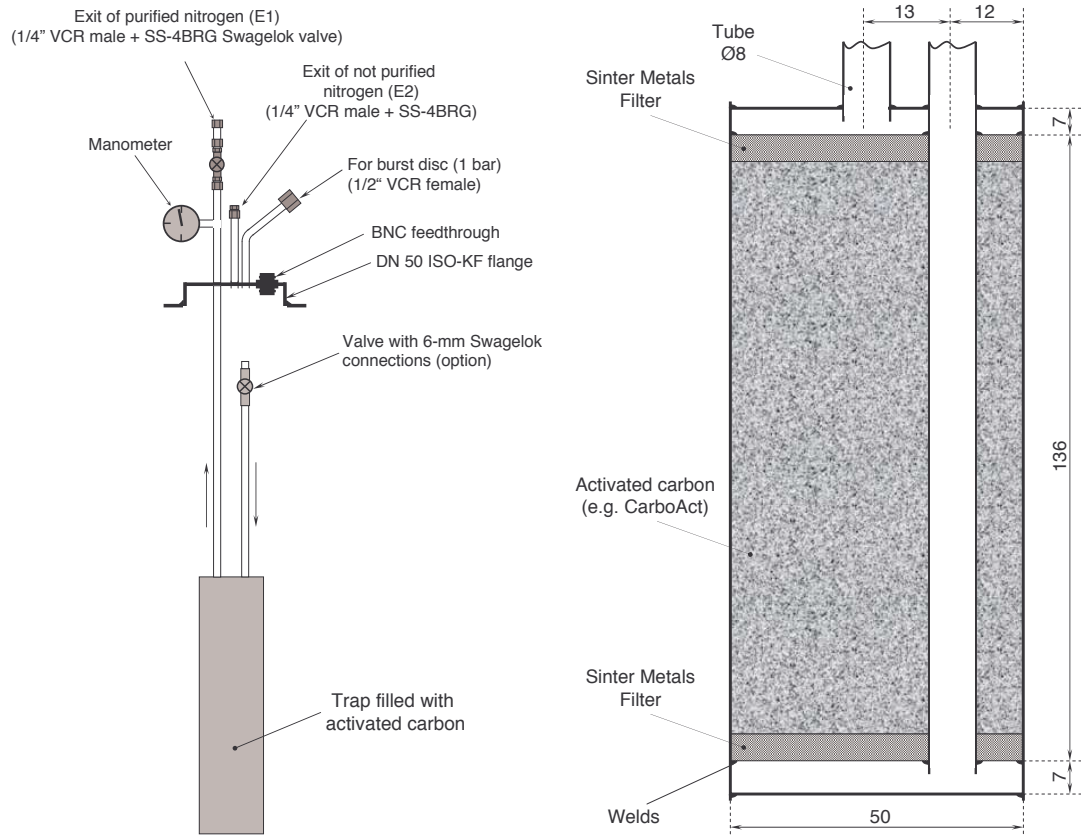
**Figure 4.5:** Comparison of the spectra taken with the 16-detector array before (red) and after (blue, preliminary) the installation of the LN<sub>2</sub>-flushing in August 2007. A significant reduction up to 4 MeV is visible; the remaining background might be explained by the activity of the red passivation paint (see Tab. 3.2). It should be noted that the data analysis contained in this work in chapter 7 was conducted on data without flushing. The shoulder below 320 keV is attributed to the decay of <sup>113</sup>Cd.

The most pure and dry nitrogen can be generated from liquid nitrogen (LN<sub>2</sub>). To accomplish the purification, a power resistor boils off liquid nitrogen from a 200-litre Dewar at a rate of several litres per minute which is then fed into an activated carbon filter kept inside the LN<sub>2</sub> at  $-196^{\circ}\text{C}$ . The design of the filter largely followed [Wój05]; a schematic drawing is displayed in Fig. 4.6. The activated carbon used was Silicarbon K48, the sinter filters are laser-cut 3 mm thick V2A steel SIKA R200 filters by GKN sinter metal filters GmbH.

Fig. 4.5 shows a first preliminary comparison of the dataset which has been used for the analysis contained in chapter 7 with data taken after the installation of LN<sub>2</sub>-flushing and Rn-trap in August 2007. A significant reduction of the count rates between the endpoint of the <sup>113</sup>Cd spectrum at around 320 keV and 4 MeV of a factor 3–5 is visible. Much of the remaining background might be explained by decays in the red passivation paint which is coating the detectors (see chapter 3.2.3).

#### 4.2.4 Environmental Radioactivity: Lead Shielding

Soil always contains certain amounts of natural radioactivity consisting mostly of long-lived but instable isotopes, e.g. from the <sup>232</sup>Th, <sup>238</sup>U and <sup>235</sup>U decay chains or from solitary instable



**Figure 4.6:** Schematic drawings of the Rn-trap [Zuz07].

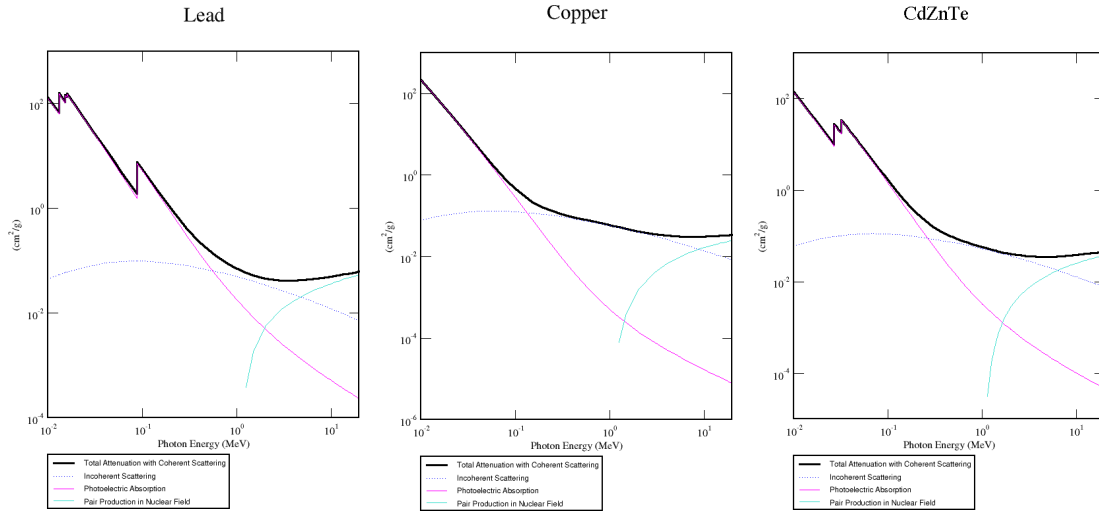
nuclei like  $^{40}\text{K}$ . These decays are both  $\alpha$  and  $\beta$ -decays, but often associated with subsequent nuclear deexcitation by emission of  $\gamma$ -quanta. While  $\alpha$  and  $\beta$ -particles have a very limited range in any given shielding material or even air,  $\gamma$ s interact only very sparsely. Furthermore, the interaction probability has a minimum in the few MeV region where the Compton effect is dominant. For details of the interaction of radiation with matter see e.g. [Kno00] or [Leo92].

To shield radiation coming from the surroundings of the experiment, it is most efficient to use dense high- $Z$  materials<sup>3</sup>. While density enters linearly into the attenuation coefficient  $\mu$  for both photoelectric (PE) and Compton (C) effects, the first strongly scales with the atomic number. At very high energies (above some MeV), pair production (PP) becomes dominant which scales with  $Z^2$ :

$$I(t) = I_0 e^{-\mu_{total} t}, \text{ with } \mu_{total} \sim \mu_{PE} + \mu_C + \mu_{PP} \sim \rho \times \left( \frac{Z^{4.5}}{E_\gamma^3} + \text{const.} + Z^2 \right) \quad (4.2.1)$$

Instead of the linear attenuation coefficient  $\mu$ , often the mass attenuation coefficient  $\mu/\rho$  is given. To reach large attenuation with as little shield thickness  $t$  as possible, it is therefore advantageous to use materials which offer a good compromise between density, atomic number  $Z$  and cost. Lead, a comparably affordable metal with the largest (stable) atomic number and relatively high density ( $11.35 \text{ g/cm}^3$ ), seems to be the best choice in most cases.

<sup>3</sup>Nuclear scientists' slang for materials with large atomic numbers, i.e. high nuclear charge.



**Figure 4.7:** From left to right: mass attenuation coefficients of lead, copper and Cd<sub>0.9</sub>Zn<sub>0.1</sub>Te. They have to be multiplied by the materials' densities (11.35, 8.96 and 5.8 g/cm<sup>3</sup>, respectively) to obtain the linear attenuation coefficient  $\mu$ . Note the different scales on the y-axis! Compiled on [Ber07].

Drawbacks of lead are radioactive contaminations that are often found, especially <sup>210</sup>Pb and its progenies <sup>210</sup>Bi and <sup>210</sup>Po which emit a 1.16 MeV  $\beta$  and a 5.30 MeV  $\alpha$ , respectively. If the  $\beta$ -particle can reach the detector volume, this might significantly contribute to the background. In these cases, it can be necessary to either use mercury which is easily purified by distillation or to have an inner shield made from ultra-pure/ancient lead or a very pure metal such as copper. To achieve compact shields with high attenuation power, the usage of tungsten might be appropriate due to its extremely high density (19.3 g/cm<sup>3</sup>). As a guide and reference, the mass attenuation coefficients of lead, copper and CdZnTe are displayed in Fig. 4.7.

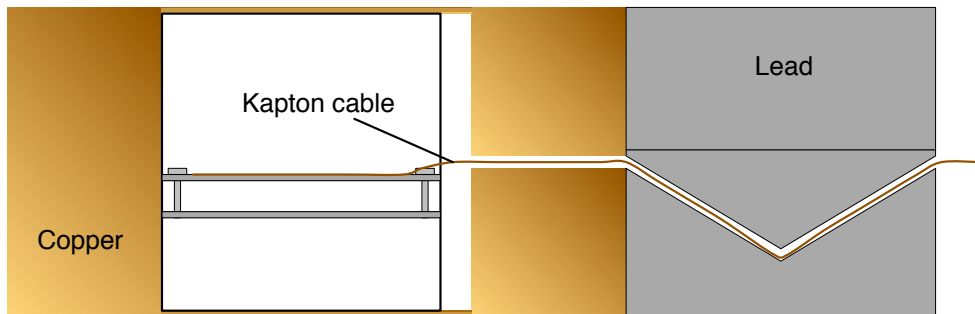
As was already pointed out, the most probable energy window in which  $\gamma$ s are likely to penetrate the shielding is in the few MeV region where the Compton effect is dominant which can fake real events: The effect yields a continuum spectrum hence every photon can deposit any given energy below the Compton-threshold which is given by [Leo92] as

$$T_{\max} = E_{\gamma} \frac{2\gamma}{1 + 2\gamma}, \quad \text{with } \gamma = \frac{E_{\gamma}}{m_e c^2}. \quad (4.2.2)$$

Applied to the case of the 2614 keV  $\gamma$  of <sup>208</sup>Tl, the equation yields 2381 keV. This means that the signal regions of both, the <sup>116</sup>Cd and the <sup>130</sup>Te decays (2805 and 2529 keV, respectively), are not 'polluted' by Compton scattered events from this background decay which produces the most energetic naturally occurring  $\gamma$ -line. However, Compton-scattered  $\gamma$ s from this decay can easily fake real neutrinoless double beta decays of e.g. <sup>70</sup>Zn at 1001 keV. Hence, appropriately thick shielding is required.

As pointed out by Theodorsson [The96], the photon flux in the detector only decreases up to a certain shielding thickness as the shielding material (usually lead) is normally radioactively contaminated and becomes a source itself. Furthermore, internal sources as surface or bulk contaminations of detectors and surrounding materials become dominant after the external sources have been attenuated by several orders of magnitude. In the literature, it is generally

assumed that 10–15 cm of lead are sufficient for low-level setups. Following this advice, it was decided for COBRA to use a  $10 \times 10 \times 10$  cm large copper holder structure (NEST) for the delrin holders inside a  $20 \times 20 \times 20$  cm large copper shielding core. Around this core, there is at least 15 cm of lead in all directions with the exception of the feedthrough-brick: Here, only 10 cm were used to keep the signal cables as short as possible (see chapter 3.5). Normally, all metals are applied in  $(20 \times 10 \times 5)$  cm<sup>3</sup> large bricks. Special care was used to prevent gaps between the bricks through which gammas could penetrate the shielding. For the feedthrough-brick, a V-shaped arrangement of two bricks was designed to also have a shielding thickness of about 9 cm of lead along the cable path (see Fig. 4.8). Drawings of the suggested arrangement can be found in appendix B, photographs are shown in Fig. 4.9.



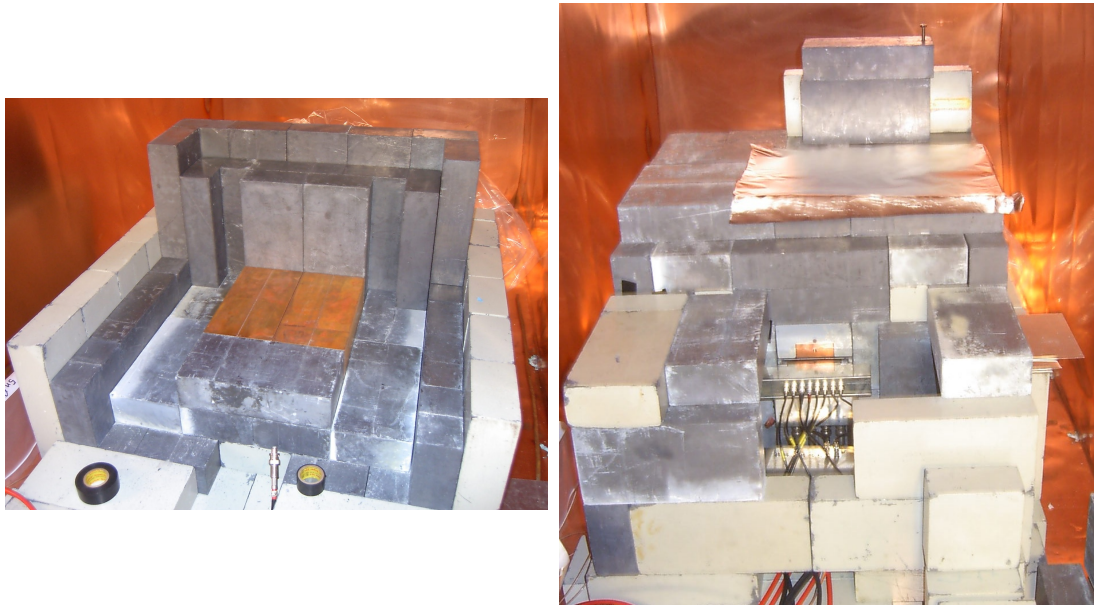
**Figure 4.8:** Schematic drawing of the shielding along the cable path. From the outside, the cable is first conducted through a V-shaped cable guide within the first lead brick. This is done to ensure that at least about 9 cm of lead have to be penetrated even by external photons that travel right along the direction of the cable guide. Between lead and NEST (see chapter 4.2.5 for details), the cable travels through a straight 5 cm long section inside of copper. Finally, it has been avoided to mount detectors in the line-of-sight of the cable guide so any photons that passed through here will have to scatter at least once before they can hit a detector.

#### 4.2.5 The Copper Core and NEST

As stated above, lead usually contains certain amounts of radioactivity, according to Heusser [Heu95] mostly  $^{210}\text{Pb}$  and its daughter nuclides  $^{210}\text{Bi}$  and  $^{210}\text{Po}$  which are more dangerous than the progenitor: While  $^{210}\text{Pb}$  only decays by emission of very soft (less than 63 keV)  $\beta$ -particles and a 46.5 keV  $\gamma$ ,  $^{210}\text{Bi}$  is  $\beta$ -decaying with an endpoint energy of 1.16 MeV and  $^{210}\text{Po}$  emits  $\alpha$ -particles of up to 5.3 MeV. It should be noted that  $^{210}\text{Pb}$  has a half-life of about 22 years and is part of the  $^{238}\text{U}$ -decay chain which also includes  $^{222}\text{Rn}$ , the long-lived Rn isotope. Therefore, a surface contamination with  $^{210}\text{Pb}$  is to be expected wherever radon-emanation is occurring as lead is chemically very adhesive.

To avoid this background, an inner lining/shielding of either ultra-pure/ancient<sup>4</sup> lead or some other radio-pure metal has to be used which absorbs all of the charged particles and x-

<sup>4</sup>Having a half-life of only about 22 years,  $^{210}\text{Pb}$  is virtually not contained any more in lead which has been smelted some centuries ago.

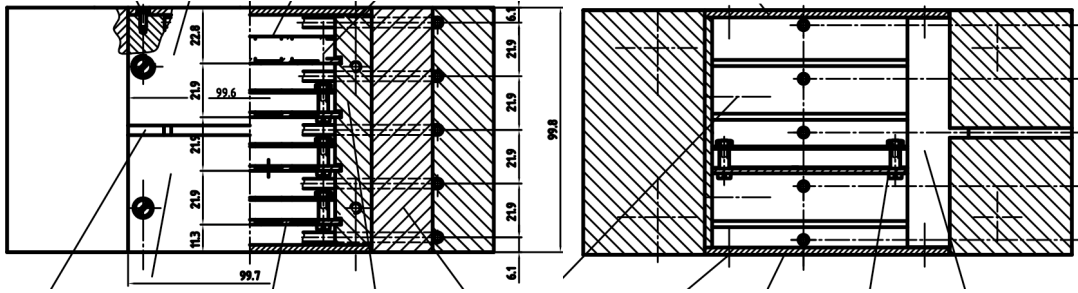


**Figure 4.9:** Left: Lead castle during set-up. The two base bricks of the copper core are clearly visible. Right: Full-sized lead castle during the late  $2 \times 2$  detector phase. Both pictures show the surrounding Faraday cage.

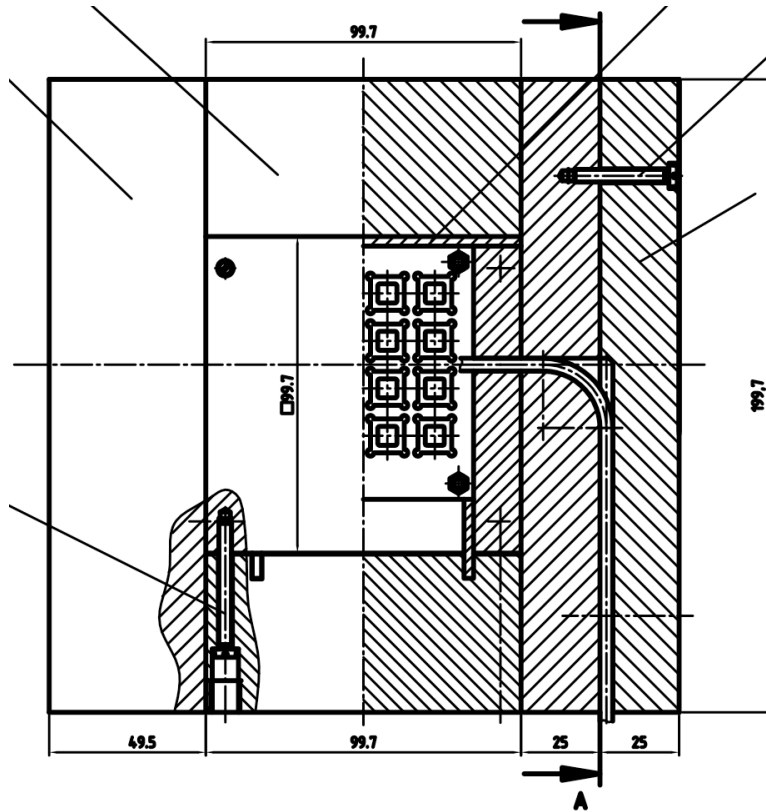
rays and most of the bremsstrahlung. Due to the poor mechanical properties of lead<sup>5</sup>, copper was evaluated as an alternative. Having a comparable density, its much lower atomic number (29 compared to 82) led to the construction of a real inner shield with 5 cm thickness instead of only a lining. Key advantages of copper are the superior mechanical properties (milling into all kinds of shapes is possible) combined with the unsurpassed radio-purity guaranteed by the production process.

Staying within the lattice of  $20 \times 10 \times 5$  cm bricks, a detector housing (NEST) of  $10 \times 10 \times 10$  cm is able to accommodate  $4 \times 4 \times 4$  detectors of one  $\text{cm}^3$  size each and can easily be surrounded by 5 cm of copper in every direction resulting in a  $20 \times 20 \times 20$  cm copper core. The NEST itself is essentially made from copper sheets and held together by nylon screws. Four Delrin holder structures (see chapter 3.3) can be inserted like drawers. Five Teflon tubes run above, below and in between the holders to be able to insert radioactive calibration sources for calibration purposes. The tubes can be accessed from outside of the neutron shield so calibrations can be made without opening the Faraday cage. The holders are kept in a reproducible position by two copper sheet spacers. The high-voltage and signal cables are collected and then fed through a central cable channel. Because this channel forms a breach of the shielding, the two middle holders are arranged in a way in which they cannot be directly illuminated by  $\gamma$ s entering through the channel. Outside of the copper core, a V-shaped lead brick of 10 cm thickness makes sure that there is no direct line-of-sight without at least several cm of shielding metal between the outside world and the detectors (see Fig. 4.8).

<sup>5</sup>Lead is too soft to be a good construction material. Threads fail after few uses, besides vapours generated during machining are toxic.



**Figure 4.10:** Side views of the NEST. In the left drawing, one can see the two copper bricks forming the cable channel on the left half while a view without them is presented on the right half. The arrangement of the four Delrin holders and the calibration Teflon tubes is visible. In the right drawing, a longitudinal cut is displayed showing the necessary room to the right of the Delrin holders where the Kapton cables are collected to feed into the cable channel. The complete drawings with labels can be found in appendix C.



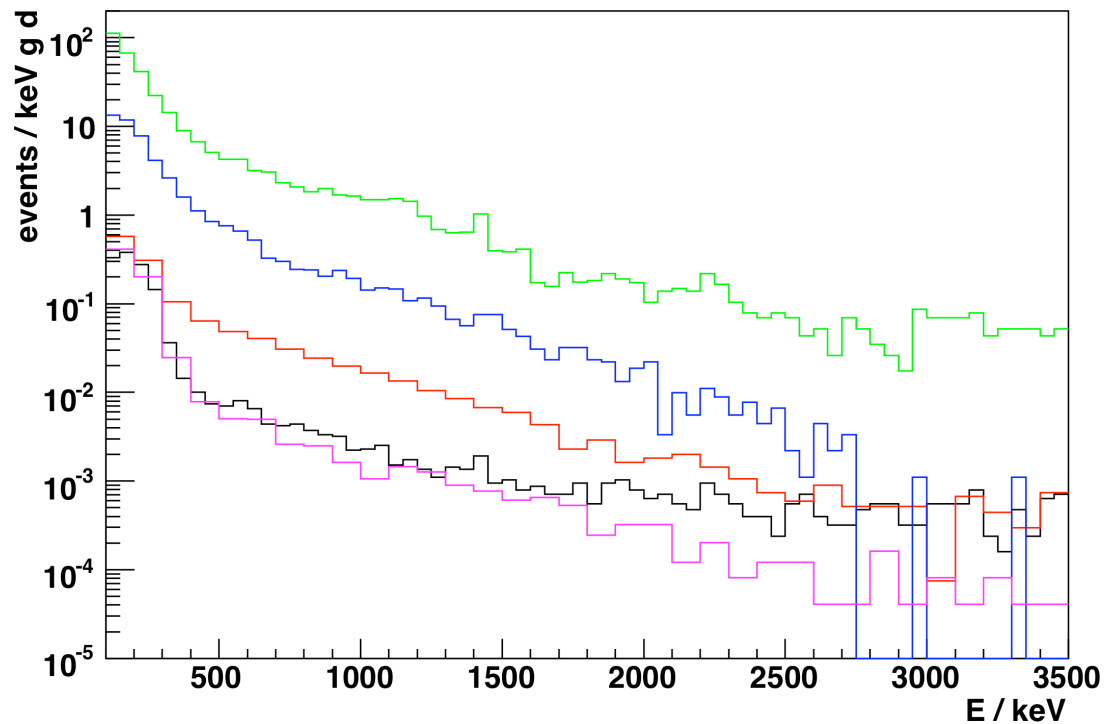
**Figure 4.11:** Top view of the NEST. The channel for the calibration sources is seen in the vertical section on the right side as well as the spacer sheets needed to keep the Delrin holders at the far side of the NEST's volume. The complete drawing with labels can be found in appendix C.



### 4.2.6 Performance of the Setup

The performance of the setup is illustrated in Fig. 4.12. The first two spectra represent standard CdZnTe spectroscopy without any shielding, the green one on the earth's surface in Dortmund and the blue one underground in the LNGS laboratory. The reduced gamma flux and also the absence of cosmic rays above roughly 2.6 MeV is clearly visible. The best performance ever achieved with a commercial detector on the surface utilising an active cosmic muon veto is depicted in red. The first spectrum of the 4-detector array with delrin holder structure is shown in black while the performance of detectors with colourless passivation resin is drawn in purple.

In the course of this work, the event rate at one of the interesting decay energies at 2.8 MeV was reduced by almost 4 orders of magnitude compared to unshielded commercial detectors. From contamination measurements at LNGS it is known (see table 3.3) that most of the present background can be expected to be surface contaminations by the red passivation paint and by Rn. It is planned to exchange the glue-based contacting for pressure-based contacting in October 2007 which would enable the removal of all passivation resin provided the detectors are always operated in a dry nitrogen atmosphere which would also remove the Rn from the detectors' surroundings .



**Figure 4.12:** Illustration of the different performance levels achieved in the course of this work. The spectra from top to bottom are from a detector without shielding on the earth's surface (green), the same underground in LNGS (blue), the best ever achieved spectrum with active veto on the surface (red), an underground measurement with delrin holder structure (black) and a measurement with clear-coated detectors (magenta). The shoulder below 300 keV can be attributed to the  $\beta^-$ -decay of  $^{113}\text{Cd}$  which has a half-life of  $8 \cdot 10^{15}$  years.

### 4.3 Outlook

Up to now, most decisions about the appropriate shielding had to be made based on general estimations on the radio-purity of several materials. In the near future, the advent of a dedicated COBRA HPGe-detector for construction-material measurements will make it possible to gain more reliable data on their radio-purity. Up to now, only few samples could be measured at LNGS due to only limited access to the infrastructure of low-level spectroscopy. These data can then be fed into COBRA's evolved Monte-Carlo simulation package VENOM to optimise the shielding design.

The shielding described above still is a rather standard low-level shielding and does not rely very much on background suppression methods. After installation of all 64 detectors of the  $4 \times 4 \times 4$ -detector array, it will be possible to use coincidences to suppress some forms of background. A first coincidence-based analysis of data collected with the first 16-detector layer of the 64-detector array is presented in chapter 7. A paper by COBRA's Birmingham group investigated coincidence-based background suppression techniques with pixel detectors [Blo07b]. COBRA's Warwick group has investigated different shielding approaches for a very large array of CdZnTe detectors [Ste07]. They all include an active liquid scintillator based veto around the detectors.

# Chapter 5

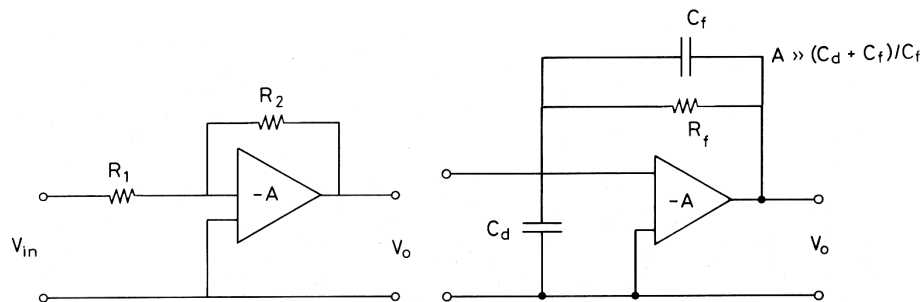
## Electronics

An excellent introduction to electronics for semiconductor detectors can be found in the text-book by Spieler [Spi06].

### 5.1 Pre-Amplifiers

#### 5.1.1 Charge Sensitive Amplifiers

The physics signature that a charged particle leaves in a semiconductor is the production of electron-hole-pairs in the detector volume. These are then separated by an applied bias voltage and start to drift to the cathode (holes) or anodes (electrons). As illustrated in many textbooks, e.g. [Leo92], it is advantageous to use a special form of amplifier for the task of converting the charge into a voltage: the charge-sensitive preamplifier. One of its key features is that the pulse height of a signal only depends on the charge, not on the capacitance of the system. Charge-sensitive preamplifiers are widely used with semiconductor and other charge-sensitive detectors.



**Figure 5.1:** Schematic representations of a voltage-sensitive preamplifier (left) and a charge-sensitive preamplifier (right). Modified after [Leo92, p. 278].

As sketched in Fig. 5.1, preamplifiers basically consist of a operational amplifier (OP-amp)  $A$  which is wired according to the task: charge-sensitive preamplifiers are implemented as integrator circuits (the feedback branch charges a capacitor) plus a high value feedback resistor to discharge the capacitor. For comparison, the standard inverting feedback circuit

normally used as voltage-sensitive amplifier is shown on the left. For an introduction into amplifier electronics, see e.g. [Tie02]. The feedback resistor's value  $R$  and the capacitance  $C_f$  are chosen to yield a signal fall-time  $\tau = RC_f$  value of several hundred  $\mu\text{s}$ . This is much longer than the charge collection time which is on the order of ns (Silicon) to some 100 ns (CdZnTe). Thereby, no relevant portion of the signal height is lost through the feedback resistor due to already discharging while still collecting charge. Resistive-feedback amplifiers have some shortcomings at very high count rates, however, this is not relevant for their use in low-level spectroscopy due to the extremely low count rates and will therefore not be discussed further.

Because of the loss of charge carriers within current CdZnTe detectors, it is desirable to only measure electrons as they have by far the greater mobility and mean free path before trapping. Besides, one has to correct for the trapping that the electrons suffer on their way to the anode. Both is accomplished with the so-called 'co-planar grid' approach by Luke [Luk94]. As discussed in chapter 3.2.2, so-called 'co-planar grid' (CPG) detectors were chosen for the COBRA experiment because of their good energy resolution combined with a comparatively large source mass per readout channel. While standard preamplifiers as sketched in Fig. 5.1 are suitable for planar detectors, CPG detectors require two such charge-sensitive preamplifier channels – one for the collecting anode (CA) and one for the non-collecting anode (NCA) – followed by a subtraction circuit which is normally implemented as series of inverter and summing amplifier. To compensate for the electron trapping according to the 'relative gain compensation technique' [Luk95], the output of the NCA-channel is attenuated via an amplifier circuit adjustable by a potentiometer. The choice of the right attenuation is important to get optimum results with symmetric photopeaks.

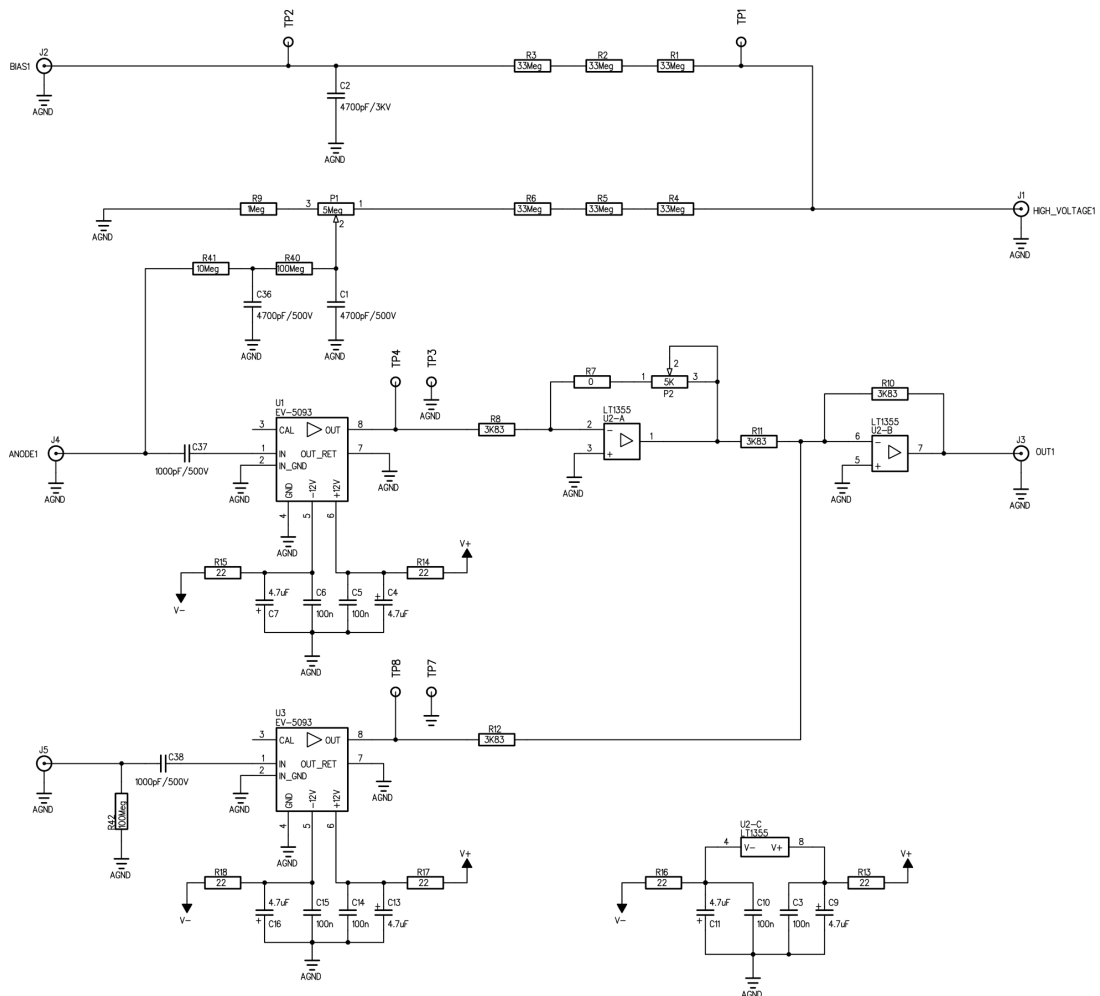
### 5.1.2 General Design Remarks

At the beginning of the electronics design, there were no reports in the literature about a specific CdZnTe-CPG electronics design for low-level applications. Therefore, it was intended to keep all parts as exchangeable and radio-pure as possible to allow for easier modifications of single components, signal outputs and the position of the first amplification stage.

The general plan was to keep the first amplification stage outside the inner shielding of roughly 10 cm of copper and 10 cm of lead. The connection from the preamplifier to the detectors first consisted of RG-174 cables and later of flat-cables made from Kapton which is a polyimide foil. Technically, these cables are flexible PCBs. The trace length is about 35 cm in the final design. The disadvantage of this decision is that the energy resolution at lower energies will drop. While in our characterisation setup resolutions as good as 18.9 keV at 662 keV have been measured, the best achieved resolution after contacting was 32 keV.

Because building low-noise charge-sensitive preamplifiers still is a tricky task, prices for these components can be quite high. Keeping in mind that lower-grade detectors start at around 500 Euros, the cost for the standard solution for CdZnTe-CPG-detectors seemed to be too high to equip a larger array: eV Products sell their eV-5093's at around 200 Euros per hybrid while two hybrids are needed to instrument one channel. Therefore, the preamplifier circuits have been designed to accept several charge-sensitive preamplifier hybrids, in particular eV-5093, Cremat CR-110 and "UK-Hybrids" which have been developed within the CHARISSA collaboration [Fre05]. In a later stage of the experiment, first tests were done using self-built hybrids (see section 5.1.6).

### 5.1.3 1st Generation: The 'Pertinax' Preamplifier



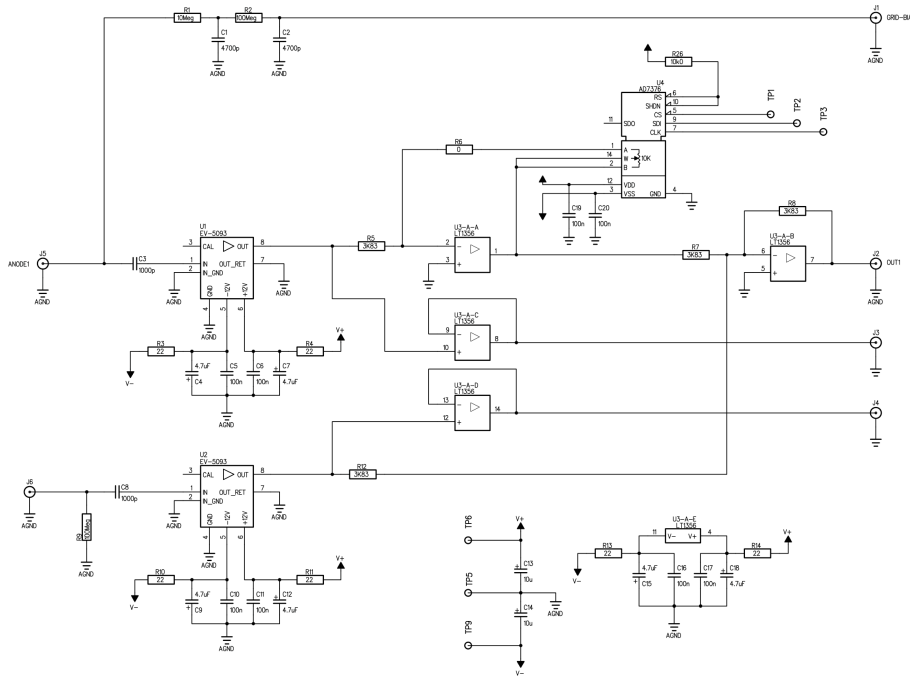
**Figure 5.2:** Schematic of one channel of the first preamplifier implemented on a FR-2 PCB. Taken from eV Product's draft, a voltage divider was included to save on an additional grid-bias voltage source. The grid-bias therefore depends on the bias voltage and on the setting of the potentiometer of the voltage divider. The AC coupling and the  $100\text{M}\Omega$  load resistor were introduced in Dortmund.

The first preamplifier was built to mimic the model commercially sold by eV Products, the manufacturer of the CPG-detectors used by COBRA. Trying to keep the rather radioactive electronics away from the detectors, eV's commercial detector mounts and electronics could not be used. Besides, our attempt to operate CPG detectors in arrays was not possible with their layouts.

The electronics development department of the faculty of physics used a schematic provided by eV Products to produce a two-channel preamplifier incorporating a low-pass filter for the bias and grid-bias, and a voltage divider to generate the grid-bias from the bias voltage. For rapid prototyping and to keep the electronics as radio-pure as possible, this was done using

single-sided FR-2 (or "Pertinax") PCBs. Two of these PCBs were used during the first stages of COBRA to operate the four crystals. The main disadvantage was that both the grid-bias and the potentiometer setting had to be operated manually, thus making it impossible to change the settings without an operator on site. Besides, having no scale at the potentiometers meant that sweeping the parameter space was not reproducible and an enormous amount of work.

### 5.1.4 2nd Generation: The Four-Channel Preampifier



**Figure 5.3:** Schematic of one channel of the four-channel preamplifier. It basically consists of two socketed charge-sensitive preamplifiers, an inverter whose amplification is not unity but adjustable, and an analogue addition stage. Apart from that, you can see a filter for the grid-bias and two impedance converters to be able to look at the outputs (J3 and J4) of the preamp chips individually without interfering with the subtraction circuit. This can be used for debugging and to explore the pulse shape using oscilloscopes or Flash-ADCs. A common grid-bias was bridged to the inputs of the low-pass filters. The digital potentiometers were daisy-chained.

To overcome the limitations of the first preamplifier, the following changes were made in the 2nd generation:

- Introduction of electronically adjustable potentiometers
- Individual outputs for the non-subtracted CA and NCA signals
- Bias voltage was kept separate to protect the electronics from discharges
- All four channels on one PCB with common GND

- Common grid-bias

As a replacement for the 20-turn potentiometers, the Analog Devices AD7376 digital potentiometer was used. Devices of this type can be daisy-chained requiring only 3 logic lines per preamplifier regardless of the number of channels. They require TTL-logic compatible input levels and use a SPI-compatible<sup>1</sup> protocol. As this version of the preamplifier was first used together with the CAMAC setup, only a fast-NIM-logic output register was available. Therefore, a four-channel fast-NIM-to-TTL converter was included which was bridged later when the VME setup was used together with a TTL I/O register.

To be able to explore the individual CA and NCA signals, impedance converters were introduced and their outputs made available on BNC-connectors<sup>2</sup> for easy access. Primarily for safety reasons, the bias voltage was kept outside the preamplifier casing while the grid-bias was distributed with insulated bridges. To prevent grounding problems, the PCB was soldered to its casing.

### 5.1.5 3rd Generation: The 16-Channel Preamplifier

To step from four detectors to the 64 detector array, a preamplifier-design had to be found that could host enough channels within the available space. Therefore, a decision was made to operate each 16-detector layer with one large preamplifier. Due to space reasons, the CA and NCA outputs were no longer routed to connectors on the casing any more and improvements were made to the grid-bias distribution: now all channels could receive individual voltages. In addition, test-pulsar inputs were introduced with all sockets having two inputs. At the same time, so-called 'UK-Hybrids' replaced eV-5093 charge-sensitive preamplifier hybrids as default hybrid primarily due to reduced cost. This meant basically the change of the preamplifier's socket. The 64 detector array will need four of these casings forming a tower of roughly 23 cm in height using a footprint of 29 by 21 cm. While this is suitable for the 64 detector array, the approach will have to be modified to be scalable beyond roughly 1000 detectors.

### 5.1.6 Outlook

During 2006, first experiments have been made with self-made charge-sensitive hybrids designed by O. Schulz. The idea was to use OP-Amp<sup>3</sup> ICs<sup>4</sup> with FET<sup>5</sup> input stages which are nowadays rather cheap but offer great specifications compared to the time of the invention of the charge-sensitive preamplifier. Tests with different OP-Amps have been quite successful though keeping the noise at an acceptable level still poses a problem at the time of writing. The performance level of the UK hybrids has been surpassed. Cremat's CR-110 hybrids are a close match while eV's eV-5093 hybrids are still superior, especially at low energies/amplitudes.

Once these remaining obstacles have been overcome, it will be possible to further miniaturize the preamplifier electronics, finally leading to a completely self-designed SMD circuit. This

---

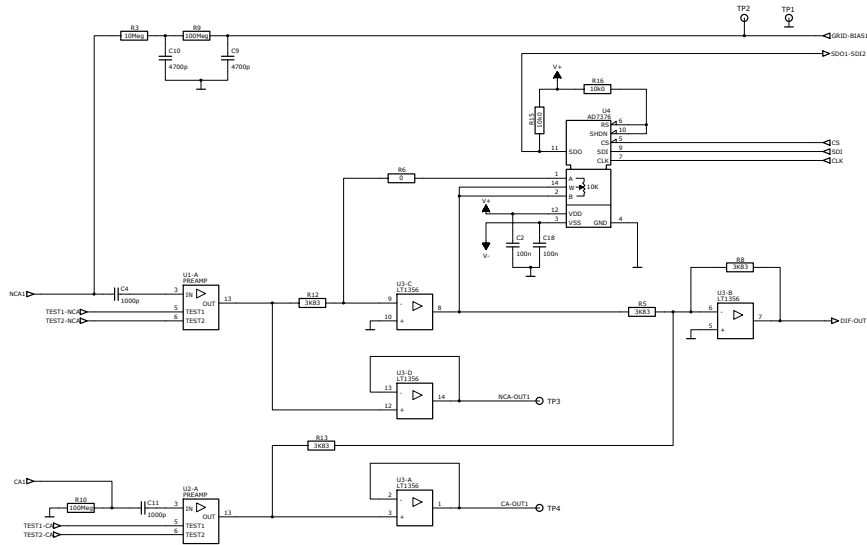
<sup>1</sup>Serial Peripheral Interface bus, a synchronous serial data link between a computer/controller and peripheral devices using four wires.

<sup>2</sup>Bayonet Neill-Concelman connector, the standard 50  $\Omega$  coaxial connector.

<sup>3</sup>Operational Amplifier

<sup>4</sup>Integrated Circuits or 'chips' in jargon.

<sup>5</sup>Field-Effect Transistor



**Figure 5.4:** Schematic of one channel of a 16-channel preamplifier. The main differences to the 2nd generation schematic are that the grid-bias is now individual for each channel, there are now test-pulsers inputs to pulse either all CA or NCA hybrids and the buffered individual CA and NCA outputs are now due to space reasons only available at so-called test-points on the PCB. If in a later stage of the experiment the collaboration decides to sample the pulse-shape of the detectors, they would have to be contacted appropriately. Besides, the pin assignment for the charge-sensitive hybrids has been changed to match that of the UK-Hybrids as default.

could be integrated "on" the signal kapton cable as part of a flex-rigid PCB to reach the integration scale necessary to host up to 64000 detectors [Wil05b]. Part of this development will be the attempt to integrate also shaping and analogue-to-digital conversion into the pre-amplifier circuit so only digital signals have to be transported out of the Faraday cage [Sch].

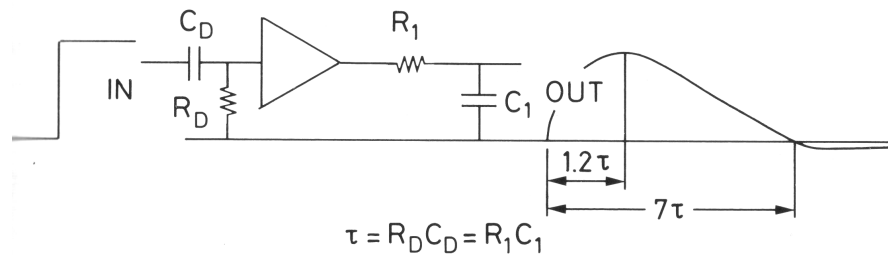
## 5.2 Shapers

### 5.2.1 Pulse Forming

Shapers have been introduced into nuclear electronics to give pulses a form better suited for analogue data handling and to reduce noise by reducing the bandwidth of the signal. In recent years, this task has normally been accomplished by main amplifiers that incorporated adjustable wide-range amplification, sophisticated pulse shaping and high counting rate circuits like baseline restorers and pile-up rejectors in one device.

The easiest form of spectroscopy shapers are CR-RC bandpass filters [Leo92, Spi06] with equal time constants  $\tau = RC$  in their high- and low-pass branch. They allow only frequencies to pass that are close to the characteristic frequencies of the sharp drop in the preamplifier signal which contains the energy information and cut out much low- (50Hz) and high-frequency noise/interfering signals. Together with a so-called 'pole-zero cancellation resistor', they can also cut all traces of the long exponential tail of the preamplifier signal.





**Figure 5.5:** Schematic of a simple CR-RC-shaper that converts the steep rise of the preamplifier signal into a rather flat-topped pulse that is also much shorter than the preamplifier signal. Typical shaping times  $\tau$  are on the order of few  $\mu s$ . Taken from [Leo92].

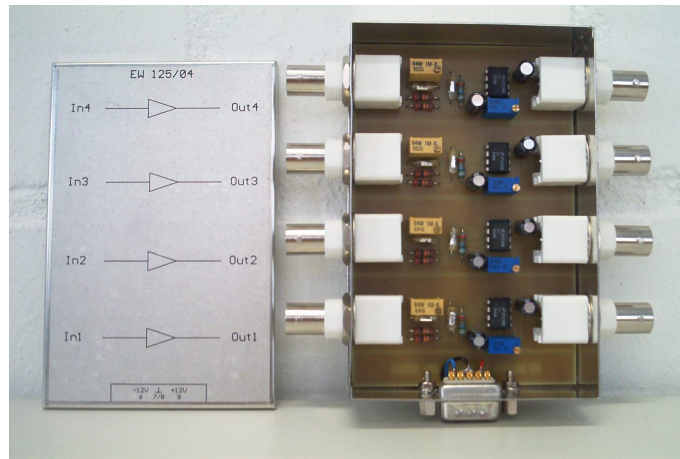
The main disadvantages of the CR-RC circuits are the non-optimal signal-to-noise ratio and high-counting-rate behaviour. The first one can be improved by stacking more integration stages (CR-RC-RC-RC-... filters) or by using an OP-Amp-based integrator circuit to get so-called 'semi-Gaussian shaping'. The latter one can be improved by using different shaping types like triangular or delay-line shaping but is not of much interest in the context of a low count rate experiment.

### 5.2.2 Main Amplifiers and shapers in COBRA

During COBRA's earlier phases [Mue01, Kie05], different types of NIM-module main amplifiers available in Dortmund were used as shapers, mainly Ortec 572, but also Canberra 2010 and 2011. Because of the moderate intrinsic energy resolution of the detectors during these phases, the sophisticated semi-Gaussian shaping of the devices, baseline-restorers and pile-up rejectors could not improve the results compared to CR-RC shapers. However, the sometimes antique devices proved to be a source of uncertainty by issuing disturbing signals that first seemed to originate from detectors or preamplifiers because of their rare and intermittent nature. It is believed that the main source for this behaviour are capacitances based on tantalum which can become low-resistive if old and under hot conditions but high-ohmic again after switching off the device during the search for defective parts. Because aged electronic devices (main amplifiers and CAMAC-ADCs, see [Kie05]) caused many outages during phase 1, the decision was made to replace them by custom-built devices that only contained the necessary functions. The most simple shaping circuit (CR-RC) seemed to be appropriate for the task; as the custom-built ADC accepts negative signals, it is non-inverting.

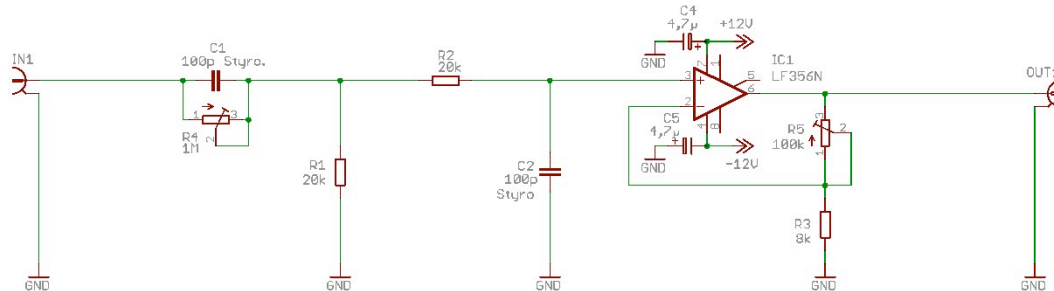
### 5.2.3 The first shaper

The first shaper was built to replace the aged main amplifiers in order to see whether more stable operation could be achieved. In an effort to keep it as simple as possible, the unit consisted of a passive CR-RC bandpass, a pole-zero cancellation potentiometer (socketed) and an impedance converter that also could deliver a moderate amplification to compensate the loss of signal amplitude. After testing the principle circuit with a breadboard setup, a compact 4-channel PCB was made by the electronics workshop of the University of Dortmund to be used with the VME ADC. After noticing that the first iteration of the ADC had problems with offset input



**Figure 5.6:** Photograph of the first 4-channel shaper. One can see the pole-zero cancellation potentiometer in yellow and the amplification adjustment in blue. Supply voltage is fed through the COBRA-DB9 connector at the bottom.

voltages, the impedance converter was supplemented with an offset-adjustment potentiometer. The full schematics and layout diagrams can be found in appendix D.



**Figure 5.7:** Circuit Diagram of one channel of the first shaper, a simple passive RC-CR band-pass with pole-zero-cancellation potentiometer and impedance converter/amplifier.

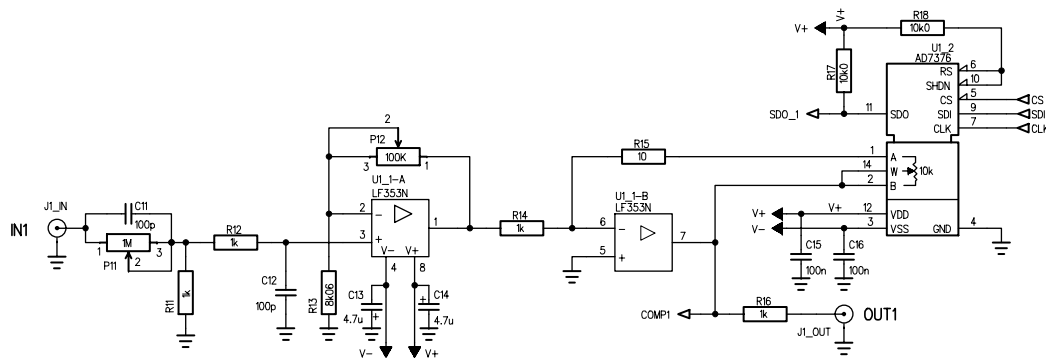
### 5.2.4 The inverting shaper

To be able to again use standard ADCs like MCA-cards and the Silena 9418 VME-ADC<sup>6</sup>, an inverting shaper was needed with an extended amplification capability. While COBRA's VME-ADC (see chapter 5.3) was designed to have a rather low input range of 0 to  $-2$  V, most commercial devices accept 0 to  $+10$  V. Additionally, the Silena 9418 required an external ECL-logic<sup>7</sup> trigger which had to be produced by either the preamplifier or the shaper.

<sup>6</sup>This ADC is of special interest because it is extensively used by many UK groups of the COBRA collaboration and is well supported by the MIDAS software.

<sup>7</sup>Emitter-Coupled Logic

The decision was made to add a second, inverting amplification stage to the original circuit. Its amplification can be adjusted by electronic potentiometers (AD7376) so the energy range is conveniently adjustable. Besides, the voltage level of all four channels is monitored by a comparator; if the threshold voltage is exceeded, a differential ECL-logic trigger signal is issued. The threshold voltage is also controlled by an electronic potentiometer. There is only one common threshold for all 4 channels.



**Figure 5.8:** Circuit Diagram of one channel of the inverting shaper. After the passive RC-CR bandpass, now an inverting op-amp with fixed amplification is used. After this first stage, a second, non-inverting amplification stage (adjustable by electronic potentiometers) is used to extend the output range to 10V, which is the input range of the Silena 9418 (compared to  $-2.5\text{V}$  of the VME-ADC). To trigger the Silena ADC, the signal is fed into a comparator.

The electronic potentiometers are daisy-chained like the preamplifier ones (see 5.1.4 and the AD7376 data sheet<sup>8</sup>): While they share their clock (CLK) and chip select signals (CS), the serial data input (SDI) is piped through the potentiometers of the different Channels CH:

$$\text{CH1} \longrightarrow \text{CH2} \longrightarrow \text{CH3} \longrightarrow \text{CH4} \longrightarrow \text{Threshold Control}$$

To operate the potentiometers, a TIP675 IP-module<sup>9</sup> that provides 48 TTL I/O channels was used on a TEWS<sup>10</sup> VME single board computer. Within the COBRA client-server architecture, it is operated via the `client-command slow/db9write`. sending five 7-bit numbers for the potentiometer values. It is also possible to use a parallel port of a standard PC to operate the potentiometers as it delivers TTL levels. For more details concerning the daq system and its operation see [Kie05].

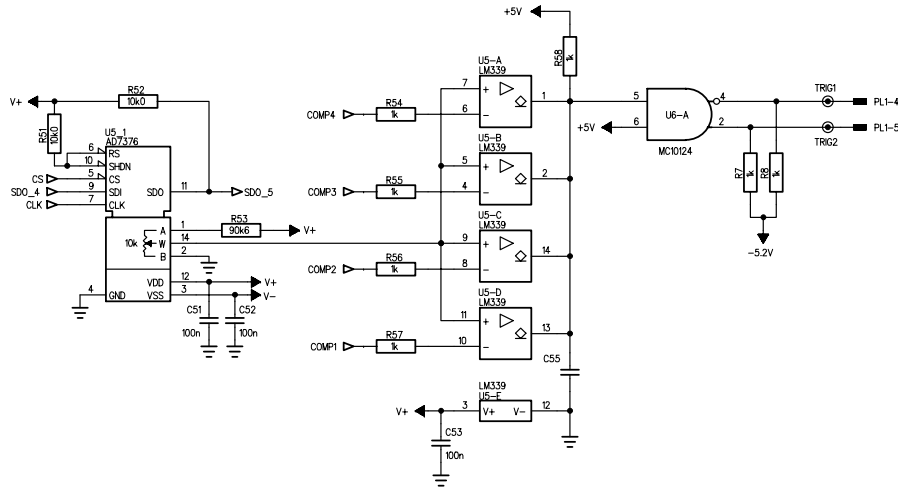
### 5.2.5 The NIM-shaper for the 64 detector array

For the 64 detector array, the CR-RC shaping circuit was improved by adding an impedance converter with some amplification capability between the low- and the high-pass filter. The improvement consists of two effects: firstly, the frequency response is better in the sense that it

<sup>8</sup>e.g. at Analog Devices ([http://www.analog.com/UploadedFiles/Data\\_Sheets/AD7376.pdf](http://www.analog.com/UploadedFiles/Data_Sheets/AD7376.pdf))

<sup>9</sup>Industry Pack, a form factor for computer extension modules comparable to PCI-cards, only with much smaller footprint.

<sup>10</sup>[www.tews.com](http://www.tews.com)



**Figure 5.9:** Circuit Diagram of the comparator of the inverting shaper.

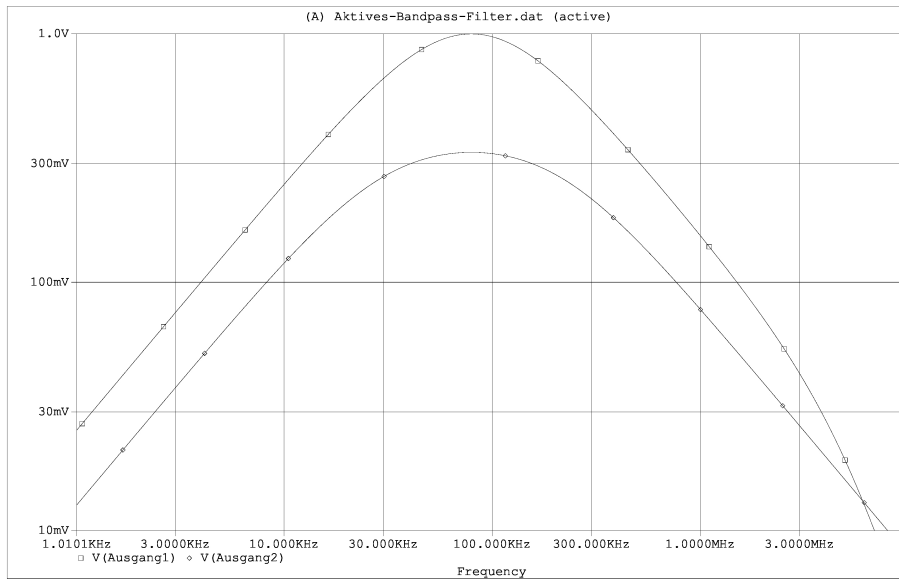
is more focused around the center frequency (see Fig. 5.10). Secondly, a larger amplification is possible without the limitation of a single frequency-bandwidth product: there are now two amplification stages that only need half the amplification factor; hence, the available bandwidth is doubled. With an amplification factor of 1, the improved circuit is widely known as 'active RC-CR bandpass'.

To cope with the large number of channels, it seemed to be useful to house 8 channels in a single-width NIM-module. The supply voltage, however, is not delivered by the NIM-crate, but by standard COBRA-DB9 connectors [Mün05] on the back panel. Thereby it is not necessary to always operate a NIM-crate, one can also operate single modules with a normal COBRA symmetric power supply ( $\pm 12\text{V}$ , GND).

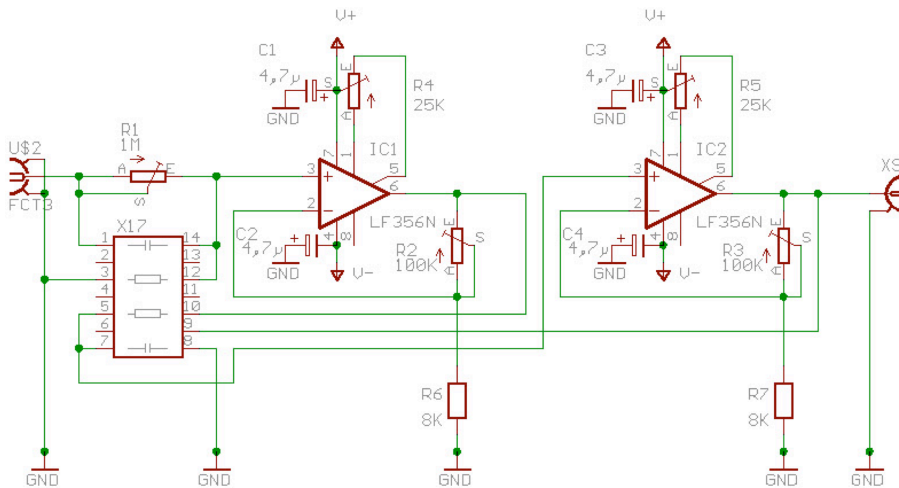
## 5.2.6 Outlook

Shaping will always be necessary to improve the signal-to-noise ratio (S/N) by discarding signal frequencies that carry only noise but no information. Due to the stringent space requirements for a 64000 detector array, however, they will have to be integrated into one monolithic circuit per channel which accomplishes the tasks of (pre-)amplifying, shaping and digitising altogether. Due to the low event rate and the moderate energy resolution (compared to e.g. Ge-detectors), the active CR-RC shaping circuit seems appropriate for this task also in the future.

A different scenario might include the use of very fast sampling ADCs (e.g. so-called Flash-ADCs). Here, the pulse shape will be recorded to extract more information from the event than only the energy – from the different rise times of CA, NCA and cathode signals one can obtain the interaction depth and even a classification of the location of the event ('central' vs. 'edge-like') in a CPG-detector [He05]. In this case it may be necessary to use a modified form of pulse shaping or even split the signal and treat different branches differently.



**Figure 5.10:** Frequency response of a passive (lower graph) and an active (upper graph) CR-RC bandpass to sine waves of 1 V input amplitude. The active bandpass possesses not only less attenuation, but also a sharper focus around the center frequency. The deformation at higher frequencies is due to the realistic PSpice-simulation of the bandwidth limitation of a real op-amp (LF356).



**Figure 5.11:** Circuit diagram of one of the 8 shaper channels. The components of the RC-CR bandpass are all stored inside a socketed package (X17) so the shaping time can be adjusted by exchanging it. The pole-zero cancellation potentiometer (R1) is also socketed. The desired amplification should be roughly equally distributed among the two OP-amps.

## 5.3 ADCs

### 5.3.1 General Remarks

Spectroscopic applications pose high demands on the conversion of the analogue signal into a digital value because of their fast speed and necessary resolution. This task is normally accomplished by ADCs<sup>11</sup> that use some kind of sample-and-hold circuit to keep the signal level steady while they compare the input voltage to reference voltages. This can be done in a variety of different ways, e.g. by discharging a capacitor linearly and measuring the time that is needed (Wilkinson method) or by using a comparator to decide whether the signal is above a reference voltage or below. The reference voltage is then adjusted in the right direction and the comparison is done again until the necessary precision was reached (successive approximation). Both methods need some time to do the conversion, normally in the range of a few to some 100  $\mu$ s, therefore they are not suitable for the sampling of fast signals that change their value significantly within these times. Therefore, spectroscopic setups normally contain so-called peak-holder circuits that are often already integrated into the spectroscopic ADC.

The rise-time of a CdZnTe detector pulse is on the order of a several 10 to some 100 ns. For the measurement of pulse-shapes, so-called Flash- or Parallel-ADCs have to be used which normally contain as many comparators and reference voltages as resolution is needed, they can determine the input level within one comparison which may be as short as some 100 ps (for 8 bit resolution). In the past years hybrid forms that are combinations with successive approximation ADCs enabled higher resolutions with comparably fast conversion times, here up to 14 bits of resolution are available within 5 ns. For more details see [Leo92].

Within COBRA, the data rate is low and the individual signal does not stay steady after the rise-time, but decays due to the use of common resistive-feedback charge-sensitive preamplifiers and subsequent CR-RC shaping. It is therefore necessary to use a peak-holding circuit which preserves the maximum amplitude of the preamplifier signal until it is reset, a simple sample-and-hold stage which is included in most ADC chips is not sufficient for spectroscopy because of the time jitter of sampling. While specialised spectroscopy-ADCs normally include such a stage and are called 'peak-sensing' ADCs, commercial ICs only include sample-and-hold stages.

### 5.3.2 Early ADCs

As described in more detail in [Mue01] and [Kie05], COBRA started using a commercial MCA<sup>12</sup> card (Ortec TRUMP 8k) as ADC. MCAs are frequently used in spectroscopy, they usually sample fast and independent of the host computer's load as they do the histogramming themselves. Besides, they already contain a peak-holder circuit. The main drawbacks for COBRA were that by histogramming, it is obviously not possible to obtain timing information from individual events (e.g. to identify decay chains), and that each MCA card can handle only one channel being rather expensive at the same time. Results obtained with this setup have been published in [Mue03] and [Kie03].

For the 4 detector array, CAMAC ADCs (Ortec 3511 and 3512) were used [Kie05]. Now it was possible to obtain timing information for each event, although only with limited accuracy

---

<sup>11</sup>Analogue-to-Digital Converters

<sup>12</sup>Multi-Channel Analyser, a special ADC with integrated buffer.

on the order of ms as only the system time at readout could be used. Due to the aged and thereby unreliable modules, however, CAMAC was only used as an interim solution until the optimized and self-built VME-ADCs were available. Data taken with the CAMAC setup was used to publish [Goe05] and in part for [Blo07a].

### 5.3.3 The VME-ADC

#### Design Goals

To provide the scalability of COBRA's ansatz, the electronics cost for each channel has to be much lower than the cost for one detector. Therefore, it was decided in 2003 to start the development of a completely self-built ADC which allowed us to define the operation parameters and layout which will be important for a later integration into a 'all-in-one' electronics block per channel (see chapter 5.1.6). The development was done in close cooperation with H. Kiel (see [Kie05, p. 56 et seqq.]) and N. Koch of the physics department's Elektronik-Entwicklung. Main design goals were

- cost effectiveness

While most spectroscopic experiments use only a limited number of detectors and ADCs, COBRA's design relies on the use of a very large number of detectors. Therefore it was necessary to develop a customized multi-channel ADC that would allow us to keep the electronics cost at a fraction of the cost for detectors while possessing the necessary specifications and scalability to operate CPG detectors without disadvantages compared to state-of-the-art commercial electronics and ADCs.

- sufficient resolution with respect to CZT's intrinsic resolution

The energy resolution obtainable with current CPG-type detectors is about 1.5 % or 11 keV FWHM at 662 keV [He05]. The batch of moderately priced detectors used for the 64-array was measured by the manufacturer to have resolutions between about 25 and 55 keV at 662 keV, the separately ordered batch of better detectors for the  $2 \times 2 \times 2$  core of the 64-array was measured to have between 14 and 20 keV.

This resolution will additionally suffer from the fact that COBRA has its first preamplifier stage only outside of the copper- and lead-shielding resulting in cable-lengths of around 35 cm prior to the first amplification of the signal. Hence it is not necessary to have ADCs with resolutions as good as necessary for Ge-spectroscopy where the detectors yield resolutions better than 0.1 %. The design goal was therefore to reach about 0.1 % FWHM which will be absolutely sufficient to not significantly affect the system's energy resolution.

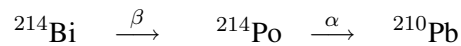
- scalability

From the beginning of COBRA it was clear that in order to reach half-lives beyond  $10^{25}$  years with current CZT crystal growth technology, a highly granular detector layout had to be used. Calculating conservatively with  $1 \text{ cm}^3$  cubes, several  $10^4$  detectors will be necessary to achieve half-lives that are predicted by theory for neutrinoless double beta decay in e.g.  $^{116}\text{Cd}$  [Wil05b]. To implement a reasonable prototype array with  $4 \times 4 \times 4 = 64$  detectors that could be extended by one to two orders of magnitude, a bus-driven

modular system had to be used. The Elektronik-Entwicklung had much experience with VME electronics development and VME crates and modules were frequently used in high energy physics, so it was decided to implement the ADC as single-width VME modules. Limitations in the availability of multi-channel ADC ICs led to the design of a four-channel module. A standard VME crate can therefore house  $4 \cdot 20 = 80$  channels, 8 crates per rack lead to a total number of roughly 640 channels per  $m^2$  area.

- time stamps

For the identification of decay chain events, a good time resolution of the events is necessary. In the case of  $\beta$ - $\alpha$ -cascades like



within the  ${}^{238}\text{U}$  decay chain, the half-life of the intermediate nucleus  ${}^{214}\text{Po}$  is only  $164 \mu\text{s}$ . The  $\beta$ -decay of  ${}^{214}\text{Bi}$  has a half-life of roughly 20 minutes and a Q-value of 3275 keV, hence it can very well fake a neutrinoless double-beta decay. By detecting the subsequent  $\alpha$ -decay with a Q-value of 7687 keV, however, one can flag the preceding decay as background event. To do so, the ADC must have a rather short duty cycle (time between triggering and being able to accept the next trigger) and the time resolution of events must be on the order of  $\mu\text{s}$ .

- veto flag input

Even at large depths underground, current low-rate experiments utilise vetos against the few remaining cosmic rays, mostly muons. COBRA possesses a plastic scintillator based cosmic ray veto since its first measurements in Dortmund [Mue01]. While first a multiplicity NIM unit was used to combine individual comparator hits into one common veto signal that was fed into a gate input (MCA card) or an I/O register (CAMAC), it was now desired to have the possibility to read the status of several TTL lines at the time of each conversion. Thereby, it would be possible to have flags from different subdetectors/scintillators to e.g. distinguish single muons from showers. This might be helpful to verify simulated background behaviour with data taken from real background events.

## Working Principles

To fulfil the design goals, N. Koch chose to conceptualise a VME-ADC that was controlled by two FPGAs<sup>13</sup>, one mainly for the communication with the VME bus and the other mainly for the control of the ADC chip. Concerning the programming they work as one unit and it would have been possible to replace the two FPGAs by one larger FPGA. From today's viewpoint, also the usage of a microcontroller would have been possible, but FPGAs are able to handle extremely fast processes and it is envisaged that the main ADC concepts might be re-used for other high-energy physics related projects. It was decided to use two EPM7128STC100 FPGAs from Altera's MAXX 7000 series. The firmware-programming was done by N. Koch using a proprietary high level language by Altera (Altera Hardware Description Language AHDL) via

---

<sup>13</sup>Field-Programmable Gate Array

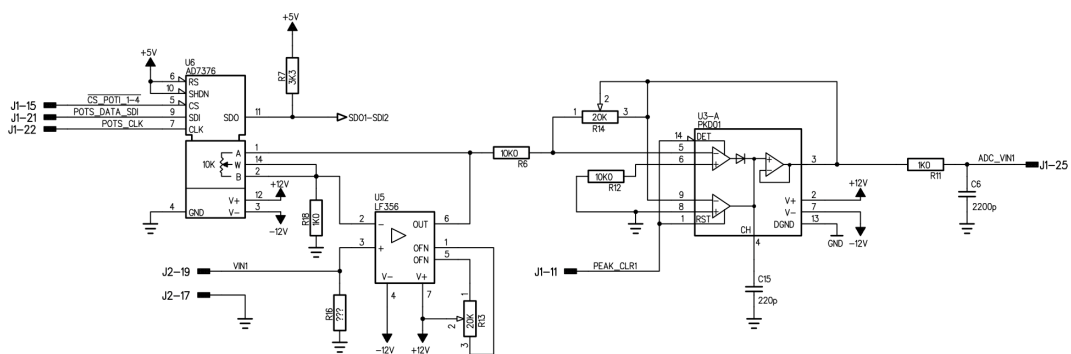


an ISP-JTAG<sup>14</sup> interface. Listings of the latest version of the firmware at the time of writing can be found in appendix D.

The ADC is operated by the server application `daq` written in C by H. Kiel running on the VME crate controller. One can give commands to this application using the `client`-command on any remote COBRA computer which serves as a client application and contacts the server via the TCP/IP<sup>15</sup> protocol. Using this three-layer approach, the ADC is normally operating autonomously, only indicating the availability of data in its buffer to the server process. It is possible, though, to adjust internal parameters conveniently from far away using the client-server-architecture of the controlling application.

The other main decision was which ADC chip to use. After a brief market survey at the start of the development, the Analog Devices AD7865 seemed to be the best suited chip available. It contains 4 track-and-hold units that sequentially feed a 14-bit successive approximation ADC with a total conversion time of only 10  $\mu$ s.

Additional circuitry was needed to implement electronically adjustable input amplification, a peak-hold circuit, an electronically adjustable trigger, and a buffer. A first prototype was built to examine possible problems before the series production for the 64-array would begin. Because the analog part of the circuit seemed to be the one that would probably see the most revisions for improvement, it was decided after the first prototype to put all analog circuits onto a daughter-board ('mezzanine') that could be exchanged easily.



**Figure 5.12:** Schematic of one of the ADC's inputs with amplification and peak-holder stage.

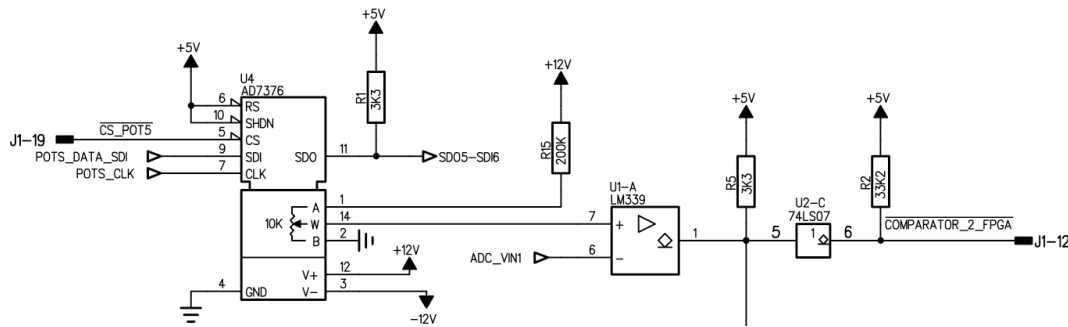
Once a signal arrives at one of the inputs, it is first amplified by a non-inverting amplifier using a LF356-type operational amplifier. The variable resistor in its feedback loop is a 7-bit AD7376 electronic potentiometer whose value can be controlled digitally through a SPI bus interface operated by the FPGA that controls the ADC. Thereby, the amplitude of the input signal can be adjusted to match the energy scale to the ADC's range.

After this, the signal is fed into a peak-holder circuit. As explained above, this is necessary as the maximum amplitude of the shaped signal peak contains the energy information hence one has to preserve and sample the maximum signal height. On the first prototype, this circuit was implemented discretely by charging a capacitor via a Schottky-diode. Because of the rather poor linearity of this circuit, a PKD01 chip by Analog Devices was used in later versions. Due to its rather slow slew rates, however, it was necessary to change the capacitor's value from

<sup>14</sup>In-System Programmability Joint Test Action Group interface according to IEEE Std. 1149.1

<sup>15</sup>Transfer Control Protocol/Internet Protocol

$C_{15} = 1000 \text{ pF}$  to  $C_{15} = 220 \text{ pF}$ . Now, the slew rates are fast enough, but the parasitic discharge is increased. Nevertheless, it has been shown that this has no ill effects on the sampling as the time walk of all measurements is very small compared to the discharging of the PKD01 (see [Kie05, p. 58]). The peak-holder is reset by the controlling FPGA essentially shorting the capacitance. Therefore, a compromise has to be chosen concerning the duration of the reset-signal: if it is too short, the capacitor will not be fully discharged, if it is too long, the dead-time of the ADC will be unnecessary high. By default, a value of  $t_{\text{clearcap}} = 50 \mu\text{s}$  is used. Changes can be made by using the command `client slow/clearcap/V` where  $V$  is the duration of the reset signal in  $\mu\text{s}$  (must be between 1 and 1023).



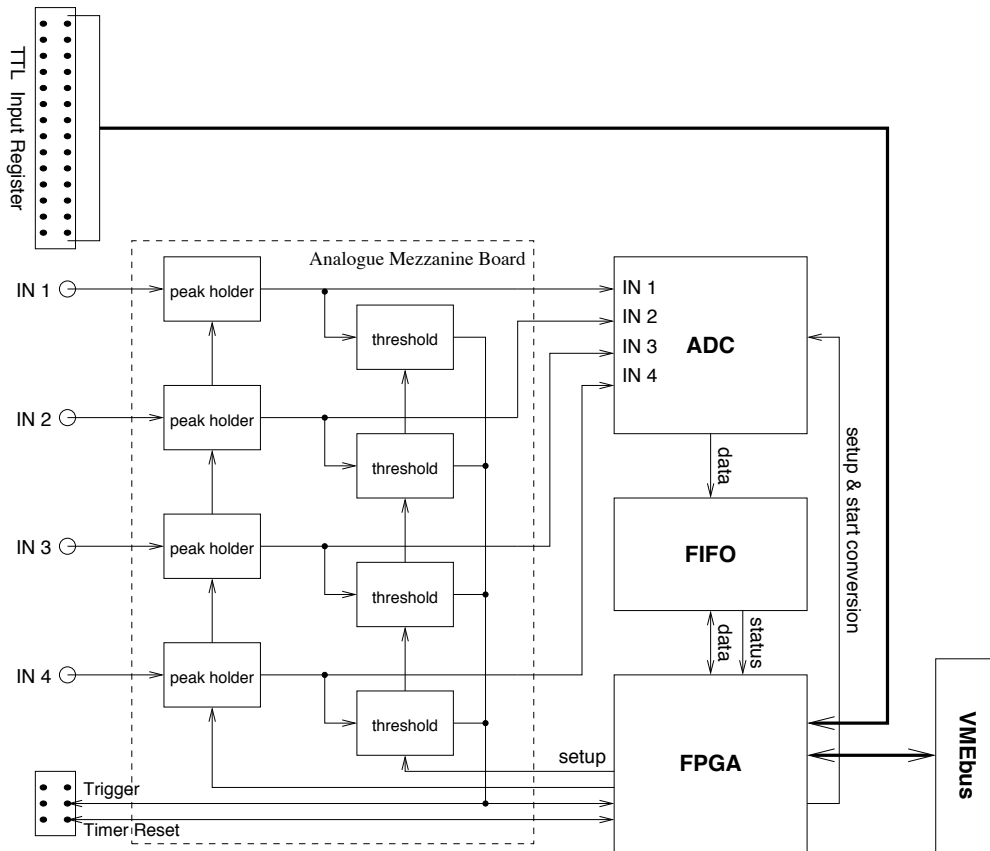
**Figure 5.13:** Schematic of one channel in the ADC's trigger stage.

The output of the peak-holder is fed into the AD7865's track-and-hold input and into the trigger stage. Here, one comparator for each channel is fed with a reference voltage adjusted by an AD7376 digital potentiometer operated by the ADC-control-FPGA. The threshold voltage is hence individually adjustable for each input while in the first prototype stage, there was only one common reference voltage for all inputs. If one or more comparators are fired, the logic level at their output pulls the voltage of the subsequent circuit to ground delivering the trigger signal to the FPGA.

Now the FPGA waits for a certain amount of time to let the PKD01s settle. This time is adjustable with the `client slow/deadtime/V` command where  $V$  denotes the 'rise-time protection' in  $\mu\text{s}$  (must be between 1 and 1023). Then, it gives the ADC chip the conversion command which triggers the ADC's internal track-and-hold stages. The active channels are now converted sequentially and the data is transferred into the buffer which has a length of 512 events where they wait to be read-out by the daq-server. While this is normally happening on a regular polling basis, the FPGA can issue interrupts asking the server to act as soon as the buffer is empty ('empty-flag'=EF), half-full (HFF) or full (FF) adjustable by the `client slow/interrupts/M/EF/HFF/FF`-command where  $M$  again designates the module's number where a 0 deactivates an interrupt while 1 activates it. Default settings are 0/1/1.

Afterwards, the FPGA resets the ADC-chip and the PKD01 and the device is ready to accept the next signal. The total dead time where the ADC cannot accept a signal is strongly dependant on the chosen rise-time-protection and clearcap times. With standard settings, the total deadtime per event is roughly  $115 \mu\text{s}$ . It has been shown, however, that the ADC can as well work with more ambitious settings approaching deadtimes of below  $40 \mu\text{s}$ .

To be able to operate many ADCs in a coincidence mode where also small energy deposits



**Figure 5.14:** Block diagram of the main components of the VME-ADC taken from [Kie05].

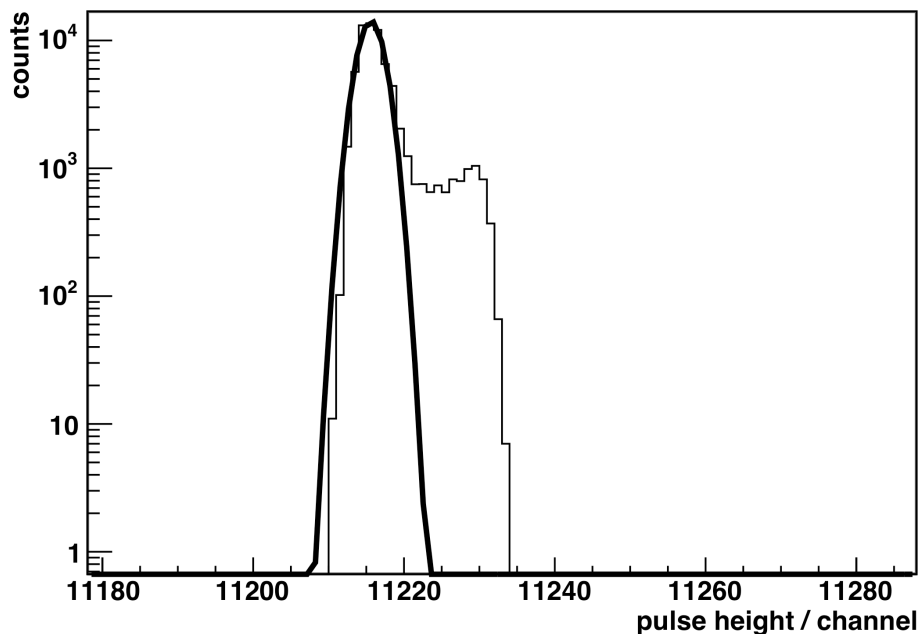
(e.g. by compton scattering or bremsstrahlung) in neighbouring crystals can be attributed to a main event in a central crystal, it was furthermore necessary to synchronise the time stamps in all ADCs and to propagate triggers - small signals that might not be large enough for their own trigger can be important hints for a multiple detector event (as opposed to a single-detector multiple-site event that could only be detected by pulse-shape analysis). This has been accomplished by a six-line front plate bus implemented with ribbon cable. The common trigger mode is only useful in low-level data taking mode and can be switched on/off with the `client slow/accepttrigger/M/V`-command where `M` is the ADC's module number and `V` is 1 for enabled or 0 for disabled. Front plate bus trigger generation of that module can be operated with `client slow/generatetrigger/M/V`.

## Operation

After booting the VME-crate controller, the root-user has to start the server-process `daq` using

```
cd /data/COBRA
nohup ./daq &
```

By doing so, the data files will be stored in `/data/COBRA` where they belong. Using the `nohup`-command will prevent the process from being closed when the user logs off. After this has been done (which could also be accomplished by a start-up-script in the future), all further commands can be sent from remote computers using the `client`-command. This command is e.g. by default installed on the workstation PC. After logging on with `ssh`, the user can operate the ADC (and also the other parts of the experimental setup like HV-supply, grid-bias supply and preamplifiers) with the help of the `client`-commands listed in appendix E either interactively or by grouping such commands as shell-scripts. For debugging and calibration purposes, graphical front ends `calib` [Kie05] and `calib64` [Wil05a] are available that internally use the `client`-application to communicate with the `daq-server` and the `ROOT`-libraries to graphically represent the received data. Fitting and the use of other `ROOT` routines is also possible.



**Figure 5.15:** Histogram of test pulses with 1 V amplitude showing the resolution reached with current firmware and daq-software versions.

Compared to the performance of the ADCs described in [Kie05, p. 60], modifications of both firmware (taking no actions during conversion) and `daq-software` (various bug-fixings [Wil05a]) enabled a further improvement of the ADCs' specifications: as can be seen from figure 5.15, the resolution measured by the width  $\sigma$  of the fitted Gaussian could be improved by about a factor 4 and is now about 2 channels or  $1.5 \cdot 10^{-4}$  yielding a full-width half-maximum (FWHM) of about 0.035% which is even further below the typical detector resolution of above 3%. A remaining asymmetric high-energy shoulder is harmless due to the small scale and content – the whole peak is much narrower than the one shown in [Kie05, p. 60].

Improvements of the interrupt handling of the `daq-software` led to the fact that the possible data rate is now only limited by the total deadtime (essentially the sum of rise-time protection, conversion time and clearcap time) or the decay times of the shaped input peaks. Repetition

rates of up to 10 kHz have been tested without degradation in resolution.

### 5.3.4 Outlook

As indicated above, the current VME-ADC is well suited for the data-taking with several tens of CPG-type CdZnTe-detectors. Upscaling to some hundred detectors is possible, but for operating up to 64000 detectors [Wil05b] the platform is not adequate due to its too large footprint per channel. Apart from that also the usage of pixelised detectors [Blo07b] will require different and integrated ADCs to cope with the number of channels. Currently measurements are being conducted by the COBRA groups in Liverpool and York to explore the advantages of pulse shape analysis. Because of the huge number of channels the decision to use this technique will also make it necessary to include fast-sampling ADCs in a monolithic detector readout circuit [Sch] instead of having only peak-sensing converters. However, it is still unclear whether a pulse-shape only readout can reach a noise level that will make the spectroscopic results comparable with current CR-RC-shaped peak-sensed results.

## 5.4 Additional Electronics

### 5.4.1 The 64-channel High-Voltage Supply

Due to the large variability of optimum bias voltages for CdZnTe detectors, an individually adjustable high-voltage supply was necessary. In addition, remote control as well as remote voltage sensing were desired. Such a device was built by the University of Warwick's COBRA group. It features 64 independent channels, a remote sensing ability and is controllable via a TTL protocol, e.g. by a parallel computer port. The necessary `client` commands have been added by J. Wilson. Comprehensive tests were conducted by the author to ensure the reliable operation of the device. Some modifications were necessary due to differences between a parallel port, which was used for development at Warwick, and the TTL-I/O-register which is used in the LNGS setup. Moreover, the usage of a TTL-buffer was necessary to ensure defined TTL levels and sufficiently fast edges of the digital signals.

### 5.4.2 The grid-bias supply

The grid-bias power supply is used to deliver individually adjustable voltages of 0–75 V to the detectors' non-collecting anodes. It was for the most part developed by O. Schulz and will be described in [Sch]. Extensive testing was done by the author finding excellent operation under the condition that – for the same reasons as above – a TTL-buffer was used.

### 5.4.3 The central control computer

The central control computer has already been described in [Kie05] to some extent. Currently, a TEWS TVME 8240 single board computer VME-module is used which is acting as the VME crate controller. It is capable of housing up to four so-called IndustryPack-modules which can provide additional I/O capabilities. At the moment, the following modules are used:

- one TEWS TIP570 module containing a 16-channel 12-bit ADC and a 4-channel 12-bit DAC<sup>16</sup> for slow-control data acquisition; e.g. for monitoring temperatures via Pt-100 sensors or the LN<sub>2</sub>-flow with a flow-meter.
- one TEWS TIP675 48-channel TTL-I/O module to control various electronic potentiometers and other settings of the preamplifier, HV-supply and grid-bias supply.
- one TEWS TIP810 CAN-bus controller for communication with CAN-bus devices as for example the VME crate.

Currently, the control computer is running the daq-server under Gentoo Linux.

#### 5.4.4 Outlook

In the future, the necessary footprint reduction of the electronics for each channel to house up to 64000 channels inside a compact shield will require the integration of HV- as well as grid-bias-supply into the preamplifier channel which must also house shaper and ADC. Then, a VME-based data acquisition system will not be sufficient any more and will be replaced by microcontroller-based intelligent electronics boxes communicating with a central daq computer via Ethernet, USB or field buses.

---

<sup>16</sup>Digital-to-Analogue converter, useful e.g. for the delivery of control voltages

# Chapter 6

## Data Collection

### 6.1 Improvement Stages

Since the start of the evaluation of CdZnTe detectors for the detection of rare nuclear decays in 2000, the COBRA experiment has passed through a number of development stages and a number of analyses have been performed. These have been described in several publications.

While the outline of the idea for COBRA was introduced by Zuber [Zub01], first results achieved with single CdZnTe and CdTe detectors were analysed by the author in [Mue01]. Subsequent publications by Muenstermann and Zuber ([Mue03]) and Kiel, Muenstermann and Zuber ([Kie03]) used data collected with the setup described by the author in [Mue01].

H. Kiel described several components of the four-detector array in [Kie05] while detector holder, contacting and both preamplifier and ADC circuits are described in chapters 3, 5.1 and 5.3 of this work. Analyses of data taken with this setup have been published in [Goe05] and [Blo07a].

The next major improvement has been the installation of the first 16-detector layer as part of a 3-dimensional 64-detector array. Main improvements compared to the four-detector array have been the scalable contacting and wiring with Kapton-cables and the introduction of scalable analogue electronics such as the 16-channel preamplifiers and NIM-shapers which are described in chapters 3, 5.1, 5.2 and 5.3 of this work. After the first layer had been installed, the primary aim was to gain experience before contacting the remaining detectors. An analysis of the data collected with this layer is presented here for the first time.

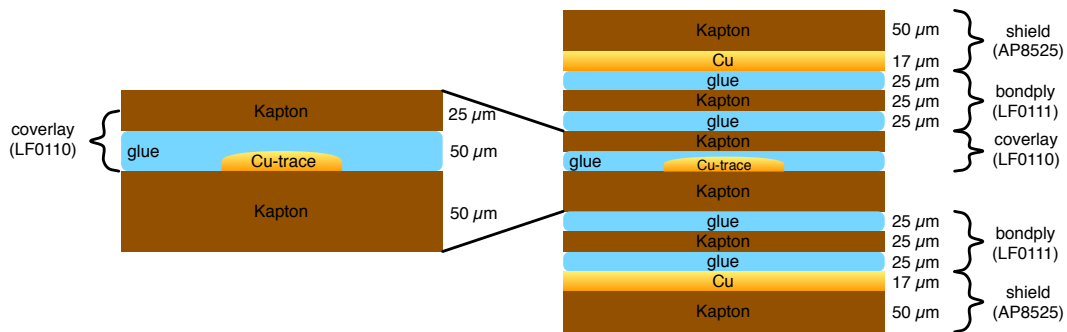
### 6.2 Data Collection

The first fully equipped 16-detector layer with Kapton cable contacting was installed at LNGS in March 2006. Unfortunately, transport damage caused the failure of the 64-channel high-voltage power supply which had been custom-built by the University of Warwick. Therefore, full operation could first be obtained after substantial repairs in September 2006. Only then, very rare crosstalk events of varying amplitude could be observed that cannot be distinguished from physical events with the current setup. As stated in chapter 3.5, they were not spotted during tests on the earth's surface due to their sparseness compared to cosmic ray events. Furthermore, due to the the initial lack of individual high-voltage control for each detector it was necessary to operate the detectors during the tests in groups of eight detectors with equal HV

values. Even if the rare events would have been spotted during the tests, it would have been more probable to believe in breakdown effects of a single faulty detector than in other rather exotic explanations for this effect.

After some literature research, it was concluded to be the best hypothesis that these events are so-called micro-discharges inside the high-voltage Kapton cables. In strong electric fields, the partial discharges can occur especially at places where the relative dielectric constant changes abruptly as e.g. at the interface between glue and copper or Kapton and copper. Details on micro-discharges can for instance be found in publications [Hee00], [Dan05] and [Ort02].

To reduce the number of fake events, two countermeasures were applied: Firstly, the high-voltage Kapton was shielded in Dortmund in a triplate manner<sup>1</sup> by laminating two extra copper-plated Kapton sheets onto the cable. A comparison of the cross-sections can be found in fig. 6.1. This lead to better control over the electric field and contains any electromagnetic waves that are generated by the very fast transient in the course of a discharge. This measure vastly reduced the number of observed fake events.



**Figure 6.1:** Cross sections of the original (left) and modified (right) version of the HV-Kapton cable. The materials used are from the Pyralux® family by DuPont™ and designated with their internal product codes. Thicknesses of the layers are given in  $\mu\text{m}$ .

Secondly, to be able to also take into account those discharges that happen very close to the detector and hence cannot be shielded or propagate through the detector, coupling capacitors and a custom-built veto-circuit were added to the high-voltage Kapton. In its first version the veto-circuit amplified the very fast discharge pulses and added them up so after shaping and inversion one standard VME-ADC channel was able to sample the combined veto signal. Drawbacks of this fan-in solution were:

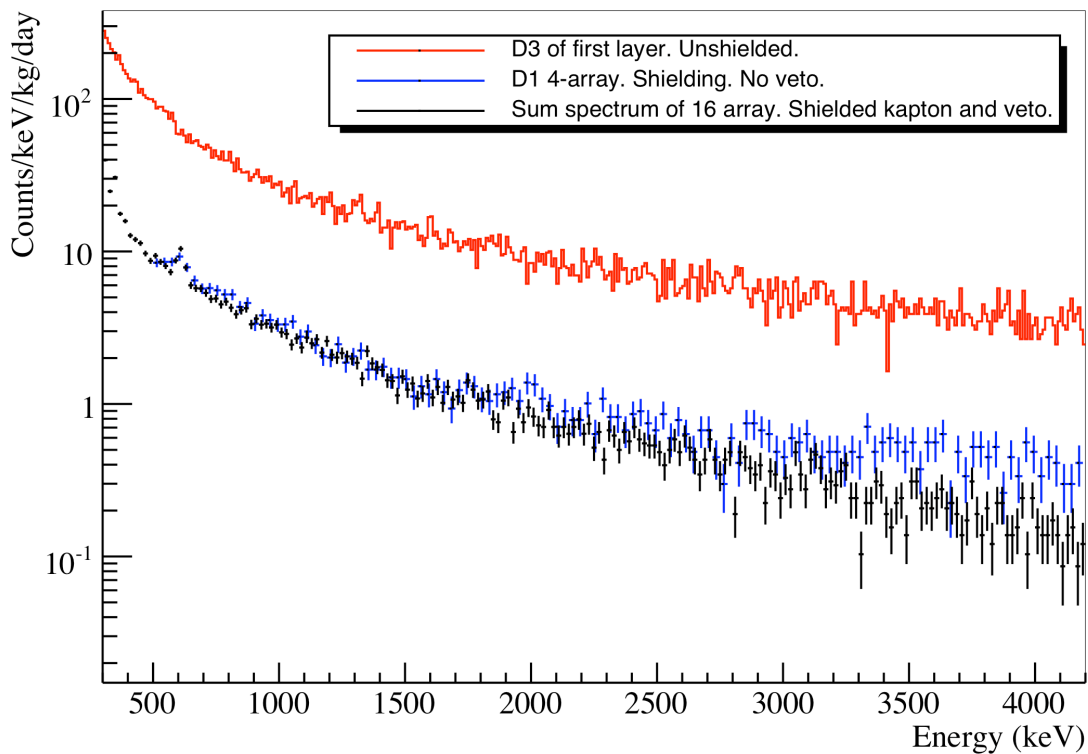
- discharges cannot be localised to investigate the cross-talk further
- pulse forms are lost
- due to a limited amplification factor, only discharges equivalent to more than about 4 MeV were recorded
- if a self-triggering ADC-channel is used then also discharges that do not cause any cross-talk at all are recorded which may lead to huge data files and large dead time

<sup>1</sup>Electronic design where the signal traces are kept between two shielding ground layers.



The latter problem was solved by modifying one ADC channel to not trigger any more; more sophisticated circuits are currently under development. Nevertheless, already this first veto circuit version was able to reduce the number of fake events, however, only above roughly 4 MeV. The effect of these measures is shown in Fig. 6.2: compared to the old  $2 \times 2$ -setup the spectrum of one of the detectors of the 16-detector layer without shielding and veto shows a steady increase of the count rate at all energies of about one order of magnitude. The shielded version returns to the previous background levels with even some improvement at higher energies.

The data used in the subsequent analysis was collected with the first 16-detector layer of the 64-detector array between January and June 2007 after the above countermeasures had been installed in December 2006. Sum spectra of the data can be found in Fig. 6.2 (black spectrum "shielded kapton and veto") as well as in Fig. 4.5 (red spectrum "without flushing"). Due to problems of reliably contacting the anodes with the copper-based glue, data of four of the 16 detectors was not available during this period. At the time of writing, a pressure-based needle contacting scheme is being tested in Dortmund to overcome this problem in the remaining three layers.



**Figure 6.2:** Spectra of the old  $2 \times 2$ -setup (blue) compared to shielded (black) and unshielded (red) runs of the first 16-detector layer. The increase in count rate by partial discharges is about one order of magnitude at all energies. The shielding of the HV-Kapton cable restores the old count rates with even some improvement at high energies. The unchanged background level is probably set by the red passivation resin and the Rn activity prior to LN<sub>2</sub>-flushing.

Calibrations were done with  $^{22}\text{Na}$  and  $^{228}\text{Th}$  at the beginning and end of the five groups of runs<sup>2</sup>. Data preparation and cleaning was done by C. Reeve with methods described in [Ree]. This includes the use of event-rate-based algorithms to detect 'noisy' runs caused e.g. by microphonics due to construction works in the tunnel and the rejection of discharge-coincident events.

The total duration of the available dataset is 1816 hours or 75.66 days, the total mass of all detectors is  $103.9 \pm 0.5$  g; the average weight of a detector is 6.5 g. To account for outages of individual detectors during certain groups and/or runs, the same cuts that were applied to the data were applied to a Monte Carlo simulation. Hence, these outages are taken into account by a reduced detection efficiency for the individual signal channels. Therefore, a precise value for the collected statistics cannot be given because this simple product approach of measurement time and detector mass does not take into account the large number of detectors and the manifold outage reasons and durations that may arise. Besides, this value is only comparable for standard data analyses but not for coincidence analyses where the array's geometry heavily influences the solid angle. Furthermore, a comparison between different detector materials, e.g. between CdZnTe and Ge, is not possible anyway due to the different photon cross sections resulting in very different efficiencies. A coarse estimation of the collected statistics for a standard analysis is about  $4.2 \text{ kg} \cdot \text{d}$  in comparison to  $4.34 \text{ kg} \cdot \text{d}$  of data analysed in [Blo07a].

---

<sup>2</sup>Nomenclature: *events* are individually recorded energy depositions that are grouped into *runs* which are collections of events occurring within one hour. A *group* of runs are all runs that share a common calibration and other parameters.

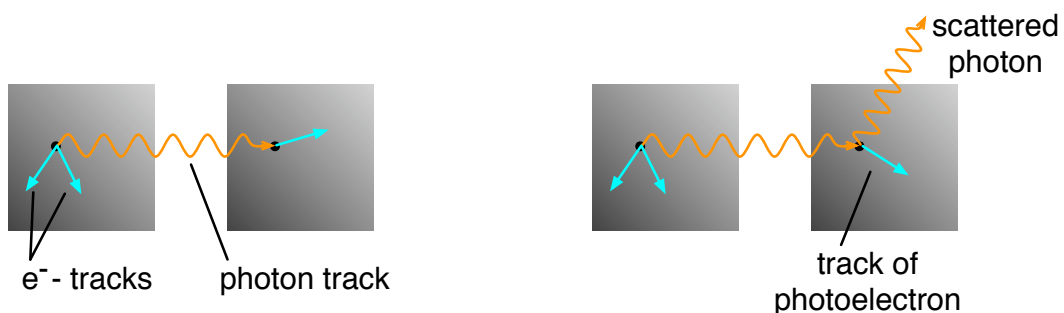
# Chapter 7

## Analysis

### 7.1 Analysis Methods

A preliminary standard analysis of the collected data like the one presented in [Blo07a] showed that no significant improvement of limits on double beta decay half-lives can be reached compared to the cited publication. This is due to the essentially unchanged background of the red passivation paint and similar statistics as before. However, the first-time availability of a significant number of neighbouring detectors allows a search for coincident events in two or more detectors which was not conducted before. It was expected that the signal-to-background ratio would improve significantly as it is highly unlikely for most of the background events to mimic concurrent energy depositions in two crystals with the correct pulse heights.

The analysis method used here is based on the evaluation of energy depositions in two or more crystals at the same time. The simultaneousness is technically defined as the occurrence of two energy depositions within a  $50 \mu\text{s}$  time window: this is the time between the triggering and voltage conversion of the VME-ADC that was used to collect the data analysed here. If a first signal which triggers the ADC would be succeeded by a second, independent event within this time window, both energy depositions could not be differentiated. However, the normal data rate of the most prominent background decay,  $^{113}\text{Cd}$ , is about one decay per three minutes



**Figure 7.1:** Illustration of the coincidence analysis method. Left: While the primary electrons deposit their energy in the source crystal, the emitted photon travels to a neighbouring crystal and deposits its full energy via a photo-electron. Right: In the case of the Compton-effect, the photon is scattered and deposits only a fraction of its energy.

per crystal. From this it is obvious that random coincidences are strongly suppressed.

While in principle also electrons or positrons could leave the source crystal and propagate into a neighbouring one, the physics signature for this process is very unfavourable due to the non-constrained individual depositions – they may lose an arbitrary amount of their energy in the source crystal and the rest in the second detector. In addition, some energy loss in air or holder structures between the active volumes is probable which cannot be seen.

Photons leaving the source crystal normally suffer no energy loss between two detectors as the interaction cross section is small thanks to the low densities and atomic numbers of air and holder structure. The two common cases of coincident photon interactions, Compton- and photoelectric effect, are illustrated in Fig. 7.1. While the photon deposits all its energy through a secondary electron in the case of the photoeffect, already for intermediate energies the Compton effect has a larger cross section (see also Fig. 4.7) where only a fraction of its energy up to the Compton edge (see eqn. 4.2.2) is deposited. While the physics signature of the photoeffect case is usually cleaner, a search for the Compton effect case can sometimes improve sensitivity because of its higher interaction probability. For future large 3-D arrays, it can be expected that in most cases the full photon energy will be recorded in form of multiple-detector events where one or more Compton-effects precede a final photoeffect.

The workhorse of neutrinoless double beta decay searches, normal  $0\nu\beta^-\beta^-$ -decays, only very rarely emit bremsstrahlung photons, therefore the efficiency to detect them with a coincidence analysis is very low. Besides, the experimental signature is diffuse due to the continuous bremsstrahlung spectrum.

$\beta^+\beta^+$  and  $\beta^+$ /EC-decays emit four and two photons, respectively, and are therefore promising candidates for a coincidence analysis. While the kinetic energy of the positron(s) is deposited within the source crystal, it is likely that the 511 keV photons escape from the source crystal yielding a line signature of the Q-value reduced by the escaped photon energies.

A disadvantage of the physics signature of  $\beta^+\beta^+$ -decays is that many background events also emit 511 keV photons. Other interesting candidates for the analysis method which do not suffer from this drawback are  $\beta\beta$ -decays into excited states. Here, the photon energies are fairly unique which makes it still less likely that they could be faked by background events.

The detection efficiency for the photons depends on their energy and on the instrumented solid angle. For gammas, the interaction probability in neighbouring crystals is already acceptably high (some percent) for a single 2-D crystal layer. This leads to a coincident signal in two or more detectors for a corresponding fraction of all events. A 3-D array like the 64-detector array will have much improved efficiencies. Ideally, in a very large CdZnTe array like the 64000-detector array under investigation by COBRA, the detection efficiency for photons emitted in center crystals of a 3-D array will reach more than 80 percent while the probability for fake events essentially stays the same. Additionally, the fact that real coincidences are more likely in neighbouring detectors while fake coincidences have a flat probability distribution can also be used.

Gammas escaping the source crystal normally interact via the Compton effect, some percent (depending on the energy) also via the photoeffect. The latter interaction yields a much cleaner signal as two well-defined energy depositions can be demanded. In the Compton case, however, only one of the two signals has a line-signature while the other can be anywhere between the noise edge and the Compton-edge of the photon. In return, the detection efficiency is roughly one order of magnitude better.

For the analysis, Monte Carlo simulations of all decays being considered were generated

within the VENOM framework that has been developed by J. Wilson and B. Morgan of the COBRA groups in Sussex and Warwick based on GEANT 4 code. Then, the simulated events were randomly distributed to all runs and smeared in energy according to the appropriate energy resolution of the particular detectors during that run. In case of a detector not being switched on during that run, e.g. because of noise or HV failure, any energy depositions in the respective detectors were discarded to mimic the behaviour of the real array.

Subsequently, searches for two lines or a line and a Compton event were conducted on both collected and simulated data. A region of  $\pm 1\Delta E$ <sup>1</sup> was chosen around the line energies which encloses more than 96 percent of all line events. For the Compton area, events between  $E_{\text{lower edge}} + 1\Delta E$  and  $E_{\text{upper edge}} + 1\Delta E$  were counted. Due to the background considerations mentioned above, the lower edge was normally chosen to be 511 keV while the upper edge was selected to be the photopeak energy to also include all photopeak events.

The search on the simulated data yielded the effective detection efficiency of a certain decay signal as the fraction of detected coincidences with respect to the number of simulated decays. Together with the number of coincidences found in the collected data, a half-life limit can be deduced with

$$t_{1/2} \geq \frac{N_{\text{nuclei}} \cdot t_{\text{measurement}} \cdot \ln 2 \cdot \epsilon}{N_{\text{observed}}} \quad (7.1.1)$$

where  $N_{\text{nuclei}}$  denotes the number of nuclei of the isotope under investigation contained in all detectors,  $t_{\text{measurement}}$  the total duration of the data gathering and  $\epsilon$  the effective detection efficiency for that particular decay and search channel. Here, also the different individual live times of the different detectors are taken into account.  $N_{\text{observed}}$  refers to the number of observed candidate events. To find a conservative measure for the half-life limit on the investigated decays, all coincidences remaining after the cuts are counted as candidate events and no expected background is subtracted as this would require a more detailed simulation of the physical Rn background as well as of the electronic/discharge background which is still being investigated at the time of writing.

## 7.2 Decays Selected for Analysis

As discussed above, neutrinoless decays into excited states are the most promising candidates to first apply the coincidence analysis method to. However, of all excited states present in daughter nuclei, only those with an angular momentum  $J$  and a parity  $\pi$  (usually written  $J^\pi$ ) of  $0^+$  or  $2^+$  are of interest: The selection rules of the mass-driven standard neutrinoless double beta decay mechanism demand a  $0^+$  state while the  $2^+$  state can be reached by alternative mechanisms that could contribute to  $0\nu\beta\beta$  decay like right-handed weak currents. In addition, the kinetic energy of the decay electrons and the gamma energy of the excited state should be large enough to avoid the noise edge and regions of elevated background. After some tests, it was decided to only include decays with signatures above 511 keV as below this value too many background events were found probably stemming from the decay of  $^{113}\text{Cd}$ , from annihilation photons of  $\beta^+$ -background decays and from (partial) crosstalk of micro-discharges. At higher

<sup>1</sup>The energy resolution  $\Delta E$  of a detector is measured as full-width-at-half-maximum FWHM ( $1\Delta E = 2.35\sigma$  for the Gaussian approximation), interpolated for all detectors from calibration spectra. The value can be given in keV or per-cent for a reference energy. In most cases, the 662 keV line from  $^{137}\text{Cs}$  is chosen.

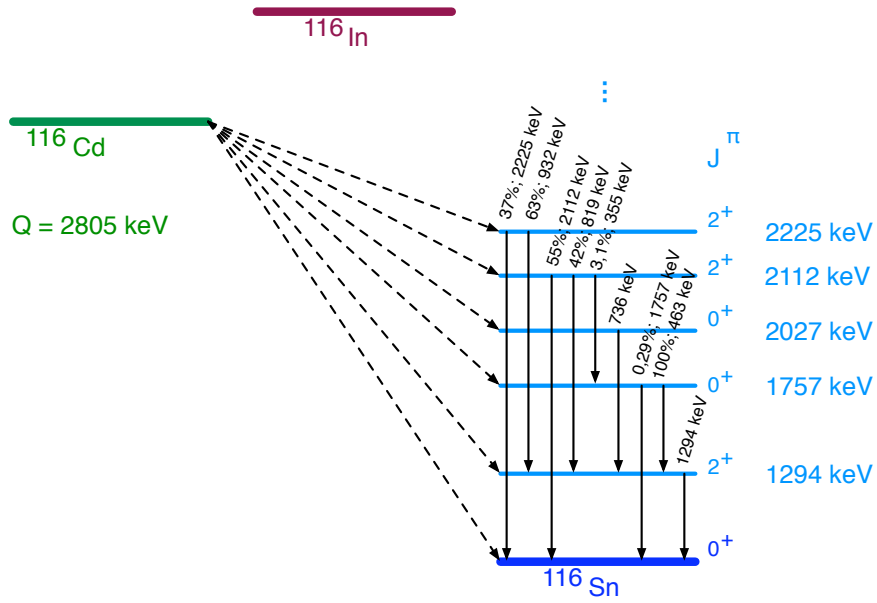


Figure 7.2: Level scheme of  $^{116}\text{Cd}$ .

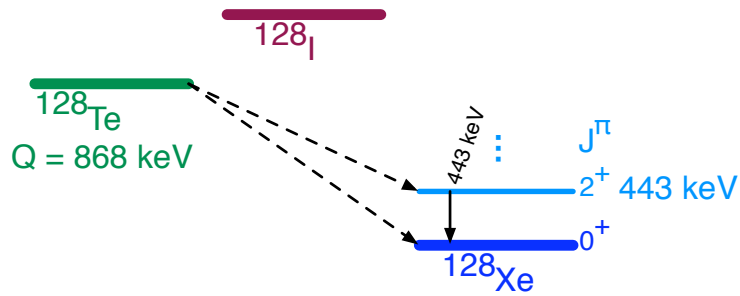


Figure 7.3: Level scheme of  $^{128}\text{Te}$ .

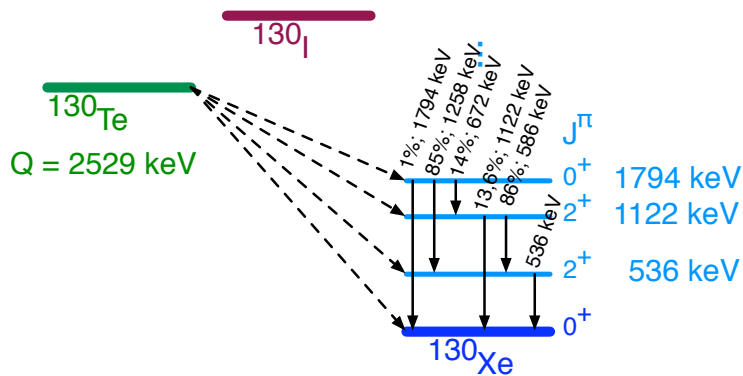


Figure 7.4: Level scheme of  $^{130}\text{Te}$ .

energies there is much less background and therefore less likelihood for accidental or crosstalk coincidences.

Of the nine double-beta isotopes contained in CdZnTe,  $^{64}\text{Zn}$ ,  $^{70}\text{Zn}$ ,  $^{108}\text{Cd}$  and  $^{114}\text{Cd}$  cannot decay into excited states because the daughter nuclei have no energy levels below the Q-value. In  $^{120}\text{Te}$ , only a EC/EC-decay could kinematically populate the  $2^+$ -state at 1171 keV which wouldn't yield a good enough signature in the source crystal with current electronics and background.  $^{106}\text{Cd}$  only has a small natural abundance of 1.25 percent resulting in a half-life limit at least one order of magnitude worse than other CdZnTe isotopes. Besides, deexcitation of the first excited daughter state at 512 keV is experimentally indistinguishable from annihilation radiation.

This leaves  $^{116}\text{Cd}$ ,  $^{128}\text{Te}$  and  $^{130}\text{Te}$  with natural abundances of 7.47, 31.7 and 33.8 percent, respectively. The number of source nuclei is calculated by

$$N_{\text{isotope}} = \frac{m_{\text{crystal}}}{\langle M_{\text{CdZnTe}} \rangle} \cdot s \cdot a_{\text{isotope}} \quad (7.2.2)$$

where  $m$  is the source mass of the crystals under study,  $\langle M_{\text{CdZnTe}} \rangle = 234.5\text{g/mol}$  is the molar mass of  $\text{Cd}_{0.9}\text{Zn}_{0.1}\text{Te}$ ,  $s$  is the stoichiometric factor (0.9 for Cd and 1 for Te) and  $a$  is the natural abundance of the isotope. All decays are  $0\nu\beta^-\beta^-$ -decays which do not generate positrons and hence possess a non-reduced phase space. Table 7.1 and the figures 7.2 to 7.4 give an overview of all relevant daughter nuclei's  $0^+$  and  $2^+$  states of the three isotopes under study. Decays to the 536 keV level of  $^{130}\text{Te}$  are being investigated at the University of Sussex within the context of a Master's thesis. It should be noted that the phase spaces of the decays into excited states are reduced with respect to the ground state transitions by the excited level's energy.

Isotope	Q-Value[keV]	$N_{\text{nuclei}}$	level energy [keV]	$J^\pi$
$^{116}\text{Cd}$	2805	$1.792 \cdot 10^{22}$	1294	$2^+$
			1757	$0^+$
			2027	$0^+$
			2112	$2^+$
			2225	$2^+$
$^{128}\text{Te}$	867	$8.424 \cdot 10^{22}$	443	$2^+$
$^{130}\text{Te}$	2529	$8.985 \cdot 10^{22}$	536	$2^+$
			1122	$2^+$
			1794	$0^+$

**Table 7.1:** Decays into excited  $0^+$  and  $2^+$  states of the three isotopes under study. The  $^{130}\text{Te}$ -decay to 536 keV is being investigated at the University of Sussex within the context of a Master's thesis so it was not examined here. The number of nuclei per isotope for the 16-detector layer was calculated from the experimentally measured masses assuming natural abundances.

### 7.3 Monte Carlo

As described above, a Monte Carlo simulation of the signal is extremely important to acquire the effective detection efficiency. H. Kiel first developed a Monte Carlo framework for COBRA

called POISON [Kie04] based on GEANT 4 which is described in [Kie05]. This framework was later re-designed using an object-oriented approach by J. Wilson and B. Morgan; it has been released as VENOM [Wil05a]. The VENOM-generated data sets as well as the experimental data sets are arranged in data containers provided by the ROOT<sup>2</sup> framework. Data analysis and plotting of both data sets are implemented by means of so-called ROOT-scripts which are small, interpreted C++ programs that make use of the ROOT classes and methods.

An important part of all elementary particle Monte Carlo codes is the particle generator. VENOM utilises mainly two independent ones, KielGen[Kie05] from POISON and DECAY0 [Pon00]. The latter one implements most decay chains and all relevant double-beta decays and was used to generate the initial decays into excited states. VENOM then manages geometry and particle transport and records the energy depositions within the crystal volumes. For all decays, at least  $10^6$  decays were simulated to achieve reasonable statistical accuracy (few percent relative uncertainty for most channels).

The decays were then virtually distributed over all 1816 runs. For each event, a check was made on whether the detector volumes in which the energies were deposited were active; if not, the energy deposition was discarded. Thereby, it was taken into account that some detectors were inactive during the whole data gathering and some only for some time. Moreover, the energy depositions were smeared with the experimentally deduced energy resolution values of the individual detectors during the respective run. This was implemented by using random numbers following Gaussian distributions with detector- and run-dependent appropriate widths. After this convolution process, a signal-only set of data was obtained which takes into account the finite experimental energy resolution as well as the live time of the different detectors.

This data set was now searched for events matching the pre-defined cuts developed above. By comparing the number of events matching the demanded signature with the total number of simulated events, the effective detection efficiency could be deduced.

## 7.4 Experimental Data

The experimental data set was scanned with the same cuts as the Monte Carlo one. During the first tests it became apparent that below 511 keV mostly too many coincidences were found to comply with the expectations for the background. These excess events were partly attributed to physical background, e.g. to the fairly frequent decays of  $^{113}\text{Cd}$  below 320 keV, to Rn and its progenies, to decays within the red passivation paint and to 511 keV annihilation photons which have a comparably high flux. In addition, crosstalk mainly from micro-discharge events was suspected to contribute a significant amount of events. Especially concerning the latter, more research is required.

The experimental signature of most excited levels under study is a cascade of gammas as direct transitions from  $0^+$  to  $0^+$  levels are forbidden by selection rules. Hence, the nucleus must use a cascade with an intermediate  $2^+$  level in the course of its deexcitation (see Figs. 7.2 to 7.4). Nevertheless, the decay signature in the source crystal is normally the same as all gammas are expected to leave the primary crystal. The probability to detect more than one of the cascade photons is negligible with the current 16-detector layer. In the whole data set, no

---

<sup>2</sup>ROOT is an object-oriented programming framework developed at CERN. Its classes provide tools and methods for data handling, analysis and plotting. More information can be found on the project's website <http://root.cern.ch>



Isotope	level [keV]	line [keV]	$\beta\beta$ line [keV]	# of counts	upper limit to # of counts (90% C.L.)	efficiency $\epsilon$ [%]
$^{116}\text{Cd}$	1294	1294	1511	0	2.44	0.13
	1757	463	1048	8	13.99	0.68
		1294	1048	0	2.44	0.13
		1757	1048	0	2.44	0.002
		734	778	3	7.42	0.53
	2027	1294	778	1	4.36	0.13
		2027	778	0	2.44	0.003
		818	693	4	8.60	0.19
	2112	1294	693	0	2.44	0.11
		2112	693	0	2.44	0.041
		932	580	7	12.53	0.24
	2225	1294	580	0	2.44	0.11
		2225	580	1	4.36	0.029
$^{128}\text{Te}$	443	443	425	11	17.60	1.47
$^{130}\text{Te}$	1122	536	1407	4	8.60	0.51
	1794	536	735	7	12.53	0.57
		1258	735	0	2.44	0.12

**Table 7.2:** Experimental results of the two-line searches. 'level' denotes which excited level's decay is being investigated, 'line' represents the photon energy that has been looked for in coincidence with the ' $\beta\beta$  line' energy of the respective decay which is the sum energy deposited in the crystal by the two  $\beta$ -electrons. The number of counts is an absolute number. The upper limit to the number of counts represents the the upper limit at 90% C.L. .The effective detection efficiency has been extracted from the Monte Carlo data set and is given in percent of detected events with respect to all decays into the excited state. The uncertainty of  $\epsilon$  is dominated by statistics and ranges from 0.7 % ( $^{128}\text{Te}$  to 443 keV, 1.47 % efficiency) to 22 % ( $^{116}\text{Cd}$  to 1757 keV, 0.002 % efficiency).

Isotope	level [keV]	lower edge [keV]	$\beta\beta$ line [keV]	# of counts	u.l. to # of counts (90% C.L.)	efficiency $\epsilon$ [%]
$^{116}\text{Cd}$	1294	511	1511	2	5.91	0.683
	1757	511	1048	13	$\approx 20$	0.765
	2027	511	778	20	$\approx 29$	1.300
	2112	511	693	35	$\approx 47$	1.028
	2225	511	580	57	$\approx 72$	1.253
$^{128}\text{Te}$	energy too low for satisfactory results.					
$^{130}\text{Te}$	1122	350	1407	14	$\approx 21$	0.936
	1794	350	735	31	$\approx 42$	1.416

**Table 7.3:** Experimental results of the line-Compton searches. The level-energy always was chosen as the upper analysis limit while the lower limit is shown in column 3. The energies within the  $^{128}\text{Te}$  decay are too low for the current background to yield satisfactory results. Besides, the photoeffect cross section for photons of 443 keV is still quite high so the efficiency of the two-line search is comparable with the efficiencies of the other line-Compton searches already. For large event numbers, the upper limits were rounded off for convenience as they were conservatively overestimated already.

3-fold line coincidence has been found matching the cuts but the drop in efficiency for this type of signature is severe in a single layer yielding non-competitive results at the moment. This will change, however, with the 64-detector 3-D array.

To conduct the searches on both data sets, individual ROOT-scripts have been written to search for two-line and line-Compton events in both simulation and experimental data sets. When the analysis was conducted, the data formats of simulation and experimental data differed; a conversion of the simulated data set into the form of the experimental data set would have been a bigger effort than to maintain two slightly differing analysis scripts. Table 7.2 contains the results of all conducted two-line searches whereas table 7.3 outlines the results of the line-Compton searches. Although the line-Compton searches are characterised by higher efficiencies, they experimentally suffer from the background components discussed above resulting in rather large numbers of candidate events. Furthermore, it can be seen that the probability to find the level's energy deposited by photons in a single neighbouring crystal is always quite low due to the cascading described above.

At the time of writing, a reliable and tested simulation of the Rn contribution to the physical background and a simulation of the discharge-related background were not available. Most conservatively, no background events are therefore subtracted. The observed event numbers are taken for candidate events and their number is increased according to [Yao06] to achieve an upper limit at 90% confidence level (C. L.). For low event numbers, tabulated data from [Yao06, Tab. 32.4] is used; for event counts larger than 10,

$$n_{\text{upper limit}} = n_{\text{observed}} + 2 \cdot \sqrt{n_{\text{observed}}} \quad (7.4.3)$$

is applied conservatively overestimating the necessary poissonian limit. Using equation 7.1.1, the upper limits for candidate events are converted into half-life limits employing the appropriate effective detection efficiencies. Typically, the obtained half-lives from the up to three

two-line searches for different signatures of the same decay into an excited state yielded one signature surpassing the others by far. In this situation, a joint limit of different signatures is showing almost no improvement. Therefore, the limit of the best signature channel is quoted. The combination of two-line and line-Compton results is difficult for statistical reasons as they are overlapping searches: The latter always contain the events of the two-line searches. Therefore, half-life limits are given for both, two-line and line-Compton searches.

## 7.5 Results

The results of the conversion are given in table 7.4 together with previously published COBRA limits and the current world limits. Except for the  $^{116}\text{Cd} \rightarrow 1294 \text{ keV } (2^+)$  decay, the two-line searches always yield similar or better half-life limits. This can be explained by the fact that currently the number of background events rises fairly steeply at lower ( $< 1 \text{ MeV}$ ) energies while the efficiency is only improved by a factor 2–3. All values are of the same order of magnitude as earlier standard analyses of COBRA data. Some surpass previously published COBRA limits.

Decay	$t_{1/2}$ [years]			
	two-lines	line-compton	COBRA	World's Best
$^{116}\text{Cd} \rightarrow 1294 \text{ keV } (2^+)$	$1.4 \cdot 10^{18}$	$3.0 \cdot 10^{18}$	$4.92 \cdot 10^{18}$ [Blo07a]	$2.9 \cdot 10^{22}$ [Dan03]
$^{116}\text{Cd} \rightarrow 1757 \text{ keV } (0^+)$	$1.4 \cdot 10^{18}$	$9.8 \cdot 10^{17}$	$9.13 \cdot 10^{18}$ [Blo07a]	$1.4 \cdot 10^{22}$ [Dan03]
$^{116}\text{Cd} \rightarrow 2027 \text{ keV } (0^+)$	$1.8 \cdot 10^{18}$	$1.2 \cdot 10^{18}$	$1.37 \cdot 10^{19}$ [Blo07a]	$2.1 \cdot 10^{21}$ [Pie94]
$^{116}\text{Cd} \rightarrow 2112 \text{ keV } (2^+)$	$1.1 \cdot 10^{18}$	$5.6 \cdot 10^{17}$	$1.08 \cdot 10^{19}$ [Blo07a]	$6.0 \cdot 10^{21}$ [Dan03]
$^{116}\text{Cd} \rightarrow 2225 \text{ keV } (2^+)$	$1.2 \cdot 10^{18}$	$4.5 \cdot 10^{17}$	$9.46 \cdot 10^{18}$ [Blo07a]	$1.0 \cdot 10^{20}$ [Bar90]
$^{128}\text{Te} \rightarrow 443 \text{ keV } (2^+)$	$1.6 \cdot 10^{19}$	—	$1.0 \cdot 10^{18}$ [Kie03]	$4.7 \cdot 10^{21}$ [Bel87]
$^{130}\text{Te} \rightarrow 1122 \text{ keV } (2^+)$	$7.7 \cdot 10^{18}$	$5.7 \cdot 10^{18}$	$1.4 \cdot 10^{19}$ [Kie03]	$2.7 \cdot 10^{21}$ [Bar01]
$^{130}\text{Te} \rightarrow 1794 \text{ keV } (0^+)$	$6.4 \cdot 10^{18}$	$4.3 \cdot 10^{18}$	$3.1 \cdot 10^{18}$ [Kie03]	$2.3 \cdot 10^{21}$ [Bar01]

**Table 7.4:** Half-life limits deduced with equation 7.1.1 at 90% C.L. compared to earlier COBRA papers and to the currently best published limits.

## 7.6 Evaluation of Method and Results

This work is the first publication that contains an analysis of data collected with the first 16-detector layer of the 64-detector array. A standard analysis did not yield any improved half-life limits due to similar statistics and background levels compared to earlier publications. Therefore, a new coincidence analysis method suited for arrays of detectors was applied to the collected 4.2 kg·d of data. It could be shown that even with the rather bad solid-angle coverage of a 2-D array and taking into account that 4–6 detectors were offline during different phases of the data collection, half-life limits comparable to COBRA's standard analysis methods [Wil05b, Blo07a, Kie05] could be reached. For one of the explored decays, the method yielded the best half-life limits extracted from COBRA data so far. No new world's best limits could be set; however, COBRA's world leadership was up to now limited to some  $\beta^+$ /EC-decays which

were not investigated in this work. In the near future, the following measures will boost the method's results by up to a few orders of magnitude allowing to probe half-lives much closer to the theoretical predictions of beyond  $10^{23}$  years:

- background simulation

The analysis presented here did not take into account Monte Carlo simulations of physical background as they can currently explain less than 10% of all the events in the analysis region. As soon as the Rn-contributions and the contents of radioactivity for the construction materials are known with better sensitivity, they will be taken into account to generate an improved background Monte Carlo data set. Subsequently, background coincidences can be subtracted before evaluating the remaining signal candidates yielding improved half-life limits.

- physical background

Currently, a new reliable pressure-based contacting scheme is being developed by O. Schulz [Sch] to be installed in October 2007 allowing the removal of the red passivation paint that acted as a stencil for the present glue-contacts. Without surface contamination, an order-of-magnitude reduction of the event rate above the endpoint of the  $^{113}\text{Cd}$  spectrum is expected which should improve the set-up's sensitivity considerably. Furthermore, in combination with the reduction of count rate achieved by  $\text{LN}_2$ -flushing to protect the detectors from Rn which could already be shown (see Fig. 4.5), a background on the order of  $10^{-2}$  counts/keV kg d in the region of the Q-value of  $^{116}\text{Cd}$  at 2.8 MeV seems to be within reach with the current setup.

- electronic background

A variety of different cables were evaluated with respect to their partial discharge behaviour by J. Dawson [Daw06]. The best candidate, RG-178, will replace the Kapton-HV-cable also in October 2007. In addition, an improved veto circuit and pulse-shape analysis methods are under consideration to reduce the rate of discharges faking coincident events even further.

- detector outages

The pressure-based contacting mentioned above should also significantly reduce outages of detectors improving the overall lifetime by up to 50%. This can be concluded from a series of contacting tests where bad needle or pressure connections could always be 'healed' by lifting and re-setting the pressure contact. While this is probably also true for glue contacts, re-working a glue contact is not easily done and also endangers neighbouring contacts so this measure has only been taken in exceptional cases.

- solid angle and effective detection efficiency

The remaining three 16-detector layers will be installed in the near future. Moreover, 64 further detectors, some of them possibly even isotopically enriched, will become available through a collaboration between the University of Dortmund and the Materialforschungszentrum Freiburg. The step from 2-D to 3-D will significantly improve the solid angle and the effective detection efficiency in addition to the larger source mass.

- improved analysis tools

The current analysis procedure will be refined to better cope with noisy and/or dirty detectors featuring an improved user interface and selection tools. Furthermore, the parameter space of the line-Compton searches can be separated from the two-line searches so the results can be combined to yield a better half-life limit.

While the coincidence analysis method has already now yielded comparable results to standard analyses given similar statistics, the above measures will ensure that even with similar statistics – which can be collected in less than a quarter of the time or roughly within two weeks – the results will improve by more than one order of magnitude. While normally decays to the ground state have the best effective detection efficiency and therefore the best sensitivity, it now appears possible that decays into excited states,  $\beta^+\beta^+$ - or  $\beta^+$ /EC-decays could reach similar sensitivities. The method has proven to be reliable, transparent and competitive.



## Chapter 8

# Summary and Outlook

The COBRA experiment is investigating neutrinoless double-beta decays of Cd, Zn and Te isotopes with an array of CdZnTe semiconductor detectors. The current development stage consists of 64 CPG-type detectors of  $1\text{ cm}^3$  size each that will be arranged in form of a three-dimensional  $4 \times 4 \times 4$ -array. At the time of writing, the first 16-detector layer was installed and has been collecting data since January 2007. The remaining three layers are currently being assembled.

Within the course of this work, key experimental components for the COBRA setup have been developed, built and tested. As CdZnTe detectors had not been used in low-background rate experiments before, a completely new radiopure detector suspension had to be designed. Several possible construction materials were evaluated and for some of them their radiopurity was assessed with ultra-low background  $\gamma$ -spectroscopy measurements using HPGe-Detectors at the LNGS. A silver-free conductive glue was developed for detector contacting. Different options for the wiring between detectors and preamplifiers were evaluated and a state-of-the-art signal wire with only  $50\mu\text{m}$  thickness was designed based on flexible polyimide PCB technology.

Concerning the necessary electronics, scalable 16-channel preamplifiers for CPG-type CdZnTe detectors were developed while minimizing the footprint per channel. In addition, reliable and cost-efficient 8-channel shapers as replacement for single-channel main amplifiers were introduced. The analogue part of COBRA's 4-channel VME-based ADC was intensively tested and enhanced.

For the operation of CdZnTe detectors in the LNGS underground laboratory, a low-background level shielding concept was developed and implemented, consisting of a copper suspension for the detector holders inside a copper shield. This was enclosed in a lead mantle housed inside of a Rn-tight Faraday cage. To suppress the neutron flux, a borated PE-based neutron shield was used. Finally, a calibration system using radioactive wire-sources inserted through Teflon tubes was designed and implemented.

Based on roughly 4.2 kg-d of data collected with the first operational 16-detector layer, a coincidence-based analysis has been performed focusing on neutrinoless double-beta decays of  $^{116}\text{Cd}$ ,  $^{128}\text{Te}$  and  $^{130}\text{Te}$  into excited states. For one of the decays, the previously published limit on the half-life could be improved as displayed below. Moreover, the power of the coincidence analysis method was demonstrated for decays involving gamma emission.

Decay	$t_{1/2}$ [years]			
	two-lines	line-compton	COBRA	World's Best
$^{116}\text{Cd} \rightarrow 1294 \text{ keV } (2^+)$	$1.4 \cdot 10^{18}$	$3.0 \cdot 10^{18}$	$4.92 \cdot 10^{18}$ [Blo07a]	$2.9 \cdot 10^{22}$ [Dan03]
$^{116}\text{Cd} \rightarrow 1757 \text{ keV } (0^+)$	$1.4 \cdot 10^{18}$	$9.8 \cdot 10^{17}$	$9.13 \cdot 10^{18}$ [Blo07a]	$1.4 \cdot 10^{22}$ [Dan03]
$^{116}\text{Cd} \rightarrow 2027 \text{ keV } (0^+)$	$1.8 \cdot 10^{18}$	$1.2 \cdot 10^{18}$	$1.37 \cdot 10^{19}$ [Blo07a]	$2.1 \cdot 10^{21}$ [Pie94]
$^{116}\text{Cd} \rightarrow 2112 \text{ keV } (2^+)$	$1.1 \cdot 10^{18}$	$5.6 \cdot 10^{17}$	$1.08 \cdot 10^{19}$ [Blo07a]	$6.0 \cdot 10^{21}$ [Dan03]
$^{116}\text{Cd} \rightarrow 2225 \text{ keV } (2^+)$	$1.2 \cdot 10^{18}$	$4.5 \cdot 10^{17}$	$9.46 \cdot 10^{18}$ [Blo07a]	$1.0 \cdot 10^{20}$ [Bar90]
$^{128}\text{Te} \rightarrow 443 \text{ keV } (2^+)$	$1.6 \cdot 10^{19}$	—	$1.0 \cdot 10^{18}$ [Kie03]	$4.7 \cdot 10^{21}$ [Bel87]
$^{130}\text{Te} \rightarrow 1122 \text{ keV } (2^+)$	$7.7 \cdot 10^{18}$	$5.7 \cdot 10^{18}$	$1.4 \cdot 10^{19}$ [Kie03]	$2.7 \cdot 10^{21}$ [Bar01]
$^{130}\text{Te} \rightarrow 1794 \text{ keV } (0^+)$	$6.4 \cdot 10^{18}$	$4.3 \cdot 10^{18}$	$3.1 \cdot 10^{18}$ [Kie03]	$2.3 \cdot 10^{21}$ [Bar01]

In the near future, the 64-detector array will be fully installed in the LNGS underground laboratory. As could be shown in this work, even if the physical background level would remain similar to the current state, significant improvements of the sensitivity with respect to COBRA's standard analyses used so far [Kie03, Kie05, Blo07a] can be expected with the coincidence-based analysis method for gamma-involving decays .



## Appendix A

# Results of Detector Characterisations

The following table contains the fitted energy resolutions of all CPG crystals forseen for the 64-detector array.

Crystal Name	FWHM@662	FWHM@2800	eV@662keV	Diff: pos is better
630332_03	22.74	73.13	18.8	-3.94
630333_01	25.81	82.89	13.7	-12.11
630333_03	28.23	95.22	14.7	-13.53
630333_05	36.26	97.17	19.3	-16.96
630334_01	25.54	70.91	16.6	-8.94
630334_03	22.64	72.17	13.7	-8.94
631101_01	26.67	86.95	18	-8.67
631101_03	30.44	104.07	18	-12.44
631101_06	28.47	98.29	17.4	-11.07
631102_01	22.18	66.39	16.1	-6.08
631102_04	24.13	76.35	14.9	-9.23
631868_01	48.1	171.28	48	-0.10
631868_03	37.43	129.37	33.5	-3.93
631868_04	38.89	94.05	43.2	4.31
631868_06	33.43	95.76	36.6	3.17
631868_07	39.06	141.34	25.3	-13.76
631869_01	41.38	140.98	39.9	-1.48
631869_04	42.73	147.39	49.6	6.87
631869_05	39.18	143.15	32.2	-6.98
631869_06	42.77	149.54	40.1	-2.67
631869_08	42	145.28	53.6	11.60
631937_02	20.8	61.41	36	15.20
631937_03	26.89	80.23	29.5	2.61
631937_05	29.46	84.99	29.6	0.14
631937_06	38.75	131.02	34.6	-4.15
631938_02	31.38	96.98	33.4	2.02
631938_04	24.87	69.59	56.3	31.43
631938_05	37.43	113.75	34.3	-3.13
631938_06	21.83	46.83	28.5	6.67
631959_01	43.42	166.11	34.8	-8.62

Crystal Name	FWHM@662	FWHM@2800	eV@662keV	Diff: pos is better
631959_02	34.96	121.69	33.5	-1.46
631959_03	32.68	103.94	41.2	8.52
631959_05	42.22	154.56	45.1	2.88
631959_06	27.96	84.35	33.8	5.84
631960_01	29.19	79.52	27.9	-1.29
631960_02	30.17	101.15	27	-3.17
631960_03	28.8	87.59	25	-3.80
631969_01	20.62	61.26	41	20.38
631969_03	21.18	65.49	43.3	22.12
631969_04	19.78	54.92	36.2	16.42
631969_05	24.71	84.45	38.5	13.79
631969_07	24.66	80.92	47.6	22.94
631969_08	22.21	67.39	38.7	16.49
631969_09	18.9	53.51	39.1	20.20
631969_10	23.03	74.35	35.2	12.17
631970_02	27.49	83.54	38.6	11.11
631971_01	27.74	89.81	37	9.26
631971_02	29.68	91.12	28.6	-1.08
631972_02	23.53	69.42	37.8	14.27
631972_03	38.61	144.84	46.1	7.49
631972_04	29.68	88.03	35.1	5.42
631972_07	23.8	59.78	52.1	28.30
631972_07_retest2	39.33	132.54	52.1	12.77
632083_01	37.2	118.01	30.2	-7.00
632083_02	42.42	144.8	41.3	-1.12
632083_04	39.82	95.37	26.8	-13.02
632879_01	34.74	116.46	46.7	11.97
632879_02	37.57	144.51	34.9	-2.67
632879_03	37.29	126.71	35.5	-1.79
633197_08	33.41	120.11	29.7	-3.71
633198_01	28.68	91.8	40.2	11.52
633198_02	32.15	101.22	40	7.85
633198_03	31.83	111.18	36.9	5.07
633198_04	36.97	140.52	37.3	0.33
633198_05	29.63	99.13	34.2	4.57
633198_06	41.17	162.84	37.1	-4.07
633198_07	58.38	235.39	44.5	-13.88

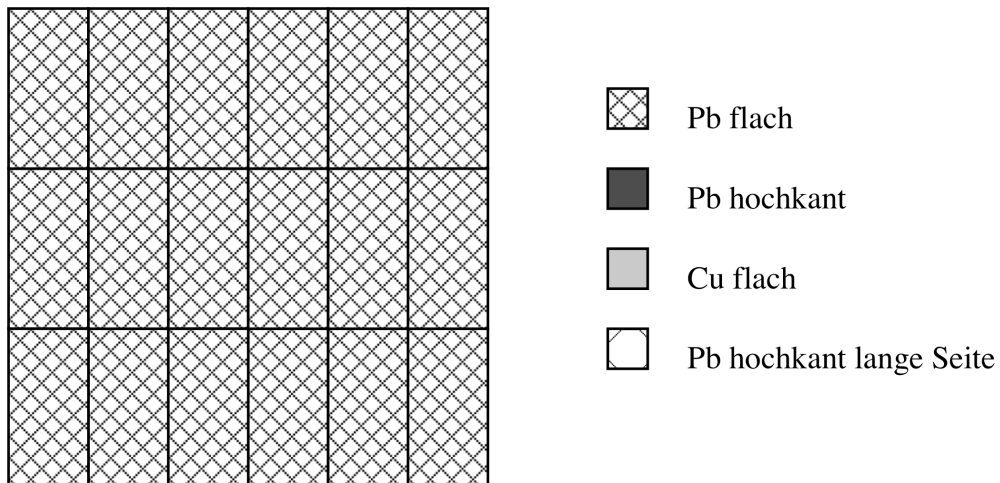
**Table A.1:** Results of the energy resolution characterisation measurements done with the Dortmund test setup compared to the value reported by the manufacturer eV Products.

## Appendix B

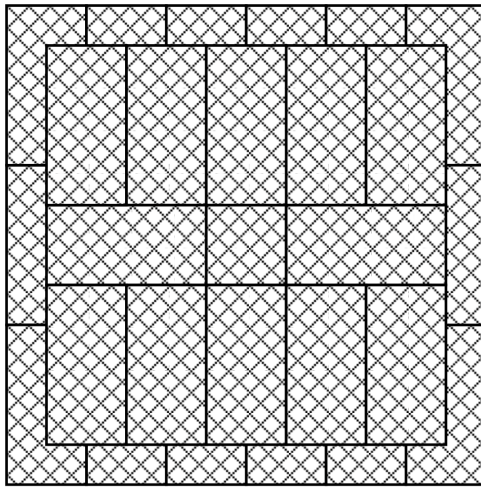
# Lead Brick Arrangement




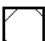
To achieve a minimum lead shield thickness of 15 cm while avoiding gaps between the bricks of more than 5 cm, the following arrangement of lead bricks was proposed (all viewed from above). If more lead is available, the arrangement can easily be modified, e.g. to add an outer layer of so-called dove tail bricks to completely avoid straight gaps between bricks.

To achieve the full 15 cm of shielding, an additional base layer of 5 cm thickness has to be installed beneath layer 1 which can possibly be substituted by a concrete base plate or similar. The language of the drawings is german, the nomenclature is 'g'(roß) for full-size bricks ( $20 \times 10 \times 5$  cm), 'm'(ittel) for medium-size bricks ( $10 \times 10 \times 5$  cm), 'hk'/'hochkant' for upright ('lange Seite' = long edge) and 'flach' for flat. The detector-brick and the calibration-brick have been replaced by the inner NEST structure.

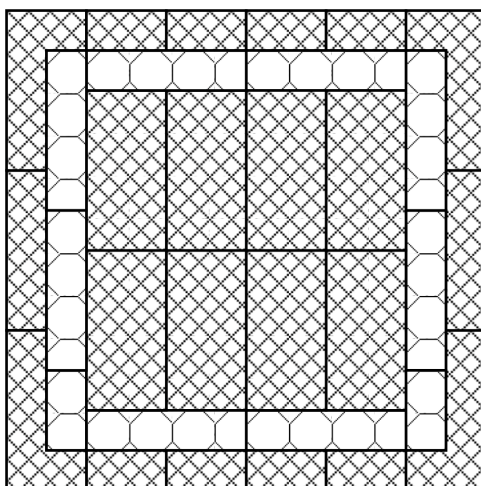






Lage 1(=50): 18 g



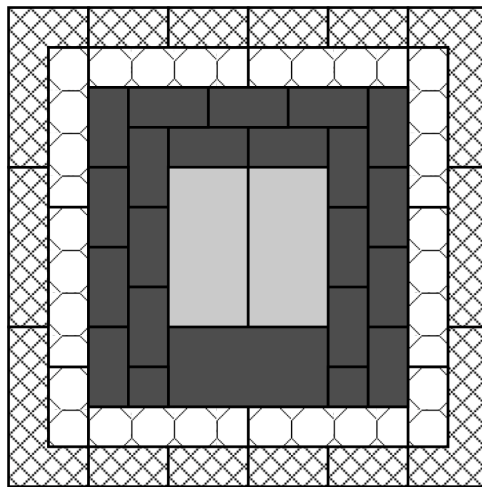
-  Pb flach
-  Pb hochkant
-  Cu flach
-  Pb hochkant lange Seite





Lage 1(=50): 18 g  
 Lage 2(=49): 12g, 1m



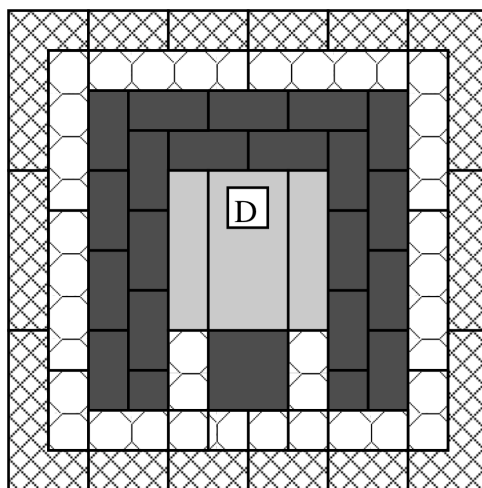
-  Pb flach
-  Pb hochkant
-  Cu flach
-  Pb hochkant lange Seite



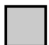
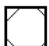
Lage 1(=50): 18 g  
 Lage 2(=49): 12g, 1m  
 Lage 3(=47): 8g flach, 8g hochkant, 2m hochkant



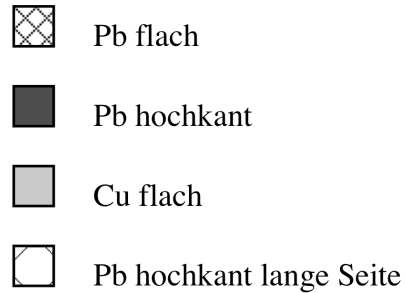
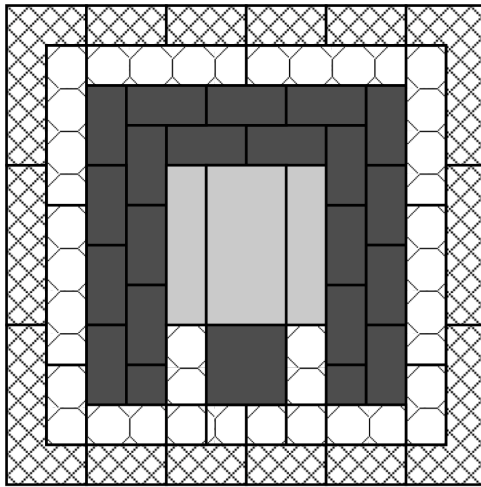
-  Pb flach
-  Pb hochkant
-  Cu flach
-  Pb hochkant lange Seite

- Lage 1(=50): 18 g
- Lage 2(=49): 12g, 1m
- Lage 3(=47): 8g flach, 8g hochkant, 2m hochkant
- Lage 4(=45): 19 g hk(kurze Seite), 1g flach, 2 Cu flach, 2 k hochkant

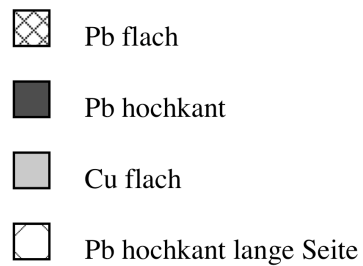
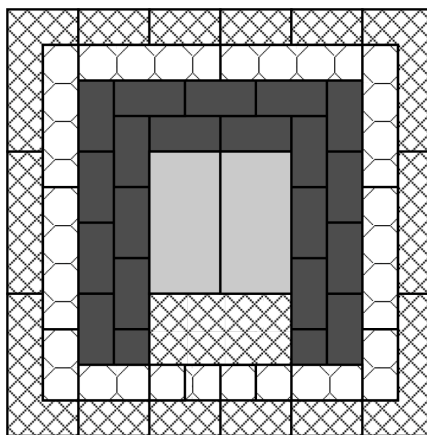


-  Pb flach
-  Pb hochkant
-  Cu flach
-  Pb hochkant lange Seite

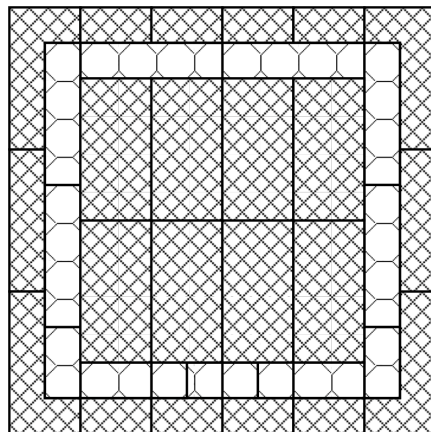
- Lage 1(=50): 18 g
- Lage 2(=49): 12g, 1m
- Lage 3(=47): 8g flach, 8g hochkant, 2m hochkant
- Lage 4(=45): 19 g hk(kurze Seite), 1g flach, 2 Cu flach, 2 k hochkant
- Lage 5(=43): 6 g hk(ls), 6m hk, 2k hk, 2 Cu hk, D-Ziegel



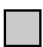
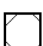


- Lage 1(=50): 18 g  
 Lage 2(=49): 12g, 1m  
 Lage 3(=47): 8g flach, 8g hochkant, 2m hochkant  
 Lage 4(=45): 19 g hk(kurze Seite), 1g flach, 2 Cu flach, 2 k hochkant  
 Lage 5(=43): 6 g hk(ls), 6m hk, 2k hk, 2 Cu hk, D-Ziegel  
 Lage 6(=41): 1 Cu (Kalib-Ziegel)



- Lage 1(=50): 18 g  
 Lage 2(=49): 12g, 1m  
 Lage 3(=47): 8g flach, 8g hochkant, 2m hochkant  
 Lage 4(=45): 19 g hk(kurze Seite), 1g flach, 2 Cu flach, 2 k hochkant  
 Lage 5(=43): 6 g hk(ls), 6m hk, 2k hk, 2 Cu hk, D-Ziegel  
 Lage 6(=41): 1 Cu (Kalib-Ziegel)  
 Lage 7(=39): 6g hk ls, 1g flach, 4m 2k, 2Cu flach



-  Pb flach
-  Pb hochkant
-  Cu flach
-  Pb hochkant lange Seite

Lage 1(=50): 18 g

Lage 2(=49): 12g, 1m

Lage 3(=47): 8g flach, 8g hochkant, 2m hochkant

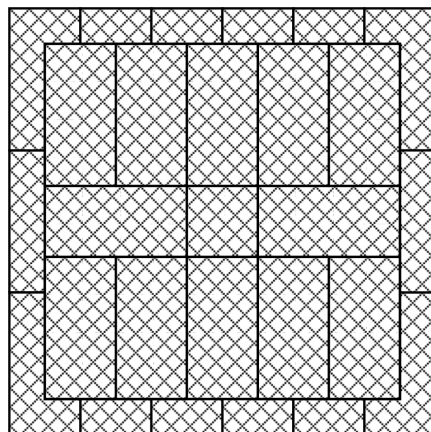
Lage 4(=45): 19 g hk(kurze Seite), 1g flach, 2 Cu flach, 2 k hochkant



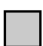
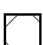
Lage 5(=43): 6 g hk(ls), 6m hk, 2k hk, 2 Cu hk, D-Ziegel

Lage 6(=41): 1 Cu (Kalib-Ziegel)

Lage 7(=39): 6g hk ls, 1g flach, 4m 2k, 2Cu flach

Lage 8(=37): 8g flach



-  Pb flach
-  Pb hochkant
-  Cu flach
-  Pb hochkant lange Seite

Lage 1(=50): 18 g

Lage 2(=49): 12g, 1m

Lage 3(=47): 8g flach, 8g hochkant, 2m hochkant

Lage 4(=45): 19 g hk(kurze Seite), 1g flach, 2 Cu flach, 2 k hochkant

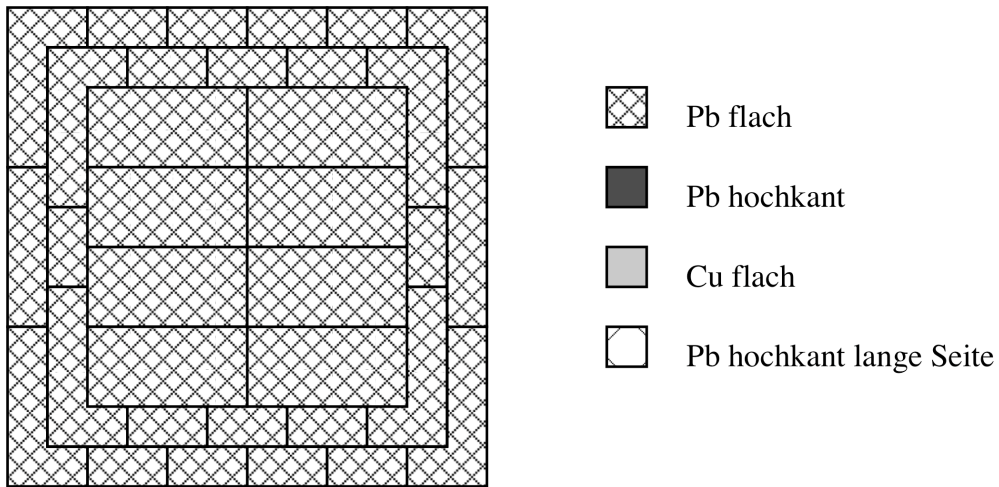
Lage 5(=43): 6 g hk(ls), 6m hk, 2k hk, 2 Cu hk, D-Ziegel

Lage 6(=41): 1 Cu (Kalib-Ziegel)

Lage 7(=39): 6g hk ls, 1g flach, 4m 2k, 2Cu flach

Lage 8(=37): 8g flach

Lage 9(=35): 12 g flach, 1 m flach



- Lage 1(=50): 18 g  
 Lage 2(=49): 12g, 1m  
 Lage 3(=47): 8g flach, 8g hochkant, 2m hochkant  
 Lage 4(=45): 19 g hk(kurze Seite), 1g flach, 2 Cu flach, 2 k hochkant  
 Lage 5(=43): 6 g hk(ls), 6m hk, 2k hk, 2 Cu hk, D-Ziegel  
 Lage 6(=41): 1 Cu (Kalib-Ziegel)  
 Lage 7(=39): 6g hk ls, 1g flach, 4m 2k, 2Cu flach  
 Lage 8(=37): 8g flach  
 Lage 9(=35): 12 g flach, 1 m flach  
 Lage 10(=33): 8 g flach

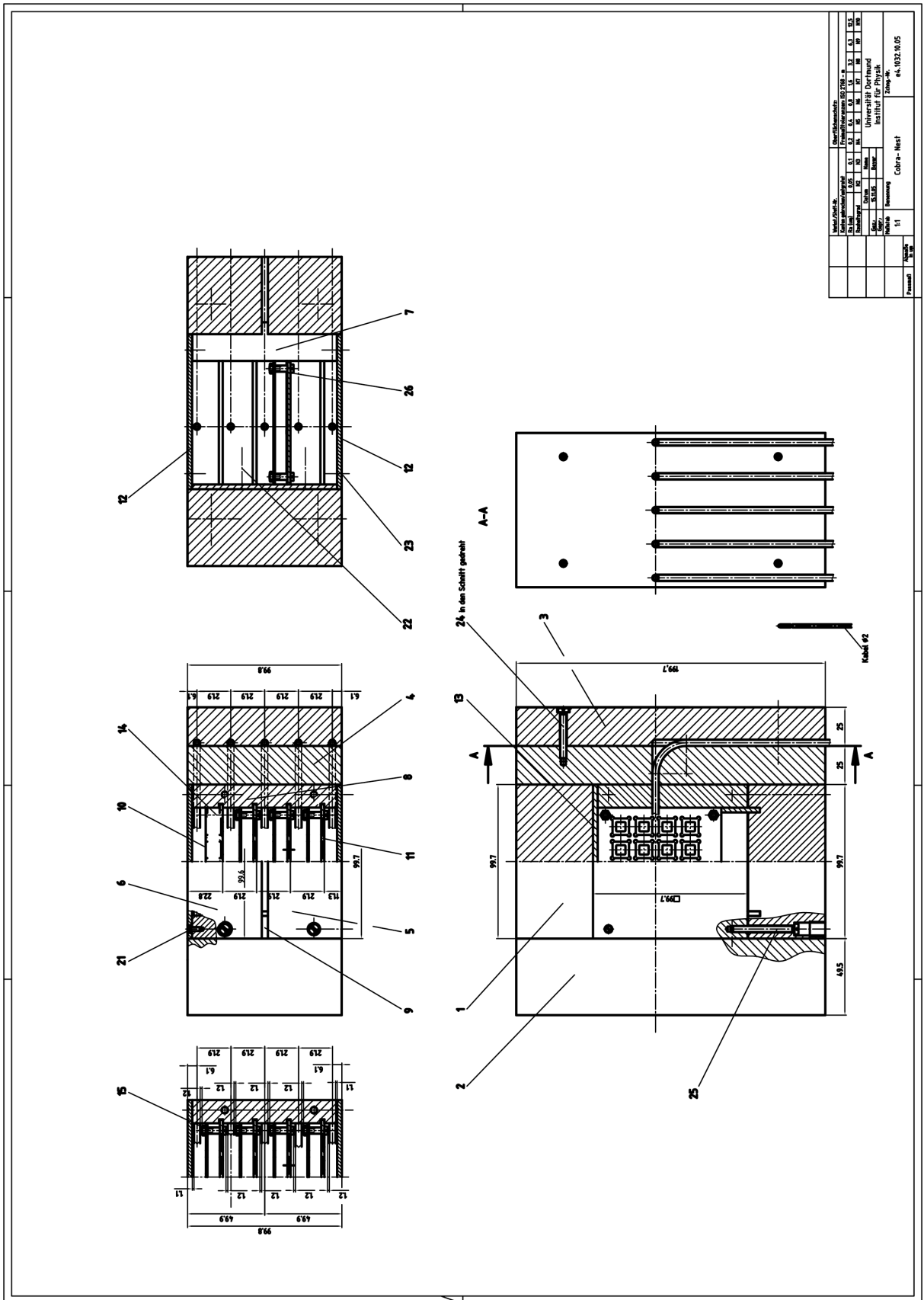


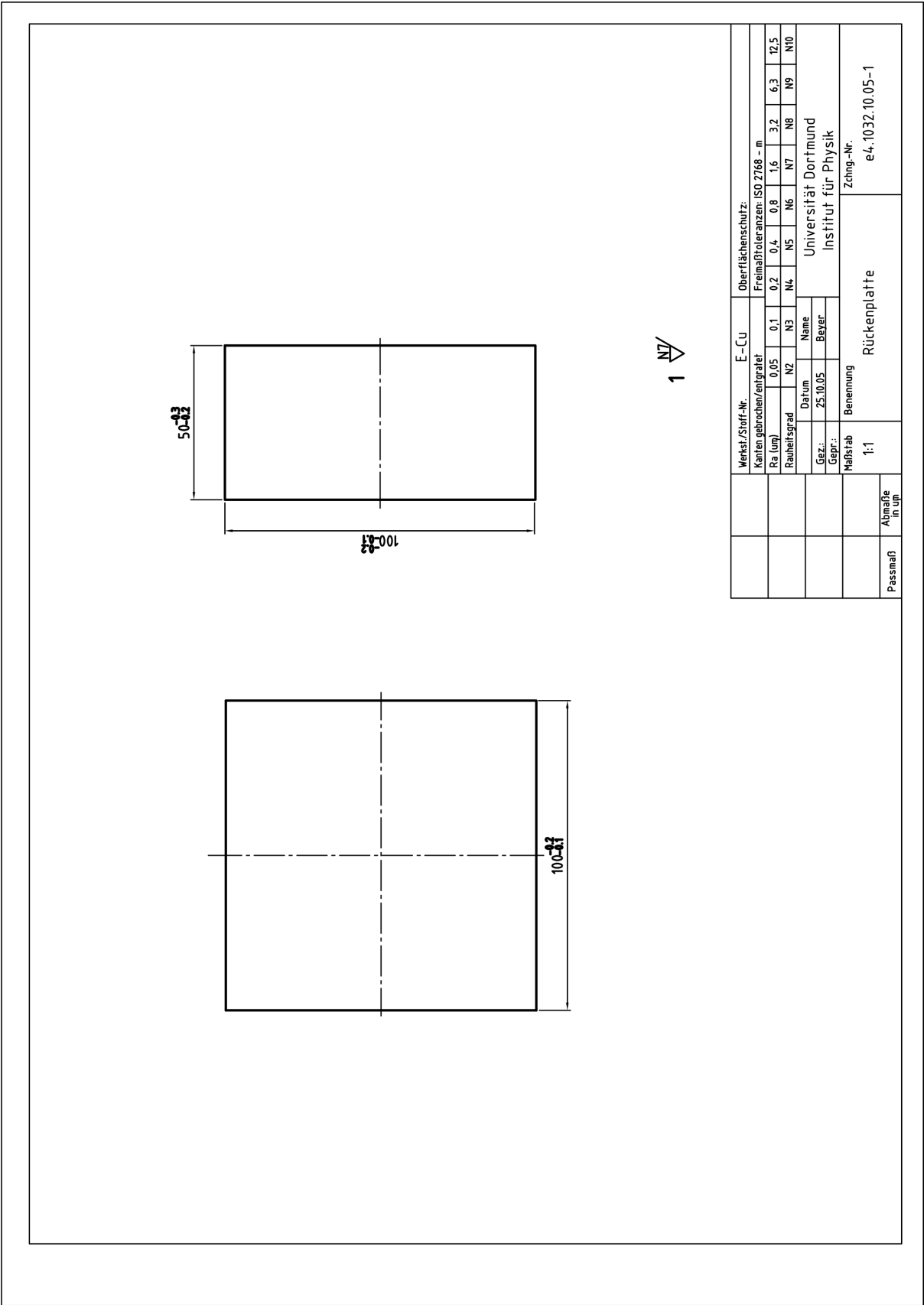
# Appendix C

## NEST-Drawings

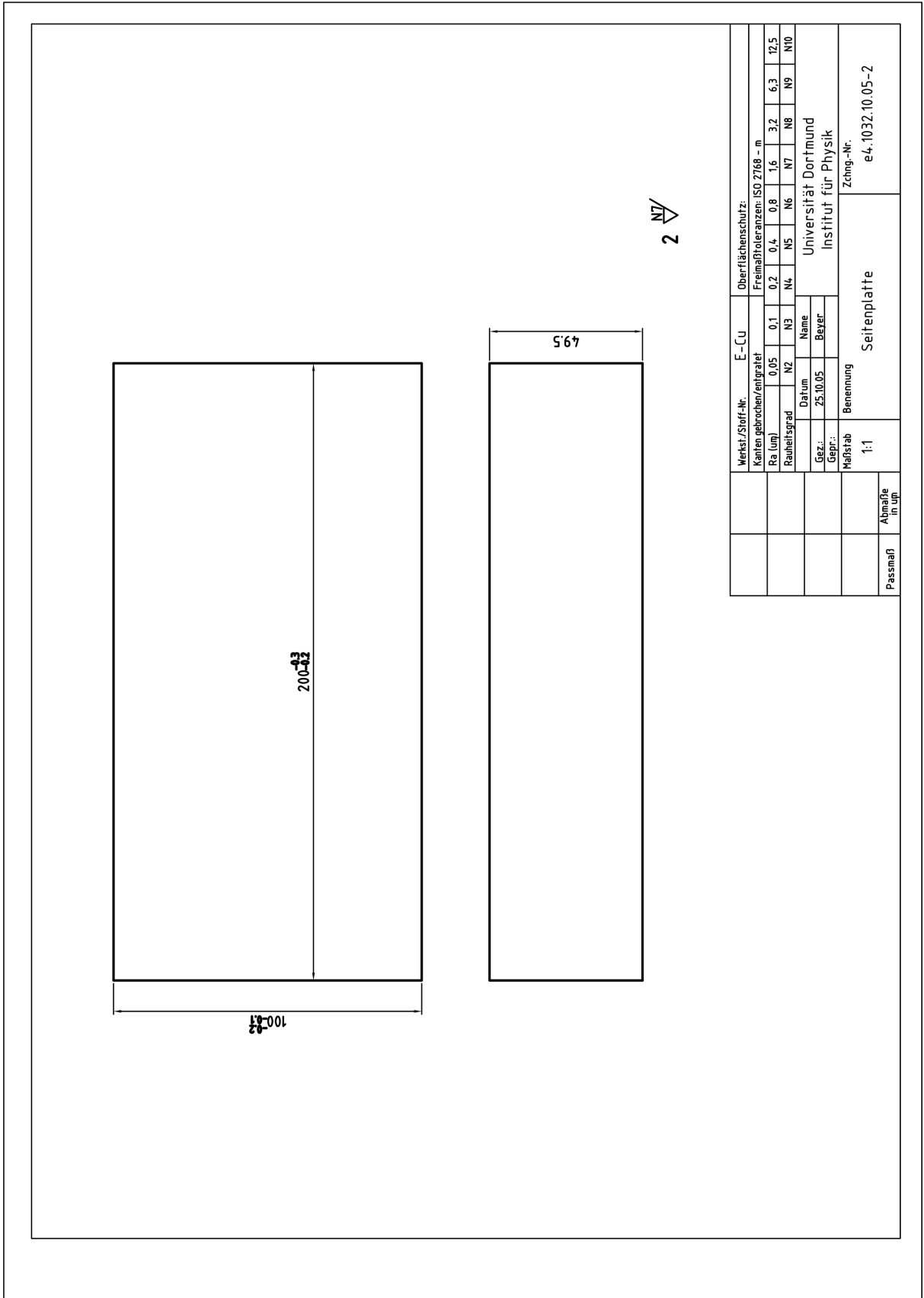
The construction drawings for the NEST are reproduced here.

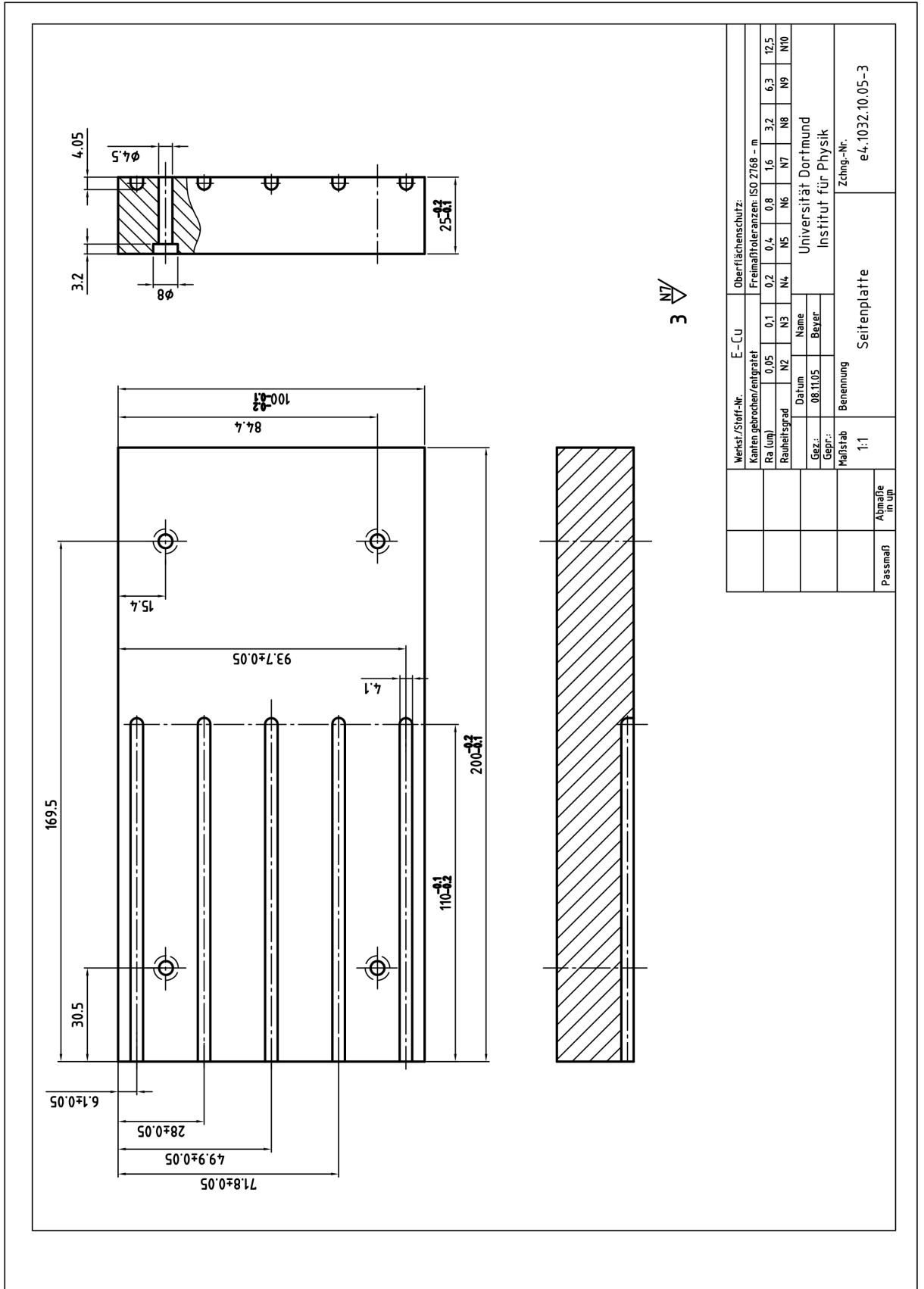
Stck.	Benennung und Fertigmaße		DIN-Nr.	Werkstoff/ Stoff-Nr/ Festigk.-Klasse	Lfd.Nr.	Zeichnungs-Nr.	Bemerkung	
1	Rückenplatte	100x50x100		E-Cu	1	e4.1032.10.05-1		
1	Seitenplatte	100x49,5x200		E-Cu	2	" - 2		
1	Seitenplatte	100x25x200		E-Cu	3	" - 3		
1	Innere Seitenplatte	100x25x200		E-Cu	4	" - 4		
1	Untere Vorderplatte	50x47,8x99,7		E-Cu	5	" - 5		
1	Obere Vorderplatte	50x48,1x99,6		E-cu	6	" - 6		
2	Führungsplatte	25x3x99,8		E-Cu	7	" - 7		
1	Rechte Aufnahmeplatte	93,7x15x97		E-Cu	8	" - 8		
1	Linke Aufnahmeplatte	93,7x15x97		E-Cu	9	" - 9		
1	Gitter	70x1x80		Delrin	10	" -10		
1	Gitter	74,2x2x80		Delrin	11	" -11		
2	Deckel	99,7x3x99,7		E-Cu	12	" -12		
1	Rückenplatte	93,7x3x99,7		E-Cu	13	" -13		
16	Schlauch	Ø4x8		Teflon	14	" -14	Schlauch im Labor e4 vorh.	
16	Zyl.-Schr.	M2,5x16	84	PA6.6natur	15	" -15		
4	Zyl.-Schr.	M2,5x6	84	PA6.6natur	21	e4.1032.10.05		
4	Zyl.-Schr.	M2,5x6	84	PA6.6natur	22	"		
4	Zyl.-Schr.	M2,5x6	84	PA6.6natur	23	"		
4	Zyl.-Schr.	M4x30	84	Nylon	24	"		
4	Zyl.-Schr.	M4x40	84	Nylon	25	"		
16	Sechskantmutter	M3	934	Nylon	26	"		
	Datum	Name	Benennung:		Stücklisten-Nr.:		Freimaßtoleranzen: DIN ISO 2768-m	Universität Dortmund Institut für Physik
geschr.:	15.11.05	Beyer	Cobra- Nest		e4.1032.10.05.st1			
gepr.:					Blatt: 1			



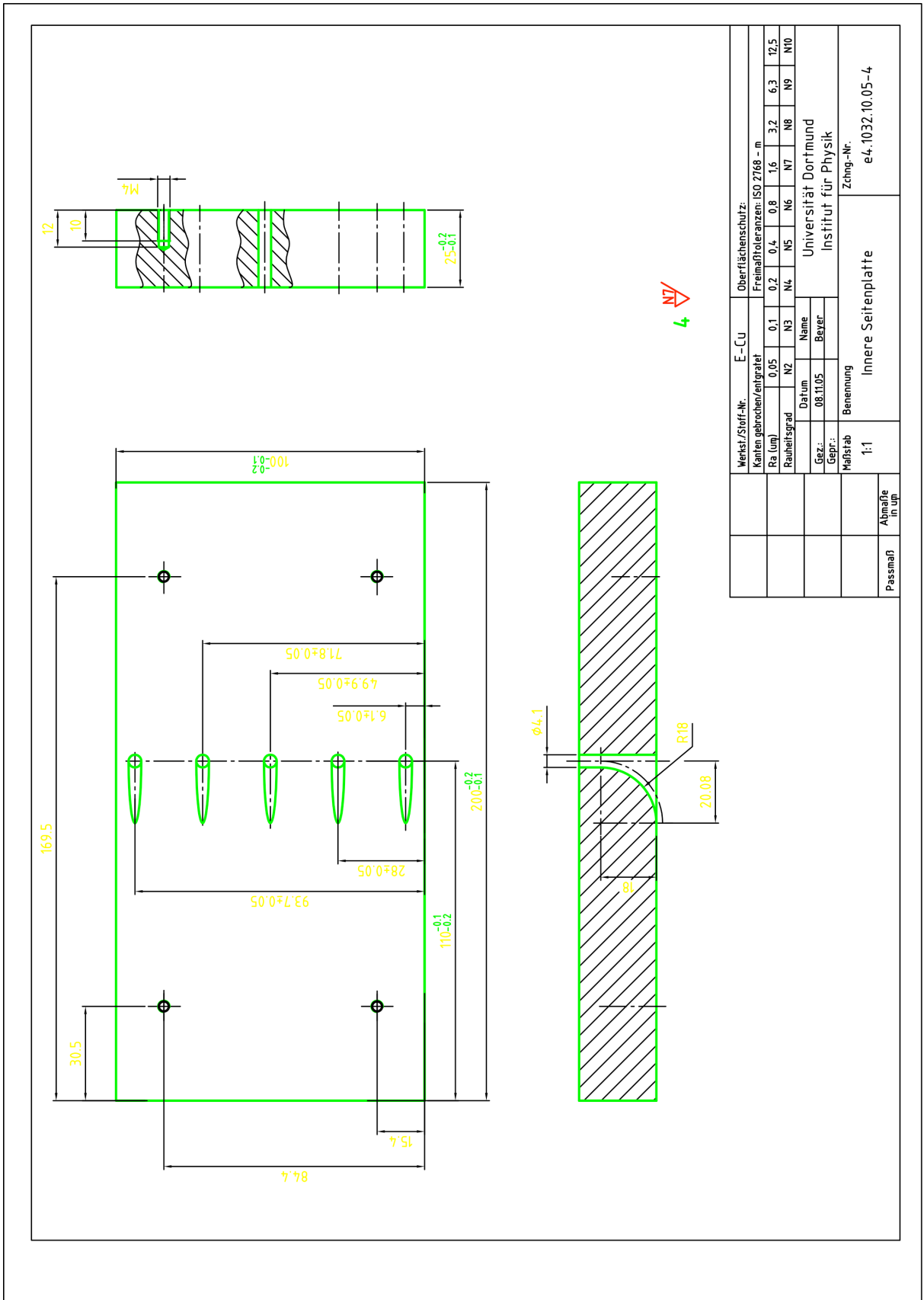


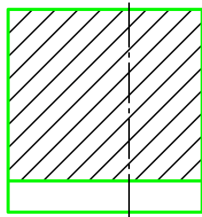
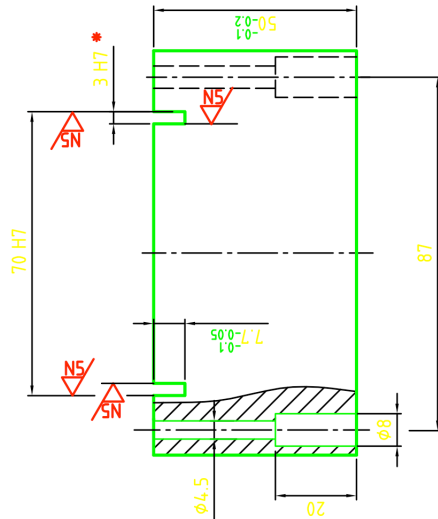
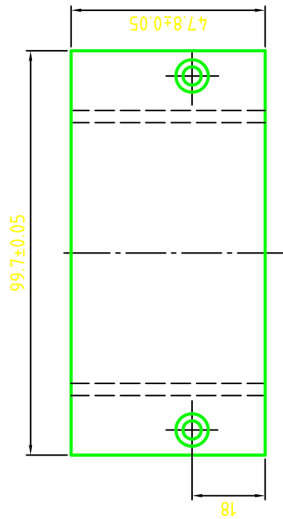
Verst./Stoff-Nr.	E-Cu	Oberflächenschutz:	
Kanten gebrochen/entgrätet		Freimaßtoleranzen: ISO 2768 - m	
Ra (µm)	0,05	0,1	0,2
Rauheitsgrad	N2	N3	N4
Datum	25.10.05	Name	Universität Dortmund
Gez.:	Beyer		Institut für Physik
Maßstab	1:1	Benennung	Rückenplatte
Passmaß	Abmaße in µm	Zchng.-Nr.	e4.1032.10.05-1





Werkst./Stoff-Nr.	E-Cu	Oberflächenschutz:	
Kanten gebrochen/entgrätet		Freimaßtoleranzen: ISO 2768 - m	
Ra (µm)	0.05	0.1	0.2
Rauheitsgrad	N2	N3	N4
Datum	08.11.05	Name	Universität Dortmund
Gepr.:	Beyer	Gepr.:	Institut für Physik
Maßstab	1:1	Benennung	Seitenplatte
Passmaß	Abmaße in µm	Zchng.-Nr.	e4.1032.10.05-3

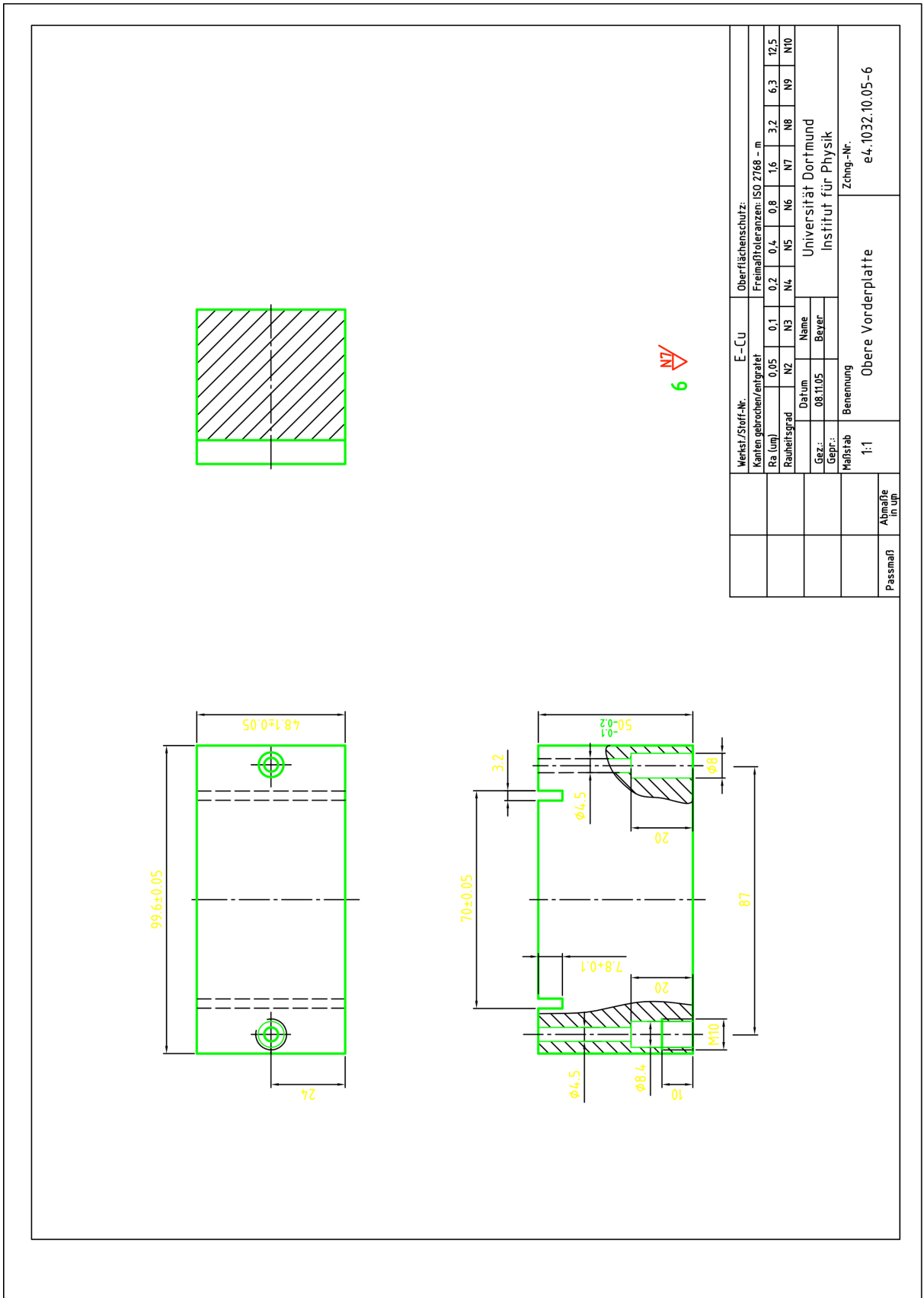




\* Pos. 7 fest eingesetzt

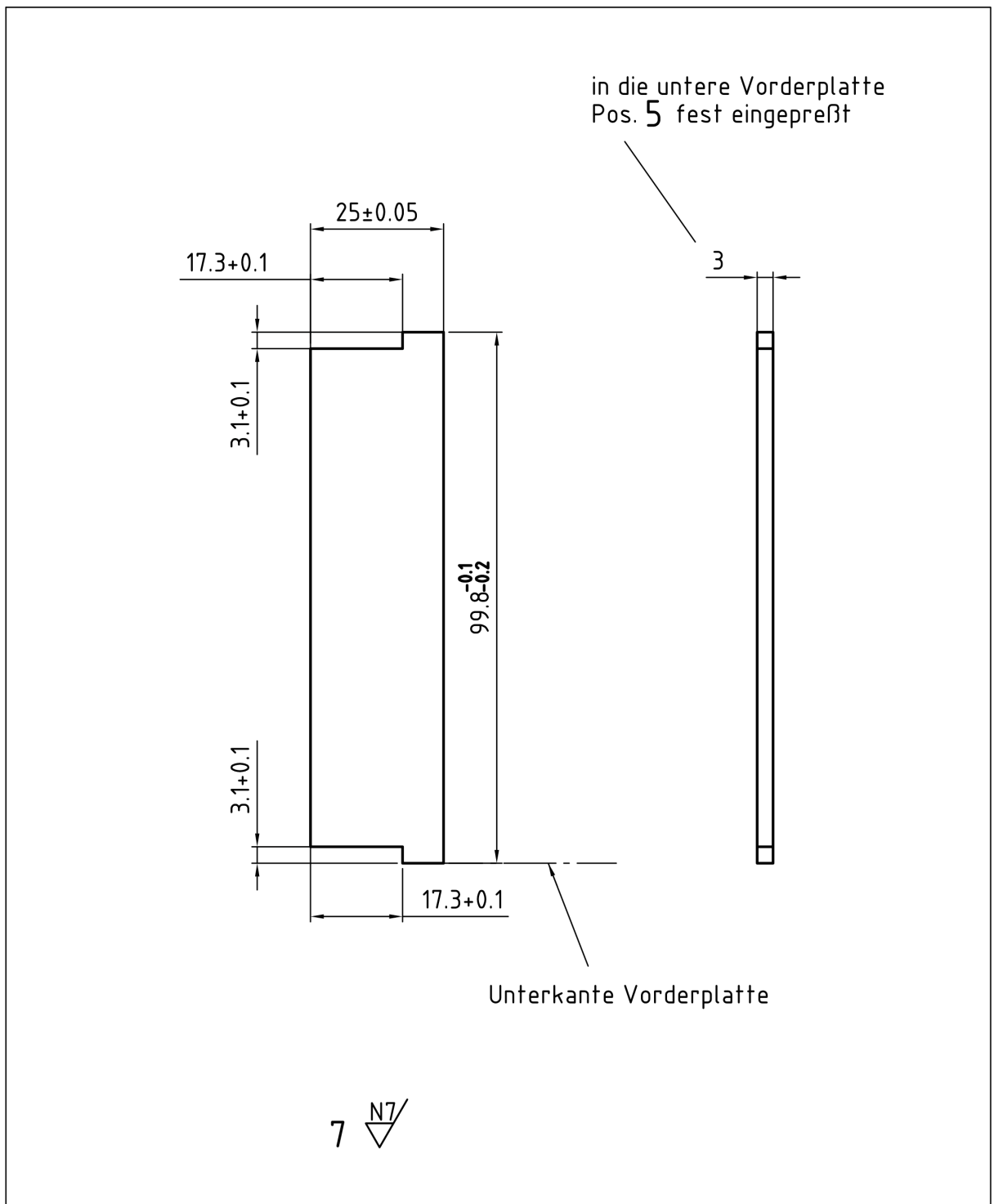
5  $\nabla$  (  $\nabla$  ) (  $\nabla$  )

Verst./Stoff-Nr.	E-Cu	Oberflächenschutz:									
Kanten gebrochen/enggrät	0,05	0,1	0,2	0,4	0,8	1,6	3,2	6,3	12,5	Freimaßtoleranzen: ISO 2768 - m	
Rauheitsgrad	N2	N3	N4	N5	N6	N7	N8	N9	N10		
Datum	08.11.05	Universität Dortmund									
Gez.:	0	Institut für Physik									
Gepr.:		Zchg.-Nr.									
Maßstab	+30	Untere Vorderplatte									
Passmaß	0	e4.1032.10.05-5									
Abmaße in µm	0										



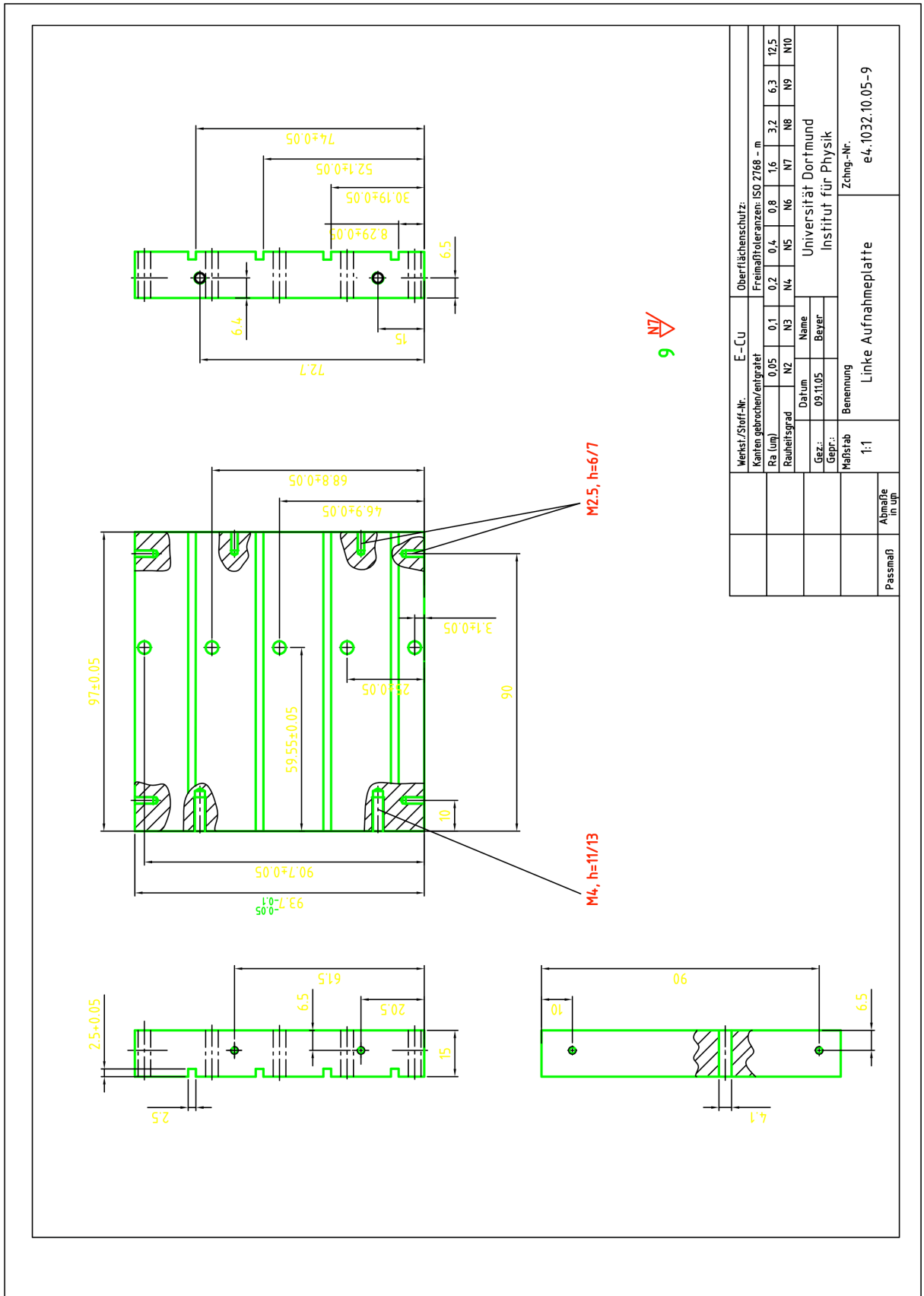
Werkst./Stoff-Nr.	E-Cu	Oberflächenschutz:									
Kanten gebrochen/entgratet	0.05	0.1	0.2	0.4	0.8	1.6	3.2	6.3	12.5	25	50
Ra (µm)	0.05	0.1	0.2	0.4	0.8	1.6	3.2	6.3	12.5	25	50
Rauheitsgrad	N2	N3	N4	N5	N6	N7	N8	N9	N10	N11	N12
Datum	08.11.05	Name: Universität Dortmund									
Gez.:	Bever	Institut für Physik									
Gepr.:		Zehng.-Nr. e4.1032.10.05-6									
Maßstab	1:1	Benennung: Obere Vorderplatte									
Passmaß	Abmaße in µm										



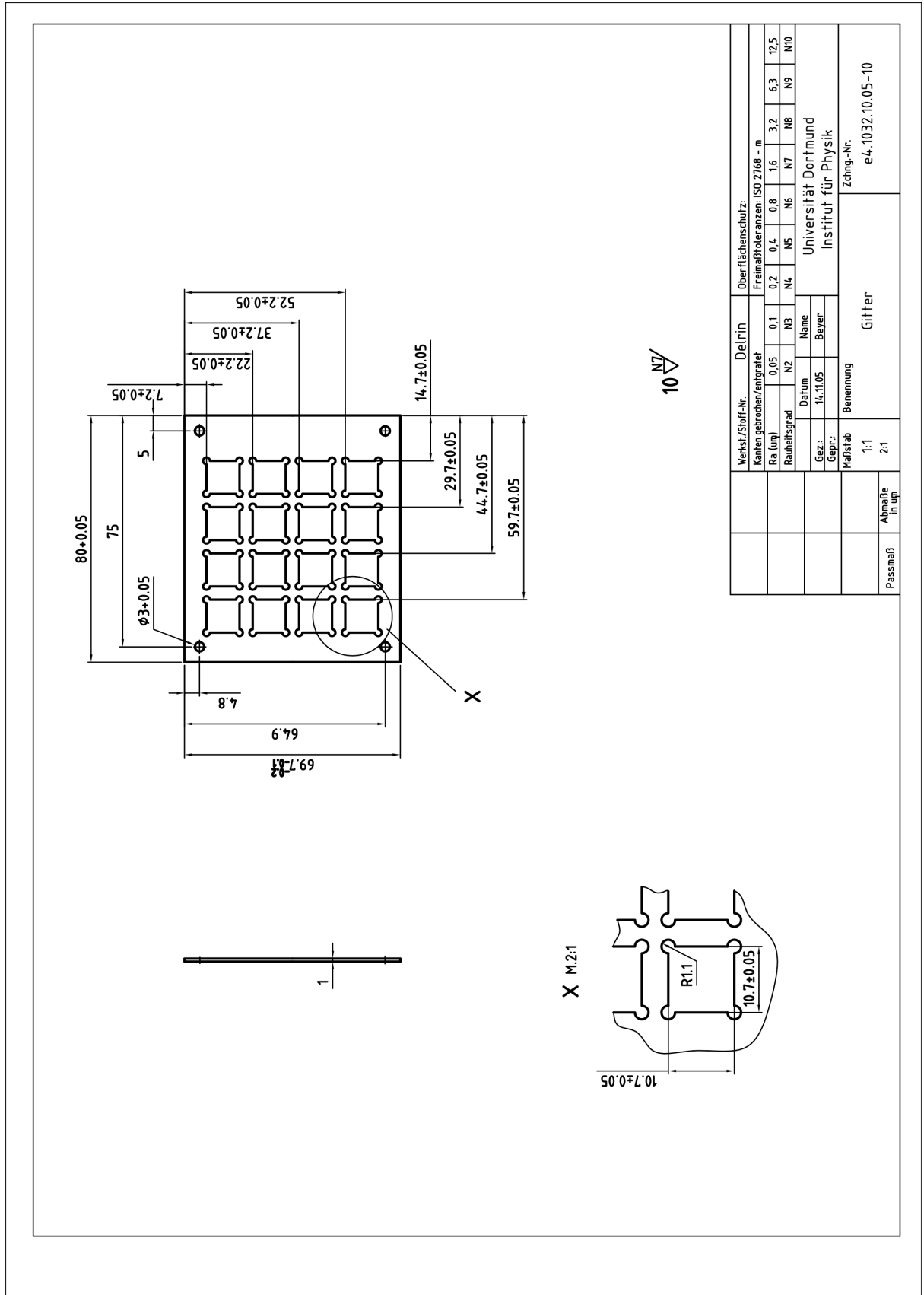


		Werkst./Stoff-Nr. E-Cu			Oberflächenschutz:							
		Kanten gebrochen/entgratet			Freimaßtoleranzen: ISO 2768 - m							
		Ra (µm)	0,05	0,1	0,2	0,4	0,8	1,6	3,2	6,3	12,5	
		Rauheitsgrad	N2	N3	N4	N5	N6	N7	N8	N9	N10	
		Datum	Name		Universität Dortmund Institut für Physik							
		Gez.:	Beyer									
		Gepr.:										
3	r6	+16 +10	Maßstab	Benennung					Zchn.-Nr.			
Passmaß	Abmaße in µm		1:1	Führungsplatte					e4.1032.10.05-7			

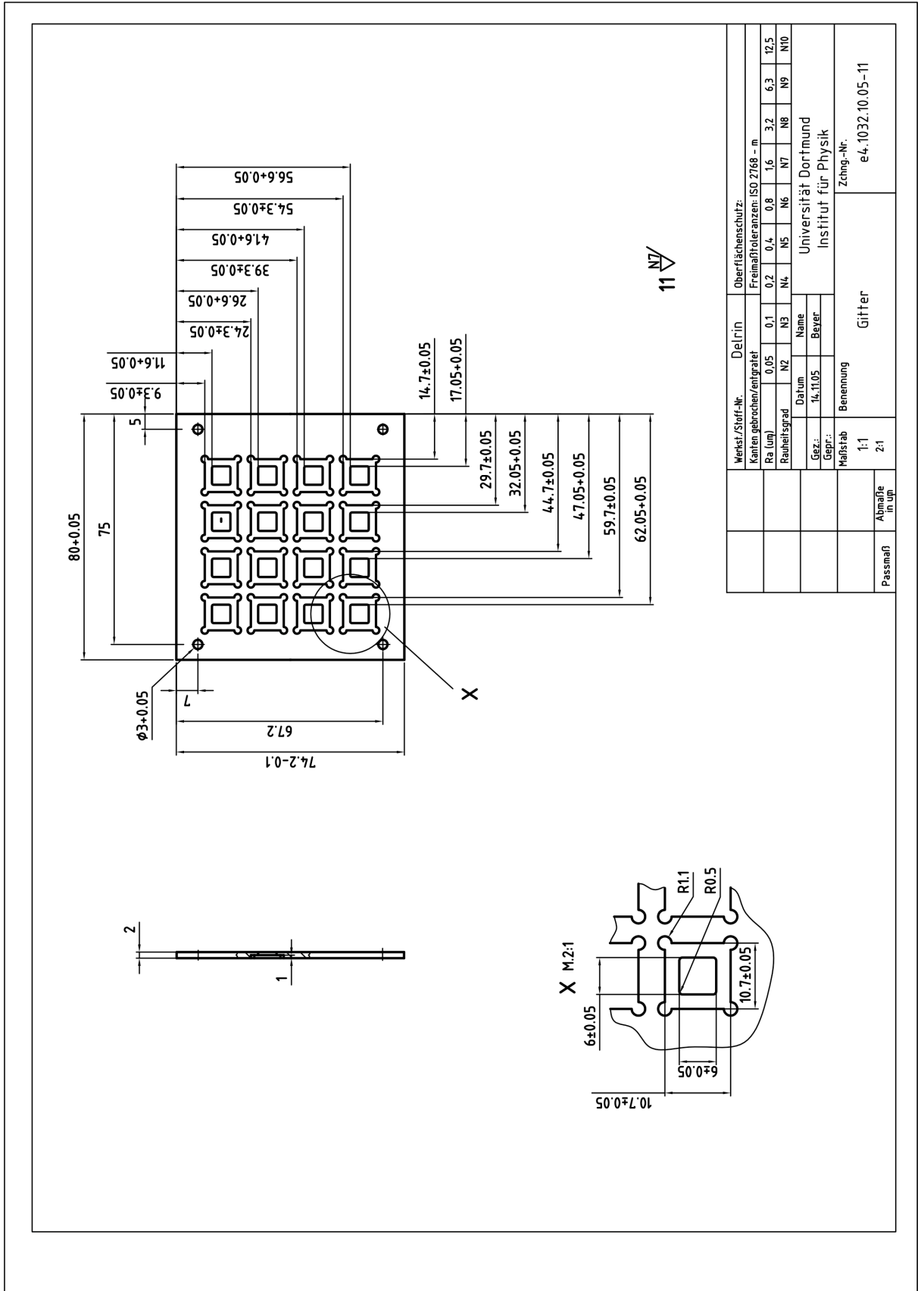


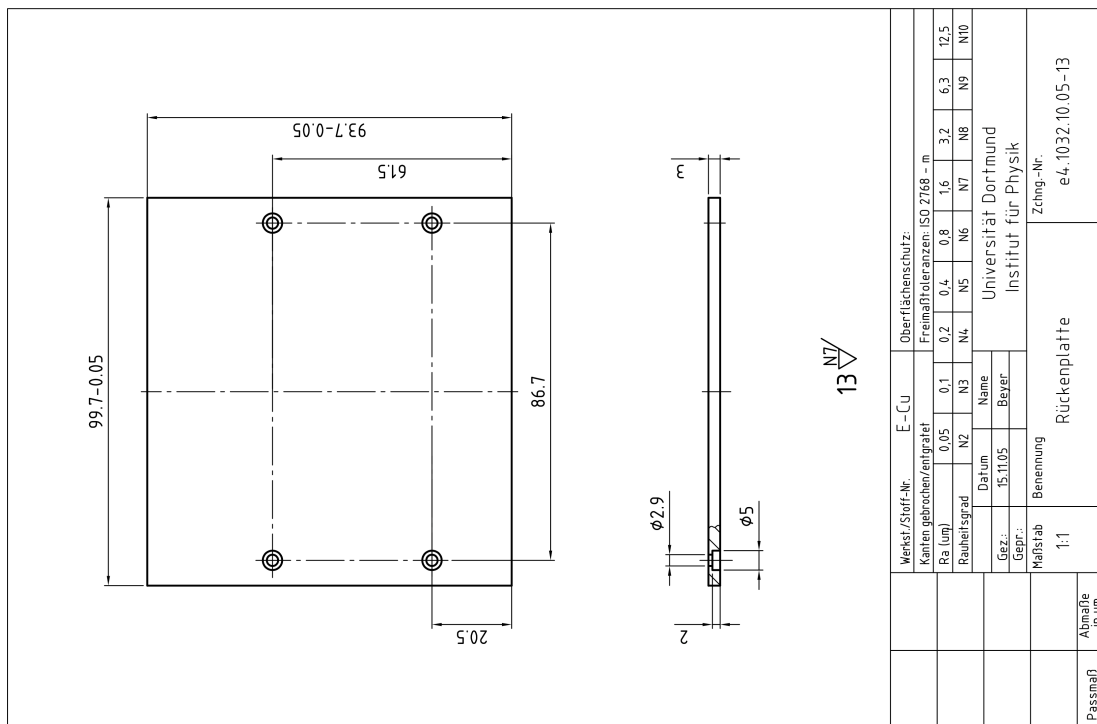
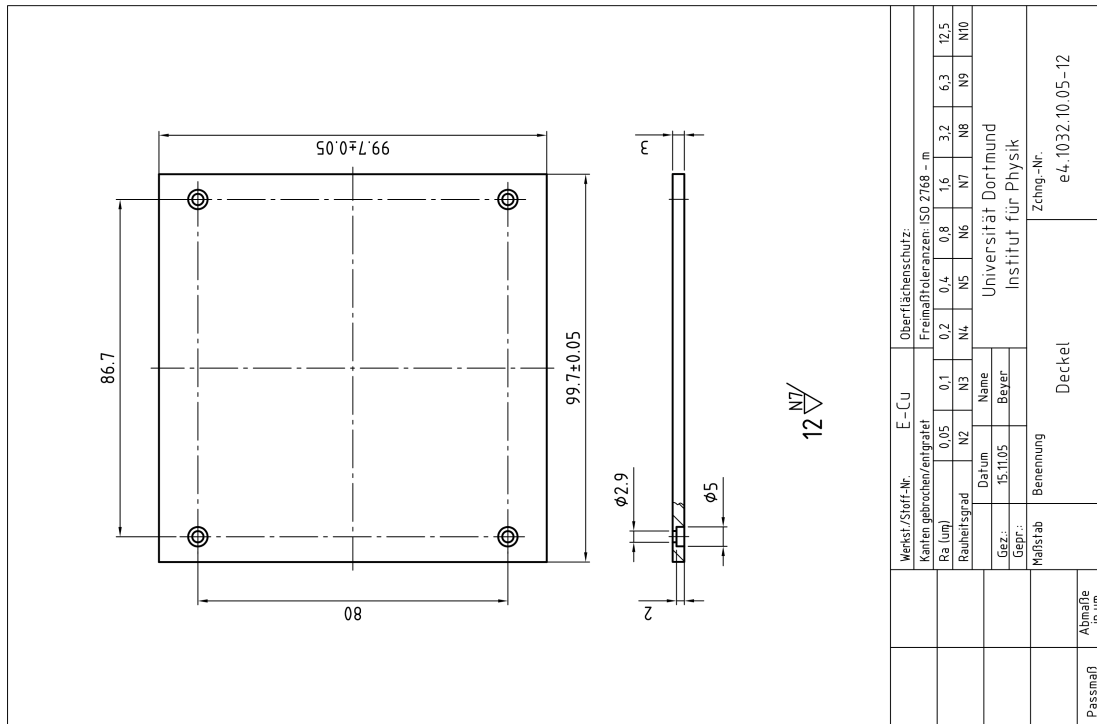


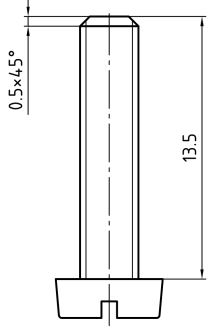

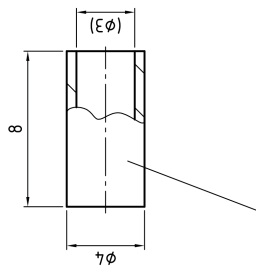

Werkst./Stoff-Nr.	E-Cu	Oberflächenschutz:														
Karren gebrochen/enigralet		Freimaßtoleranzen: ISO 2768 - m	0.2	0.4	0.8	1.6	3.2	6.3	12.5							
Ra (µm)	0.05		0.1	0.2	0.4	0.8	1.6	3.2	6.3	12.5						
Rauheitsgrad	N2		N2	N3	N4	N5	N6	N7	N8	N9	N10					
Datum	09.11.05	Name	Universität Dortmund													
Gepr.:	Beyer	Gepr.:	Institut für Physik													
Maßstab	1:1	Benennung	Linke Aufnahmeplatte													
Passmaß	Abmaße in µm	Zchng.-Nr.	e4.1032.10.05-9													



Werkst./Stoff-Nr.	Delrin	Oberflächenschutz:									
Kanten gebrochen/entgratet		Freimaßtoleranzen: ISO 2768 - m									
Ra (µm)	0,05	0,1	0,2	0,4	0,8	1,6	3,2	6,3	12,5		
Rauheitsgrad	N2	N3	N4	N5	N6	N7	N8	N9	N10		
Datum	Name		Universität Dortmund								
Gez.:	Bevor.		Institut für Physik								
Gepr.:	Benennung		Züch.-Nr.								
Maßstab	1:1		e4.1032.10.05-10								
Passmaß	Abmaße in µm		Gitter								
	2:1										





 <p>Kunststoff-Zylinderschraube DIN 84, M2.5x16 Werkst.: PA 6.6 natur</p> <p style="text-align: center;">15 </p>	 <p>Teflon-Schlauch im Labor e4, vorhanden</p> <p style="text-align: center;">14 </p>																																																																																																				
<table border="1"> <tr> <td>Passmaß</td> <td>Abmaße in µm</td> <td>5:1</td> <td>Zylinderschraube</td> <td>Zchg.-Nr. e4.1032.10.05-15</td> </tr> <tr> <td></td> <td></td> <td></td> <td>Benennung</td> <td></td> </tr> <tr> <td></td> <td></td> <td></td> <td>Gez.: 15.11.05</td> <td></td> </tr> <tr> <td></td> <td></td> <td></td> <td>Name: Bever</td> <td></td> </tr> <tr> <td></td> <td></td> <td></td> <td>Datum: 15.11.05</td> <td></td> </tr> <tr> <td></td> <td></td> <td></td> <td colspan="2">Universität Dortmund Institut für Physik</td> </tr> <tr> <td></td> <td></td> <td></td> <td>Rauhheitsgrad</td> <td>N2 N3 N4 N5 N6 N7 N8 N9 N10</td> </tr> <tr> <td></td> <td></td> <td></td> <td>Ra (µm)</td> <td>0.05 0.1 0.2 0.4 0.8 1.6 3.2 6.3 12.5</td> </tr> <tr> <td></td> <td></td> <td></td> <td>Kanten gebrochen/entgratet</td> <td></td> </tr> <tr> <td></td> <td></td> <td></td> <td>Werkst./Stoff-Nr.</td> <td></td> </tr> </table>	Passmaß	Abmaße in µm	5:1	Zylinderschraube	Zchg.-Nr. e4.1032.10.05-15				Benennung					Gez.: 15.11.05					Name: Bever					Datum: 15.11.05					Universität Dortmund Institut für Physik					Rauhheitsgrad	N2 N3 N4 N5 N6 N7 N8 N9 N10				Ra (µm)	0.05 0.1 0.2 0.4 0.8 1.6 3.2 6.3 12.5				Kanten gebrochen/entgratet					Werkst./Stoff-Nr.		<table border="1"> <tr> <td>Passmaß</td> <td>Abmaße in µm</td> <td>5:1</td> <td>Schlauch</td> <td>Zchg.-Nr. e4.1032.10.05-14</td> </tr> <tr> <td></td> <td></td> <td></td> <td>Benennung</td> <td></td> </tr> <tr> <td></td> <td></td> <td></td> <td>Gez.: 15.11.05</td> <td></td> </tr> <tr> <td></td> <td></td> <td></td> <td>Name: Bever</td> <td></td> </tr> <tr> <td></td> <td></td> <td></td> <td>Datum: 15.11.05</td> <td></td> </tr> <tr> <td></td> <td></td> <td></td> <td colspan="2">Universität Dortmund Institut für Physik</td> </tr> <tr> <td></td> <td></td> <td></td> <td>Rauhheitsgrad</td> <td>N2 N3 N4 N5 N6 N7 N8 N9 N10</td> </tr> <tr> <td></td> <td></td> <td></td> <td>Ra (µm)</td> <td>0.05 0.1 0.2 0.4 0.8 1.6 3.2 6.3 12.5</td> </tr> <tr> <td></td> <td></td> <td></td> <td>Kanten gebrochen/entgratet</td> <td></td> </tr> <tr> <td></td> <td></td> <td></td> <td>Werkst./Stoff-Nr.</td> <td></td> </tr> </table>	Passmaß	Abmaße in µm	5:1	Schlauch	Zchg.-Nr. e4.1032.10.05-14				Benennung					Gez.: 15.11.05					Name: Bever					Datum: 15.11.05					Universität Dortmund Institut für Physik					Rauhheitsgrad	N2 N3 N4 N5 N6 N7 N8 N9 N10				Ra (µm)	0.05 0.1 0.2 0.4 0.8 1.6 3.2 6.3 12.5				Kanten gebrochen/entgratet					Werkst./Stoff-Nr.	
Passmaß	Abmaße in µm	5:1	Zylinderschraube	Zchg.-Nr. e4.1032.10.05-15																																																																																																	
			Benennung																																																																																																		
			Gez.: 15.11.05																																																																																																		
			Name: Bever																																																																																																		
			Datum: 15.11.05																																																																																																		
			Universität Dortmund Institut für Physik																																																																																																		
			Rauhheitsgrad	N2 N3 N4 N5 N6 N7 N8 N9 N10																																																																																																	
			Ra (µm)	0.05 0.1 0.2 0.4 0.8 1.6 3.2 6.3 12.5																																																																																																	
			Kanten gebrochen/entgratet																																																																																																		
			Werkst./Stoff-Nr.																																																																																																		
Passmaß	Abmaße in µm	5:1	Schlauch	Zchg.-Nr. e4.1032.10.05-14																																																																																																	
			Benennung																																																																																																		
			Gez.: 15.11.05																																																																																																		
			Name: Bever																																																																																																		
			Datum: 15.11.05																																																																																																		
			Universität Dortmund Institut für Physik																																																																																																		
			Rauhheitsgrad	N2 N3 N4 N5 N6 N7 N8 N9 N10																																																																																																	
			Ra (µm)	0.05 0.1 0.2 0.4 0.8 1.6 3.2 6.3 12.5																																																																																																	
			Kanten gebrochen/entgratet																																																																																																		
			Werkst./Stoff-Nr.																																																																																																		





## **Appendix D**

# **Circuit Diagrams and Silk Screens**

In this part of the appendix all relevant circuit diagrams and silk screens of hardware that was developed as part of this work were collected. Most development was done with Mr. Koch from the 'Elektronik-Entwicklung', Physics Department, University of Dortmund.

In the published version of this work, the complete set of circuit diagrams and silk screens as well as the firmware listings for the VME-ADC is not contained due to IP concerns. They can be obtained, however, by contacting the author ([Daniel.Muenstermann@gmx.de](mailto:Daniel.Muenstermann@gmx.de)) or via Prof. Dr. C. Gößling, Lehrstuhl für Experimentelle Physik IV, University of Dortmund, D-44221 Dortmund.



## Appendix E

# DAQ-commands

This is a list of commands that can be given to the `client`-application to operate preamp, ADC, grid-bias, HV and slow control. It is current at the time of writing and has been compiled largely by H. Kiel and J. Wilson. An up-to-date version of this list can be found on COBRA's internal website.

The commands can be separated into different classes which are in different command 'directories'. Firstly there are the basic commands in the base 'directory'.

- HELLO  
This command simply checks that the daq is alive and listening. If the client is used in string (-s) mode it will return the string `YES MASTER`, otherwise a series of integers is seen.
- QUIT  
This command closes down the daq process in a clean manner. If the client is used in string (-s) mode it will return the string `GOODBYE`, otherwise a series of integers is seen. All ADC channels will be deactivated, the HV will be turned off and the output file will be closed cleanly if this command is received.
- README  
This command creates a template for a README file called `newREADME` in the directory where the daq code is running (ie. `/data/COBRA`) with the current run settings (online channels, HV settings, GB settings, ADC amplification and threshold settings, potentiometer settings, clearcap, deadtime and relais settings). This file can then be copied and edited by the shift operator to include data that cannot be accessed through the DAQ such as the operator's name and the presence of calibration sources.

A set of commands to control histograms stored by the daq process are preceded by the directory name `HISTO`. ie. To execute them type `client HISTO/INSTRUCTION`.

- HISTO/LIST  
This command will list the available histograms by number. One histogram is created for each detector so the numbers will range from 1-64 for the 64-array setup. Each histogram has 16384 ( $2^{14}$ ) bins relating to the number of bins (or channels, I shall use bins here to avoid confusion in terminology) of the ADC.

- HISTO/GET/N  
The user must specify the required histogram number, N. This command will get the required histogram which will be returned as a series of integer numbers relating to the number of counts in each of the 16384 bins. The best option is to pipe the required histogram into a text file, or to use the `calib` tool which interfaces with the daq through a root GUI.
- HISTO/CLEAR/N  
The user must specify the required histogram number, N. This command will clear any entries stored in the given histogram, ie reset the contents of all bins to zero. An argument of N=-1 will clear all the histograms.

A set of commands relating to slow control are preceded by the directory name `SLOW`. In the following commands the number, N, relates to the crystal number which runs from 1–64 in the case of the 64-array setup, whilst M is ADC module number which runs from 1–16 with each module hosting 4 channels.

- SLOW/DEBUG/V  
This command changes the output verbosity level of the daq code to integer value V. If no argument V is supplied, the current verbosity level is returned.
- SLOW/UPTIME  
This command returns the time in seconds that the daq has been running for.
- SLOW/GETDEADTIME  
This command returns the risetime protection<sup>1</sup> on all detector channels in microseconds. The default value is 50  $\mu$ s.
- SLOW/DEADTIME/V  
This command sets the risetime protection on all detector channels to V microseconds. V can take a value in the range 0–1023  $\mu$ s.
- SLOW/CLEARTIMER  
This command resets the timer on the first VME board. The clear signal is then distributed via Front End Bus (ie. the 6-pin connector).
- SLOW/INTERRUPTS/M/F/F/F  
This command allows the user to change which states generate interrupts on a module-by-module basis. M is the ADC module number. The three flags (F) are set to 1 to enable interrupts and 0 to disable them for each of the three conditions: module empty (default=0), module half-full (default=1), module full (default=1). It appears that this can be used as a sort of work-around when modules fail to generate interrupts (state where things appear to hang and the IRQ light is permanently on). The command sometimes has to be sent multiple times.
- SLOW/GETTHRESHOLD/N  
This command returns the ADC threshold setting for detector N. The default value is 10.

---

<sup>1</sup>Risetime protection is the time between the leading edge of the signal crossing the trigger threshold and the start of the conversion to a digital signal. The conversion takes about 2.5  $\mu$ s.

- SLOW/THRESHOLD/N/V  
This command sets the ADC threshold for detector N to V. This can take a value in the range 0–127.
- SLOW/GETAMPLIFICATION/N  
This command returns the ADC amplification setting for detector N. The default value is 2.
- SLOW/AMPLIFICATION/N/V  
This command sets the ADC amplification for detector N to V. This can take a value in the range 0–127. 0 relates to an amplification factor of 1 and 127 gives the maximum amplification factor of 10.
- SLOW/GETCLEARCAP  
This command reports the length of the peak clear signal in microseconds and at the same time the signal pulls capacitors on the ADC back to zero. The default value is 50  $\mu$ s.
- SLOW/CLEARCAP/V  
This command sets the length of the peak clear signal to V microseconds. A negative value will not change this setting.
- SLOW/AUTOCLEARCAP/V  
This command initiates an automatic peak clear roughly every V seconds. If no argument V is supplied, the current rate of clearing is returned. A negative argument will disable the automatic peak clear. The default is for no peak clearance - ie this won't happen when the daq is restarted unless this command is provided.
- SLOW/ACCEPTTRIGGER/M/V  
This command sets all the detectors on ADC module M to recognise external triggers from the front-end bus if V=1, and the opposite if V=0. This applies when there are more than 1 ADC module. The default setting is V=1.
- SLOW/GENERATETRIGGER/M/V  
This command enables all the detectors on ADC module M to generate external triggers across the front-end bus if V=1, and the opposite if V=0. The default setting is V=1.
- SLOW/DB9WRITE/N/V1/V2/V3/...../V16  
This command writes up to 16 7 bit data words (arguments V1,V2....) to the DB9 port N. For the 64-array 4 DB9 ports will be used to control the potentiometer settings in the preamplifiers. One port controls a whole layer of 16 crystals. The V arguments can take values in the range 0–127. Currently no other DB9 ports are used/available as a total of 48 TTL lines are available (controlled by the TIP675 board) and the control of the HV supply uses 24 of these and each of the 4 DB9 ports uses 5.
- SLOW/DB9CHECK/N  
This command returns the last set of values sent to DB9 port N (ie. the last DB9WRITE command). If no DB9WRITE command has been issued since the current daq process was started, the V1–V16 values returned are all -1 and the user must refer to the daq.log

file for the latest settings (preamp potentiometer settings do not reset when the daq process ends).

- `SLOW/DB9SPI`  
This can be used for testing and hardware/software development purposes. You can use it to write (and read) arbitrary raw data over the DB9 connectors working in SPI-Bus mode. This is a direct interface to `io_spi_transceiver`. You could, for example, also use it to set the pots inside the pre-amp (have to calculate the correct byte-string though, since the pots are 7-bit, this is done in `slow_amp_setpot` in `slow_amp.c`).
- `SLOW/READADC/N`  
This command reads back the value from the slow control ADC, channel N. In LNGS channels 1–3 are used for the temperature measurements. The values are read through the TIP850 mezzanine board so this command won't work on systems without this board like in Sussex.

A subset of slow control commands are used to control the new GRID bias supply. These commands are all preceded by `SLOW/GB/`

- `SLOW/GB/SETVOLTAGE/N/V`  
This command sets the grid bias voltage on channel N to voltage V.
- `SLOW/GB/READVOLTAGE/N`  
This command reads the grid bias voltage on channel N. Returns -1 if that GB channel does not exist (note N runs from 1 to number of GB channels, not number of detectors).

A subset of slow control commands relate to operations that can be performed on the TTL lines connected to the last 8 TTL lines. At present these lines are connected to a DB9 connector but soon they will actually be used in the control of the HV supply, so these commands will be unsafe when that supply is connected. They remain in the code now for diagnostic purposes but will be removed in the near future. These commands are preceded by `SLOW/TTL/`.

- `SLOW/TTL/SET/V`  
This command activates the bits of bit pattern V on the 8 TTL lines. eg 170 is equivalent to the bit pattern 10101010 and will set pins in an alternating pattern to logic levels 0 (actually about 0.65V) and 1 (about 5V).
- `SLOW/TTL/RESET/V`  
This command deactivates the bits of bit pattern V on the 8 TTL lines. So if the command `SLOW/TTL/SET/170` has just been applied, those bits that were set to 1 will be reset to 0.
- `SLOW/TTL/FLASH/V`  
This command activates and then deactivates (just flashes) the bits of bit pattern V on the 8 TTL lines.

The high voltage supply is controlled by a set of commands preceded by `HV`. The high voltage supply made by Warwick supplies 64 channels of high voltage in the range 0–2500V (negative). The voltages are controlled by setting integer values on a scale 0–255 so the control

accuracy is roughly  $\pm 10V$ . Therefore, all set-voltage values are input as integers and a slight difference with the read-back voltage is expected. The channel numbers referred to below (N) run from 1–64. However, it is sometimes useful to control a whole layer of crystals (ie 16 crystals at once for the NEST setup) so some commands refer to the layer, L, where L runs from 1–4.

Note that smaller high-voltage supplies were also made for some of the member institutions such as Sussex University. These consist of 6 channels rather than 64.

- HV/ON  
This command initialises the HV supply. Unless a status bit is set to 1, the HV supply is effectively off and no voltages can be set (although it is possible to read back values which should all be  $\approx$ zero). The return value from this command should always be 1.
- HV/OFF  
This command turns the HV supply off. The 'ON' status bit is set to zero and all voltages are set to zero too. The return value from this command should always be 1.
- HV/SETVOLTAGE/N/V  
This command is used to set the voltage for channel number N to V Volts. If this command is unsuccessful due to one of the following reasons -1 is returned.
  1. The voltage selected exceeds the maximum allowed (2550 V).
  2. The selected HV channel does not exist. (There are 6 channels on the Sussex supply and 64 channels on the LNGS supply. This is defined in `config.h`.)
  3. The HV supply has not been turned on with the `hv/on` command.

Otherwise, the return value is the word sent to the HV-supply which takes inputs 0-255 to set the voltages (ie the chosen voltage divided by 10).
- HV/READVOLTAGE/N  
This command reads the voltage for channel number N and returns it as an integer number of Volts.
- HV/DEFAULTS  
This command is used to set the voltages of all 64 (6 for the test supplies) channels to a set of default values stored in the file `hv.h`. If the write to any of the channels fails, -1 is returned, otherwise the return value is the word sent to the HV-supply for the last channel.
- HV/ZERO/L  
This command is used to set the voltages of layer L (eg L=2 is crystals 17–32) to zero. If the selected layer does not exist, -1 is returned, otherwise the return value is 0 (the word sent to the HV supply for each channel).
- HV/SETLAYER/L/V  
This command is used to set the voltages of layer L (eg L=2 is crystals 17–32) to V Volts. If the selected layer does not exist, -1 is returned, otherwise the return value is V/10 (the word sent to the HV supply for each channel).

- HV/READLAYER/L

This command is used to readback the voltages of layer L. The client process must be used in string (-s) mode in order to read the output which is an array of 16 voltage values.

Commands can also be sent to the serial port through the command

- SERIAL/SEND/S

This sends the string S to the serial port.

Finally there are a set of commands relating to the acquisition of data which are preceded by DAQ. In the following commands the number, N, relates to the crystal number which runs from 1–64 in the case of the 64-array setup, whilst M is ADC module number which runs from 1–16 with each module hosting 4 channels.

- DAQ/RUNNO

This command returns the current run number if a data file is being written out. The run number is composed from the time when writing out the file commenced:

year\_month\_day\_hour\_minute\_second so a series of integer values relating to each part is returned.

- DAQ/CONT/N

This command activates detector number N. The return value is the bit pattern for active channels on the ADC module hosting N (once N has been activated). eg. N=6 is the second channel on ADC2. If this is the only channel active on ADC2, the return value is  $0 \times 8 + 0 \times 4 + 1 \times 2 + 0 \times 1 = 2$ . If all channels on ADC2 are then active the return value would be  $1 \times 8 + 1 \times 4 + 1 \times 2 + 1 \times 1 = 15$ .

If N=0, all channels are activated. If N<0 this command does the same as the DAQ/STARTWRITE command.

- DAQ/STOP/N

This command deactivates detector number N. The return value is the bit pattern for active channels on the ADC module hosting N (once N has been turned off). If N=0, all channels are deactivated. If N<0 this command does the same as the DAQ/ENDWRITE command.

- DAQ/ACTIVE/M

This command returns the bit pattern for active channels on ADC module M as an integer. (All four channels on =  $1111 \equiv 15$ )

- DAQ/NMOD

This command returns the number of ADC modules known to the DAQ. For the 64-array it should be 16.

- DAQ/STARTWRITE

This command will start writing out to a datafile. If a datafile is currently open for writing, this file will be closed and a new file will be opened. The return value is the run number in the same format as returned by the DAQ/RUNNO command.



- DAQ/ENDWRITE  
This command will stop writing to file and close the current data file. The return value is the run number in the same format as returned by the DAQ/RUNNO command.
- DAQ/TRIG/M  
This command is used to force a trigger of ADC module M. (Can be useful in debug mode when you will see the event output to screen).



# List of Tables

2.1	Decay modes, Q-values and natural abundances of isotopes contained in CdZnTe [Kie03]. . . . .	19
2.2	Lower limits (90% C.L.) for $\beta^-\beta^-$ , $0\nu\beta^+\beta^+$ , $0\nu\beta^+EC$ and $2\nu EC$ EC-decay to ground state (g.s) and some excited states obtained with the first COBRA test setup (a 0.5 cm <sup>3</sup> CPG-type CdZnTe detector operated in Dortmund) compared with limits existing at the time of the study. Modified after [Kie03]. . . . .	22
3.1	Some crystal properties of CdZnTe, CdTe, Si and Ge measured at room temperature [eV-07]. . . . .	26
3.2	Radioactive contaminations of detector and passivation materials as measured at LNGS. . . . .	33
3.3	Activities of different construction materials . . . . .	42
3.4	Results of resistivity-measurements of conductive glue test-joints. . . . .	45
4.1	Neutron flux in hall A of the LNGS underground laboratory [Bel89]. . . . .	56
7.1	Decays into excited 0 <sup>+</sup> and 2 <sup>+</sup> states of <sup>116</sup> Cd, <sup>128</sup> Te and <sup>130</sup> Te. . . . .	95
7.2	Experimental results of the two-line searches. . . . .	97
7.3	Experimental results of the line-Compton searches. . . . .	98
7.4	Resulting half-life limits of <sup>116</sup> Cd, <sup>128</sup> Te and <sup>130</sup> Te. . . . .	99
A.1	Results of the energy resolution characterisation measurements done with the Dortmund test setup compared to the value reported by the manufacturer eV Products. . . . .	107



# List of Figures

1.1	Sketch of normal and inverted neutrino mass hierarchies. . . . .	11
1.2	Schematics of different $0\nu\beta\beta$ decays. . . . .	12
1.3	Mass parabola. . . . .	14
2.1	Rendered drawing of COBRA's first stage with 64 detectors[Dob05]. . . . .	21
2.2	Picture of the $2\times 2$ detector array. . . . .	23
3.1	Sketch illustrating the dependence of the pulse height in planar detectors on the interaction depth in the case of hole trapping. . . . .	28
3.2	Schematics on charge collection in pixel detectors. . . . .	29
3.3	Schematics on charge collection in co-planar grid detectors. . . . .	30
3.4	Drawings of different co-planar anode grid designs. . . . .	31
3.5	Photographs of CdZnTe detectors. . . . .	31
3.6	Exemplary CdZnTe spectra of $^{137}\text{Cs}$ as published by detector developers. . . . .	34
3.7	Photograph of the characterisation setup. . . . .	37
3.8	Overview of all measured I-V- and I-V-ag curves. . . . .	37
3.9	Exemplary I-V-curve. . . . .	38
3.10	Exemplary I-V-ag-curve. . . . .	38
3.11	Exemplary I-t-curve. . . . .	39
3.12	Exemplary C-V-curve. . . . .	39
3.13	Examples of fits to calibration spectra. . . . .	40
3.14	Comparison of manufacturer-supplied energy resolution data with own measurements. . . . .	40
3.15	Technical drawings of the Delrin (POM) holder structure for the $4\times 4\times 4$ -detector array. . . . .	43
3.16	Photographs of glue-contacted detectors. . . . .	44
3.17	Screenshot of the simulation program 'Maxwell's Dream' which was used to calculate the Kapton cable's capacitance. . . . .	47
3.18	Photographs of Kapton cables. . . . .	49
3.19	Technical drawings of the Kapton cables. . . . .	51
3.20	Cross section of a Kapton cable. . . . .	51
4.1	Muon intensity vs. depth. . . . .	54
4.2	Schematic drawings of the neutron shield. . . . .	56
4.3	Cross section of $^{113}\text{Cd}$ and results of MCNP neutron flux simulations. . . . .	57
4.4	Photograph of COBRA's second Faraday cage. . . . .	58

4.5	Comparison of spectra with and without LN <sub>2</sub> -flushing of the setup. . . . .	59
4.6	Schematic drawings of the Rn-trap [Zuz07]. . . . .	60
4.7	Mass attenuation coefficients of Pb, Cu and Cd <sub>0.9</sub> Zn <sub>0.1</sub> Te. . . . .	61
4.8	Schematic drawing of the shielding along the cable path. . . . .	62
4.9	Photographs of the lead castle. . . . .	63
4.10	Side views of the NEST. . . . .	64
4.11	Top view of the NEST. . . . .	64
4.12	Illustration of the performance levels achieved with different setups. . . . .	65
5.1	Sketches of a voltage-sensitive and a charge-sensitive preamplifier. . . . .	67
5.2	Schematic of one channel of the first preamplifier . . . . .	69
5.3	Schematic of one channel of the four-channel preamplifier. . . . .	70
5.4	Schematic of one channel of a 16-channel preamplifier. . . . .	72
5.5	Schematic of a simple CR-RC-shaper . . . . .	73
5.6	Photograph of the first 4-channel shaper. . . . .	74
5.7	Circuit Diagram of one channel of the first shaper . . . . .	74
5.8	Circuit Diagram of one channel of the inverting shaper. . . . .	75
5.9	Circuit Diagram of the comparator of the inverting shaper. . . . .	76
5.10	Frequency response of a passive and an active CR-RC bandpass. . . . .	77
5.11	Circuit diagram of one of the 8 shaper channels. . . . .	77
5.12	Schematic of one of the ADC's inputs with amplification and peak-holder stage. . . . .	81
5.13	Schematic of one channel in the ADC's trigger stage. . . . .	82
5.14	Block diagram of the main components of the VME-ADC. . . . .	83
5.15	Histogram of test pulses recorded with a VME-ADC. . . . .	84
6.1	Cross sections of the original and modified version of the HV-Kapton cable. . . . .	88
6.2	Spectra of the old 2 × 2-setup compared to shielded and unshielded runs of the first 16-detector layer. . . . .	89
7.1	Illustration of the coincidence analysis method . . . . .	91
7.2	Level scheme of <sup>116</sup> Cd. . . . .	94
7.3	Level scheme of <sup>128</sup> Te. . . . .	94
7.4	Level scheme of <sup>130</sup> Te. . . . .	94

# References

- [Aal02] C. E. AALSETH ET AL. *Comment on 'Evidence for neutrinoless double beta decay'*. Modern Physics Letters A **17**, 1475 (2002).
- [Aha05] B. AHARMIM ET AL. (SNO). *Electron energy spectra, fluxes, and day-night asymmetries of B-8 solar neutrinos from the 391-day salt phase SNO data set*. Phys. Rev. **C72**, 055502 (2005). nucl-ex/0502021.
- [Aha07] B. AHARMIM ET AL. (SNO). *Measurement of the  $\nu e$  and total B-8 solar neutrino fluxes with the Sudbury Neutrino Observatory phase I data set*. Phys. Rev. **C75**, 045502 (2007). nucl-ex/0610020.
- [Ahn06] M. H. AHN ET AL. (K2K). *Measurement of neutrino oscillation by the K2K experiment*. Phys. Rev. **D74**, 072003 (2006). hep-ex/0606032.
- [Ale00] A. ALESSANDRELLO ET AL. *New experimental results on double beta decay of  $^{130}\text{Te}$* . Physics Letters B **486**, 13 (2000).
- [Alk67] G. ALKHAZOV ET AL. Nuclear Instruments and Methods in Physics Research **48**, 1 (1967).
- [Arn03] C. ARNABOLDI ET AL. *A calorimetric search on double beta decay of Te-130*. Phys. Lett. **B557**, 167–175 (2003). hep-ex/0211071.
- [Arn04] C. ARNABOLDI ET AL. (CUORE). *CUORE: A cryogenic underground observatory for rare events*. Nucl. Instrum. Meth. **A518**, 775–798 (2004). hep-ex/0212053.
- [Avi05a] F. T. AVIGNONE. *Strategies for next generation neutrinoless double-beta decay experiments*. Nucl. Phys. Proc. Suppl. **143**, 233–239 (2005).
- [Avi05b] F. T. AVIGNONE, G. S. K. III and Y. G. ZDESENKO. *Next generation double-beta decay experiments: metrics for their evaluation*. New Journal of Physics **7**, 6 (2005). URL <http://stacks.iop.org/1367-2630/7/6>.
- [Bar90] A. BARABASH, A. KOPYLOV and V. CHEREHOVSKY. *Search for double  $\beta$ -decay of  $^{100}\text{Mo}$  and  $^{116}\text{Cd}$  to the excited states of  $^{100}\text{Ru}$  and  $^{116}\text{Sn}$* . Physics Letters B **249**, 186 (1990).
- [Bar95] H. H. BARRETT, J. D. ESKIN and H. B. BARBER. *Charge Transport in Arrays of Semiconductor Gamma-Ray Detectors*. Phys. Rev. Lett. **75** (1), 156–159 (Jul 1995).

- [Bar96] A. BARABASH ET AL. *Theoretical and experimental investigation of the double beta processes in  $^{106}\text{Cd}$* . Nuclear Physics A **604**, 115 (1996).
- [Bar01] A. BARABASH ET AL. *New limits on the beta beta decay of  $^{130}\text{Te}$  to excited states of  $^{130}\text{Xe}$* . The European Physical Journal A **11**, 143 (2001).
- [Bel87] E. BELLOTTI ET AL. *A Search for Double Beta Decay of  $^{128}\text{Te}$  and  $^{130}\text{Te}$  Leading to the First Excited State of Daughter Nuclei*. Europhysics Letters **3** (8), 889 (1987).
- [Bel89] P. BELLI ET AL. *Deep underground Neutron Flux Measurement with Large  $\text{BF}_3$  Counters*. Il nuovo Cimento A **101**, 959 (1989).
- [Bel99] P. BELLI ET AL. *New limits on  $2\beta^+$  decay processes in  $^{106}\text{Cd}$* . Astroparticle Physics **10**, 115 (1999).
- [Ber53] A. BERTHELOT ET AL. Compt. Rend. **236**, 1769 (1953).
- [Ber07] M. BERGER ET AL. *XCOM: Photon Cross Section Database (version 1.3)*. available online: <http://physics.nist.gov/xcom> (2007). National Institute of Standards and Technology, Gaithersburg, MD, USA.
- [Blo07a] T. BLOXHAM, A. BOSTON, J. DAWSON ET AL. (COBRA). *First results on double beta-decay modes of Cd, Te, and Zn Isotopes*. Physical Review C **76** (2), 025501 (pp. 7) (2007). URL <http://link.aps.org/abstract/PRC/v76/e025501>.
- [Blo07b] T. BLOXHAM and M. FREER. *Evaluation of pixellated CZT detectors for neutrinoless double beta-decay measurements*. NIM A **572**, 722–728 (2007).
- [Boe87] F. BOEHM and P. VOGEL. *Physics of Massive Neutrinos* (Camebridge University Press, 1987).
- [Bol07] A. E. BOLOTNIKOV ET AL. *Cumulative effects of Te precipitates in CdZnTe radiation detectors*. Nuclear Instruments and Methods in Physics Research A **571**, 687–698 (2007).
- [Cau07] E. CAURIER, F. NOWACKI and A. POVES. *Nuclear Structure Aspects of the Neutrinoless Double Beta Decay* (2007). arXiv:0709.0277[nucl-th].
- [Chu99] S. CHU, L. EKSTRÖM and R. FIRESTONE. *WWW Table of Radioactive Isotopes* (database version 2/28/1999). URL <http://nucleardata.nuclear.lu.se/nucleardata/toi/>.
- [Cow53] C. COWAN, F. REINES, F. HARRISON ET AL. *Large Liquid Scintillation Detectors*. Physical Review **90**, 493 (1953).
- [Dan96] F. DANEVICH ET AL. *Investigation of  $\beta^+\beta^+$  and  $\beta^+/\text{EC}$  decay of  $^{106}\text{Cd}$* . Zeitschrift für Physik A **355**, 433 (1996).
- [Dan00] F. DANEVICH ET AL. *New results of  $^{116}\text{Cd}$  double beta decay study with  $^{116}\text{CdWO}_4$  scintillators*. Physical Review C **62**, 045501 (2000).



- [Dan03] F. DANEVICH ET AL. *Search for  $2\beta$  decay of cadmium and tungsten isotopes: Final results of the Solotvina experiment*. *Physical Review C* **68**, 035501 (2003).
- [Dan05] M. DANIKAS and N. VRAKOTSOLIS. *Experimental Results with Small Air Gaps: [...]*. *Journal of Electrical Engineering* **56** (9-10), 246–251 (2005).
- [Dar05] Z. DARAKTCHIEVA ET AL. (MUNU). *Final results on the neutrino magnetic moment from the MUNU experiment*. *Phys. Lett.* **B615**, 153–159 (2005). hep-ex/0502037.
- [Daw06] J. DAWSON. personal communication (2006). University of Sussex, Brighton, UK.
- [Dob05] D. DOBOS. personal communication (2005). Physik E 4, University of Dortmund, Germany.
- [Eid04] S. EIDELMAN ET AL. *Review of Particle Physics*. *Physics Letters B* **592**, 1 (2004).
- [eV-07] EV-PRODUCTS (2007). [http://www.evproducts.com/material\\_prop.pdf](http://www.evproducts.com/material_prop.pdf).
- [Fan47] U. FANO. *Physical Review* **72**, 26 (1947).
- [Fau06] A. FAULER. personal communication (2006). Materialforschungszentrum Freiburg, Germany.
- [Fer02] F. FERUGLIO, A. STRUMIA and F. VISSANI. *Neutrino oscillations and signals in  $\beta$  and  $0\nu 2\beta$  experiments*. *Nuclear Physics B* **637**, 345 (2002).
- [Fer03] F. FERUGLIO, A. STRUMIA and F. VISSANI. *Addendum to: Neutrino oscillations and signals in  $\beta$  and  $0\nu 2\beta$  experiments [Nucl. Phys. B 637 (2002) 345] - First KamLAND Results*. *Nuclear Physics B* **659**, 359–362 (2003).
- [Fio67] E. FIORINI ET AL. *Physics Letters B* **45**, 602 (1967).
- [Fre52] J. FREMLIN and M. WALTERS. *An experimental investigation of the stability of nuclei against double beta-disintegration*. *Proceedings of the Physical Society, Section A* **65**, 911 (1952).
- [Fre05] M. FREER. personal communication (2005). University of Birmingham, UK.
- [Fur39] W. H. FURRY. *Physical Review* **56**, 1184 (1939).
- [Geo95] A. GEORGADZE ET AL. *Study of  $^{116}\text{Cd}$  Double Beta Decay with  $^{116}\text{CdWO}_4$  Scintillators*. *Physics of Atomic Nuclei* **58** (7), 1093 (1995).
- [Gil95] G. GILMORE and J. HEMINGWAY. *Practical Gamma-Ray Spectrometry* (John Wiley & Sons, Inc., 1995). ISBN 0-471-95150-1.
- [GM35] M. GOEPPERT-MAYER. *Physical Review* **48**, 512 (1935).
- [Goe05] C. GOESSLING ET AL. *Experimental study of  $^{113}\text{Cd}$  beta decay using  $\text{CdZnTe}$  detectors*. *Phys. Rev.* **C72**, 064328 (2005). nucl-ex/0508016.

- [He96] Z. HE, G. F. KNOLL ET AL. *1-D position sensitive single carrier semiconductor detectors*. Nuclear Instruments and Methods **A380**, 228–231 (1996).
- [He98] Z. HE, G. KNOLL ET AL. *Coplanar grid patterns and their effect on energy resolution of CdZnTe detectors*. Nuclear Instruments and Methods A **411**, 107–113 (1998).
- [He05] Z. HE and B. STURM. *Characteristics of depth-sensing coplanar grid CdZnTe detectors*. Nuclear Instruments and Methods in Physics Research, Section A **554**, 291 (2005).
- [Hee00] K. HEEGER ET AL. *High-Voltage Microdischarge in Ultra-Low Background  $^3\text{He}$  Proportional Counters*. IEEE Transactions on Nuclear Science **47** (6), 1829–1833 (2000).
- [Heu95] G. HEUSSER. *Low-Radioactivity Background Techniques*. Annu. Rev. Nucl. Part. Sci. **45**, 543–590 (1995).
- [Hir94] M. HIRSCH, K. MUTO, T. ODA ET AL. *Nuclear structure calculations of  $\beta^+\beta^+$ ,  $\beta^+/\text{EC}$  and  $\text{EC}/\text{EC}$  decay matrix elements*. Zeitschrift für Physik A **347**, 151 (1994).
- [Hos06] J. HOSAKA ET AL. (Super-Kamiokande). *Three flavor neutrino oscillation analysis of atmospheric neutrinos in Super-Kamiokande*. Phys. Rev. **D74**, 032002 (2006). hep-ex/0604011.
- [KAT01] KATRIN COLLABORATION. *KATRIN: A next generation tritium beta decay experiment with sub-eV sensitivity for the electron neutrino mass* (2001). hep-ex/0109033.
- [Kie03] H. KIEL, D. MUENSTERMANN and K. ZUBER. *A Search for various Double Beta Decay Modes of Cd, Te and Zn Isotopes*. Nuclear Physics A **723**, 499 (2003).
- [Kie04] H. KIEL. *POISON Version 0.9.3, COBRA GEANT4 Monte Carlo - User Manual* (2004). COBRA manual.
- [Kie05] H. KIEL. *Determination of the Half Lives of Rare Decays of Cd, Te and Zn Isotopes for the COBRA Experiment*. PhD thesis, University of Dortmund, Germany (2005). URL <http://hdl.handle.net/2003/21509>.
- [Kir67] T. KIRSTEN, W. GENTNER and O. A. SCHAEFFER. Zeitschrift für Physik **202**, 273 (1967).
- [KK01a] H. V. KLAPDOR-KLEINGROTHAUS, A. DIETZ, H. L. HARNEY ET AL. *Evidence for neutrinoless double beta decay*. Modern Physics Letters A **16**, 2409 (2001).
- [KK01b] H. V. KLAPDOR-KLEINGROTHAUS ET AL. *Latest results from the Heidelberg-Moscow double-beta-decay experiment*. The European Physical Journal A **12**, 147 (2001).
- [KK04] H. V. KLAPDOR-KLEINGROTHAUS, I. V. KRIVOSHEINA, A. DIETZ ET AL. *Search for neutrinoless double beta decay with enriched Ge- 76 in Gran Sasso 1990-2003*. Phys. Lett. **B586**, 198–212 (2004). hep-ph/0404088.

- [Kno00] G. F. KNOLL. *Radiation Detection and Measurement*. (John Wiley & Sons, Inc., 2000), 3rd edition. ISBN 0471073385.
- [Kra04] O. KRASEL. *Charge Collection in Irradiated Silicon-Detectors - A Study of the Operation Conditions of Silicon Sensors in the ATLAS Pixel Detector*. PhD thesis, University of Dortmund, Germany (2004). URL <http://hdl.handle.net/2003/2354>.
- [Kra05] C. KRAUS ET AL. *Final results from phase II of the Mainz neutrino mass search in tritium beta decay*. *Eur. Phys. J.* **C40**, 447–468 (2005). [hep-ex/0412056](http://arxiv.org/abs/hep-ex/0412056).
- [Lau04] M. LAUBENSTEIN. personal communication (2004). Laboratori Nazionali del Gran Sasso, INFN, Italy.
- [Leo92] W. LEO. *Techniques for Nuclear and Particle Physics Experiments*. (Springer Verlag, 1992), 2nd edition.
- [Luk94] P. LUKE. *Single-polarity charge sensing in ionization detectors using coplanar electrodes*. *Appl. Phys. Lett.* **65**, 2884 (1994).
- [Luk95] P. N. LUKE. *Unipolar charge sensing with coplanar electrodes – application to semiconductor detectors*. *IEEE Transactions on Nuclear Science* **42**, 207–213 (1995).
- [Maj99] B. MAJOROVITS and H. KLAPDOR-KLEINGROTHAUS. *Digital pulse shape analysis by neural networks for the HEIDELBERG-MOSCOW double beta-decay experiment*. *European Physical Journal A* **6**, 463–469 (1999). [hep-ex/9911001](http://arxiv.org/abs/hep-ex/9911001).
- [Mak62] Z. MAKI and S. NAKAGAWA, M. SAKATA. *Remarks on the unified model of elementary particles*. *Progress of Theoretical Physics* **28**, 870 (1962).
- [Mic06] D. G. MICHAEL ET AL. (MINOS). *Observation of muon neutrino disappearance with the MINOS detectors and the NuMI neutrino beam*. *Phys. Rev. Lett.* **97**, 191801 (2006). [hep-ex/0607088](http://arxiv.org/abs/hep-ex/0607088).
- [Mit88] L. MITCHELL and P. FISCHER. *Rare decays of cadmium and tellurium*. *Physical Review C* **38**, 895 (1988).
- [Mue01] D. MUENSTERMANN. *Untersuchung seltener Kernzerfälle mit Cadmium-Tellurid-Detektoren*. Diploma thesis, University of Dortmund, Germany (2001).
- [Mue03] D. MUENSTERMANN and K. ZUBER. *An alternative search for the electron capture of  $^{123}\text{Te}$* . *Journal of Physics G* **29**, B1 (2003).
- [Mün05] D. MÜNSTERMANN and H. KIEL. *COBRA-DB9 Connector*. technical report, University of Dortmund (2005). COBRA note 2005-a.
- [Nor84] E. NORMAN and M. DE FACCIO. *Searches for double  $\beta^+$ ,  $\beta^+/\text{EC}$  and double electron-capture decays*. *Physics Letters B* **148**, 31 (1984).
- [Nor85] E. NORMAN. *Improved limits on the double beta decay half-lives of  $^{50}\text{Cr}$ ,  $^{64}\text{Zn}$ ,  $^{92}\text{Mo}$  and  $^{96}\text{Ru}$* . *Physical Review C* **31**, 1937 (1985).

- [Oeh04] S. OEHL. *A Shielding System Against Neutrons for the COBRA-Experiment and Characterisation of CdZnTe Detectors with the Transient Current Technique*. Diploma thesis, University of Dortmund, Germany (2004).
- [Ort02] H. E. ORTON. *Partial Discharge Testing of In-Situ Power Cable Accessories – An Overview*. *Electric Energy T & D* **6**, 48 (2002). [www.electricenergyonline.com/article.asp?m=9&mag=6&article=44](http://www.electricenergyonline.com/article.asp?m=9&mag=6&article=44).
- [Pau30] W. PAULI. *Brief an die Radioaktiven* (1930).
- [Pie94] A. PIEPKE ET AL. *Investigation of the  $\beta\beta$  Decay of  $^{116}\text{Cd}$  into excited States of  $^{116}\text{Sn}$* . *Nuclear Physics A* **577**, 510 (1994).
- [Pon00] O. PONKRATENKO, V. TRETYAK and Y. ZDESENKO. *Event Generator DECAY4 for Simulating Double-Beta Processes and Decays of Radioactive Nuclei*. *Physics of Atomic Nuclei* **63**, 1282 (2000).
- [Pre01] T. H. PRETTYMAN ET AL. *Effect of Surfaces on the Performance of CdZnTe Detectors*. In: RALPH B. JAMES, Editor, *Proceedings of SPIE, Volume 4507, Hard X-Ray and Gamma-Ray Detector Physics III*, 23–31 (2001).
- [Rac37] G. RACAH. *Nuovo Cimento* **14**, 327 (1937).
- [Ram39] S. RAMO. *Currents induced by electron motion*. *Proceedings of the Institute of Radio Engineers* **27**, 584 (1939).
- [Ree] C. REEVE. PhD Thesis, in preparation.
- [Sch] O. SCHULZ. PhD Thesis, in preparation.
- [Spi06] H. SPIELER. *Semiconductor Detector Systems* (Oxford University Press, 2006). First Corrected Reprint, ISBN 978-0-19-852784-8.
- [Sta90] A. STAUDT, K. MUTO and H. V. KLAPDOR-KLEINGROTHAUS. *Calculation of  $2\nu$  and  $0\nu$  double-beta decay rates*. *Europhysics Letters* **13**, 31 (1990).
- [Sta06] C. STAHL. personal communication (2006). NASA, Goddard Space Flight Center.
- [Ste07] D. Y. STEWART, P. F. HARRISON, B. MORGAN ET AL. *Radiation shielding for underground low-background experiments*. *NIM A* **571**, 651–662 (2007).
- [Stu05] B. STURM, Z. HE ET AL. *Investigation of the Asymmetric Characteristics and Temperature Effects of CdZnTe Detectors*. *IEEE Transactions on Nuclear Science* **52** (5), 2068 (2005).
- [Suh98] J. SUHONEN and O. CIVITARESE. *Weak-interaction and nuclear-structure aspects of nuclear double beta decay*. *Phys. Rept.* **300**, 123–214 (1998).
- [Sze98] C. SZELES and M. DRIVER. *Growth and properties of semi-insulating CdZnTe for radiation detector applications*. *Proceedings of SPIE* **3446**, 2 (1998).

- [Sze04] C. SZELES ET AL. *Development of the High-Pressure Electro-Dynamic Gradient Crystal-Growth Technology for Semi-Insulating CdZnTe Growth for Radiation Detector Applications*. *Journal of Electronic Materials* **33**, 742 (2004).
- [Tak01] T. TAKAHASHI ET AL. *High-Resolution CdTe Detector and Applications to Imaging Devices*. *IEEE Transactions on Nuclear Science* **48**, 287 (2001).
- [The96] P. THEODORSSON. *Measurement of Weak Radioactivity* (World Scientific, 1996). ISBN 9810223153.
- [Tie02] U. TIETZE, C. SCHENK and E. GAMM. *Halbleiter-Schaltungstechnik* (Springer Verlag, 2002), 12th edition.
- [Veg21] L. VEGARD. *Die Konstitution der Mischkristalle und die Raumbfüllung der Atome*. *Zeitschrift für Physik* **5**, 17–26 (1921).
- [Wat62] D. WATT and R. GLOVER. *A Search for Radioactivity among the Naturally Occurring Isobaric Pairs*. *Philosophical Magazine* **7**, 105 (1962).
- [Wei99] C. WEINHEIMER ET AL. *High precision measurement of the tritium beta spectrum near its endpoint and upper limit on the neutrino mass*. *Phys. Lett.* **B460**, 219–226 (1999).
- [Wil05a] J. WILSON. personal communication (2005). University of Sussex, Brighton, UK.
- [Wil05b] J. WILSON. *Predicted Sensitivities for COBRA using Maximum Likelihood*. technical report, University of Sussex, Brighton, UK (2005). COBRA memo 2005-06.
- [Wój05] M. WÓJCIKA and G. ZUZEL. *Low-<sup>222</sup>Rn nitrogen gas generator for ultra-low background counting systems*. *NIM A* **539**, 427–432 (2005).
- [Yao06] W.-M. YAO ET AL. *Review of Particle Physics*. *Journal of Physics G* **33**, 1+ (2006). URL <http://pdg.lbl.gov>.
- [Zde02] Y. G. ZDESENKO, F. A. DANEVICH and V. I. TRETYAK. *Has neutrinoless double beta decay of Ge-76 been really observed?*. *Physics Letters B* **546**, 206 (2002).
- [Zha05] F. ZHANG, Z. HE ET AL. *3-D Position Sensitive CdZnTe Spectrometer Performance Using Third Generations VAS/TAT Readout Electronics*. *IEEE Transactions on Nuclear Science* **52** (5), 2009 (2005).
- [Zub01] K. ZUBER. *COBRA: Double beta decay searches using CdTe detectors*. *Physics Letters B* **519**, 1 (2001).
- [Zub04] K. ZUBER. *Neutrino Physics* (Institute of Physics Publishing, 2004). ISBN 0-7503-0750-1.
- [Zuz07] G. ZUZEL. personal communication (2007). MPI für Kernphysik, Heidelberg, Germany.



# Publications

## Articles

D. Muenstermann and K. Zuber

*An Alternative Search for the Electron Capture of Te-123*

**Journal of Physics G: Nuclear and Particle Physics** 29, B1 (2003)

H. Kiel, D. Muenstermann and K. Zuber

*A Search for various Double Beta Decay Modes of Cd, Te and Zn Isotopes*

**Nuclear Physics A** 723, 499 (2003)

C. Gößling, . . . , D. Muenstermann et. al.

*Experimental Study of  $^{113}\text{Cd}$  Beta Decay Using CdZnTe detectors*

**Physical Review C** 72, 064328 (2005)

D. Muenstermann on behalf of the COBRA collaboration

*Current Status and Recent Results of the COBRA Experiment*

in proceedings of the "EPS HEP2005 International Europhysics Conference on High Energy Physics" **PoS** (HEP2005)170 (2006)

T. Bloxham, . . . , D. Muenstermann et. al.

*First Results on Double Beta Decay Modes of Cd, Te and Zn Isotopes with the COBRA Experiment*

**Physical Review C** 76, 025501 (2007)

## Articles in preparation

D. Muenstermann et. al.

*A Multi-Detector Precision Measurement of the Beta Decay of Cd-113*

D. Muenstermann et. al.

*Searches for Neutrinoless Double Beta Decays of Cd, Zn and Te with a 3-Dimensional Detector Array*

## Conference Talks

D. Muenstermann, H. Kiel, Y. Ramachers und K. Zuber

*Suche nach Neutrinomassen mit COBRA*

**Particle Physics DPG Spring Meeting**

March 18 – 22 2002, Leipzig (Germany)

D. Muenstermann

*COBRA – A new Approach to  $\beta\beta$ -Decay*

**UK HEP Forum**

May 11, 2003, Abingdon (UK)

D. Muenstermann für die COBRA-Kollaboration

*Status des COBRA-Experiments*

**Particle Physics DPG Spring Meeting**

March 04 – 09 2005, Berlin (Germany)

D. Muenstermann for the COBRA collaboration

*Current Status and Recent Results of the COBRA Experiment*

**EPS HEP2005 International Europhysics Conference on High Energy Physics**

July 21 – 28 2005, Lisbon (Portugal)

D. Muenstermann für die COBRA-Kollaboration

*COBRA – Auf der Suche nach neutrinolosen  $\beta\beta$ -Zerfällen mit CdZnTe-Detektoren*

**Particle Physics DPG Spring Meeting**

March 28 – 30 2006, Dortmund (Germany)

D. Muenstermann für die COBRA-Kollaboration

*Status des COBRA-Experiments*

**Particle Physics DPG Spring Meeting**

March 05 – 09 2007, Heidelberg (Germany)

D. Muenstermann für die COBRA-Kollaboration

*Status des COBRA-Experiments*

**Nuclear Physics DPG Spring Meeting**

March 12 – 16 2007, Gießen (Germany)

### **Conference Posters**

K. Zuber, C. Goessling, H. Kiel, D. Muenstermann and Y. Ramachers

*COBRA - A New Approach to Double Beta Decay Using CdTe*

**Neutrino 2002**

May 25 – 30 2002, Munich (Germany)

D. Muenstermann, H. Kiel, O. Krasel, S. Oehl and K. Zuber

*COBRA - An Ultra-Low-Rate Application of CdZnTe Detectors*

**13<sup>th</sup> International Workshop on Room Temperature Semiconductor X- and Gamma-Ray Detector (RTSD) 2003**

October 19 – 25 2003, Portland, Oregon (USA)



# Acknowledgements

Many people were involved in the completion of this work – most of them voluntarily; others simply had to accept my decision to strive for a PhD. The least I can do is to show all of them my appreciation and acknowledge their support.

First of all, I would like to thank my advisor Priv.-Doz. Dr. Kai Zuber for offering me the opportunity to continue working on the COBRA experiment, for trying to share his incredible knowledge about neutrino physics with me, and for his sometimes tedious but always productive suggestions. I was able to take part in the formation of the COBRA collaboration and had the opportunity to meet and work with many truly outstanding people, which was a precious experience.

Prof. Dr. Claus Göbbling was a great host to the Dortmund group of COBRA, who supported our nuclear physics experiment in a particle physics environment. I owe him gratitude for always encouraging me, especially towards the final stage of my thesis, and for kindly addressing himself to the task of being my second examiner.

Apart from being host to my doctoral examination, I would like to thank the dean of the Department of Physics at the University of Dortmund, Prof. Dr. Metin Tolan, for enriching the faculty's curriculum with seminars and lectures about the physics of special fields. Discussions with him were always pleasurable and his remarks about the physics of Star Trek and James Bond especially illuminating.

I would also like to express my gratitude to Dr. Julia Becker for taking part in my examination, for fun conversations and for reassuring me that "it can be done".

Working on COBRA was (almost) always fun, in a large part thanks to the people working with me. I would like to thank all members of the collaboration for the great time, most notably Dr. Jaime Dawson, Dr. Jeanne Wilson, Dr. Henning Kiel, and Christopher Reeve who managed to always keep me on the brink of mental breakdown. Oliver Schulz has not only been a dear friend for many years but also did me the favour of joining COBRA when we needed his support and knowledge urgently. Though stays at LNGS were often stressful due to the permanent lack of time, people like Dr. Matthias Junker, Dr. Daniel Bemmerer, and Oleg Chkvorets helped to make them very enjoyable. They guided me around all pitfalls of the LNGS and its administration and we had motivating discussions at superb Italian dinners and at whisky tasting sessions.

In addition, I would like to thank all members of the Lehrstuhl für Experimentelle Physik IV for providing a warm and pleasurable atmosphere in Dortmund, especially Daniel Dobos, Theo Villett, Dr. Martin Mass, Dr. Jonas Klaiber-Lodewigs, Dr. Olaf Krasel, Jens Weber, Krissi Hoffmann, and Georg Troska; as well as Gundula Weber and Dr. Bärbel Siegmann of the

teaching lab, and Ines Knäpper. Besides, I am exceedingly indebted to Priv.-Doz. Dr. Reiner Klingenberg for many instructive discussions in which I realised that most of my questions weren't as simpleminded as I had thought. Without the invaluable support of the mechanical and electronics workshops as well as the electronics development of the Department of Physics it would not have been possible to realise the experimental setup for COBRA.

Several colleagues and friends had the doubtful honour of reading several versions of this thesis; I am deeply indebted to them for helpful suggestions.

Special thanks are due to my family and my friends who have had to cope with me and my varying levels of despair during the last years. Regular sessions with Dr. Birgit Lessmann and Markus "Charlie" Alex helped me to retain my sanity. Conversations with my fellow sufferers Dr. Robert Fendt and Ilka Hegemann also working on their theses reassured me that apparently all PhD candidates have to cope with certain degrees of exasperation. My mother Silvia and my sister Susanna were invaluable sources of support and encouragement. Finally, words cannot express how thankful I am to my wife Stephanie for her endless love and for being patient and understanding while I indulged in my passion for science.